Bauhaus-Universität Weimar

Stress Distribution in Buried Defective PE Pipes and Crack Propagation in Nanosheets

Dissertation
Zur Erlangung des akademishen Grades
Doktor-Ingenieur (Dr.-Ing.)

an der Fakultät Bauingenieurwesen
der Bauhaus-Universität Weimar

vorgelegt von
Reza Khademi Zahedi
geboren am 08. June 1981 in Izeh, Iran

Mentor:
Prof. Dr.-Ing. Timon Rabczuk

June 2021

Declaration of Authorship

I, Reza Khademi Zahedi declare that this thesis titled, 'Stress Distribution in Buried Defective PE Pipes and Crack Propagation in Nanosheets' and the work presented in it are my own. I confirm that:

- This work was done wholly or mainly while in candidature for a research degree at this University.
- Where any part of this thesis has previously been submitted for a degree or any other qualification at this University or any other institution, this has been clearly stated.
- Where I have consulted the published work of others, this is always clearly attributed.
- Where I have quoted from the work of others, the source is always given. With the exception of such quotations, this thesis is entirely my own work.
- I have acknowledged all main sources of help.
- Where the thesis is based on work done by myself jointly with others, I have made clear exactly what was done by others and what I have contributed myself.

Signed: _____

Date: _____

Abstract

Worldwide developments in science and technology and the production of new materials have prompted the quality of life. Oil and natural gas which are discovered within the earth are building block of many other products from polymers to advanced nanomaterials. Engineering structures made from aforementioned products, which bear or transfer several loads are expected to undergo the mechanical loading conditions during desired lifetime. However, the structures and materials may be defected during their lifetime due to several reasons. One of the problems associated with this concept is the determination of the strength of defective parts and to evaluate the loads that such an structure is capable to sustain. An understanding of failure mechanisms and fracture mechanics of an structure weakened by the presence of a defect play an important role in structural materials safe design. This dissertation is devoted to the numerical modeling and simulation of defective structure.

The focus of present dissertation is two folds which these are accomplished by means of large-scale and nano-scale software simulators. Medium density (MD) and high density (HD) polyethylene pipes and related fittings are widely adopted for above-ground and buried gas distribution networks. Under ground PE gas pipes may experience simultaneous effect of soil column weight, surcharge loads, internal pressure and temperature variations. In spite of the outstanding material properties and excellent underground installation techniques, defects with a wide variety of shapes and sizes, during construction, while installation or in the operation never can be excluded. The failure of natural gas pipelines can lead to serious human and environmental damages, with everlasting consequences. Thus, the predictability of pipeline failure is an important research field. According to the gas companies' reports, in real operating conditions the most common and dangerous types of defects in the buried pipe wall, which significantly limits the lifespan of the pipeline as well as its capability to carry loads are in the form of local partial or complete through-wall holes. Furthermore, polyethylene may fail when subjected to severe stress concentrators such as notches, welded joints and other form of defects introduced during installation or their lifetime period. These stress raisers weaken pipe strength and also reduce the pressure carrying capacity of the pipe. The actual 3D stress distributions in the vicinity of defects in the form of partial or complete circular holes are very complex and these stresses may exceed the yield limit of the pipe material in the small neighborhood around the defect. It is well known that the existence of defects in real material has a significant effect on the mechanical strength of the structure as they cause local stress concentrations and even may cause catastrophic

events. Thus, the importance of safety issues during pipeline operation, stresses investigating the mechanical behavior of defective PE gas pipes to a great significance for natural gas distributor companies. It is important to ensure that the stresses in the pipe remain below the allowable levels. Therefore, load capacity of the defective PE pipe should be determined, through the investigation of stress concentration factors and also stress distribution around the defects. Furthermore, there is the possibility of a singular stress state at sharp corners of the damage and cutout in the pipe wall.

Repair patches can be used in numerous applications to reinforce structural components or repair damaged parts by enhancement of the strength and stiffness of defective components and by reducing stresses in the area around the defect and delaying the initiation and propagation of the cracks. Patch repair strengthening approach, reduces the failure-extension driving forces. No approach currently exists to evaluate the stresses around partial hole defects in buried PE pipes in gas distribution systems. One of the objectives of the present dissertation is to evaluate and qualify the mechanical behavior of the PE pipe. We assess the effect of hole shape defects on stress values around the defect area and its variation through thickness within the pipe. Also the effectiveness of polyethylene (PE) repair patches which are perfectly bonded onto burird gas pipes by electrofusion welding is investigated. This is done by estimating elastic stress distribution using finite element method (FEM). Different reinforcing patch configurations were applied to the widely encountered damage senario in gas PE pipe i.e. complete and partial boreholes and studied for each defect case. The three-dimensional elastic stress field in the area around the defect was calculated, prior and after patch repairing. A fundamental approach of FEM in structural mechanics is outlined first by modeling defective pipelines. The numerical simulations were performed by ANSYS 16/2 mechanical and ANSYS workbench 19.2 which are commercially available finite element softwares. Since stress concentrations are very important, 3D SOLID95 elements, available in ANSYS software package elements library were employed to model pipe, reinforcing patch and surrounding medium. For the models with stress singularities, the linear elastic fracture mechanics for pipe strength assessment was employed to describe the stress field near the interior sharp corners. The method is based on the numerical calculation of stress intensity factors (SIF), in accordance with brittle failure using ANSYS workbench platform. SIF is a function of external loading, geometry of the pipe and geometry of damage and crack.

Based on the obtained results, in both above-ground and underground polyethylene gas pipes, stress concentration factors, maximum first principal stresses and maximum von Mises stresses, generally increase with increasing hole diameter and also hole depth (reducing wall thickness). Additionally, temperature changes in the defective PE pipes exhibits a direct and significant effect on thermal stresses produced in the pipe. For defect depth ratios (thickness reduction) below 8% and hole diameters up to 30 mm, the

peak stresses are close to unflawed (intact with no defect) simple pipe manufactured by polyethylene and are not influenced significantly by the damage itself, therefore these defects can be considered as non-intensive. Meanwhile, FE modeling results show that patch repair can strengthen the defected pipe section and reduce the imposed first principal and von Mises stresses significantly.

Today two dimensional (2D) materials play an important role in ours daily life and have attracted the attention of researchers and engineers. The second objective is to study the defects in two dimensional nanosheets by performing a molecular dynamics simulation. Experimentally fabricated two-dimensional materials have lately evoked significant attention in nanodevice fabrication industry. Therefore, we study the mechanical response of crystalline boron-carbide with the stoichiometry of BC_3, which is a novel two-dimensional (2D) graphene-like material. We investigate the mechanical properties of pristine (intact with no defect) and defective BC_3 nanosheets through classical molecular dynamics (MD) simulations. Therefore, several crack lengths and notch diameters were examined to predict the mechanical response at different temperatures under the uniaxial tensile loading. Our results indicate that larger cracks and notches decrease the strength of 2D graphene-like BC_3 nanosheets. Additionally, it was revealed that a temperature increase has a weakening effect on the tensile strength of BC_3 monolayer. Nonetheless, our MD results not only highlight the outstanding mechanical properties of graphene-like BC_3, but also reveal its advantages regarding its thermo-mechanical properties, which are critical for the design of nanodevices. Additionally we performed molecular dynamics simulation on pre-cracked all MoS_2 hetero structures. Our ReaxFF models reveals that for all studied crack sizes, 2H phase of MoS_2 films has larger strength. Fracture properties of composite 2H/1T MoS_2 nanosheet is higher than those for the equivalent 1T phase. We can imply that the pre-cracked composite structure is remarkably stronger than equivalent 1T phase.

Acknowledgements

First of all, I am highly thankful of my God who granted me the strength and the determination to complete my PhD study at Bauhaus Universität-Weimar in Germany.
I am deeply indebted to my dear academic supervisor Prof. Dr.-Ing.Timon Rabczuk, who is also the Chair of Computational Mechanics, Institute of Structural Mechanics, at Bauhaus University Weimar, for his constant support, valuable advice and guidance. Actually without his encouragement and understanding of many obstacles encountered during my PhD study, it would have been nearly impossible to continue and complete. He has been a very supportive supervisor and has given me the opportunity to pursue various projects without objection.
I would like to thank my co-supervisor prof. Rohan Rafiee from university of Tehran, faculty of New Sciences and Technologies for assisting me in many directions during my PhD studies, I am grateful to him. He was not only an excellent advisor but also a friend, who has taught me lessons which will always be important to me in my professional career. A special thanks to Prof. Dr. Mohammad Shishesaz from Shahid Chamran University of Ahvaz, Iran, as he provides me the vision of underground space.
I wish to offer special thanks to my late friend Ali Nasirian, who, although no longer with us but his memory is always with me.
I would also like to give a special thanks to Dr. Bohayra Mortazavi and Dr.-Ing. Ali Shirazi for providing a wealth of helpful advice and guidance related to the area of molecular dynamics simulation.
On a personal note, I would like to express my gratitude to my best friend and beloved wife Anis for her encouragement, undying devotion and her incredible patience. I owe my sincere gratitude for my daughter Arosha and my son Arad for enduring so much and remaining alone for a long time so that to support me. They have given me every reason to make them proud. I will always be indebted to my mother Mahin and my late father NezamAli, for their constant prayers and without whom none of the opportunities in my life would have ever been possible. I wish I could show my family, my endless love for them.
Lastly, this dissertation is dedicated to my late father, NezamAli, who has been constant source of inspiration to my life.. . .

Contents

List of Figures

List of Tables

Abbreviations

AASHTO	**A**merican **A**ssociation of **S**tate **H**ighway and **T**transportation **O**fficials
Ansys	**An**alysis **SyS**tems Inc.
FEM	**F**inite **E**lement **M**ethod
HDPE	**H**igh **D**ensity **P**oly **E**thelene
IPS	**I**ron **P**ipe **S**ize
ISO	**I**nternational **O**rganization for **S**tandardization
LAMMPS	**L**arge-scale **M**assively **A**tomic/**M**olecular **P**arallel **S**imulator
LEFM	**L**inear **E**lastic **F**racture **M**echanics
MD	**M**olecular **D**ynamic
MDPE	**M**edium **D**ensity **P**oly **E**thylene
MRS	**M**inimum **R**equired **S**trength
OVITO	**O**pen **VI**sualization **TO**ol
SCF	**S**tress **C**oncentration **F**actor
SIF	**S**tress **I**ntensity **F**actor

Symbols

Symbol	Description	Unit
a	half crack length	$\mathring{A}$
b_{ij}	bound function	
E	modified Tersoff potential	j
E	Elastic modulus	MPa
f_A	Repulsive potential	j
f_C	cutoff function	
f_R	attractive potential	j
K_{IC}	critical stress intensity factor	MPa.m$^{0.5}$
K_I	opening mode of SIF	MPa.m$^{0.5}$
K_{II}	sliding mode of SIF	MPa.m$^{0.5}$
K_{III}	tearing mode of SIF	MPa.m$^{0.5}$
h	half nanosheet width	$\mathring{A}$
i	marks an atom	
j	marks an atom	
k	marks an atom	
L	nanosheet length	$\mathring{A}$
r_{ij}	Position vector between i and j atoms	
χ_{ij}	fitting parameter	
ε	strain	
σ_f	fracture stress	MPa
ω	angular frequency	rads^{-1}
K_t	stress concentration factor	
$T(y,t)$	soil temperature	k
y	depth in question	cm

t	time	sec
$\bar{T}$	average climate temperature	k
A	a temperature difference	k
α	thermal diffusivity	cm^2/sec
t_0	time	sec
E_p	pipe elastic modulus	MPa
α_t	coefficient of thermal expansion	$1/°C$
ΔT	temperature change	k
σ_s	design stress	MPa
σ_{MRS}	minimum required strength	MPa
C	design coefficient	
D_{SDR}	standard dimension ratio	
P_{max}	maximum operating pressure	MPa
Δx	horizontal deflection	m
K_b	bedding factor	
L_d	deflection lag factor	
E'	embedment soil modulus	MPa
D_i	pipe inner diameter	m
D_o	pipe outer diameter	m
$\sigma_{\theta\theta}$	maximum circumferential stress	MPa
σ_{rr}	maximum radial stress	MPa
σ_{zz}	maximum longitudinal stress	MPa
k	diameter ratio	
ν	Poisson's ratio	
P_i	pipe internal pressure	MPa
σ_e	von Mises stress	MPa
σ_{max}	stress	MPa
σ_{nom}	nominal (reference) stress	MPa

This work is dedicated to:

My loyal wife (Anis)

My lovely daughter (Arosha) and dearest son (Arad)

My beloved mother

and

The soul of my father

Chapter 1

Introduction

1.1 Motivation

Worldwide developments in science, industry and technology and the production of new materials, improved machinary and equipment have prompted the quality of lives. One of the major goals that is often followed by manufacturing and production industries is the reliability of their products [1]. The existence of defects in some produced parts will cause the catastrophic failure of whole structure which will result in loss of life and property. Cracks, holes and notches are among the major defects which may appear in a structure. Therefore, the evaluation of structural integrity of a defective structure has become an important mater in the industrial field. As the final failure in parts and structures usually happens by the initiation and propagation of the crack, investigation and research in these fields will be effective and appropriate [2]. The increasing daily need for the detection and evaluation of flaws and defects in overall parts of a complicated structure and to understand the physical mechanisms behind the mechanical behavior of a defected structure lead to the chasing of some methods by researchers in which the variation in specification of whole structure to be investigated [3].

1.1.1 Finite element modeling of defective pipes

Since plastics are used to design many products, a complete understanding of the mechanical behavior of these materials is of great importance. Specially, the increasing demands for polymeric materials in engineering applications require new methodologies to evaluate material capability to withstand applied loads. The existence of defects in real material has a significant influence on the mechanical strength of the structure as

they cause local stress concentrations. Thus, the importance of safety issues during pipeline operation, stresses investigating the mechanical behavior of both above-ground and buried defective PE gas pipes to a great significance for natural gas distributor companies. It is obvious that such defects, introduce geometric discontinuities to the pipe configuration and hence a stress singularity locus, when the pipe is loaded. One of the main objectives of this dissertation is to understand the physical mechanisms behind the mechanical behavior of the aforementioned defective pipes. In order to investigate failure behavior, stress analysis around the damage area of the pipeline must be performed in advance. It is important to ensure that the stresses in the pipe remain below allowable levels. Therefore, load capacity of the defected PE pipe should be determined [4]. Additionally, in linear elastic fracture mechanics (LEFM), parameter stress intensity factor is one of the most imperative fracture parameters used to determine the structural integrity of components with flaws. The ability of FEA to determine the fracture parameters of defective PE pipe is also studied. A proper understanding of the severity of the stress in the regions of high stress field would lead to usage of less conservative safety factor, enhanced safety, better design method and consequential increase in above-ground or buried pipe life.

Repair patches can be used in numerous applications to reinforce structural components or repair damaged parts. This process of structures repair increases the service life of damaged components. Repair patches enhance the strength and stiffness of defective components and their proper application will reinforce the damaged component and delay the initiation and propagation of the cracks in damaged section of the structure such as defective buried PE gas pipe [5, 6]. Compared with bolted patches, bonded patches are known to be more efficient beacause they can avoid the risk of further damage caused by stress concentration around the side holes on both the patch and the substrate [7]. The mechanism in patch repair approach is to have reinforcing patch material in the defect and fracture zone which can do bridging and strengthening. The patch material increases the fracture resistance of the materials by reducing the failure-extension driving forces, as a portion of the load is carried by the reinforcing patch. The reinforcing patch do not fail, because it has a very higher strength. Therefore, the other objective in this dissertation is to conduct numerical simulations to understand the physical mechanisms behind defective pipe strengthening by repair patches, which carried out to the widely encountered defect in underground gas pipe i.e. notches.

1.1.2 Molecular dynamics simulation of two-dimensional materials

Two-dimensional (2D) materials has been in increasing demand since fabrication of the graphene. These single-layered nanosize materials represent extra-ordinary thermal, mechanical, and optoelectronic properties. Nano-materials have promising and industrial applications e.g. in energy storage and supply, nanosensors, spin filter devices and fuel cells. Nevertheless, defects consistently exist in two dimensional materials, because there is no ideal fabrication process. Among the most significant defects in materials are nano-cracks which can extremely weaken the mechanical properties of the nano-material. Newly synthesized crystalline boron-carbide with the stoichiometry of BC_3 has attracted many attentions due to its extraordinary mechanical and thermal properties. The other two dimensional nano-material is molybdenum disulphide (MoS_2) which has triple atomic planes with different stacking sequences. The failure behavior of MoS_2 nanosheet is more complicated than those of graphene, BC_3 and other graphene-like materials. It is worth to investigate their fracture properties in its pristine and defective states. We hope that the results obtained from MD simulations in the present study not only be helpful for both experimental and theoretical researches but also apply to design advanced nano-devices.

1.2 Objectives of the dissertation

Determination of the strength of structures and the mechanism of their failure play an important role in structural safe design. Specially, the existence of defects is then a major source of weakness in the material due to high stresses that occur. Meanwhile, buried pipe systems and also two-dimensional nano-material prototype testing is very complex, expensive and time consuming. It is also very difficult where the measurement of stresses and strains is concerned. Numerical models are important type of models established to predict mechanical behavior of structures. Reduction in cost and time, required to develop model, is the most significant advantages of the numerical models over other kinds. Additionally, more availability of powerful computational tools and software in the last decade compared to the time initial models introduced is an additional motivation of researchers to try to propose models of structural failure prediction. The work in this dissertation aims to:

1- Performing numerical simulation to investigate mechanical behavior of above ground polyethylene pipelines of natural gas distribution systems, under the effect of internal pressure, daily and seasonal temperature variations and in the presence of defects which lead to stress concentrations due to local changes in the pipe geometry, through ANSYS

16.2 mechanical finite element analysis software. As the severity of high stress concentrations in the pipe depends on the geometrical configuration of the defect, therefore, different configurations of partial and through-wall radial hole diameter and depth are examined.

2- Constructing proficient finite element models to perform three-dimensional elastic stress analysis and calculations on underground defective polyethylene pipes for gas distribution by considering the effect of applied loads including seasonal and daily temperature variations in the soil (and therefore in the pipe), the weight of the soil column above the pipe, the surcharge loads including live traffic (vehicle wheel) and dead loads above the pipeline, gas internal pressure which is considered to be approximately 4 bar (405300 Psi) and stress concentrations due to local changes in the pipe geometry.

3- Determining the character of the singular stress state which exists at the iterior sharp corners resulting from partial circular voids in the PE pipe wall by using a standard 3D-FEM model based on LEFM for the stress intensity factor characteristics to predict the stability of pipes to prevent a brittle failure.

4- Predicting the role of different polyethylene reinforcing patch configurations in reinforcement of the defect area in the pipe, for each defect case. Therefore, in order to the determination of relieving effect of the patch on the stress concentration at the defect, the stress field in the area around the defect is calculated, prior and after patch repairing.

5- Estimating the physical properties and thermo-mechanical responses of BC_3 monolayers, not only in pristine form but also to study models containing cracks and notch shaped defects by carrying out uniaxial tensile simulations. We predict the crack and notch propagation in two dimensional (2D) materials for several crack lengths and notch diameters and at temperatures from 200 K to 900 K. The location of the crack and notch shaped defects are assumed to be in the middle of nanosheet (centrally cracked/notched sheet) .

6- Using ReaxFF molecuar dynamic simulations to investigate fracture behavior and crack propagation in MoS_2 nanosheets (with a central crack/notch) including both 2H and 1T phases and also 2H/1T hetero-structure by carrying out uniaxial tensile simulations for several crack lengths and notch diameters at ambient temperatures.

1.3 Outline of the dissertation

As summarized, the current understanding of defective gas pipe strengthening and the mechanisms behind it is still under debate. In addition, mechanical and fracture behavior of new two-dimensional materials requires more investigation. This dissertation is

summarized in seven chapters. **Chapter 1**, presents an overview of numerical simulation, motivation and objectives. The outline of presentation can be listed as below:

Chapter 2, Presents a literature review of the research. As the main attention of the research is two folds, therefore, this chapter also is splited into two main sections.

Chapter 3, Generally introduces and presents an overview of the above-ground and buried polyethylene pipelines in natural gas distribution systems and discusses some fundamental concepts in linear elastic stress analysis to understand the effect of several damages mainly complete through-wall holes and local partial holes in the gas pipe wall under several loading conditions. In addition, the chapter introduces a strengthening mechanism for the pipes under aforementioned imposed damages. Where possible, analytical and theoretical equations and loading conditions are discussed.

Chapter 4, Presents an overview of stress analysis and evaluates the results of stress distribution in above ground pipelines subjected to partial and complete circular holes, by performing a three dimensional finite element analysis. Since the near defect stresses especially hoop, first principal and von Mises stresses play an important role in this study, a clear understanding of these stresses is required. Details of proper finite element model for predicting aforementioned stress distribution are presented. A fracture mechanics analysis is performed to determine stress intensity factors at interior sharp corners of the defect. Meanwhile, the problem considered in the last section of this chapter is the determination of the relieving effect of reinforcing patches on the stress concentration at the vicinity of the defect in the above-ground PE pipe.

Chapter 5, Investigates the effect of local partial and complete through-wall circular holes on stress distribution in buried defective polyethylene gas pipes, as the buried pipe is under the simultaneous effect of several complicated loads. This sections includes three dimensional finite element analysis and solution to predict near defect stresses in buried gas pipes. Finally, the simultaneous effect of several loads on mechanical behavior of patch repaired pipeline is well evaluated in order to predict whether successful pipe strengthening operation is applied. A deep insight on the methods and analysis used in this part of research is provided.

Chapter 6, Predicts mechanical properties of graphene-like BC_3 nanosheets through a molecular dynamics simulation. All molecular dynamics modeling in this study were carried out using open-source software LAMMPS (Large-Scale Atomic/Molecular Massively Parallel Simulator) [8]. In order to determine the bonding interactions between carbon-carbon atoms, we employed the optimized Tersoff potential proposed by Lindsay [9]. Furthermore, the Tersoff potential parameters used to introduce the bonding interactions between the boron-carbon atoms were adopted from Kinaci et al. [10]. In this chapter, an overview of fracture behavior and fracture growth which governs the fracture pattern in graphene-like BC_3 nanosheets is examined. Simulations in this work assume Mode-I fracturing in centrally cracked nanosheet.

Chapter 7, Investigates the fracture strength and crack propagation of all phases (2H, 1T and 2H/1T hetero structures) of MoS_2 single-layer structures with pre-existing central crack and notch defects by conducted ReaxFF based molecular dynamics (MD) simulations. We studied the effect of different nano-crack sizes (lengths) and nano-notch diameters on the single-layer MoS_2 mechanical and failure response, especially on elastic modulus, tensile strength and strain at failure, by uniaxial tension tests. To better understand the underlaying mechanisms resulting in tensile response of defective single-layer MoS_2, we analyzed the deformation process by calculating the tensile strains corresponding to the point where fracture occurs.

Chapter 8, Presents and summarizes the main conclusions obtained from this dissertation and suggests extensions to the current work and recommendation for future research.

Chapter 2

Literature review

2.1 Defective pipe and buried pipe design

As mentioned previously, the main attention of the present research is two folds. Therefore, this chapter is splited into the two main sections, where the first section discusses the mechanical behavior of defective buried pipes.

2.1.1 Introduction

Oil and gas industry is one of the largest industries in the world with a very exceptional impact on the world economy. Although in recent two decades, worldwide research has been conducted by scientists into renewable energy resources, including solar, wind and ocean energy to replace petroleum, natural gas and condensates, the demand for fossil fuels energy sources are still increasing. Petroleum, natural gas, and condensates are naturally occurring substances which are discovered within the earth's crust, are thought to originate from decomposed animal and plant matter. Scientists believe the plants and animals died in the distant past, and were gradually buried by thick layers of sediments. Over a long period of time, and with pressure and temperature, the organic materials were transformed into the oil and gas which are found today. When oil and gas are removed from the ground they are sent to refineries by pipelines. Then, many products from these materials, which potentially contain several chemicals called hydrocarbons, can be obtained including energy for power, motor oil, gasoline for cars, diesel fuel for trucks and trains, hi-octane fuels for planes, heating oil for houses etc. Several other materials also come from petroleum such as plastics, asphalt, grease, lubricating oil, materials for clothes, chemicals for everyday use, paints etc. Since oil has natural gas in it, when oil is produced often some gas is produced with the oil if natural gas is in the

solution. The majority of oil is trapped in the tiny pore spaces between grains of rock or sand. Oil and gas are discovered in natural traps which consist of domes or faults within the earth. Impermeable rock above the trap that fluid cannot pass through it stops the oil and gas from move up to the surface. Without traps, the oil and gas could migrate all the way to the surface and evaporate. Fig. 2.1 shows an example of an oil reservoir with a gas cap. As illustrated in this figure, buried pipelines are recognized as main choice for transporting natural hydrocarbon fluids (ie. oil and gas). Buried pipelines cross various regions including both remote countryside and urban areas, which make them at the risk of environmental threats.

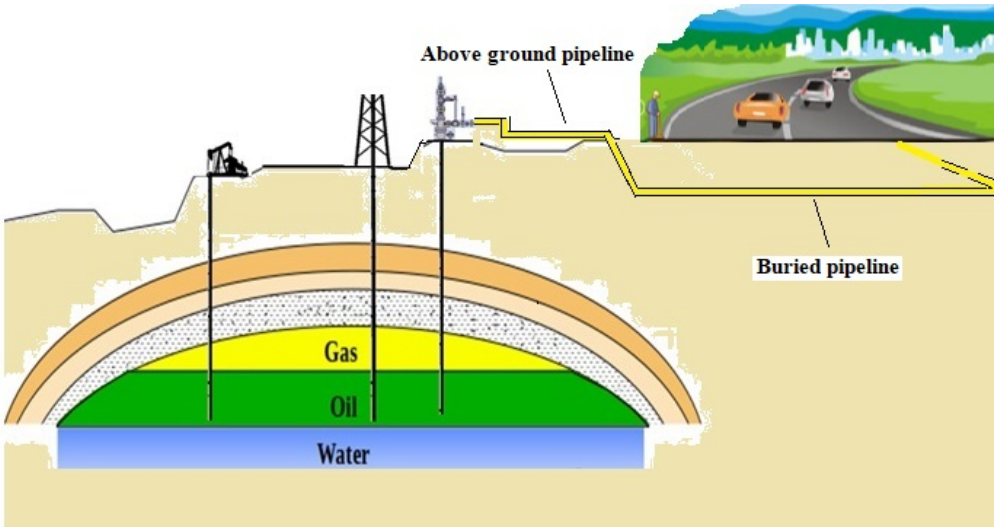

FIGURE 2.1: An example of an oil reservoir with a gas cap and transmission pipeline.

After geophysicists find reservoirs and process the data to construct pictures of what the earth looks like underground, drilling companies start to drill into the proposed reservoirs. A drilling rig is a package of special equipment put together that enables us to create a hole to a projected depth for producing oil or natural gas [11–14]. Finally, the well is produced into a pipeline, which takes it to production facilities on surface. The production facilities on surface separate out the gas, oil, and water into their separate phases. From there, the oil and gas may be refined further before being ready to market. Finally, the gas and oil can be sold to power cars and heat houses. One of the major aspects of the petroleum industry is oil and gas transmission section. The oil and gas transmission industry is a technology dependent industry. It is considered to be one of the most expensive operations in the world as they require huge expenses to be spent on transmission pipelines. A pipeline network needs a long length pipe to dispatch natural gas. It is troublesome to produce long pipes, hence the needed lengths of pipe is assembled by connecting short pipes together. Additionally, in order to construct long

pipe networks, it is essential to utilize joining methods. Therefore, any sorts of tools and methods that can improve the gas and oil transmission operation at a low expense are essential and required during any activity. Today polymer materials are widely used in construction areas and especially in the pipeline industry.

As mentioned above, the use of petroleum transmission pipelines originated with the drilling of first commercial oilwell in 1859. Since then, the pipeline industry has grown rapidly and continues to produce more reliable pipe materials and find better ways to install pipelines under the ground. Therefore, decades of experience have proved that, pipelines are the safest, most reliable and economical transportation products to convey hazardous substances such as natural gas.

Worldwide developments in science and technology and the production of new materials have prompted the quality of lives. Plastics materials are derived from petroleum or natural gas after processing in refinery. The use of polymers in load-bearing structural components is increasing. Since plastics are used to design many products, a complete understanding of these materials is of great importance. Polyethylene (PE), in its many resin grades and densities, is by far the most widely used plastic in the world. Polyethylene (PE), is obtained from petroleum or natural gas mainly by polymerizing ethylene gas. This thermoplastic polymer is composed of long chains of monomer ethylene. High density polyethylene (HDPE) is sometimes referred to as linear polyethylene (LPE) due to its very low level of branching. The principal advantages of polyethylene including its balance of physical properties in the solid state, its chemical inertness, its low cost and ready processability make it the material of choice for a wide range of applications. Polyethylene is a tough and flexible material with a high electrical resistance. The mechanical properties of polyethylene material may be categorized into two wide types including low strain properties such as yield stress and initial modulus, and high strain properties. Like other engineering materials, the modulus of elasticity of polyethylene sample, which is a measure of its rigidity, is normally estimated from the initial slope of the force versus elongation plot. Up to the yield point the deformation in polyethylene specimen is principally elastic. The tensile strength also known as ultimate tensile stress of this polymeric material, which is the force required to break it divided by its cross-sectional area, depends largely upon the draw ratio at break of a sample. For high density samples the true ultimate tensile stress is approximately inversely related to their molecular weight. The tensile properties of polyethylene specimens are greatly affected by temperature where the response of samples to temperature is affected strongly by their molecular characteristics [15].

Polyethylene pipes and related fittings are widely adopted for water, sewage, and natural gas distribution networks in several countries. Additionally, industry interest in the use of PE pipes as an alternative to traditional steel or metal pipes remains high. Over a period of several years, PE pipes provide numerous benefits when compared to traditional

steel or metal pipes. The commercial advantages include their coilability, durability, light weight, flexibility, high ductility, weldability, reduced installation costs and low life cycle expenses. Particularly, polyethylene material is resistant to corrosion and chemicals, abrasion impact and fatigue and seismic loads. The aforementioned advantages provide both performance and economic benefits that in turn lead to the popularity of polyethylene pipes in ploughing-in and trenchless technology applications. Nowadays, polyethylene (PE) composes a large number of natural gas distribution pipelines which are being installed under the ground because the physical properties of polyethylene perfectly meet the requirement of natural gas distribution lines [16]. Beside the mentioned advantages, there are some limitations in the application of polyethylene. These disadvantages include its high thermal expansion, poor weathering resistance, stress cracking effects, bond difficulties, poor temperature capability and flammability. Polyethylene indicates a high tendency toward stress relaxation. Failures caused by stress relaxation consist of leakage from compression fitting and joints which are formed by forcing flexible polyethylene tubing over a rigid pipe. Therefore, polyethylene is rarely used in applications in which stress relaxation is likely to happen [15]. In addition to stress relaxation polyethylene can fail in a brittle manner when subjected to stress concentrators such as scratches, notches, joints formed by welding, incisions on the surface and inclusions or scratches introduced during installation, especially in gas and water distribution pipes [15]. Flame retardancy of polyethylene is becoming an important issue for its industrial application. Since polymer combustion includes a certain pattern of: preheating, decomposing, ignation and combustion, flame retardants have been used to interrupt the cycle [17].

In the recent 60 years, several advancements occurred in polyethylene production technology. This has led to different products including PE80, PE80B, PE80C, and PE100 materials that are currently used across the world. Specifically, PE80B and PE80C pipe materials are recognized as offering excellent long-term performance as pressure pipes. Medium density polyethylene (MDPE) or yellow PE80B and high density polyethylene (HDPE) PE100 materials find immense utility in ploughing-in applications due to their flexibility and ease of coiling. The steady growth in the use of polyethylene pipelines for natural gas transmission and distribution networks and the plan of natural gas distribution companies to extend the number of miles of distribution and transmission PE pipes in the immediate future warrants the need for safe, reliable and efficient operation of these pipelines [18]. Therefore, the aforementioned desired applications require PE pipelines to undergo the mechanical loading during lifetime.

Generally, buried pipes are divided into two categories: flexible pipes, where the pipe deforms under applied loads at least 2 percent of the pipe diameter without any effect to the pipe material, and rigid pipes where the pipe structure changes (for example with crack creation) in the aforementioned deformation [19]. PE pipes behave as flexible pipes

when installed underground. In the underground application of PE pipes, the installation procedure and the design method are of great importance for natural gas distributor companies. The traditional method of installing underground utilities such as pipes is cutting a trench and then covering pipelines. After the excavation of a long trench, pipes are buried and supported by embedment which is built by surrounding pipes with firm and stable material. Gas company officials and engineers must provide the soil to establish an envelope of supporting material around the pipe and its related socket so that the deflection to be preserved at an allowable tolerance. The pipe deflection range is determined by the aforementioned enveloping support, the burial depth, traffic loading from the surface, the pipe internal pressure, the pipe standard dimension ratio (SDR), and any local discontinuities resulting from different joints, reinforcing patches or other accessible causes [20]. The first step in buried pipe design is to determine the soil dead load and surcharge loads on the pipe and ensure the safe operation of the PE pipes for a long period of time. The applied loads on underground polyethylene pipes for gas distribution which should be considered in all designs and stress analysis and calculations can be categorized as follows [21, 22]:

1- Seasonal and daily temperature variations in the soil (and therefore in the pipe).

2- The weight of the soil column above the pipe.

3- The surcharge loads including live traffic (vehicle wheel) and dead loads above the pipeline.

4- Gas internal pressure which is considered to be approximately 4 bar (405300 Psi).

5- Stress concentrations due to local changes in the pipe geometry.

The above mentioned loads induce horizontal and vertical deflections along with significant stresses in the pipe wall. Consequently the soil reacts to the aforementioned pipe action and will limit the pipe deflection. Careful attention is required to minimize the stress level on the buried pipe caused by the aforementioned applied loads.

The design, analysis and modeling of a structural component can be done successfully through an understanding of the mechanical properties of the material. Engineering structures bear or transfer several loads and may be defected during their lifetime due to several reasons. An understanding of fracture mechanisms plays an important role in structural materials safe design. Like most engineering components, gas supply pipelines may experience some kinds of defects during their lifetime. While defect management has been employed in many industries, its importance in some sections of gas and oil industry still is not completely understood. The defects in natural gas distribution pipes are especially in the form of cracks and notches. These geometrical discontinuity cause local stresses and strains in the damage neighborhood. Failure in load bearing structure may occur mainly at stress concentration regions. The actual 3D stress distributions in the vicinity of the defects in the form of notch or circular side hole are very complex and

these stresses may exceed the yield limit of the pipe material in the small neighborhood around the defect. If the proper 3D stress fields in the region of the pipeline defects not to be considered, dangerous failure might encounter to the pipelines of gas distribution systems, above the ground and also under ground applications. The reason is that for example when cyclic loading is applied to the pipeline with notch shape defect, cyclic inelastic strains in the region of the stress and strain concentrations may cause the nucleation of the cracks and their subsequent propagation could result in catastrophic fracture. Although some experimental and theoretical studies on defective gas pipes have been reported, it is not understood to what extent of defects in pipes, the stresses still remain below the allowable limits. How important are loading conditions and defect size and shape? What should be done with a new defect in the pipe wall and what is the upper bound for defect size increase? However, it has been found that polyethylene pipe material behave in a brittle manner in the presence of cracks and small flaws with sharp edges. As a result, rather than fail by yielding, service failure can occur by brittle fracture at stresses below the design yield strength of the material. This brittle fracture will initiate at points of high stress. One location of these high stresses is at interior sharp corners or the tip of cracks where the stress field theoretically has a singularity of order $r^{0.5}$, where r is the distance from the crack tip [23].

Due to the vast usage of polyethylene lines in the natural gas industry, gas companies are repeatedly seeking ways to develop repair methods. Even with previously mentioned enhanced properties, polyethylene pipe lines are still expose to damage during their lifetime. Therefore, efficient repair methods have been in development since polyethylene gas pipelines were installed under the ground. Normally, butt fusion and electrofusion weld procedures are used to join polyethylene pipe sections together. Furthermore, the increasing complexity of modern assembled structures and the diverse types of materials used have led to many joining applications that would not be possible with more conventional joining techniques. Adhesives are also being used either in conjunction with or to replace mechanical fasteners and welds [24]. The conventional repair methods for underground polyethylene pipelines which includes large excavating sites of the damaged pipeline, isolating and squeezing off a large section of the pipe, cutting out the defected piece and fusion welding in a replacement section of pipe, is very expensive and time consuming, and specially these repairs unpleasantly affect traffic during the repair procedures. Therefore, gas companies have been moving toward keyhole isolation and repair technologies.

For polyethylene materials, the rupture properties involves the generation of fresh surfaces under the effect of suddenly imposed tensile or flexural stresses. The main type of polyethylene rupture in thick specimens is crack propagation through material, such as the wall of a pipe. Inelastic deformation and the formation of new surface areas are the

two processes that absorb energy in the rupture of polyethylene. The items manufactured from polyethylene are not stable under the application of the prolonged stresses. Morphological instability can display itself as creep, stress relaxation, brittle failure, and environmental stress cracking.
Over the years, finite element method (FEM) has been applied and proven as a powerful and useful tool for solving practical problems in several areas of petroleum industry. Finite element models have the capability of considering geomechanical properties of the soil and formation. Wherein, the existing analytical solutions can not accurately predict soil-pipe interaction behavior due to the complexity of the process and boundary conditions. The increasing number of publications on the application of FEM in gas and oil transmission industry shows that this is a potential methodology to decrease transmission expenses, increase gas and oil transmission operation safety, by solving previous problems and experiences reported by experts. One of the main objectives of this research is to investigate the aforementioned concepts of defects in above-ground and buried pipelines of natural gas distribution systems and also their strengthening by patch repair method, using the numerical simulation (FEM). In patch repairing, part of the applied loads is transferred from the pipe to the reinforcing patch. ANSYS 16.2 mechanical APDL and ANSYS workbench finite element analysis softwares are used to model and analyze the PE gas pipe problem.

2.1.2 Literature review of defective pipes and buried pipe design

While many cylindrical pressure vessels or piping systems may be 'perfect' in the sense that no geometric discontinuity, or stress-raiser, is introduced into the cylindrical barrel, many other cases arise where for practical reasons some kind of a small transverse openning or bore holes are unavoidable [25]. Analytical solutions for stress distributions around an isolated circular and elliptical hole in a plate have been investigated [26–28]. By using the classical solution to the problem of a round hole in an infinite plate subjected to uniform tension [26], the elastic stresses surrounding a small round cross-bore drilled radially through the wall of a cylinder can be found approximately. The effect of cross bore size and configuration on the stress distribution in a thick-walled cylinder have been cited [29, 30]. The effects of radial cross bores on both stress concentration factors and stress distributions in thick walled cylinders have extensively been studied [29, 31–36]. Noteworthy, in each case the cross-bores were in the form of circular holes of small diameter, running diametrically across the main cross-section. The investigations were primarily experimental but the researchers drew attention to the elastic stress analysis. The severity of these high stress concentrations depends on the geometrical

configuration of the cross bore at its junction with the main bore, such discontinuities frequently produce a loss of strength and hence a reduction of pressure carrying capacity of the container [29]. Although some experimental and analytical attempts have been made to predict stress distributions as well as stress concentrations, numerical methods was also used to analyse the stress distribution and stress concentration on radial circular cross-bores in thick-walled cylinders. Masu [37], performed a three-dimensional finite element analysis for closed ended thick-walled cylinders with a cross-bore under internal pressure. In this research, the cross-bore diameter size effect on the principal stress distribution as well as stress concentration factors were investigated.

In summary, for a buried pipe, a supporting envelop is constructed by the surrounding soil with firm and stable materials. The envelop is often referred to as the "embedment". The amount of support by the embedment is directly proportional to its stiffness. Hence, often the embedment material is compacted [38]. The stiffness of the materials placed above the pipe may also affect the pipe's performance. A significant load reduction on the pipe may occur due to the arching effect in the soil. This results in a complex stress distribution in the soil above and around the pipe. An increase in the stiffness of the backfill above the pipe increases the amount of arching that occurs. Therefore, while installing the polyethylene gas pipe under the ground, to obtain the needed standards, suitable materials must be employed in each layer around the pipe.

The use of any pipe in conjunction with its mechanical properties and geometric design requires strict attention to minimize the stress level caused by the applied loads [20, 38]. The required information to investigate polyethylene pipes and fittings can be obtained via stress and strain analysis. The applied loads on a buried gas pipe must include daily and/or seasonal temperature changes, weight of the soil above the pipe, surcharge loads, inside pipe pressure, and stress concentration due to any local discontinuity or any external attachment to the pipe [21, 22]. Several experimental and analytical methods have been proposed by researchers to calculate the applied loads, deflections, and stresses on the buried pipes and although suitable for most underground applications, do not produce accurate results. The modern buried-pipe design was proposed by Marston from Iowa University in the early 20th century. He determined the resulting stress produced in a buried pipe due to the applied loads. Subsequently, Spangler continued theoretical studies on flexible buried pipes by assuming soil and pipe as linear elastic and isotropic materials and also in conjunction with experimental studies, he propose the Iowa's modified formula. The formula predicts flexible buried pipe deflection under applied loads [39]. Using simple linear-elastic formulations to study buried pipe problem is a very simplistic approach. These models are very convenient and easy to implement; however, when the outcomes compared with related experiments, it revealed that linear elastic deformation simplifies the results to a great extent. Watkins et al. [20] developed a more advanced formula to calculate the elastic modulus of the soil around a buried pipe

that yields better results when compared to Sprangler's formula. Afterward flexible pipe materials including aluminum, polyvinyl, and polyethylene were used in underground applications to improve pipe-soil behavior and reduce costs.

With respect to a better estimation of the behavior of PE pipes under the applied loads, several authors [40, 41] attempted to investigate the soil–pipe interaction effect of sewerage plastic pipes. The performance of elevated temperature on the buried high density polyethylene (HDPE) pipes was also investigated by Alawaji, [42]. In his study, the effect of temperature on deformation characteristics and performance of HDPE was investigated. The testing program was composed of a ring pipe submerged in heated water at various temperatures. Popelar [16] investigated the mechanical and creep properties of polyethylene gas pipe materials, namely PE23061X and PE3408IV. In the study, stress-stain diagrams were obtained under different conditions. Teoh and Ong [43] also investigated the pressure rupture in HDPE pipes.

In structural design process, it is necessary to properly design structures such that they perform safely during their life time expectancy. Thus, it is necessary for designers to possess a fundamental understanding of the behavior and failure [44–49]. Due to several reasons, polyethylene gas pipes can be damaged during long term use. This can result in the leakage of gas that must be prevented in the shortest possible time with minimum repair cost. Thus, different repair methods were developed including patch repair (or saddle fusion) bonded to the injured portion of the pipe. The method of electrofusion for joining two PE pipes was discussed by Mehrabi and Bowman in Ref. [50] while Refs. [18, 51, 52] focus on the design tools and repairing methods applied to defective polyethylene gas pipes. As mentioned, actually the damaged structures are repaired by reinforcing patches, but some researches are carried out to elongate the lifetime of the structures by attaching the reinforcing patch to the undamaged structure [7, 53].

In the study conducted by Green et al., [18] a remote external tool was developed to repair a defective PE gas pipe by using a polyethylene patch without introducing any interruption in gas flow inside the pipe. Harris K. E. [51], examined the development of a reinforcing patch composed of a solvent swollen polyethylene film that could be applied to a live natural gas line. The patch was applied under elevated temperature conditions allowing for a modified solvent weld and effectively repairing the pipe line in a quarter of the time required for repairing process. The aforementioned advantages of PE patch repairs, as well as the good output from limited existing repairs in gas pipes, have triggered the interest towards the further investigation of this new technology so as to be widely accepted as a repair method. Different defect shapes, positions and lengths is considered as well as different reinforcing PE patch configurations for the rehabilitation of these defects. In this research, we perform a numerical investigation on these cases so as to evaluate the effectiveness of the repair.

Experimental studies performed by Chua [54] included the time dependence interaction

of the soil and flexible pipes. Popelar et al. [55] performed a comprehensive study to determine the mechanical behavior and properties of medium density polyethylene (MDPE) and HDPE that are commonly used in the gas pipe industry.

Experimental investigations of underground space are cumbersome, expensive and in some cases impractical. On the other hand, pipe-soil interaction is a combination system that significant share of the applied load is carried by the soil around the pipe which makes it difficult to calculate the induced stresses in the pipe material. Furthermore, while the finite element method (FEM) is mostly used in CAE, several researchers employed commercial FE packages to model the buried pipe problem. Finite element method is one of the strongest numerical approaches to investigate underground structure responses to the applied loads. Abaqus and Ansys software has been used by several researchers for three-dimensional modeling of the aforementioned structures. For example, Shishesaz and his colleague [21] applied finite element method and used ANSYS software in order to analyze the resulting stress effects of different simultaneous loads on buried gas distribution pipes in 120 centimeters depth in soil. In this research the capability of utilizing Medium Density Polyethylene Pipes (MDPE) and the proper sockets made of High Density Polyethylene material (HDPE) in natural gas distribution networks in areas with hot climate conditions like south western of Iran and Ahwaz city is investigated. After that Nasirian [56] continued the research in reference [21] and investigated stress in simple pipes with 90 millimeter diameter and polyethylene material with connections buried in 1.45 meter depth of ground. The gas pressure in pipe was considered to be 4 bars. In the mentioned analysis, soil and pipe were assumed to be elastic and isotropic. Soil, pipe and the surrounding are meshed using ANSYS software and discretized with appropriate finite elements (SOLID95), which adopted in the present paper. Afterwards, Khademi Zahedi [57] performed a comprehensive finite element simulation to calculate stress distribution in underground patch repaired polyethylene gas pipes using ANSYS software.

Due to the complexity of the model, buried pipe simulations are computationally expensive and involve several minutes to hours of CPU usage. Improvements in the accuracy of the results without increasing the computational costs is of immense concern. Generally, the uncertainty in the model outputs increases as the models become increasingly complex. This is due to the randomness in the input parameters [58]. Therefore, uncertainties that could arise in the input parameters, such as internal pressure, temperature changes, surcharge load, soil column weight, defect geometry, and pipe and patch mechanical properties, should be carefully considered to determine the change in the model output (maximum von Mises stress) due to variation in the aforementioned inputs. Uncertainty and sensitivity analysis are very important for the aforementioned purposes [58, 59]. Recent developments which account for the important problems of

fluid-structure interaction driven fracture as in the immersed particle method is discussed in [60]. The method is aimed at problems with high-pressure and low-velocity fluids, and is illustrated by the simulation of problems involving fracturing cylindrical shells coupled with fluids.

2.2 Molecular dynamics simulation of two-dimentional materials

2.2.1 Introduction

Carbon based two-dimensional (2D) materials with honeycomb atomically thin lattices, have attracted the attention of numerous researches, especially since the development of graphene [61]. Numerous experimental and theoretical studies have confirmed that, graphene has outstanding electrical, thermal, chemical and exceptional mechanical propertiesdue to the planar arrangement of carbon atoms. Graphene is commonly fabricated by mechanical exfoliation of a single sheet of graphite [62, 63]. Unfortunately, this production method is labor-intensive, slow and scale and quality control is difficult. Despite all the wonderful properties of graphene, its reliable and cheap large-scale production remains a major challenge for the industry. Therefore, new fabrication ways are currently under development. Oil and gas which are mostly used to generate electricity are crucial for the production of plastics, food and many other materials [11–13]. Graphene manufacturers often use a thermal process to 'bake it' out of methane gas (CH_4) which is widely accessible. In this method, chemical bonds between carbon and hydrogen atoms are broken until carbon atoms finally form graphene. This method can produce sufficiently large sheets which can be of (5×5) cm^2 dimension in a very short time and high quality [64]. Graphene is a very good chemical barrier and flame retardant coating preventing oxygen to reach the flame and therefore preventing fire from spreading. The maximum allowable tensile stress for graphene is 130.5 GPa, i.e. it can withstand tensile loads hundred times more than high strength metals [65]. The extremely high thermal conductivity of graphene outperforms all other known materials [66]. Because of the above mentioned enhanced properties and several other extraordinary properties, graphene has been used in the construction of advanced materials such as display screens in mobile devices, batteries and components with higher strength to weight ratios such as wind turbine blades, aircraft components and polymer matrix composites (PMCs) [67–72]. The great success of graphene raised the attraction toward other two-dimensional (2D) materials as new class of materials with exceptional and tunable properties. Nonetheless, the extensive application promises of graphene has motivated investments in the synthesis of other two-dimensional (2D) compounds fabricated from

carbon and other atoms which not only supply a recent group of materials with outstanding properties but even provide appropriate building blocks for the next-generation energy conversion and electronic devices. Beside the aforementioned enhanced properties, graphene has a few drawbacks that hinder some of its applications in some critical technologies. For example, the lack of an electronic bandgap restricts its application in several nanoelectronic devices, such as nanotransistors. The investigation for ways to improve graphene properties has been the subject of several researches in recent years. Graphene can also be improved by foreign atoms including nitrogen, oxygen and boron to obtain better properties [73]. Chemical doping of nanosheets with foreign atoms is a helpful method for the improvement of their physical properties.

2.2.2 Graphene-like boron carbide (BC_3) nanosheet

Boron is an excellent option for chemical doping of graphene due to its close atomic size to carbon and its powerful valance bonds with carbon atoms. Nanomaterials resulting from the doping of graphene by boron atoms have promising and practical applications e.g. in nanosensors, spin filter devices and fuel cells [74]. The intense attention toward the production of single-layer materials with honeycomb structure fabricated only from carbon (C) and boron (B) atoms seems to be very fascinating, and so that an interesting experimental advance has just occurred among material scientists regarding the synthesis of 2D crystals with BC_3 stoichiometry. Boron, like nitrogen, is also a neighbouring element of carbon. The close atomic size of boron and carbon, and their ability to form strong chemical bonds raise attentions toward the stability and physical properties of graphene-like BC_3 monolayers. Tanaka et al. [75] experimentally grew uniform, thermally stable, macroscopic BC_3 layered sheets with honeycomb structure and high crystalline quality, by using carbon substitution technique in the boron atoms of honeycomb structure in metal diboride (MB_2). Recent studies indicate that single crystalline boron-carbide (BC_3) monolayers are among the most promising candidates for energy storage, nanoeloctronics and catalysis [76–79]. They are suggested as anchoring materials for lithium-sulfur batteries with high performance, owing to its enhanced conductivity, strong anchoring ability, and improved rate capacity [76]. Nonetheless, the evaluation of intrinsic properties of the novel 2D graphene-like BC_3 monolayer consequently captured the attention of scientists. Extensive investigation of the magnetic, electronic, optical, chemical, thermal and mechanical properties of 2D crystalline boron-carbide may also suggest them as reasonable candidates for new real applications other than their usage in nanodevices and composites. In spite of the synthesis of BC_3 layered sheets more than a decade ago, the published information regarding their extraordinary

mechanical properties are restricted yet. Hence, in recent years the extraordinary mechanical properties of this novel graphene-like BC_3 2D material has attracted scientists' attentions. In the structure of graphene-like BC_3 monoleyer, the boron atoms are uniformly distributed over nanosheet.

Because of the complicated, time consuming and expensive process of investigating material properties at nanoscale by experimental methods, computer simulations are viable alternatives. Besides, recent progress of simulations/modeling at the nano-scale has led to more accurate understanding of the mechanical behaviors of two dimensional materials. Mechanical properties of materials are among the key factors for the application of materials and play an important role since they are significantly related to the safety and stability of the structure under the imposed mechanical forces occurring during their lifetime. Recently, Mortazavi et. al. [80], conducted first-principles calculations to estimate the mechanical behavior, electronic, optical and thermal transport characteristics of graphene-like BC_3 monolayer via density functional theory (DFT) calculations. Based on their electronic structure calculations, graphene-like BC_3 monolayer is an indirect bandgap semiconductor.

2.2.3 Monolayer molybdenum disulphide (MoS_2) heterostructure

Molybdenum disulphide (MoS_2) is well known for its various applications in industry and recently, its two-dimensional forms which are parts of the large family of so-called Transition metal dichalcogenide (TMD), have attracted growing attention in high strength nanocomposites and in the nano-electronic technology. Like graphite, molybdenum disulfide crystals are composed of atomic layers with hexagonal lattices held together by van der waals forces. Even though MoS_2 crystals exist in nature, its purification is difficult and expensive. On the other hand, natural gas and crude oil are sources of large amount of sulfur because they contain hydrogen sulphide (H_2S). Chemical companies produce pure MoS_2 crystals via the reaction of hydrogen sulphide with molybdenum oxide [81]. There are several methods to prepare single layer forms of MoS_2 including mechanical and chemical exfoliation of bulk crystals by peeling off the layers of MoS_2 into 2D layers and vapour-phase growth of large-scale 2D monolayer MoS_2 sheets [82]. In a recent method, Mo layers react with H_2S and form large-areas of MoS_2 monolayers [83].

Molybdenum disulphide (MoS_2) is a very attractive 2D material due to its outstanding electronic properties. Mono-layer MoS_2 structures show extraordinary prospects for applications in flexible electrical and optical nanodevices for which mechanical stability is crucial [84, 85]. One advantage of MoS_2 over graphene includes its direct-bandgap,

i.e. quasi-two-dimensional semiconducting behavior, while graphene is classified as a semi-metal, an electrically conducting metal. Another interesting property of MoS_2 is its polymorphism characteristic. The electrical characteristics of single-layer MoS_2 significantly depends on the S atoms locations. Current experimental approaches show that extra tuning of the electrical properties of MoS_2 monolayers by the fabrication of mono-layer heterostructures is possible [86].

Several authors have studied 2H phase of MoS_2 sheets both experimentally and theoretically [87–95]. Experimentally fabricated MoS_2 membranes will always contain different types of defects and impurities in their atomic lattices. For instance, crystal growth arising throughout the chemical vapor deposition (CVD) fabrication of monolayer MoS_2 causes the formation of grain boundaries with different types of defects [96, 97]. MoS_2 nanosheets may also contain several atomic impurities like oxygen [98, 99]. The aforementioned effects can consequently influence the mechanical behavior of MoS_2 membranes.

Chapter 3

Stress analysis of Defective Polyethylene Gas Pipes

3.1 Quantitative Risk Assessment and Safety of pipelines

In gas supply, even though polyethylene (PE) pipes have proven themselves for decades all over the world, simultaneously, transmission lines safety regulations have drawn more attention, as they continue to perform a great role in the oil and gas industry. In spite of the outstanding material properties and excellent underground installation techniques, defects in operation never can be excluded. Inescapably, damage to the pipelines may occur by interference from third parties, human errors and so on during the operation of pipeline. The defects may range from a local damage to the pipe surface, grooving, gouges, flaws and scratches, to the severe damages which might penetrate the pipe wall and results in significant danger and effects. It is well known that the existence of defects in real material has a significant influence on the mechanical strength of the structure as they cause local stress concentrations and even may cause catastrophic events. The major concern for all gas companies is the ignition possibility of the blowing gas which can blow from the defects and holes in the pipeline. Thus, the importance of safety issues during pipeline operation, stresses investigating the mechanical behavior of defected PE gas pipes to a great significance for natural gas distributor companies. Nevertheless, it is required to investigate pipelines safety parameters via quantitative risk assessment. Pipeline officials and managers can increase pipeline safety as reduce the risks to minimum level. From the structural mechanics point of view, pipelines quantitative risk management includes the evaluation of failure probablity and failure consequences. In order to investigate failure behavior, stress analysis around the damage area of the pipeline must be performed in advance. It is important to ensure that the stresses in

the pipe remain below allowable levels. Therefore, load capacity of the defected PE pipe should be determined. Repair patches can be used in numerous applications to reinforce structural components or repair damaged parts. This process of structures repair increases the service life of damaged components. Repair patches enhance the strength and stiffness of defective components and their proper application will delay the initiation and propagation of the cracks in damaged section of the structure [100]. Welded patches are more efficient than for example bolted patches as they can prevent the possibility of stress concentrations caused by bolts at the holes. In investigation performed by Green et al. [18], a remote external tool was invented to repair defective MDPE gas pipes by applying a HDPE patch. In order to examine the ability and applicability of the tool and patch repair, they performed a series of laboratory tests. First, in order to simulate critical damages produced by large gauges, they drilled different circular holes into sections of MDPE pipe walls. Afterward, they applied HDPE patches over the simulated damages and performed hydrostatic pressure tests, according to ASTM1598 standard (sastained pressure) test method for plastic pipes under constant internal pressure. Although their experimental laboratory tests verified the applicability of reinforcing HDPE patches to withstand only pressure load during test, but neither test was conducted to examine the performance of the patch repair method for real buried gas pipe applications, where the pipe and its repair patch are under the effect of several complicated simultaneous loads and in presence of defects in the pipe. However, repairing imperfections or damaged sites of underground gas pipelines is very difficult, costly and time consuming, because the commonly used repair method consists of cutting and removing the defected pipe section and fusing a replacement pipe section into the system.

To the author's knowledge, it appears that all previous studies that used finite element analysis (FEA) codes to investigate the soil-pipe interaction of the buried PE pipes did not focus on the particular case of a local patch repair effect on 3-dimensional (3D) states of stress, in overall behavior of the defective pipe. Thus, the purpose of this study is to investigate the effect of different reinforcing polyethylene patch size and shape and a saddle fusion repair which is bonded perfectly on the pipe, by accurately calculating stress distribution that arises around the defective portion of the substrate material (PE buried gas pipe). This can lead to a safe and solid field repair (when applicable) without any interruption in gas flow through the pipe. In this technique, a portion of the load sustained by the substrate is transferred to the reinforcing PE patch.

This "pre-simulation" should help in later gas transition practice to avoid dangerous and environmentally damaging situations, reduce costly downtime and enable long-term stable structures in the geological subsoil. The scientific results obtained at the research will thus find their way into the conception, planning and realization of future underground projects in Iran and abroad.

3.2 Failure mechanisms and modes in pressure vessels and piping systems

Based on the definition, a failure can be associated with either the loss of function capacity by the system or the undermining of its safety [101, 102]. Pressure vessels and piping systems are designed, fabricated, and operated to ensure a high level of structural integrity because the consequences of structural failures can be severe. Although, service experience over the last century indicates an excellent record of reliability, efforts continue to improve and maintain the reliability of vessels and piping systems, catastrophic failures still occur on rare occasions and other failures of a less significant nature (cracks and leak) are more commonly reported. Therefore, before the reliability of a pressure vessel or piping system is evaluated, it is first necessary to identify the potential failure mechanisms and failure modes of concern. Engineers an designers must also relate different failure modes to possible safety and/or economic consequences. Judgment is required to focus evaluation on those failure scenarios having highest likelihood of occurrence. Meanwhile, several modes could be considered and defined as failure modes in pressure vessels and pipelines, but the major failure modes include small cracks, local corrosion/wall thinning, excessive distortion, leaking through-wall crack, through-wall corrosion/wall thinning, excessive leakage, and fracture rupture [103]. For example, corrosion defects in external surfaces of steel pressurized pipes or impact of a bucket excavating machinery with gas transmission PE pipelines can lead to a thinner pipe wall thickness which will directly increase the von Mises stresses in the thin area in the pipe [104, 105]. An important reason to consider a failure mode to highest concern level is that the failure will result in catastrophic rupture, and that it will threaten personnel's lives working around the vessel or pipeline and possible properties damage due to rupture. On the other hand, in lower level of concern, there is enough time to take suitable actions like repair or component replacement to avoid disaster consequences. Depending on working condition of the vessel and piping systems, the failure mode classifications might be different. For example, small leakage in water pipe system, which cause only a small amount of water loss, is not the same level of the same event in a vessel containing pressurized toxic gas [106]. The less severe modes (small cracks) are most probable to occur than the more severe modes (rupture). Moreover, degradation if not detected and repaired will generally progress over time from a less severe mode (small crack) to more significant modes (leaking through-wall crack) and ultimately even to catastrophic failure.

Usually, the stresses acting in principal directions in a structure with simple geometry, are evaluated from basic established equations. In design of pressure vessels and pipe systems, normally the working stresses are kept below the yield stress of the material

and to ensure that yielding does not occur in the region of discontinuities, or due to unknown factors, a safety factor, is incorporated into the design. More accurate study of these systems shows that, two modes of failure need to be considered: plastic deformation of the vessel or pipe walls and fracture. As the internal pressure of the material passing through the pipe raises, depending on amount of pressure, four stages are possible to happen in sequence, elastic, yield, plastic deformation, and fracture. When plastic deformation occurs, deformation will be permanent and load capacity of the vessel increases. By increasing the pressure, at special values, load capacity rise because of strain hardening will not be enough, so, as a result, rapid reduction in wall thickness and burst will happen [106].

Most of the traditional design codes for pipelines were traditionally based on the allowable strength design (ASD), also known as permissible stress design, in which the unfactored stress calculated from the most adverse combination of loads, must not exceed a permissible stress, which is equal to the ultimate stress divided by a safety factor [101]. However, depending on the location of the pipes (above the soil, in the ground or under water), there are several theories regarding the analysis of their elastic-plastic behavior. Therefore, for pipelines installed above the ground some engineers use Timoskenko and Goodier's elastic behavior theory for the purpose of sizing pipes and choosing the material [107]. Previous studies indicate that pipe burst failure behavior induced by internal pressure is a material plastic collapse behavior. Specially for pipes with corrosion defects, pipe failure occurs when the von Mises stress in the critical section of the defect area reaches the flow stress of pipe material.

Polyethylene piping systems demonstrated satisfactory performance compared with traditional pipeline materials such as iron, steel and concrete, but areas for improvement were identified such as joint quality and stress-raising defects and flaws in the material structure, arising from point loading with stones, root systems, soil settlement, excavation damage and incorrect operation. Additionally, buried plastic pipe may be exposed to deterioration or destruction by animals, insects, and microbiological organisms during storage and in service. So, the root cause of the PE pipe failure consist of mentioned flaws, which leads to a reduction in the thickness of the PE pipe at which failure occurs. In the absence of stress singularity, in the literature, there are numerous theories in predicting the behavior of pipes depending on the thickness of the walls (thin-wall pipes/thick-wall pipes), such as von Mises yield criterion and Hill criteria, Tresca yield criterion [107]. However, all the results produced in this part of study assume the polyethylene pipe material to behave elastically with no yielding occurring at the defect region such as the point of pipe main bore to radial bore intersection.

3.2.1 Failure behavior of polyethylene pipe

With the increasing application of PE pipelines in natural gas transmission systems, their structural integrity and also their fracture behavior has received considerable attention. Owing to its time dependent properties, high molecular weight and also different loading conditions, there are several fracture modes for PE pipes [108]. The cracking of polyethylene pipes consists of two modes: ductile or brittle mode. Ductile deformation and failure caused by high stress levels and is associated with macroscopic yielding. On the other hand, brittle failure is associated with crack growth. It was suggested that the two processes occur simultaneously, and the final failure depends on which process is faster under given stress, temperature and damage shape and depth [109]. Ductile failure exhibit large material pull-out (or yielding) adjacent to the failure location. This mechanism is related to the viscoelastic behavior of polyethylene pipe material and specially refers to the creep rupture. The resulting failure shows large deformation accumulating in this process. However, the part of cracking taking place in the field does not exhibit large deformation. There is no pull-out or thinning down of material adjacent to the crack. This type of failure is defined as brittle (or brittle-like) failure.

Brittle failure in polyethylene pipe usually occurs under low stresses and takes a long period of time to propagate through the material thickness via the process of slow crack growth (SCG). SCG which can be resulted of creep- and fatigue-loading, can happens in years of lifetime. The SCG fracture surface appears brittle and this behavior is a common failure mode in underground polyethylene piping which were designed for 50-years services [108]. In the majority of cases, cracks initiate from defects in the material such as flaws, notches created by installation, impingement and bending loads and slow crack growth (SCG) starts from the initial defects in the pressurized PE pipe wall, evoked by unavoidable stress peaks at inherent defects. While cracking might happen under static loading conditions (creep), dynamic loading (fatigue), can also induce cracking. The driving parameter for SCG is the stress intensity factor (SIF) K_I (index "I" presents the crack opening mode) which describes the stress field in the vicinity of a crack tip. A summary of the failure modes that could occur in high density polyethylene pipes is depicted in Fig. 3.1.

Linear elastic fracture mechanics (LEFM) have often been used to analyze the cracking of pipes by estimating the stress intensity factor (K).

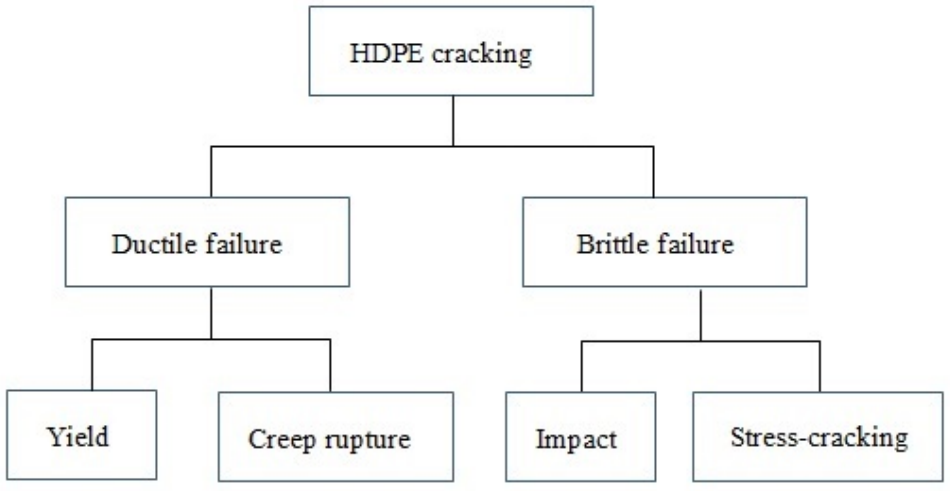

FIGURE 3.1: Failure modes that could occur in high density polyethylene pipes.

3.3 Stress concentration and stress intensity factors

A discontinuity in geometry of an object, e.g., cracks, sharp corners, holes and changes in cross-sectional area, causes localized increase in the intensity of stress field around discontinuity locations, which is known as stress concentration. Understanding the physical mechanisms behind this mechanical behavior is of great importance as these information can be used in predicting the lifetime and finding the optimum strengthening method of defective structures. At points of discontinuities, the stress concentrations must be precisely evaluated and this leads to increase the structure life. Maximum stress felt near these locations occurs in the areas of lowest radius of curvature. Therefore, as the value of curvature radius approaches zero, the peak stress approaches infinity. Stress concentration factor (SCF) is defined as the ratio of the highest stress (σ_{max}) to a nominal (reference) stress (σ_{nom}) of the cross-section according to Eq. (3.1).

$$K_t = \frac{\sigma_{max}}{\sigma_{nom}}, \tag{3.1}$$

If the concentrated stress exceeds material's strength, material will fail quickly following a crack propagation. Also, local stress concentrators significantly reduce elastic limit of the material [110].

It is worth mentioning that if for example in the above defects the stress concentration factor of 2 is calculated it seems the specimen will fail at one-half the load required for an unnotched specimen. Depending on the material type, such is not often the case, since for ductile materials stress concentration factors are valid only while the material behave elastically. Beyond the elastic limit, plastic flow action can cause a stress redistribution

to an almost uniform stress across the defect cross section. That is to say at the crack tip there exists a yielding domain. However, the member may fail in a brittle manner under some loading conditions. The effects of a discontinuity in a brittle material are very much different than ductile material. With brittle materials, no stress relieving plastic flow action is possible and the full value of the stress concentration is valid right up to the fracture strength. For these materials, then we expect the fracture strength to be reduced from the unnotched fracture strength by the value of stress concentration factor (K_t) [111]. Therefore, designing with brittle materials must be done with a great deal of care to avoid undesirable failure.

Meanwhile, during performing elastic analysis, if the void (defect) introduce a sharp corner in the structure, the stress at the sharp corner may theoretically tends to infinity because the radius is approaches zero at the sharp corner tip. These regions act similar to a crack that might eventually propagate through the component to complete failure. As a simple example to explain stress singularity, one can consider an elliptical hole of length $2a$ and width $2b$ under a nominal or far-field stress σ_{nom}. The stress at the ends of the major axes is given by Inglis equation [112]:

$$\sigma_{max} = \sigma_{nom}(1 + 2\frac{a}{b}) = \sigma_{nom}(1 + 2(\frac{a}{\rho})^{\frac{1}{2}}), \tag{3.2}$$

where ρ is the radius of curvature of the elliptical hole (or distance from the crack tip). As the radius of curvature approaches zero, like the tip of a sharp crack, the maximum stress approaches infinity and therefore, stress concentration factors cannot be used for this problem and similar problems including cracks and notches with sharp corners. In this case, one can say the stress field theoretically has a singularity of order $\rho^{-0.5}$. Computationally, a singularity is a point in the mesh of finite element model where the stress does not converge towards a specific value. As the mesh is refined, the stress at this point increases with no apparent limit. A FEA analyst must recognize these singularities in the model and interpret them correctly. In reality, there is no such thing as infinite stress even at singular points. Physically depending on the material type sharp corners are the points from where a crack would rather start (for brittle materials) or a point at which the material will yield (for ductile materials). Therefore, in these cases analysis of strength using stress/strain criteria is highly mesh dependent due to stress singularities at sharp corners of the defect, and it is required to treat these defects by fracture mechanics approach and to perform fracture analysis using linear elastic fracture mechanics (LEFM). Fracture mechanics gives precise details of the distribution of stress and deformations near the defect zone and in addition can indicate an estimative lifetime of the resistance of these structures according to the critical defect size.

The stress fields near a crack tip in a flat plate can be divided into three basic types: (1) the opening mode, I, is associated with in-plane stresses and displacements which

are symmetric with respect to the crack line; (2) the sliding mode, II is associated with in-plane stresses and displacements which are antisymmetric with respect to the crack line; (3) the tearing mode, III, is characterizing by displacements perpendicular to the plate which are antisymmetric with respect to the crack line. The most general crack-tip deformation and stress field can be described by combining the three modes [23].
Fracture mechanics provides a theory background for material and structures containing cracks and faults, and the stress intensity factor (SIF) is a key parameter in crack analysis. In LEFM, the strength of the singularities, which are proportional to the coefficients of the singular terms in the stress and strain states, are called, stress intensity factors (SIFs). SIF is used to describe the effect of a crack or sharp corner at the crack tip or corner edge under static loads and should not be confused with the stress concentration factor. Because of the importance of SIF, its solution have been paid very much attention since the beginning of the fracture mechanics. The SIF is a function of the global loading σ, the crack length a_c, and a geometric factor Y that is known for several specimens and component shapes [113]:

$$K_I = \sigma\sqrt{a_c}Y, \tag{3.3}$$

Estimating SIFs by theoretical methods is a very difficult problem and exact solutions exist only for very simple problems like elliptical cracks in infinite domains, one can look it up in SIF manuals. For other crack shapes and geometries and complicated configurations, where exact solutions are both difficult to obtain and generally not available, a numerical technique which has been very popular is the finite element method. The early works on determining stress intensity factors has been limited to the crack, which might be described as a notch with zero opening angle. By the way, there are an other location of high stresses in structures under loading, and that is at interior sharp corers or notches of nonzero opening angle, as shown in Fig. 3.2. In this figure a notch of right angle is formed with two traction-free edges. The origin of coordinate system lies at the tip of the notch and the x-axis bisects the notch angle. One can again define three types of stress states which contain singularities: (1) mode I, symmetric about the notch bisector (x-axis in Fig. 3.2); (2) mode II, antisymmetric about notch bisector (x-axis in Fig. 3.2); and (3) mode III, nonplanar and antisymmetric about the notch bisector [23]. For these modes the strength of the singularities will again be defined as proportional to the singular terms in the stress state. In sec. 4.3 of the present research, the effect of the local stress state on three-dimensional sharp corner of partial circular cutout in the pipe wall will be well discussed and three-dimensional static stress intensity factors will be determined. This will be achieved using finite element method (ANSYS workbench).

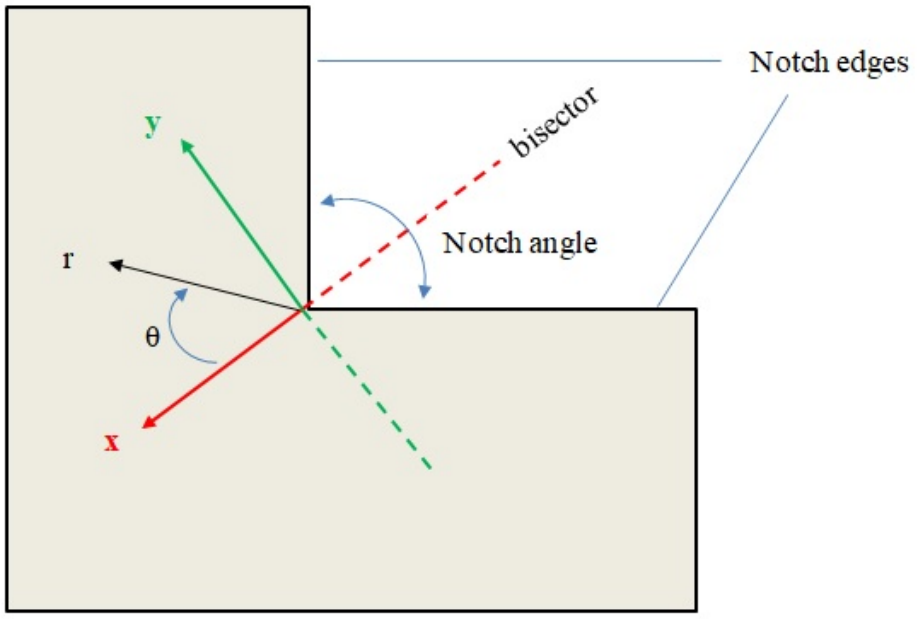

FIGURE 3.2: A schematic of sharp corner with right notch angle and the coordinates in the neighborhood of the sharp corner.

Fracture toughness (K_{IC}), which is a measured material property represents the resistance to catastrophic growth of a natural flaw in a material. For stress intensity factors below critical intensity factor of the material (K_{IC}), the crack is fully arrested.

3.4 Effect of partial local and complete through-wall holes

Situations do arise when it becomes necessary to create complete through-wall radial holes in the wall of pressure vessels or piping systems and such openings introduce geometric discontinuities to the cylinder or pipe configuration and hence a stress concentration locus. When these vessels are pressurized, the stresses concentrate around the hole due to the discontinuity in the geometry. This results in a major source of weakness and a reduction in the pressure carrying capacity of the vessel below that of a plain undisturbed (intact) cylinder [114]. In this case, the pipe or vessel stress imposed by the three orthogonal stresses is removed and replaced by fluid internal pressure. However, this internal pressure does not exactly match the stresses removed, so it causes stress concentration effect in the vicinity of hole and therefore decreases the required load to initiate plasticity in the pipe. Whereas, for the same unflawed (intact with no defect) pipe with no hole, plastic state generates at the loads several times higher than in pipe

with side holes. This situation is especially dangerous in case of cyclic (fatigue) loads. The plastic zone can rapidly propagate along the hole and reach the external edge. For a pipe featuring a bore hole, the stress concentration factor can be calculated by:

$$K_t = \frac{\sigma_L}{\sigma_H}, \tag{3.4}$$

where σ_L is the local maximum principal stress or maximum von Mises stress at a point in a bore hole and σ_H is the identical stress at the same corresponding point in a plain (intact) pipe without bore hole [114]. Also, local defects in external surfaces, such as corrosion in steel pipes or flaws from scratches or stones point loading and body (pipe wall) cut-out from third party damage in polyethylene pipes may lead to a thinner pipe wall thickness and therefore increase the von Mises stress in the defect area in pipe. Therefore, the presence of local thinning areas can limit the capacity of the pipe to sustain applied loads. As mentioned above, the stress concentrations produced by voids and notches in pipe wall are strictly responsible for crack initiation and slow crack growth (SCG).

As mentioned in the previous section (3.3), if the damage (pipe wall cutout) introduce a sharp corner in the pipe wall, the stress at the sharp edge of the defect theoretically tends to infinity. These regions act similar to a crack that might eventually propagate through the component to complete failure. Therefore, at the defect area, the ductile mechanical behavior is not applicable to the pipe wall material under the applied loads and we can not use stress concentration factors. Therefore, because the pipe material behave in brittle manner in presence of cracks and at the location of stress singularities, LEFM should be employed to calculate stress intensity factors. Since SIFs have been discovered to be controlling parameters for predicting crack propagation, their calculation has been the starting point for many regular fracture mechanics analyses, and much attempt is required to determine their magnitudes for various defect geometries and external loadings. By analyzing the stress intensity factor and comparing it with the critical one (fracture toughness), it is easy to judge whether a PE pipe will fracture failure.

By proper understanding of the severity of the stress in these regions of high stress fields, the accurate evaluation of the remaining strength of a defective pipeline can bring substantial benefits. In the light of this knowledge, less conservative safety factors in the design of such vessels is required. Most of pipeline repair expenses may be saved if we understand that some of small defects are not dangerous and may be considered as permissible damages which do not need to be repair immediately. Unfortunately, gas companies waste a huge amount of money annually for maintenance and repairs which are not necessary. If we realize that some defected structures can function well and safely without repair, as the stresses in the areas around damage are low enough, then we may stop a huge amount of expenses.

3.5 Polyethylene repair patch

Even though products from PE material are designed with a safety factor, failures can and do occur due to unforeseen loading scenarios and/or product use beyond the manufacturers designed service factor. The vast majority of buried polyethylene pipes in natural gas distribution networks are inevitably facing typical defects such as holes, throughout their operational life. Some of these defects can be classified as critical and will need to be repaired immediately, after they are detected. One of the key failures in structural components made from polymer materials is fatigue which demands specific devotion to develop procedures to stop fatigue crack initiation and propagation. The process of fatigue failure itself includes several other processes which involve initial cyclic damage, crack initiation, crack propagation and final failure [115].

Conventional repair methods are primarily based on the replacement of defected parts, which involve cutting and welding processes. Inevitably these repair methods in many occasions lead to the interruption of the pipeline service. Additionally, These methods are dangerous, expensive and very time-consuming. When replacement of these PE parts due to damage is not an option, proper repair becomes the only feasible choice short of complete replacement. However, one of the effective procedures to stop this effect and to mitigate fracture-crack propagation is by shielding the singularity area which results in the fracture resistance increase [116]. Therefore, increasing defective pipe fracture and failure resistance is possible by shielding the defect area using appropriate fracture and failure filling materials such as reinforcing patches. By applying shielding material, the local driving force decreases at the defect area. The successfulness of this procedure depends on the properties of the sealant material and how to effectively apply it. An important finding in the study conducted by Sin and Cai [117] was that "A higher sealant Young's modulus increases the amount of induced crack closure; however, the modulus should be above a certain value in order to have a significant closure effect." By the way, it is difficult to fully treat the surfaces of a crack or a defect. Cracks or pinholes go through the thickness and rarely spread sufficiently to have access to the actual surfaces that need to be joined. Therefore, especially across the thickness, any bonding that occurs will be weak and will not withstand typical design loads.

An important technique, besides the use of adhesives that is used to bond materials is to bond materials together by fusion. In this technique, the two parts to be joined are brought into actual physical contact and then heated. A new and quite promising repair method which shields the defect area of the pipe is using polyethylene material patches. Perhaps, the most attractive feature of PE pipeline systems is the ability to rapidly fuse sections together to form joints with strength equivalent to the parent material. Based on the definitions, "patch" is a small piece of material used to mend a tear or break, to cover a hole, or to strengthen a weak place [118]. Further, if you have a hole or crack

in almost anything, including pipes, you can fix it in a short time using a rigid patch. Available in several sizes, the reinforcing patches can be used separately or side by side to repair large areas. When positioning the patch over the area to be repaired and pressing into place, the edges of the patch should extend a few past all sides of the repair area. The reinforcing patch should be accurately designed so that it fits into the new hole on the pipe surface, easily without being forced. In patch repairing, part of the applied load is transferred to the patch. The patch repair is carried out in order to arrest a defect that had developed and to restore material loss. The patch material increases failure resistance of the pipe material by deforming to bridge the faces of propagating crack or other defect and absorbing its energy through applying closure stress in the crack tip and defect region. The aforementioned advantages of PE patch repairs, as well as the good output from the limited existing repairs in underground gas distribution lines have triggered the interest towards the further investigation of this new technology so as to be widely accepted as a repair method. For treating a defect with patch, first we should prepare and clean the pipe surface by removing soil and dirt in a wide border around the hole or defect and then place the reinforcing patch over the defect section. The patch size should be slightly larger than the hole or defect in the pipe. It is important to decide the patch shape and also to determine how much the reinforcing patch should be larger than the hole or defect.
This work consists of a numerical simulation of such repairs in a damaged pipe. circular hole defects of different sizes and depth at the crown of buried MDPE pipe were modeled. Different HDPE patch configurations were applied and studied for each defect case. The stress field in the area around the defect was calculated, prior and after patch repairing. The effect of the reinforcing patches on the strength of the stress concentrators is found by comparing the two similar problems of the defective pipe with and without patch. Results showed that stresses are significantly reduced after the repair, compared to the unpatched cases.

3.6 Methodology to globalize the study

This section outlines the research methodology and the tasks performed to address the study objectives. First, the main hypothesis of this research and objectives are presented. Second, a general summary of finite-element modeling used is provided which is followed up by the numerical description and the main steps conducted.
The stresses in unflawed (intact with no defect) buried pipes without geometrical discontinuities or damages can be evaluated using existing design procedures [119]. On the other hand, limited approach currently exists to evaluate the stresses around some

shapes of defects in buried PE gas pipes and our knowledge about the influence of defects on the structural performance of the buried PE gas pipes is little. However, it is important to ensure that the stresses in buried pipe remain below allowable levels. Gas distribution lines may experience defects with a large variety of shapes and sizes during their lifetime. The most common and dangerous type of defect in the pipe wall which has been reported by gas companies is in the form of circular notches. This kind of severe defect will create considerable stress and strain concentrations. If stress concentration takes place in the mechanical structure, its strength is often lower than that measured in pristine (unflawed) structure. It is required to evaluate stress concentration areas around the circular notch defects and calculate the maximum stress values in this area in order to determine the probable sites of crack initiation, which can significantly decrease the overall strength of the structure.

The objective of present research is to investigate and quantify mechanical behavior of the pipe material and assess the impact of hole shape defects on stress values and fracture properties around the defect area and its variations through thickness within the buried PE gas pipe. Some aspects of material behavior including stress distribution around partial hole in pipe external surface and complete through-wall holes, the effect of hole diameter and depth, stress intensity factors at stress singularities resulting from defect sharp corners and also the simultaneous effect of other loads are investigated. Gas distributors require to estimate stress and strain distribution around the defect areas in order to determine crack initiation sites. In order to reach this objective, in this research, we perform a comprehensive three dimensional (3D) finite element (FE) process for the aforementioned purpose and analysis where the defects are assumed to be several circular holes with different hole diameters and through pipe wall depths, and the pipe is subjected to several loads and mainly the internal pressure. Holes in pipe wall are assumed to be round and are located radially to the pipe axes, that means the major axis of the hole is perpendicular to the longitudinal axis of the cylinder. Complete through-wall open holes extending from outer to inner pipe surfaces experience stress concentrations at the hole areas located at inner pipe surface. Local partial holes with sharp corners experience high stress values at sharp corner areas. Several hole diameter and hole depth of the defect section are the main parameters to be investigated.

Certain cares are taken in the pursuit of creating a successful numerical model, such as: mesh refinement study, proper boundary conditions, load applications, proper element choice and use of true material property. Therefore, three dimensional elastic finite element analysis that can fully capture the geometry, applied loading and boundary conditions of soil-structure interactions will be used to solve the problem of a buried pipe with some noticeable configuration of defects. The numerical simulations were performed by ANSYS 16/2 APDL and ANSYS workbench which are commercially available

finite element softwares. Damage initiation can be specified by different criteria according to the defect type. As stress concentrations and stress singularities are a common occurrence in FEM of defective structures, it is very important to know how to deal with them. Typical geometric induced singularities exist at defect sharp corners. Therefore, if the stress concentration/singularity at a region is of importance, then the mesh must be locally refined to capture their effects. Based on the results, the maximum stresses around the defect areas were found to be depend on the thickness and diameter of the pipe and the diameter and the depth of the radial bores (holes). The results of the proposed procedure for estimating the maximum stress values around the defect areas will be useful to minimize the stress concentration in buried pipes.

In this study, any variation in the soil temperature is necessary to calculate elastic thermal stresses in the buried pipes, and thus Eq. (3.7) was used to determine any seasonal changes that may occur in the soil at any depth in question. Based on Eq. (3.7), on a daily basis, at different depths at approximately 125 cm, the ground temperature is nearly constant [21]. This implies that increases in the pipe installation depth to any logical value causes the pipe (or repaired pipe and its surrounding medium) to become insensitive to any changes in temperature during the daytime at ground level. Additionally, polyethylene possesses a high value of the coefficient of thermal expansion when compared to metals, and thus any temperature decrease in the pipe exhibits a direct and a meaningful effect on thermal stresses developed in the pipe. Thus, the aforementioned results can also be applied to other regions with similar or smaller changes in climate temperature (annually) provided that other factors do not exceed the values used in the study.

Finally, the physical mechanisms for defective pipe strengthening is well investigated. The mentioned strengthening physical mechanism is based on sealing defective areas with specially designed patches. Strengthening patch design mainly consists of design, modeling and analysis steps. Once all processes of the design and modeling steps are completed, the maximum stress values obtained in the analysis step are compared with those prescribed by the regulations to complete strengthening patch design. This objective was achieved by numerical simulations of finite element method to model and analysis the defective pipe patch repaired. If the maximum stress values do not satisfy those provided by regulations, the entire design must be modified. In the analysis step, bottlenecks occur because both design and modeling be re-performed. This procedure requires considerable time and effort from the designer. A schematic of procedure, major steps and workflows followed up for this phase of present research is simply described in Fig. 3.3. According to this figure, in the first step, basic shape information is required for defective pipe analysis. Shape information includes the spatial coordinates, length, thickness and diameter of the pipe, defect shape and size, surrounding soil and material dimension and also repair patch shape and dimensions. Next, property information and

operating conditions are required to determine the characteristics of structural components presented in the problem. For example, property information of the pipe, patch and surrounding soils includes the property of the mentioned components' material, such as elastic modules, poisson's ratio, density and thermal coefficient. Operating conditions includes the operating environments of the actual problem and consider factors such as internal pressures, soil column weight, surcharge loads and temperate variations. Results for defective pipe and patch maximum stresses are recorded after each step of the simulation to test the failure hypothesis. Furthermore, where applicable to verify results from numerical simulation, analytical methods to estimate the stresses are conducted. Since there are no existing solutions which can be used to measure accuracy, the best that can be done is to compare the stress results for various geometries of defective pipe and confirm the expected trends. Since the proposed numerical simulation accurately predicts the 3-dimensional stresses in a PE patch bonded on the PE gas pipe, it can be used as a simple and efficient numerical tool for designing such structural components.

3.7 Basic design theory

In this section, some basic governing equations from the applied mechanics, applicable to the present problem will be discussed. For any continuum in equilibrium, the following relation known as equilibrium equation must be satisfied:

$$\bigtriangledown^T \mathbf{T} + \rho \mathbf{B} = 0 \tag{3.5}$$

where $\mathbf{T}$ is the stress tensor, $\mathbf{B} = B_i \mathbf{e}_i$, is the body force (such as weight) per unit mass, $\mathbf{e}_i$ are unit vectors of fixed directions in Cartesian coordinates, ρ is the mass density at the position x_i. An ideal material where the deformations are small and the rate of load application has no effect, is called the linear elastic or the Hookean elastic solid, and for this material the constitutive relation of stress and strain can be formulated as follows:

$$\mathbf{T} = \mathbf{DE} \tag{3.6}$$

where $\mathbf{T}$ is Cauchy stress tensor and $\mathbf{E}$ is the infinitesimal strain tensor and $\mathbf{D}$ is a symmetric fourth-order tensor known as elasticity tensor [120]. The equations given here have to be solved by given certain boundary conditions. It is not surprise that exact analytical solutions of the three-dimensional elasticity problems present a formidable task, and as a consequence they are scarce. Moreover, these solutions are confined to physically simple problems with uncomplicated geometry. But when the geometry is arbitrary and also the boundary conditions are complicated, the exact solution of the problem can

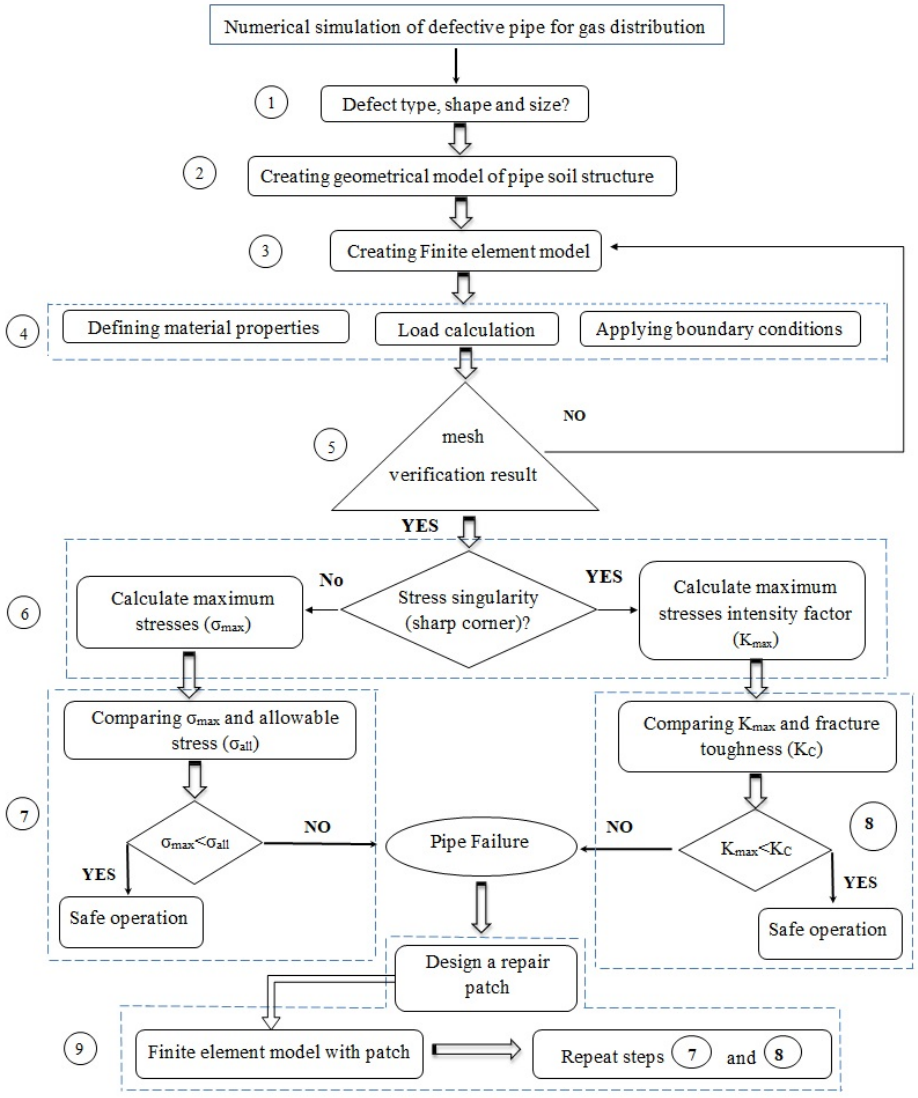

FIGURE 3.3: A schematic of major steps and workflows followed up for present research.

not be obtained. This inability to obtain an exact solution may be attributed to either the complex nature of governing differential equations or the difficulties that arise from dealing with the boundary or initial conditions. To deal with such problems, numerical approximations are therefore made. In the numerical solutions the parts are divided into numbers of elements so that the desired matrices are formed. These matrices are solved and therefore, they approximate exact solutions only at discrete points, called nodes.
The design of underground gas pipes is based on the principle of soil–pipe interaction. Thus, the pipe and its surrounding soil act collectively to control the pipe performance. The terms described in this section are the basis for the numerical simulations in future sections. There are two sets of principal stresses important in the analysis of pipe-soil structure analysis and its stability: Near buried pipe stresses and far-field stresses. Near

buried pipe stresses can be categorized as axial, radial and tangential stresses. The tangential stress, often called the hoop stress, is the most critical near buried pipe stress for the structure stability analysis. Far field stresses exist in the surrounding soil far away from the buried pipe and are not affected by the pipe-soil interaction. Near buried pipe stresses are controlled mostly by pipe internal pressure, overburden stress from soil column weight, surcharge loads and temperature variations. In this study, in order to incorporate the interaction and determine the effect of a saddle fusion repair (or a patch fusion repair) on resulting stresses, the following thermal and mechanical loads (explained in sections 3.7.1, 3.7.2 and 3.7.3) are recognized and applied to the buried gas pipe for selected patch arrangements, namely, saddle, semi cylindrical, partial square, and circular patches.

3.7.1 Temperature variation in the soil

Temperature variations in the soil (and thus in the pipe) might occur during a day or annually during any seasonal changes. Information on ground temperature is necessary to calculate the thermal stresses developed in the buried pipe. In the present study, the selected area was assumed as city of Ahvaz (south-west of Iran) in which the average ground or asphalt temperature in summer varies from 30 °C in the morning to approximately 67 °C in the early afternoon [121]. Similarly, on a cold winter day, the variation ranges from 0 °C in the morning to approximately 28 °C in the afternoon. Thus, at any depth, the ground temperature may be calculated based on Eq. (3.7) as follows:

$$T(y,t) = \bar{T} + Aexp\left[-y\left(\frac{\pi}{\alpha t_0}\right)^{\frac{1}{2}}\right] \times cos\left[\frac{2\pi t}{t_0} - y\left(\frac{\pi}{\alpha t_0}\right)^{\frac{1}{2}}\right], \tag{3.7}$$

where, $T(y,t)$ denotes the induced temperature in the soil, y denotes the depth in question (cm), t denotes the time (sec), $\bar{T}$ denotes the average climate temperature for the time period and location of interest, A denotes the difference between maximum and minimum temperatures for the time period and location of interest, α denotes the thermal diffusivity of the soil (cm^2/sec) at the penetration depth and t_0 denotes the time for a complete temperature cycle. This equation also shows that increasing the pipe's installation depth to any reasonable value makes the pipe (and its surrounding medium) more insensitive to changes in temperature during the daytime at ground level. Although the results in the study are obtained for city of Ahvaz, they can be applied to any other location with similar seasonal changes in climate during a year.
Based on TR-21/2001 [122], in the absence of any other effects, the thermal stresses induced in PE pipes are calculated based on Eq. (3.8) as follows:

$$\sigma = E_p \alpha_t \Delta T, \tag{3.8}$$

where, E_p denotes the pipe elastic modulus, α_t denotes the pipe coefficient of thermal expansion $1/^{\circ}C$, and ΔT denotes the temperature change in the pipe within any specific period.

Based on Eq. (3.7), on a 50 °C hot summer day in city of Ahvaz, at a depth of approximately 120 cm, the soil temperature remains constant and equal to approximately 35 °C. Therefore, assuming the worst case of a sudden temperature reduction in a pipe which is in direct contact with the soil, it can experience a 15 °C temperature reduction $\Delta T = (35 - 50)\,^{\circ}C$ after installation. Additionally, on a cold winter day, at the same depth, the equation predicts a constant ground temperature of 13 °C on a daily basis. If a pipe with minimum temperature of 8 °C is installed, a +5 °C temperature increase $\Delta T = (13 - 8)\,^{\circ}C$, will occur in the pipe. Thus, on an annual basis, a buried pipe at a depth of 120 cm experiences a seasonal cyclic temperature change of 22 °C [21]. Additionally, polyethylene material exhibits a high value of coefficient thermal expansion when compared to metals, and thus temperature changes in the pipes made of polyethylene material exhibits a direct and significant effect on thermal stresses produced in the pipe. Thus, in this research, the effects of temperature variations are also investigated based on the aforementioned temperature changes.

3.7.2 Soil column weight above the pipe

The calculation of the dead load that is the permanent load from the weight of the soil as well as that of the pavement is extremely important in buried pipe design. In buried pipes, the radial compressive load imposed by ground (soil and pavement) to the pipe is not uniformly distributed and therefore the pipe deflects under this load. The level on pipe deflection depends on the soil weight and the value of pipe and soil stiffness. As mentioned above, the compressive pressure form ground to pipe is not uniform but in polyethylene pipe design, for the sake of simplicity in analytical calculations it is assumed that the overburden load applied to the pipe crown is uniform and equal to the weight of the soil column projected above the pipe. Theoretical approaches for calculating soil column weight load on the buried pipe crown are well described by Chevron Philip Chemical Company [123]. One simple source for calculating overburden stress is using the following equation:

$$\sigma_v = \int_0^D \rho(z) g dz \tag{3.9}$$

where σ_v is vertical stress, $\rho(z)$ is bulk density of overburden soils, and dz is depth increment. Assuming the surface is flat, the vertical stress will be one of the principle stress directions [124]. This load is often referred to as prism load. The prism load is a simple way of estimating the earth pressure on PE pipes when calculating the vertical deflection. There are special cases where other factors affect the overburden stress such that it cannot be easily calculated based on density integration; for instance, areas of stress arching above depleted and compacted soil layers. Any stress state in the subsurface will consist of three principle stresses 90 degrees apart. Therefore, any stress in the subsurface can be expressed as the function of vertical stress and two horizontal stresses. Assuming linear elastic behavior, the relationship between vertical and horizontal stresses will be expressed solely on Poisson's ratio. Assuming linear elastic behavior, the relationship between vertical and horizontal stresses will be expressed solely on Poisson's ratio, and the minimum horizontal stress can be determined by:

$$\sigma_h = \frac{\nu}{1-\nu}\sigma_v \tag{3.10}$$

The above equation is valid for geologically relaxed areas and when assuming soil behaves as a linear elastic and isotropic material which is undergoing one-dimensional compression. The above equation is based on total stresses. In buried PE pipe design, for the estimation of any dead load, it is common to use Eq. (3.9) which suppose that the overburden load imposed to the pipe crown is equal to the weight of the soil column projecting above the pipe [123]. However, the actual load applied to a buried polyethylene gas pipe may indeed be significantly lower than that of the aforementioned load since the shear resistance transfers part of the soil load to the trench sidewalls and embedment. As mentioned previously, this transfer is called "arching effect". To account for arching effect, the imposed load at the pipe crown is calculated through Marston equation which is given by Eq. (3.11):

$$P_M = C_D W B_D \tag{3.11}$$

Here, P_M denotes the vertical soil pressure, W shows the unit weight of the soil, B_D denotes the trench width at pipe crown and C_D indicates load coefficient which is calculated according to Eq. (3.12) as below:

$$C_D = \frac{1 - e^{-\frac{2ku'H}{B_D}}}{2ku'} \tag{3.12}$$

where, u' is the friction coefficient between backfill and trench soil and k is Rankin earth pressure coefficient which is calculated by Eq. (3.13):

$$k = \tan^2(45 - \frac{\phi}{2}) \tag{3.13}$$

Here, ϕ is the internal friction angle in soil. The values of ku' for various soil types are given in Table 3.1.

TABLE 3.1: The values of ku' for various soil types [123].

Item	**Type of the soil**	**Typical value for ku'**
1	Saturated clay	0.110
2	Ordinary clay	0.130
3	Saturated top soil	0.150
4	Sand and gravel	0.165
5	Clean granular soil	0.192

In buried flexible pipes, arching effect is generally accompanied by the deflection of the pipe crown. In this stage there is a tendency in soil to displace downward. This behavior is effected by the shear resistance from the soil as it sticks to the trench sidewalls and therefore, some part of the soil weight above the pipe is transferred to the surrounding soils. In buried flexible pipe design, a more conservative approach is to combine Equations (3.9) and (3.11) and use the modified arching load. Therefore, based on ref. [123], the soil pressure load on the buried pipe crown is given by Eqn. (3.14), as follow:

$$P_C = 0.6P_M + 0.4\sigma_v \tag{3.14}$$

Here, σ_v denotes the prism load which is calculated from Eqn. (3.9). It should be noted that aforementioned equations estimate the value of pressure at the pipe crown. These equations assume that the resulting stress remains constant all around the pipe. Obviously, due to flexibility of PE pipes and soil-pipe interaction, this assumption is not correct and hence, the stress might change locally. Additionally, in buried pipes which are under the simultaneous effect of soil weight and internal pressure, if the pipe internal pressure exceed the soil compressive load, the tensile stresses will develop in the pipe wall.

3.7.3 Surcharge load in terms of traffic load on the pipe

The pressure on the pipe due to a surface vehicular live load (mainly wheel loads from trucks and trains) depends on vehicle weight, tire pressure and size, vehicle speed, and several other factors. The most common loading used in design is the H20 highway loading. The wheel loading for H20 trucks is calculated based on the American Association of State Highway and Transportation Officials (AASHTO) standards. Wheel loading may be treated to act as a distributed or a concentrated load on the pavement. References [21] and [123] describe theoretical approaches for calculating vehicular live load on buried pipes. In addition to the loads described in subsection 3.7.1, 3.7.2 and 3.7.3,

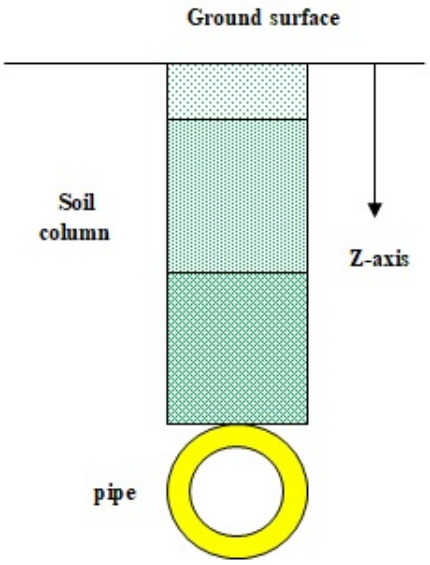

FIGURE 3.4: Schematic illustration of overburden soil above the pipe.

the inside gas pressure results in significant stresses in the pipe wall material. In the study, the operating inside pressure is assumed as equal to 4 bar. This is the working pressure in the metropolitan gas line in Iran. Additionally, it is possible to postulate the presence of stress concentration in the pipe due to a local discontinuity (or external attachments) that may arise from a major repair in the form of a saddle or patch fusion.

3.8 Gas pipe load calculations and models

For many configurations an exact solution for the stress distribution from the theory of elasticity is very hard to obtain. By the way, a notable amount of information that is beneficial and adequate for practical applications has been obtained by assuming several idealizations and simplifications of the problems.

As mentioned previously, three-dimensional elastic finite element simulations are carried out in this dissertation to simulate defects in above-ground and buried gas pipes and the sealing and strengthening. In addition, analytical models to estimate gas pipe loads, can be used to further understand the physical mechanisms behind the mechanical behavior and also to support results obtained from the numerical simulations. Since the imposed stresses in the gas pipe especially hoop, first principal and von Mises stresses play an important role in this research, a clear understanding of these stresses is require. Some of these formulations are discussed in the following subsections.

3.8.1 Designing polyethylene gas pipes to withstand loads

Pipe failures are associated with pipe characteristics, material properties, environmental and loading conditions. Understanding the impact of individual factors and their interactions is extremely complex. The induced stresses in polyethylene gas pipes are due to a combination of internal and external loads. The most common internal force originates from the gas pressure. Conversely, in buried gas pipes, the most common external loads are the earth and surcharge loads and the thermal and soil–pipe interactions.
There are a few methods to calculate buried defective PE pipe stresses. However, regarding the simulation of the models, it is worth to describe the methodology adopted to determine the failure point. One of the major failure criteria for PE pipe is ductile failure. Ductile failure was associated with yielding and reflected a material's tendency to undergo large-scale, irreversible plastic deformation when under stress, the yield stress describing the load intensity at which such effects occur. This mechanism, results from localized yielding and thinning, usually in an area of lowest wall thickness. This is followed by localized expansion of the wall section and final rupture of the deformed zone when the local stress exceeds the mechanical strength across the newly oriented polymer structure. Ductile failure is characterized by creep deformation and this mode is known as the classic 'Parrot's break failure' form of pipe fracture. The design of polyethylene pipelines take this failure mode into account by testing the material to specify its long-term ductile strength and by applying a safety factor, decreasing the operating pressure to a level that ductile failure will not occur in less than 50 years [125].
Essentially, polyethylene pipes are viscoelastic in nature. Thus, as the first method, the effect is included in the modeling process in any stress calculation. Another method that is vastly used by several designers involves treating PE as a linear elastic and isotropic material and comparing the resulting stresses with the minimum required strength (MRS) that account for the reduction in strength of polyethylene due to its viscoelastic nature in time (at any specific temperature) [126]. Based on results from internal pressure tests, the standard extrapolation described in EN ISO 9080 [127] classified these pipe grades by their MRS to ensure service times of at least 50 years [128]. ISO 9080 has been successfully used by gas distribution companies in qualifying pipe body materials which fail in ductile mode. Table 3.2 shows the σ_{MRS} values of PE100 and PE80B for a life expectancy of 50 years, according to International Standard ISO 12162 [126].

Based on ISO (International Organization for Standardization) Standard 12162 [126], or EN 1555-1 [129], with respect to thermoplastic pipe materials, the design stress (or maximum allowable stress that can be applied to the pipe) at 50 years of life expectancy can be estimate by dividing σ_{MRS} by a coefficient C, according to Eq. (3.15) as follows:

TABLE 3.2: σ_{MRS} values of PE80B and PE100 for a life period of 50 years [126].

Working temperature °C	**Working (years)**	**PE100 (MPa)**	**PE80B (MPa)**
20	50	10.0	8.0
25	50	9.4	7.5
30	50	8.7	7.0
35	50	8.0	6.4
40	50	7.3	6.0
45	50	6.6	5.6
50	50	5.9	5.2

$$\sigma_s = \frac{\sigma_{MRS}}{C}, \tag{3.15}$$

Here, σ_s denotes the design stress, σ_{MRS} corresponds to the minimum required strength, and C denotes the overall service (design) coefficient with a value greater than one (at least 1.25 for all PE types). This coefficient takes into consideration the service condition as well as properties of the components of a piping system other than those represented in the σ_{MRS}. Based on the latter standard that is widely used by Iranian gas companies, the maximum operating pressure (P_{max}) is calculated as follows:

$$P_{max} = \frac{20 \times \sigma_{MRS}}{C(D_{SDR} - 1)}, \tag{3.16}$$

In Eq. (3.16), D_{SDR} denotes the standard dimension ratio. This is the ratio of outside diameter to the wall thickness of the pipe. In addition to any numerical solution, a method to calculate the plastic pipe deflection denotes the use of Sprangler's Modified Iowa Formula [123] that is expressed as follows:

$$\frac{\Delta x}{D_i} = \frac{P_T}{144}\left(\frac{K_b L_d}{\frac{2E_p}{3}\left(\frac{1}{D_{SDR}-1}\right)^3 + 0.061E'}\right), \tag{3.17}$$

Here, Δx denotes the horizontal deflection of the pipe, K_b denotes the bedding factor (typically, 0.1), L_d denotes the deflection lag factor, E_p denotes the pipe elastic modulus, E' denotes the embedment soil modulus, and D_i denotes the inner diameter of the pipe. Evidently, in the aforementioned pipes, the percent deflection is as follows:

$$Deflection = \frac{\Delta x}{D_i} \times 100\%, \tag{3.18}$$

Based on [123], in order the results to be valid based on the elastic assumption for the pipe material, the maximum allowable percent deflection for the flexible pipes with $D_{SDR} = 11$ is $\leq 3\%$.
There remain some concerns about the failure mode of polyethylene pipes featuring some types of geometrical discontinuities like cracks or voids with sharp corners which results in stress singularity. As mentioned in sec. 3.2.1, it has long been established that in this case, the primary long term failure mode of PE pipe is slow crack growth (SCG) from the area of highest stress concentrations. Therefore, LEFM theory should be employed to calculate maximum SIFs.

3.8.2 Analytical stress calculations in an unburied, thick-walled cylindrical pipe with diametral circular holes under internal pressure

Pressure vessels plays a main role in wide range of applications to store or transfer gas or liquid substances. Integrality of the vessel is one of the most crucial factors in safe design, maintenance and operation. It becomes more vitally when they need to work under harsh conditions like high temperature or pressure. The developed models to investigate pressure vessels can be categorized into two groups: thin- and thick-walled pressure vessels. Once ratio of thickness to outer diameter is very small, in the order of 1/20, the vessel is named thin-walled. Under this condition, complex theoretical conditions are yielded to simple equations. In another classifications, the models are classified into empirical, theoretical and numerical. Throughout the past few decades, various experimental, analytical and numerical formulas have been developed through criteria to predict the vessel failure under several assumptions and circumstances by researchers [130, 131]. Elastic stress calculations in a plain undisturbed thick-walled cylinder (without the presence of holes) under the effect of internal pressure are well known, e.g. [132]. By employing classical Lame's equation and taking the plane containing highest stress values which occur at the inner surface of the cylindrical pipe (main bore hole surface), the calculations for maximum hoop (circumferential), radial, and longitudinal stresses in a thick walled vessel yield to Eqs. (3.19), (3.20) and (3.21) for a large cylinder, respectively:

$$\sigma_{\theta\theta})_{vessel} = \frac{P_i(k^2+1)}{(k^2-1)}, \tag{3.19}$$

$$\sigma_{rr})_{vessel} = -P_i, \tag{3.20}$$

$$\sigma_{zz})_{vessel} = \frac{2\nu P_i}{(k^2-1)}, \tag{3.21}$$

Here, $k = \frac{D_o}{D_i}$ is the diameter ratio (where D_i and D_o denote the inner and outer pipe diameters, respectively), ν denotes the Poisson's ratio and P_i denotes the pipe internal pressure. It can be employed from the equations that the hoop stresses are higher than radial and longitudinal stresses.

Due to range of available materials in manufacturing pipe and vessels under different working conditions, several criterion to forecast failure of the vessels have been developed and used by designers. Selecting the proper criterion according to working condition and the material is a vital task to meet design requirements, as the inappropriate criterion may lead to unsafe vessel or over design [106]. In mechanical engineering design, it is typical to compare equivalent stresses to the actual three-dimensional stress state and link them to yield and failure criteria. As mentioned previously, theoretical-based models like maximum shear stress criterion, von Mises and maximum normal stress are types of equations. For example, maximum shear stress criterion is one of failure theories that is applicable to any mechanical systems. This theory states that when combination of principle is beyond specific value, failure happens. Each theory has its own advantages and disadvantages, additionally might be not fitted to design requirements or not accurate under specific conditions. For example, the aforementioned theory is more conservative than von Mises in predicting failure. Therefore, design according to maximum shear stress theory could lead to over design, which will increase cost of manufacturing due to more material required to be consumed [106]. By the way, one commonly used criterion involves the definition of von Mises stress σ_e as below:

$$\sigma_e = [\frac{(\sigma_1-\sigma_2)^2 + (\sigma_2-\sigma_3)^2 + (\sigma_3-\sigma_1)^2}{2}]^{\frac{1}{2}}, \tag{3.22}$$

in which σ_1, σ_2, and σ_1 are the principal stresses. Therefore, by substituting the principal stresses from equations (3.19), (3.20) and (3.21) in Eq. (3.22), the equivalent (von Mises) stress for a long cylindrical pressure vessel is:

$$\sigma_e)_{vessel} = \frac{P_i\left[3k^4 + 1 + 4\nu(\nu-1)\right]^{\frac{1}{2}}}{(k^2-1)}, \tag{3.23}$$

It is frequently necessary to drill a bore hole through the wall of a cylindrical pressure vessel, where the bore itself of circular section should lie along a diameter of the main cross-section [25]. In this section we investigate the weakening effect of the aforementioned circular bore which is introduced at radial position from the cylindrical pipe

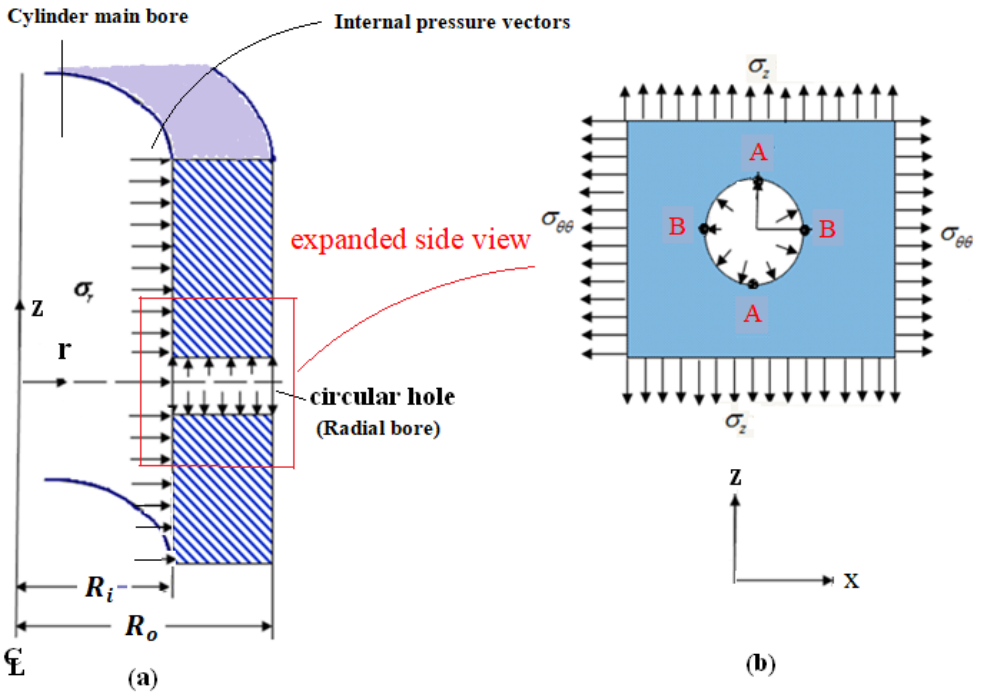

FIGURE 3.5: Thick walled cylinder having a normal hole of circular cross-section. (a) Cylinder or large size pipe under internal pressure, (b). Hoop and axial stress distribution on a portion of the cylinder or pipe in the x – y plane.

radial line. Analytical approaches to deal with stress calculations in the vicinity of a radial hole in a thick-walled cylinder are very limited. However, the above mentioned analytical formulations for the stress calculations can be derived to estimate maximum stresses associated with the presence of small diametral round holes in the pipe wall of an unburied, large thick-walled cylindrical pipe which is under internal pressure of the fluid passing through the pipe. Fig. 3.5, demonstrates the geometry of a small circular hole which is created radially in the wall of a pressurized cylinder and shows the applied effective stress field to the hole in plane perpendicular to its axis. Applied loads on the pipe are considered as static pressure vectors as shown in Fig. 3.5(a) and (b). The present assumptions (other than those automatic for a Hookeian elastic system) are that:

1- The cylinder is loaded solely by internal pressure P which of course will act also inside the radial bore itself.

2- The cylinder is long so that plane strain assumption is applicable to both cylinder ends.

3- The sectional dimensions of bore hole are small compared with the main bore diameter.

Radial stress with respect to the cylinder axis which is applied normal to the plane shown

in Fig. 3.5(b) equals to $\sigma_{rr} = -P_i$. The general level of stress in an intact cylinder is of course greatest at the main bore, and due to the presence of tensile stress $\sigma_{\theta\theta}$, the stress concentration effects of the diametral circular hole of Fig. 3.5(b) should be greatest at points "A" at the outlets of the main bore. The applicability of the classical theories of stress concentration at a circular hole on a plane stress field can be argured for the material at the bore surface at points "A". For perforated plates it can be proven that the maximum tensile stress is $\sigma_{xx} = 3\sigma_{\theta\theta}$ [26]. The problem of a pipe including a round hole in the wall can be compared to the aforementioned flat plate. Considering this assumption and from Eq. (3.19) for cylindrical wall, we can write:

$$\sigma_{xx} = \frac{3P_i(k^2+1)}{(k^2-1)}, \tag{3.24}$$

where the x-axis is in the hoop direction of the cylindrical pipe. This stress occurs at the hole edges in the internal surface of the pipe. Due to the presence of tensile stress σ_{zz}, its effect should also be considered on the tensile stress at point "A". Therefore, the greatest stress concentration occurs at the points "A", where:

$$\sigma'_{xx} = \sigma_{xx} - \sigma_{zz} = \frac{3P_i(k^2+1)}{(k^2-1)} - \sigma_{zz}, \tag{3.25}$$

By substituting Eqs. (3.21) and (3.24) into the above equation, we obtain:

$$\sigma'_{xx} = \frac{P_i(3k^2+3-2\vartheta)}{(k^2-1)}, \tag{3.26}$$

Now, if the internal pressure of the fluid passing through the pipe is also applied inside the hole, stress value at point A in the axial direction (x-direction) is more than σ_{xx}, obtained from Eq. (3.26), because further contribution of pressure at point A imposes an effective hoop stress at the inner wall equal to that in a cylindrical pressure vessel with an infinite radius ratio. It can be shown that the aforementioned extra hoop stress in the limit will approach $+P_i$, which may be superimposed on Eq. (3.26) to obtain maximum hoop stress in a large cylindrical pipe with a small circular hole as:

$$\sigma_{\theta\theta} = \frac{P_i(4k^2+2-2\vartheta)}{(k^2-1)}, \tag{3.27}$$

For an isotropic elastic pipe material of MDPE, with Young's modulus of $E = 427$ MPa and Poisson's ratio of $\vartheta = 0.35$, (similar to polyethylene pipes in gas transmission networks), the aforementioned equations can be simplified to obtain principal stress

values. Therefore, in the presence of a small radial hole, the principal stresses in three principal coordinate directions at point A of the inner wall of perforated MDPE pipe (at radial hole-main pipe bore intersection) can be simplified as follows:

$$\sigma_{\theta\theta} = \frac{P_i(4k^2 + 1.3)}{(k^2 - 1)}, \tag{3.28}$$

$$\sigma_{rr} = -P_i, \tag{3.29}$$

$$\sigma_{zz} = \frac{0.7P_i}{(k^2 - 1)}, \tag{3.30}$$

Additionally, in the present problem, by substituting the principal stress equations for a perforated pipe Eqs. (3.28, 3.29 and 3.30) into Eq. (3.22), equivalent (von Mises) stress at point A in the presence of a hole is:

$$\sigma_e)_{vessel} = \frac{P_i\left[21k^4 + 3.6k^2 + 0.27\right]^{\frac{1}{2}}}{(k^2 - 1)}, \tag{3.31}$$

However, research on the mechanics of shell is complex compared to continuum problems due to the combination of in-plane and out-of-plane loading. Because analytical solutions have been derived only for shells of simple geometries and boundary conditions, numerical methods have been developed to address practical shell problems with complicated shapes and boundaries. A popular method to analyze shell structure is the finite element method (FEM).

3.8.3 Buried pipe model

In engineering design, soil classification systems for structural applications are based on soil mechanical and physical properties including grain sizes. Commonly, AASHTO and ASTM standards are used as guides for these purposes [19, 133]. If the trench is created to install underground polyethylene pipes in their application for gas transportation, it is recommended to use the dimensions and surrounding materials as described in Fig. 3.6 [134].

In order to investigate the stress distribution in a pressurized PE gas pipe, a pipe with an outer diameter of 114.3 mm was selected with D_{SDR} =11.5. Based on selected pipe diameter, the thickness was calculated based on the D_{SDR} value.

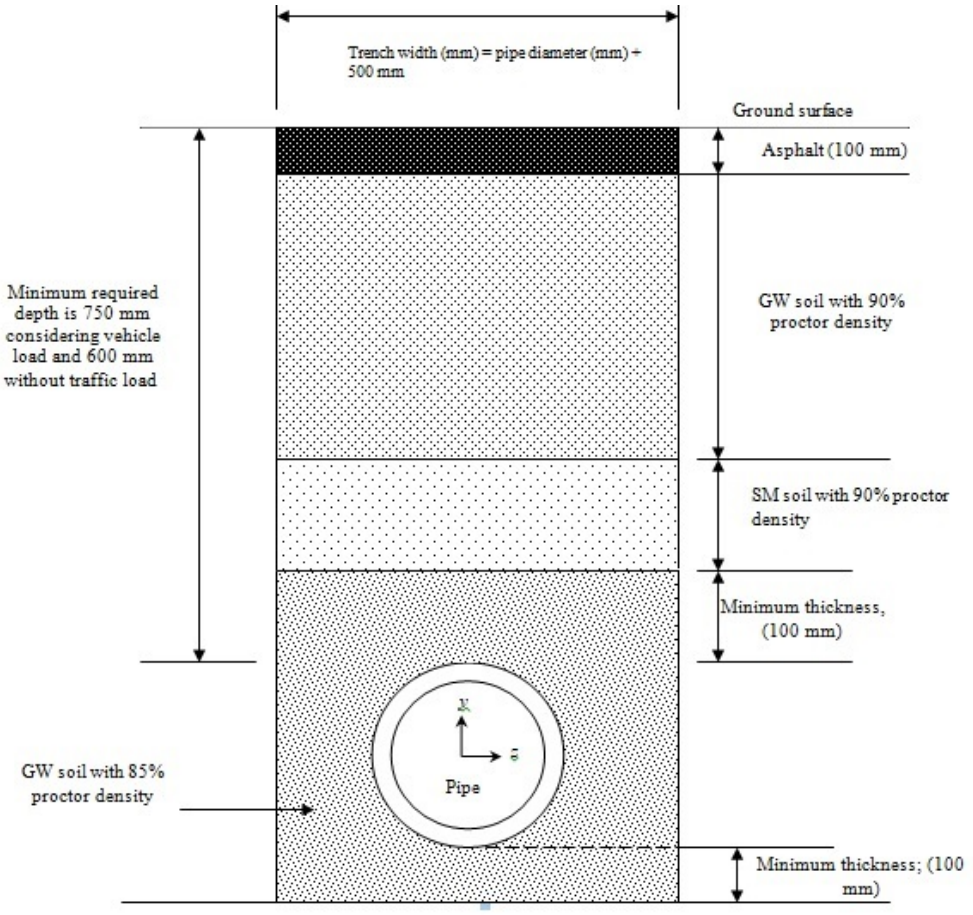

FIGURE 3.6: Properties and dimensions of the pipe surrounding layers in the trench [134].

Therefore, in this research the trench dimensions and pipe surrounding were selected based on ref. [134], as depicted in Fig. 3.7(a). As mentioned previously in Sec. 3.7.3, the most common traffic load used in pipe design is the H20 highway loading. Based on AASHTO standards, the wheel loading for H20 trucks is calculated based on Fig. 3.7(b). Furthermore, the pipe itself is surrounded by different layers of soil in which the properties of each layer are listed in Table 3.3. As stated previously, polyethylene material undergoes creep in the long term, and thus it is customary in design to use a reduced strength based on a 50 years life time and treat the material as linear elastic and isotropic in calculations ([123] and [38]). The magnitude of traffic load due to H20 truck loading was selected as 544 780 Pa. This accounted for any dynamic load exerted on the pipe by wheels. Additionally, as stated previously, inside pipe pressure was assumed as equal to 4 bar (405 300 Pa). This is the actual pressure that used in domestic gas pipelines in the metropolitan area of Iran.

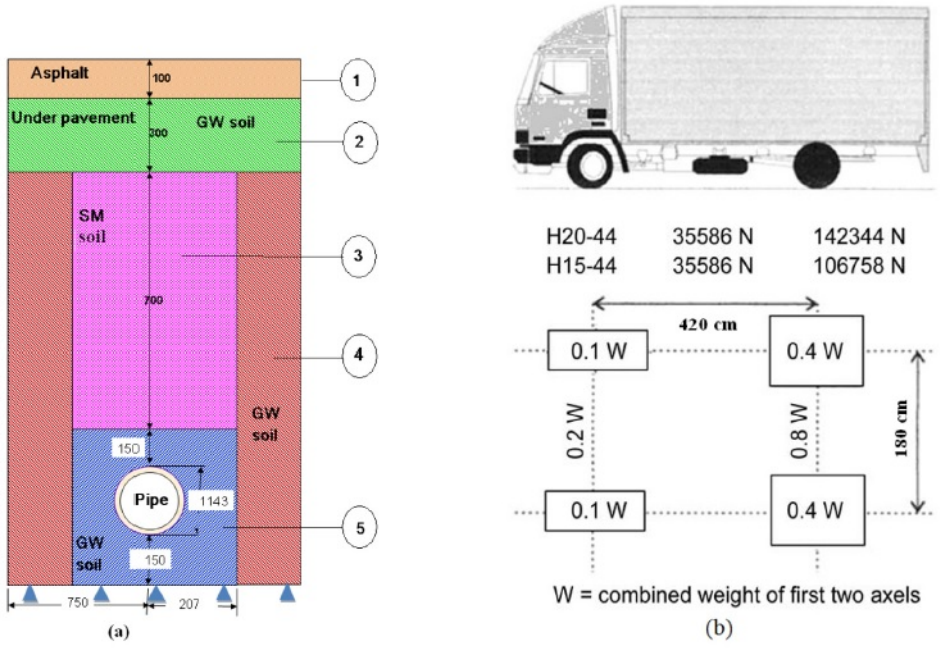

FIGURE 3.7: (a) Trench dimensions and pipe surrounding in mm (for description of soil layers 1 to 5, see Table. 3.3) (b) traffic loading [21].

TABLE 3.3: Properties of each soil level around and above the pipe (see Fig. 3.7(a)).

Layer No.	**Type of the soil**	**Modulus of elasticity (MPa)**	**Density ($\frac{kg}{m^3}$)**	**Poisson's ratio**
1	Asphalt	173.0	2200	0.35
2	GW soil with 90% Proctor density	6.9	1700	0.20
3	SM soil with 90% Proctor density	6.9	1900	0.35
4	GW soil with 95% Proctor density	15.0	2000	0.35
5	GW soil with 85% Proctor density	4.8	1600	0.20

3.8.4 Finite element model of above-ground and buried damaged gas pipe

Finite element analysis which is a numerical solution technique for obtaining approximate estimations in a wide field of continuum mechanics [135], has been used also in the study of problems related to oil and gas industry. In underground problems, the interaction between soil and pipe is very complicated especially in the presence of internal pressure, traffic load and defects in the pipe wall. Therefore, we expect both compressive and tensile loads to be imposed in the pipe wall. Therefore, estimating stress distribution in the pipe by analytical techniques is very difficult and numerical approaches like FEM is suggested to obtain accurate results. As mentioned previously, analytical formulations can only be used to estimate stress values at the crown of buried simple pipes. Meanwhile, in underground structural design, we need to know maximum stress values

resulting from all superposition of stress components. On the other hand, finite element method assumes a linear relation between stress and strain and then by using this relation, all stress components and specially maximum stress values in the pipe and soil can be determined. Finite elements work by creating geometry regions of the problem, setting discrete approximation functions in every region and then connecting them together. In other words, a finite element simulation of a physical structure introduces a piecewise approximation to the governing equations. Consequently, a physical model is split into several solution regions which will be evaluated analytically by substituting the aforementioned solution regions with a group of discrete elements. As we can put these elements together by several methods, they can be employed to model extremely complex structure. A short description of the finite element method is presented in Appendix A. In this research, the geometric models were built using modeling tools existing in preprocessing module of ANSYS 16.2 software. Then the finite element analysis was also conducted by ANSYS. For the cases with stress singularities, ANSYS workbench was employed enabling us to use fracture mechanics tool available in the software.

3.8.4.1 Input data collection

Collecting input data is a very critical task when conducting a finite element simulations. According to this study, pipe, patch and surrounding material mechanical properties, trench dimension and environmental condition are required. Different sources of data can be used for collecting input parameters, these include: Published data in literature related to similar problems; and Simultaneous lab experiments and/or field tests. Polymer pipes made of medium density PE and high density PE with nominal diameter of 4 in. (IPS Standard) and standard dimension ratio (D_{SDR}) of 11.5 are widely used in the gas distribution industry ([136]). In the pipe manufacturing industry, especially for plastic pipes, the standard dimension ratio (D_{SDR}) is defined as the ratio of pipe outside diameter, D_o to the pipe wall thickness t, as ([137]):

$$D_{SDR} = \frac{D_o}{t}, \tag{3.32}$$

In this research, to investigate the stress distribution in a pressurized PE gas pipe, a 114.3 mm outside diameter pipe was selected with $D_{SDR} = 11.5$. Based on the selected pipe diameter, its thickness was calculated according to this SDR value. Table 3.4 presents a summary of the geometry of the equivalent pipe in this analysis, which is widely used PE pipe in gas transmission networks, based on the standard tables provided by the dominant polyethylene pipe manufacturers.

TABLE 3.4: Geometrical parameters and characteristics of a widely applied polyethylene pipe for gas distribution based on ASTM D 2513 ([18]).

Nominal diameter (inch)	**Actual outer diameter inch (mm)**	**Actual inner diameter inch (mm)**	**Standard Dimension Ratio (D_{SDR})**	**Minimum pipe thickness inch (mm)**
4	4.5 (114.30)	3.718 (94.44)	11.5	0.391 (9.93)

For computational models in this research, the physical and mechanical properties of yellow MDPE pipe of type PE80 and HDPE pipe of type PE100 which are obtained from tensile tests are used, according to the properties of polyethylene materials manufactured in Iran. These material properties are uniformly distributed along the pipe for each case of finite element model. A summary of the convenient MDPE and HDPE material properties used in this research are presented in Table 3.5. All the results produced in this research assume the pipe and patch material to behave elastically with no local yielding occurring in the region of the bore hole.

TABLE 3.5: Mechanical properties of medium density polyethylene pipe of type PE80 and high density polyethylene pipe of type PE100 ([21]).

Pipe material	**Elasticity module (MPa)**	**Yield stress (MPa)**	**Poisson's ratio (ν)**	**Thermal expansion coef. ($^{\circ}C^{-1}$)**
PE80	427	19.3	0.35	0.0002
PE100	1034	24.8	0.4	0.0002

Soil grades around the pipe's circumference were selected based on ASTM standards. With reference to Eq. (3.7) and according to Fig. 3.7, a burial depth of 125 cm was selected for the pipe. At this depth, on a daily basis, any climate changes at the ground level do not appear to affect the pipe temperature [21]. The pipe was assumed as buried in a trench with a width of 414 mm while surrounded by a layer of fine gravel. The ground surface was assumed as covered by a thick layer of asphalt. The effect of traffic load in terms of distributed or concentrated loads on the pipe was also included.

3.8.4.2 Mesh generation and discretization

Mesh quality is a significant issue in generating accurate results for finite element analysis (FEA). Literature concerning mesh optimization includes many different techniques and procedures for mesh refinement and smoothing [138–140]. The mesh model size requires to be selected so that end effects are prevented. Further mesh refinement is required in the pipe internal surface, near defect region and other zones of interest. This decision is even more critical when three-dimensional models are employed. Increasing

the number of elements with additional degrees of freedom highly adds to the complexity of the finite element model. Additionally, adding more complexity to the models like including non-linear elements may create convergence problems, especially with a high number of integration points.

Various types of finite elements can be used for computational analysis of the problem. ANSYS V16/2 finite element analysis (FEA) program was used for the three-dimensional (3D) modeling and performing static analysis of the pipe, related patch and its surrounding. Since stress distribution in the pipe wall is very important, 3D homogeneous elements called SOLID95, available in the ANSYS software package elements library, are employed to model the pipe, patch, and the surrounding medium. This element with mid-side nodes is designed for structural purposes in which each node exhibits three degrees of freedom (three translations in x, y, and z directions).

Two options of SOLID95-3D elements are available in Ansys library. One options is Tetrahedron (Tet) element and the other one is Hexahedral (Hex) element and both can be chosen for simulating complex models like this problem. Hexahedron (having six faces), twenty-node element is designed for modeling complex structural problems. As the simulations involves pipe, patch, different soil grades and asphalt, then multi-zone meshing method is required. The soil–pipe interaction was also incorporated in the model by using face to face contact elements (contacta 172 and target 170). For the patch repair section, in order to model pipe/patch connection by electro-fused welding, all nodes and elements at the region where the pipe material and the patch material meet, were merged together. No special contact or cohesive element were used at the patch/pipe interface.

We used bottom up approach in meshing process by meshing lines then surfaces and finally volumes. A geometric computer model of the pipe was created in ANSYS so that the center of coordinate system aligned with the center of pipe and the z-axis aligned with the pipe's axis. The defect is modeled as a local circular thinning area and also complete hole located at the pipe mid-length. This way of modeling the defect translates into a conservative approach in which any defect shape is represented by the affected region. Because of the geometry and load symmetry, only a quarter model is sufficient for FE analysis. The application of adequate boundary conditions plays an important role in the numerical analysis. Therefore, suitable boundary conditions where applied on the four surfaces on the one quarter model, that is Surface A, Surface B, Surface C and Surface D, as shown in Fig. 3.8. The finite element model is constrained by symmetry boundary conditions in both z- direction (along the pipe and the trench) and x- direction. u_z of surface A and u_x of surface B are restrained to simulate the symmetric boundary conditions of the two surfaces [6, 104]. As we are modeling a long pipe that there is insignificant strain in the pipe longitudinal direction, u_z of surface C is also restrained to simulate the plain strain state of buried pipelines induced by soil

constrains. At the same time, u_x, u_y and u_z of surface D are restrained to model the bottom part of the trench where the ground is not excavated. Boundary conditions for all under ground pipe finite element models are applied on the nodes at the mentioned location as given by Eqs. (3.33-3.35):

$$@\ z = 0,\ z = -\frac{l}{2};\ u_z = 0; \tag{3.33}$$

$$@\ x = 0,\ u_x = 0; \tag{3.34}$$

$$@\ y = -207.15\ mm,\ u_x = u_y = u_z = 0; \tag{3.35}$$

Gas pressure load of 405300 Pa is allowed to apply on the main cylinder bore (internal surfaces of the pipe) as well as on the wall of the radial bore hole. Additionally, an optimum dimension for finite element model of the pipe, soil and surroundings, is required. Therefore, investigation of simultaneous effects of soil column weight and internal pressure of the fluid passing through the pipe for various x and y (per the upper surface of Fig. 3.8) on the maximum first principal and maximum von Mises stresses in the defective buried pipe shows that $x = 1.5\ m$ and $z = 1.5\ m$ can be employed as acceptable model dimensions. With these dimensions, maximum values of hoop and von Mises stresses in a pipe with a certain type of damage will not vary significantly as we increase model dimension [4]. Therefore, results indicated that any model bigger than $x = 1.5\ m$ and $z = 1.5\ m$ will yield results in an acceptable range.

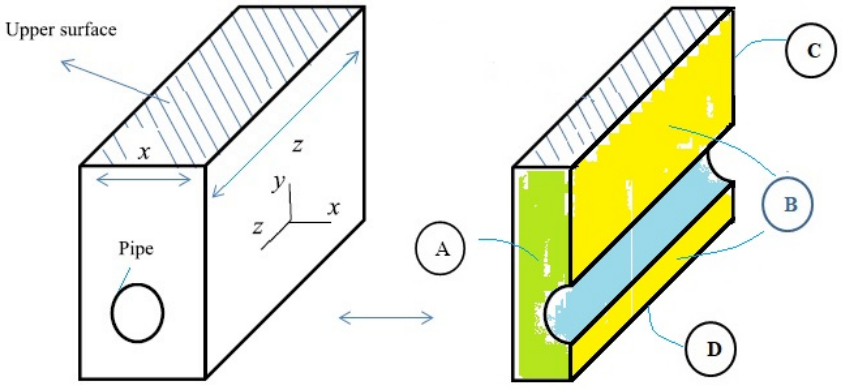

FIGURE 3.8: Three dimensional view of trench and buried pipe to illustrate model size.

We changed the mesh several times with the goal of increasing the speed and accuracy of the numerical calculations performed over the model. In finite element solution, using too small elements could increase computational cost and decrease solution speed while

too large elements could not provide required accuracy. Therefore, optimal finite element sizes are required to model defective pipe models. We used small elements around the defect area as we require accurate solution in this region. Larger elements were used for regions of the pipe which are away from the hole location.

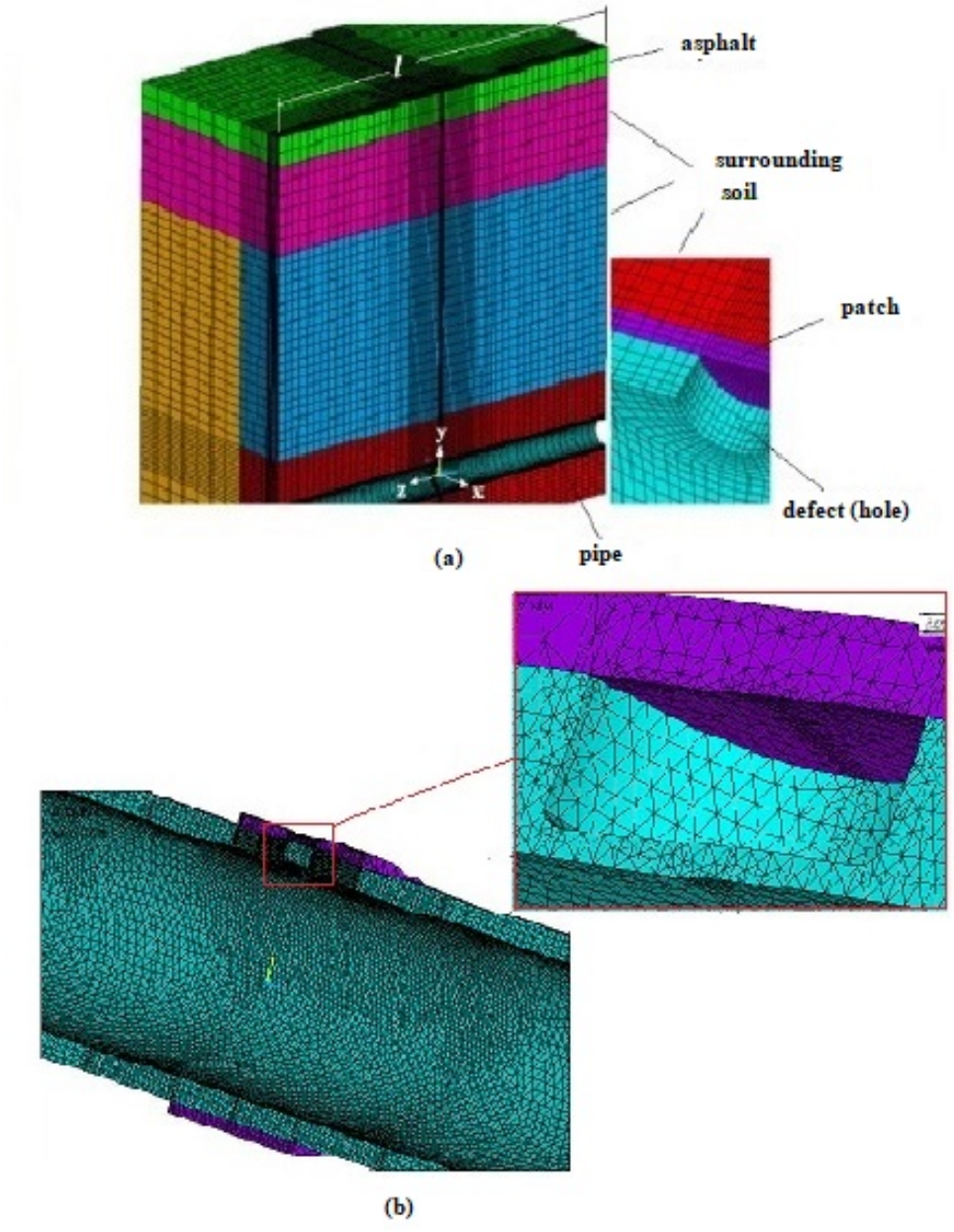

FIGURE 3.9: Illustration of the element plot of the buried pipe modeled by SOLID95 elements. (a) Finite element model of the patched pipe with surrounding soil using Hexahedral (Hex) elements. (b) Defective pipe and surrounding patch model using Tetrahedron (Tet) elements and an expanded view (surrounding soil is removed).

As mentioned previously, in order to conduct a strength analysis of a buried PE pipe

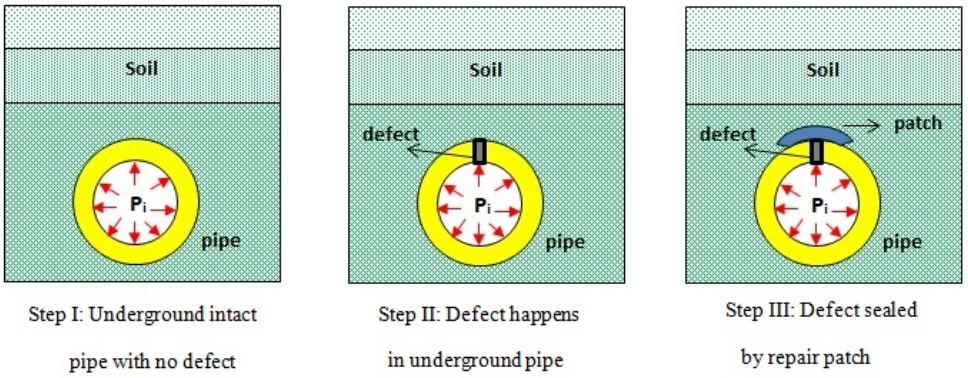

FIGURE 3.10: A schematic of steps required for a detailed buried pipe strengthening study.

using the finite element method, a three dimensional model of the pipe and its surrounding is required. Additionally, Fig. 3.9 illustrate the element plot of the buried pipe modeled by SOLID95 elements for the geometry shown in Fig. 3.7. Fig. 3.9(a) shows the FE model of a half of the pipe in its surrounding medium. A magnified view of the pressurized pipe (with a patch on its defective area) is shown in Fig. 3.9(b). The pipe material was selected from PE80 while PE100 was used for the patch. Furthermore, the effect of the traffic load, soil weight, temperature change of the pipe, inside pressure, and the presence of patch on the defective area were all included to investigate their overall effect on stress distribution in the repaired PE pipe. A fine mesh was applied to regions near the defective area while it was allowed to become coarser in areas far from the defect. In order to obtain accurate results, the postulated model was executed based on different mesh conditions (and element numbers) until adequate convergence was reached.

It is critical to mention the assumptions considered for this study. Without making these assumptions, the problem becomes very complex and cannot be easily solved with the methodologies described in here. Further, using linear elastic and isotropic material model is the easiest approach for underground simulations. Therefore, for all the FE models in this study we considered linear elastic and isotropic material properties. For simplicity, this study only considers horizontal buried pipes where overburden stress is normal to the pipe crown. For the patch investigation it is assumed that:

1- Fusion welding process is well performed to avoid any defect or crack in the weld region.

2- The residual stresses in welding are ignored.

An important concern in our finite element analysis is the existence of discontinuities in the models. Typical discontinuities can be joints, fissures, fractures and faults. As we

investigate the effect of several defects in gas pipes, these defects are sources of discontinuity in the model and therefore, features are required to have discontinuities in the numerical model. These issue is well discussed in the related sections. A schematic of steps required for a detailed buried pipe strengthening study is depicted in Fig. 3.10. SI units are used to illustrate the parameters and dimensions of the variables. Solver assumes negative stresses as compressive stresses and positive stresses as tensile stresses.

Chapter 4

Finite Element Analysis Results of Stress Distribution in Defective above-ground Polyethylene Gas Pipes

4.1 Finite element model results of above ground damaged gas pipe

In this part of the research, the results of geometric and finite element models for above-ground polyethylene gas transportation pipe, which were built using ANSYS 16.2 software are presented and discussed. As mentioned in Sec. 3.8.4, medium density PE and high density PE with nominal diameter of 4 in. standard dimension ratio (D_{SDR}) of 11.5 are selected to investigate the stress distribution in a pressurized PE gas pipe. Geometrical properties of the equivalent pipe in this analysis are summarized in Table 3.4. Additionally, the physical and mechanical properties of yellow MDPE pipe of type PE80 and HDPE pipe of type PE100 used in this part of study are based on Table 3.5. As mentioned previously, for FE analysis, only a quarter model is sufficient since symmetry boundary conditions in both z- direction (along the pipe) and x- direction, are applicable. Pipe internal pressure is assumed to be 405300 Pa.

In order to investigate polyethylene pipeline for long life period (50 years) and include the viscoelastic behaviour of the polyethylene pipe material, peak values of the resulted stresses in the pipe are compared to their corresponding values of σ_s, which are according to their σ_{MRS} values. Based on Eq. (3.15), σ_s is calculated by dividing σ_{MRS} values by C. In this research, C is assumed to be between 1.25 to 2 according to reference [21].

σ_{MRS} values of PE80 and PE100 are given on Table 3.2 for various working temperatures.

For a plain undisturbed PE pipe, our numerical simulation shows that the stress distribution obtained from finite element analysis matches the analytical (Eq. (3.19)) for the identical long plain PE pipe. However, the introduction of a small partial or through-wall bore hole to the pipe wall, seems to produce a complex stress field, which requires much more effort to investigate.

4.1.1 Above ground pipeline with complete and partial hole damages in pipe wall

Investigating mechanical behavior and the performance of polyethylene (PE) pipelines in natural gas distribution systems and specially the applicability range of PE pipes with local defects, in hot climate areas, based on the life time of 50 years has been of great importance for natural gas distribution companies. This concern is due to the fact that, above ground gas pipeline can experience high stress values because of internal pressure, temperature variations and local defects in the pipe wall. Therefore, in this section, we propose a novel simple process to study mechanical response of defective pipeline under the combination of these parameters, by evaluating maximum stress values imposed to medium density (MD) and high density (HD) polyethylene gas pipe. The simple pipe geometry was presented in Table 3.4 and material properties of MDPE and HDPE materials were presented in Table 3.5.

Fig. 4.1 shows a cross-section of the half equivalent pipe in the presence of a defect. The expanded views on right top and left top of this figure show the details around two defects, i.e. local partial round hole and complete through-wall hole respectively, as seen from the outside of the pipe. In order to model a local defect in external surface of polyethylene pipe, such as flaws from scratches or stones point loading, it is assumed that the defect geometry is a partial round hole which has not fully penetrate the wall thickness, as shown in the right top of Fig. 4.1. As mentioned before, this kind of defect may introduce thinning effect on the pipe's cross section. Also, a leak opening through-wall complete hole with circular shape in the pipe wall, as shown in the left top of Fig. 4.1 is created and modeled.

As this part of research focuses on the above ground distribution system, therefore only the elastic stresses and deformations induced by internal pressure and pipe temperature variations on the circular hole in the pipe are considered. In other words, soil column weight, traffic loads, plastic deformation and other effects are not included in the numerical calculations. The numerical simulations and calculations are carried out by a commercially available finite element software (ANSYS 16.2 Mechanical APDL) and the

obtained results are compared to the critical stress values for an operating pressure of 4 bars and various temperatures, using Table 3.2 and employing a safety factor. Because of the geometry and load symmetry, the finite element model is constrained by symmetry boundary conditions in z-direction (along the pipe), where u_z of surface A is restrained and also x-direction, where u_x of surface C is restrained, as shown on Fig. 4.1. Therefore, only a quarter model is simulated for FE analysis. Plane strain constraint in the direction of the pipe axis (z-direction) is assumed for the long pipe where u_z of surface D is restrained and this constraint is applied to the nodes located at the pipe ends. At the same time, u_y of the line at the bottom of the pipe has been also restrained to prevent the pipe free to move. The pressure load is applied to the internal surfaces of the pipe. Several simulations were performed by varying the defect geometry, including the hole radius and hole depth.

In order to verify the applicability of finite element method (FEM) for solution of such problems, several unburied pipe was modeled and loaded to a final pressure of 405300 Pa (4 bar) while subjected to circular holes of various sizes (from a small hole of 2.5 mm diameter to a large hole of 30.0 mm diameter and from a shallow defect of 8% hole depth to pipe thickness ratio (thickness reduction) to a deep one of 100% complete hole) at the pipe crown.

Although, hexahedral mesh reduces element count and run time, but for smaller size holes, small mesh size on holes need to transition to larger size elsewhere, but transitioning hex mesh can be a problem. Therefore we used tetrahedral elements throughout in the finite element analysis, which is easier to mesh more complex geometry. Fig. 4.3 shows a finite element model of the equivalent perforated pipe and a magnified view at the defect vicinity, as seen from inside of the pipe. Displacement scale factor of 5 was selected to better displaying deformations around the defect area. In order to determine the optimal finite element size, a sensitivity analysis was performed for each model. Too coarse meshes would not provide the required accuracy, while too fine meshes could decrease computational speed.

Thermal stresses in above ground plastic pipes are considerable and must be calculated and superimposed to the stresses resulting from pipe internal pressure. For the calculation of thermal stresses we require the information of ambient temperature of the environment where the pipeline is installed and operated. To a better evaluation, in this section we select a particular region which is city of Ahvaz located south-west of Iran, where the weather is unstable and although the city experiences hot weather days in the middle of summer, it experiences cold days during winter. As mentioned previously, in a very hot summer day, the above ground PE pipeline may experience a temperature change of around 30 °C, as the average surrounding temperature varies from 20 °C in the morning up to above 50 °C in early afternoon. Additionally, the same

pipeline may experience a temperature change of 15 °C during a cold day as the temperature changes from 5 °C in the morning up to about 20 °C in the afternoon. Evidently, this severe temperature variations effects the resulting thermal stresses in the pipe wall significantly. Therefore, we investigate the critical stresses in the previously mentioned defected pipes under simultaneous effects of internal pressure and severe temperature variations of $\triangle T = \pm 30\,^{\circ}\mathrm{C}$.

The maximum first principal and von Mises stresses obtained from numerical solutions (FEM) closely matches the analytical solutions from Lame' equations (Eq. (3.19)) and show that the maximum von Mises stress and maximum first principal stress (here, maximum circumferential stress) in a similar long plain (intact/without any defect) MDPE pipe under the effect of 4 bar internal pressure reaching 2.24 MPa and 2.15 MPa, respectively at the pipe bore. Also, for the similar pipe of HDPE (PE100) material, maximum von Mises stress and maximum first principal stress are around 2.22 MPa and 2.15 MPa, respectively. Obviously, in the presence of aforementioned defects and also temperature variations, the maximum stresses will be significantly higher than those for simple pipe and the resulting stresses may cause severe damage to the pipeline. The obtained finite element results allows evaluating of the critical stress values, stress concentration areas and also finding the damage status which means if it is permissible or seriously dangerous.

TABLE 4.1: Verification of finite element mesh refinement.

Hole Dia. (mm)	**Number of elements**	**Number of nodes**	**Length of element (mm)**	**Maximum stress (MPa)**		
				Circum-frential	**First principal**	**von Mises**
5.0	144509	228408	2.0	6.47	6.47	6.24
	146270	231168	1.0	6.31	6.31	6.42
	153776	237305	0.3	6.24	6.24	6.35
	234500	356547	0.08	6.24	6.24	6.34
20.0	140396	222442	2.0	7.99	7.99	8.39
	141917	224750	0.4	7.95	7.95	8.36
	147096	232398	0.3	7.95	7.94	8.35
	171669	266773	0.08	7.94	7.94	8.35

4.2 The effects of complete circular hole damage

In this section, we investigate mechanical behavior and stress distribution in an above-ground PE gas pipe under the effect of internal pressure and temperature variations and in the presence of complete circular holes with several diameter sizes, as was depicted in Fig. 3.5 and also at top-left side of Fig. 4.1. Radial bore diameter size effects on the principal and von Mises stresses as well as the resulting stress concentration factors in the vicinity and along the holes are investigated. It is assumed the pipe is 1 meter

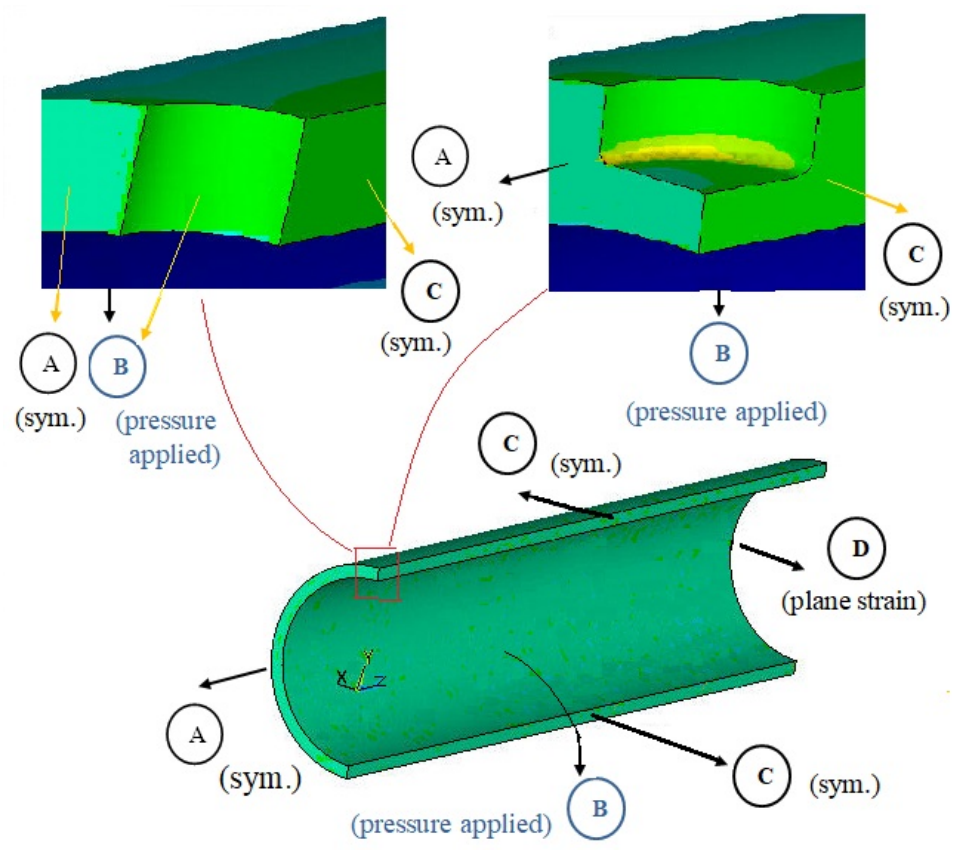

FIGURE 4.1: Pipe model for finite element analysis including expanded view of pipe segments for a complete circular hole and a partial circular hole.

long, with 4 inch nominal diameter. Nevertheless, before investigating several finite element models of above ground PE pipe subjected to several complete circular holes, and presenting the results, firstly, the good performance of our new finite element models should be examined accurately.

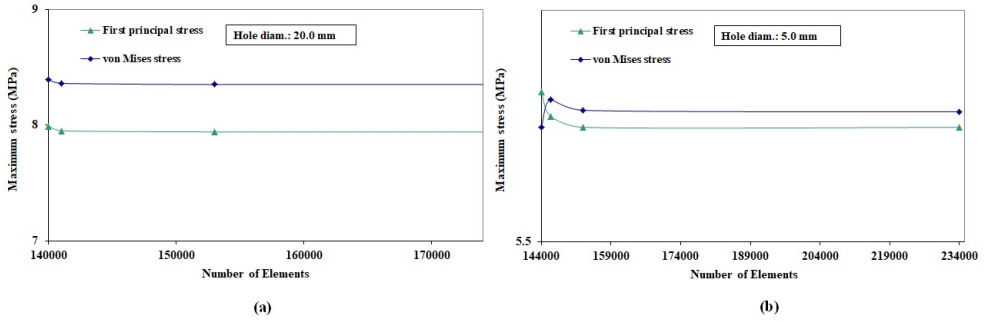

FIGURE 4.2: Trends of maximum von Mises and first principal stresses around complete round bore to study convergence problem (a) For a 20.0 mm hole diameter. (b) For a 5.0 mm hole diameter.

4.2.1 Model verification and meshing refinement and convergence study

The analysis of meshing convergence is crucial to determine a proper refinement for the general model and specially, the defect area. This refinement influences the slope between defective and non-defective regions in the pipe wall. Although may seem important to accurately model the defective area, one should evaluate the influence of the refinement in the results of internal pressure load simulations to determine an efficient meshing for the model.

In this section, in order to evaluate the accuracy and validity of the initial finite element model, the effect of mesh refinement on the model generated with twenty-noded Tetrahedron (Tet) Solid95 elements is investigated using modify mesh module in ANSYS and the results for a PE pipe in the presence of complete holes with 5 and 20 mm diameter size, are compared in Table. 4.1. The material which is uniformly distributed along the pipe is MDPE and the material model is established using mechanical properties mentioned in Table 3.5. First principal stresses, maximum circumferential stresses and also maximum von Mises stresses are calculated regarding the variation of element size and quantity especially around the circular hole region. Based on the results, for both small and large circular holes, further refinement of the generated mesh size in the region of radial bore, produces no significant changes in the elastic stress distribution in the region of bore. For example, finite element analysis performed for a sample with 5.0 mm diameter bore hole yielded similar results for all mesh sizes, since refining mesh in defect region to a high ratio of $\frac{1}{25}$ initial mesh, results in only 3.5 % change in maximum circumferential and first principal stresses, and only 1.6 % in maximum von Mises stress. Additionally, in the pipe with a 20.0 mm complete hole, $\frac{1}{25}$ mesh refinement around defect, results in only 0.6 % change in maximum circumferential and first principal stresses, and only 0.47 % in maximum von Mises stress, which are really infinitesimal. Therefore, the generated finite element model is not mesh dependent and is acceptable for using in the next stage of the research. The curves showing trends of maximum first principal and von Mises stresses are also depicted in Fig. 4.2. All the curves show a converging trend in the results by refining mesh around the defect. It worth mentioning that, the introduction of a small 5.0 mm diameter radial bore into the wall of a PE pipe with 4 inch diameter, is seen to produce a von Mises stress of around 6.30 MPa at the radial bore- main pipe bore intersection which is much higher than the value for similar undisturbed PE pipe. Additionally, maximum von Mises stress resulting from the introduction of a 20 mm diameter radial bore, approaches 1.33 times that in the 5 mm bore diameter size.

The good performance of the present approach and the validity of the initial finite element model can be examined by comparing the numerical results with analytical solutions for some pipe samples with circular holes. For this reason, different complete

holes ranging from 2.5 mm to 10.0 mm of hole diameter were created in pipes. The pipe inside diameter was set to be fixed an equal to 94.44 mm. and several values of k was selected namely, 1.2103, 1.1577, 1.1059 and 1.0526 for comparing the results. The pipe is loaded to 4 bars internal pressure. The pipe material is assumed to be MDPE (PE80). Table. 4.2 shows simulation results for several complete holes in pipe wall of a gas pipeline under internal pressure. In order to confirm simulation results obtained by finite element solution using tetrahedral and hexahedral solid elements, analytical results obtained by Eq. (3.28) are also presented. A sensitivity analysis was performed to ensure that the selected pipe section is long enough to prevent end effects affecting the simulation results around the round bore. Considering the obtained results for maximum stresses from finite element solution and comparing with analytical solutions, it can be conducted that:

1- The introduction of a small bore hole in the PE pipe wall, has a significant effect on the stress distribution and the maximum stress values around the hole region is significantly larger than the stresses in the rest region of the pipe (undisturbed pipe region).

2- Maximum stress values and the stress distribution in the pipe are seriously influenced by complete hole defects in the pipe wall which in most cases exceeds polyethylene's allowable stress for a life expectancy of 50 years.

3- Localized pipe behavior is mostly affected by circumferential (hoop) stresses at the area of the complete round defects.

4- For a fixed pipe thickness, maximum stress values increase significantly with increasing diameter of the holes.

5- For a fixed hole diameter, maximum hoop stresses and maximum von Mises stresses increase significantly by reducing pipe thickness (decreasing the values of k). For example, for a 2.5 mm hole diameter, a 13 % decrease in k (from 1.2103 to 1.0526) causes around 250 % increase in both maximum hoop and von Mises stresses.

6- For all models, the difference between finite element model estimations and analytical results (Eq. (3.28)) are not significant. The predictions by FEM for maximum stresses are in good agreement with analytical results. Therefore, the good performance of finite element analysis and proper boundary conditions are confirmed by comparing both solutions. Such results give credibility to the assumptions and mesh size used in the finite element calculations.

7- The difference between FE results and analytical solutions decreases significantly by increasing pipe wall thickness. For example, in the case of a 2.5 mm hole diameter, a 13 % increase in pipe wall thickness (increasing k from 1.0526 to 1.2103) causes relative difference between FEM and analytical solutions for maximum von Mises stress to reduce from 7.62 % to a small value of 1.59 %. The calculated maximum stresses falls in an excellent agreement for thick-wall pipe. Interestingly, the predictions by Solid95 finite elements for the first principal stress and maximum von Mises stress are in good

agreement with analytical results. We expect this behavior because our assumptions for analytical solution was based on thick-walled vessels. We used thick-walled cylinder equations to derive our equations for defective pipe. Therefore, decreasing pipe wall thickness effects the validity of this assumption and so, will not deliver accurate results for thin-walled pipes.
8- The results obtained by both quadratic hexahedral and Tetrahedron Solid95 elements are acceptable and both element types can be used in the remaining part of the research.

Fig. 4.4 (a) illustrates the finite element model (FEM) of half the pipe in the presence of a hole, to use a symmetric boundary condition, where the meshes are generated by quadratic hexahedral Solid95 elements. Defected pipe is loaded to 405300 Pa internal pressure. Additionally, contour plot of elastic von Mises stresses is depicted in Fig. 4.4 (b). As expected form analytical solution for a pressure loaded cylinder with a hole, the maximum elastic stress values occurred at pipe internal surface and the internal edge of circular hole. As mentioned previously, initiation of plasticity can take place at this region. The values of hoop and von mises stresses obtained through finite element analysis and those in Eqs. (3.28) and (3.31) are reported in Table. 4.2. As shown in this table, for small size hole defects, the percentage differences between finite element results and those obtained through Eqs. (3.28) and (3.31) are low. This difference increases by increasing hole diameter and also decreasing the values of k. The aforementioned differences appear as a function of hole size and pipe diameter. Based on the results, both tetrahedral and hexahedral solid95 elements deliver acceptable results and are proposed for the next steps of this research. Additionally, the applicability of FEM for stress distribution in buried PE pipes was verified in [21]. The length of established pipe was selected to be long enough (one meter) in order to avoid boundary effects on calculated stress results. Also, we modeled longer pipes and the results showed, for damaged pipe models longer than 1.0 m, increasing the pipe length will not affect the maximum stress values at the damage location, significantly.

When the validity of initial model was inspected, the foregoing defects were simulated in the pipe and also loads resulting from temperate changes were superimposed on the pipe and their effects were thoroughly studied through a comprehensive finite element study. This procedure of study is well being employed by many design experts in many areas of engineering [21].
In order to further study the effect of geometry change in the pipe wall in the form of complete circular hole defect, stress concentration factors were calculated after performing finite element analysis and using Eq. (3.4). Maximum von Mises stresses and maximum first principal stresses in the vicinity of the holes were used as highest stresses (σ_{max}) and equivalent stresse values in the simple pristine pipe, was used as nominal

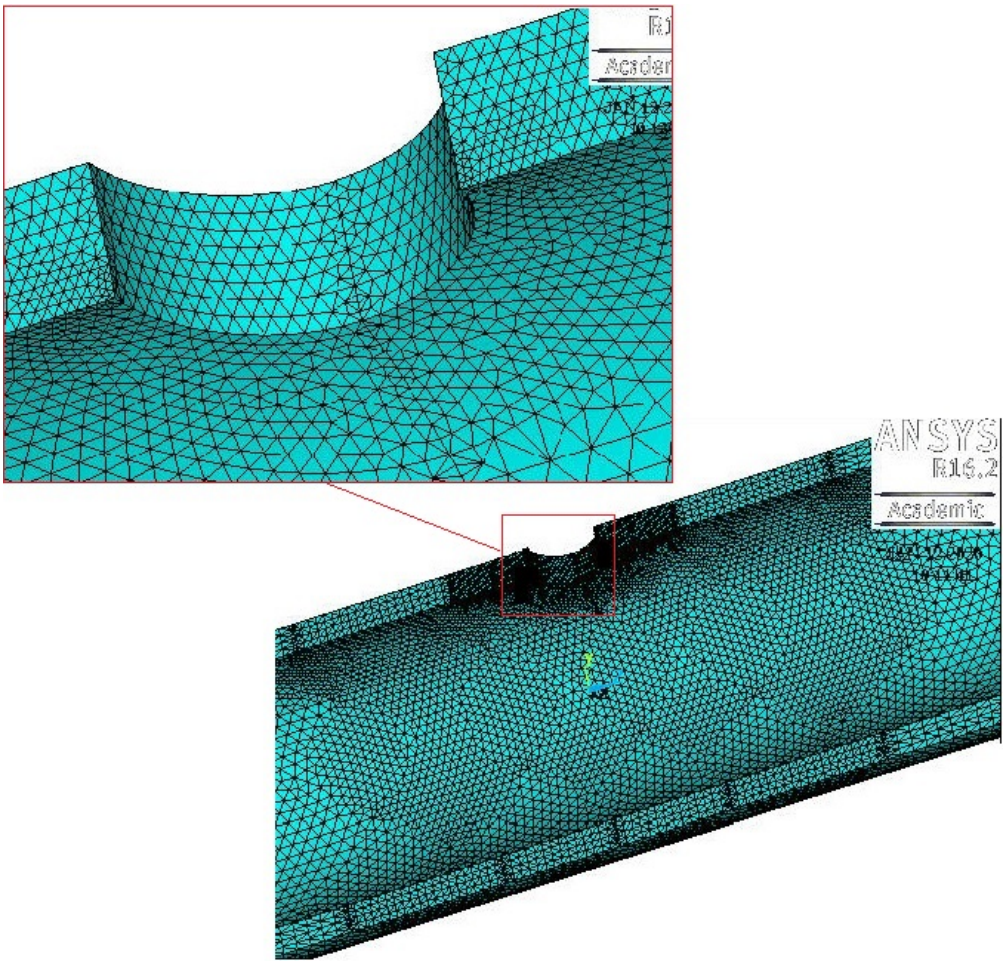

FIGURE 4.3: Illustration of the finite element model (FEM) plot of the perforated pipe using Solid95 elements of Tetrahedron type and magnified view of the pressurized pipe.

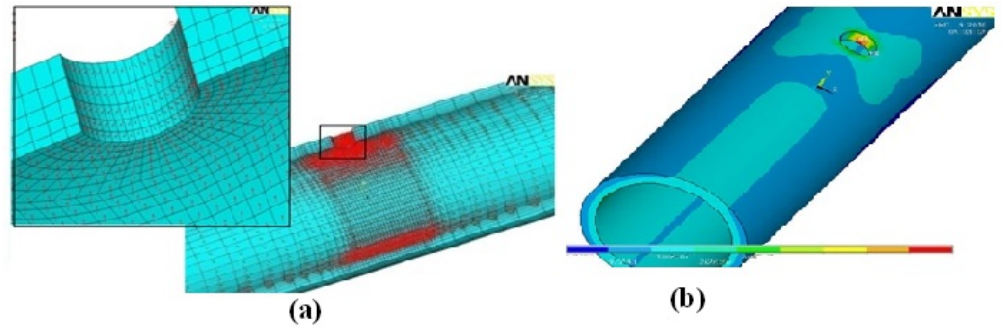

FIGURE 4.4: Finite element modeling (FEM) of the perforated pipe. (a) Solid95 elements of Hexahedral type and presentation of internal pressure vectors and magnified view of the pressurized pipe. (b) Contour plot of von Mises stresses.

TABLE 4.2: Comparison of hoop and von Mises stresses obtained through FE solution and those from Eqs. (3.28) and (3.31) due to an inside pressure only for MDPE pipe.

Hole diam. (mm)	**pipe diam. ratio (k)**	**Type of solid95 Element**	**Max. hoop stress (MPa)**		**Differ. (%)**	**Max. Von-Mises stress (MPa)**		**Differ. (%)**
			FEM	**Eq. (3.28)**		**FEM**	**Eq. (3.31)**	
2.5	1.2103	Tet.	6.57	6.24	5.02	6.30	6.20	1.59
	1.1577	Tet.	8.4	7.93	5.60	7.95	7.79	2.01
	1.1059	Tet.	12.1	11.25	7.02	11.3	10.92	3.36
5.0	1.2103	Tet.	6.47	6.24	3.55	6.42	6.20	3.43
	1.2103	hex.	5.82	6.24	6.73	5.71	6.20	7.90
	1.1059	Tet.	12.1	11.25	7.02	12.00	10.92	9.00
7.5	1.2103	hex.	6.02	5.24	3.40	6.11	6.20	1.47
	1.2103	Tet.	6.46	6.24	3.40	6.55	6.20	5.34
	1.1577	Tet.	8.43	7.93	5.93	8.56	7.79	8.99
10.0	1.2103	hex.	6.43	6.24	2.95	6.47	6.20	4.17
	1.2103	Tet.	6.59	6.24	5.31	6.75	6.20	8.14

(reference) stress (σ_{nom}). Unburied pipe was modeled and loaded to a final pressure of 405300 Pa (4 bar) and the leak-openings were various sizes from 5.0 mm to 35.0 mm hole diameter for both MDPE and HDPE pipe materials and the results are presented in Fig. 4.5. Trends of stress concentration factors which are calculated based on maximum first principal stress and maximum von Mises stress are displayed on Figs. 4.5(a) and 4.5(b) respectively. Obviously, stress concentrations approach unity when the hole diameter approaches to zero. The curves show that stress concentrations increase with increasing hole diameter. For example, in MDPE pipe, the von Mises stress concentration factor in the 35 mm radial bore approaches 1.8 times that in the 5 mm bore diameter size. The curves for both MDPE and HDPE pipe materials display similar trends. For both cases, MDPE pipe material shows higher values of stress concentration than HDPE pipe for all hole sizes, as the related curves for MDPE pipe are above the curves for HDPE material. Even though, the values are close for both materials but the difference between stress concentrations increases for larger holes. The rate of stress concentration rise, increases by increasing hole diameter. In other world, the curves display higher slopes for larger holes. As can be seen, both first principal and von Mises stress concentration factors reach around 5 for holes of 35 mm diameter in the pipe wall, which means a radial hole local stress consentrator significantly increase peak stress values which threaten material elastic limit at the vicinity of the hole and increase the danger of pipe failure especially in presence of cyclic loads. The results of study show that the maximum stress levels are highly effected and increased by complete hole defects. Therefore, in the next section we analyze the stress response of above ground PE pipe under considerable loading conditions.

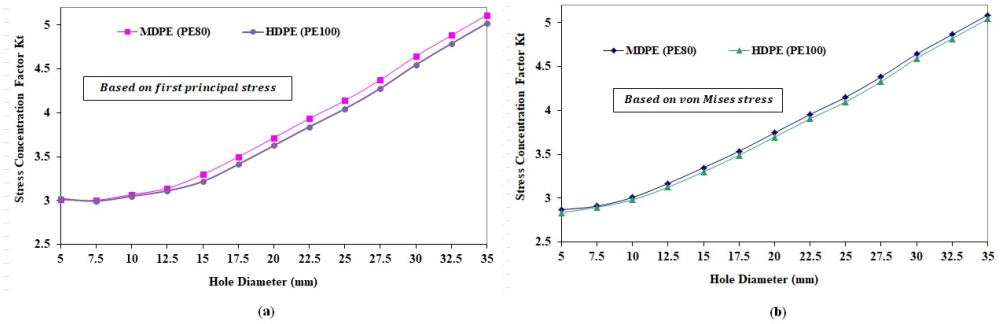

FIGURE 4.5: Trends of stress concentrations factors for above ground MDPE and HDPE pipe materials in natural gas distribution systems in the presence of complete circular holes. (a) Calculations performed based on first principal stresses. (b) Calculations performed based on von Mises stresses.

4.2.2 Simultaneous effects of temperature variations and pressure on complete circular hole

As discussed in Sec. 4.2, in order to further investigate the simultaneous effect of inside pressure and temperature change, on the above ground pipe with respect to stress concentration stemming from the complete circular hole defect in the form of a leak-opening, the finite element model of the defective pipe was considered. Unburied pipe was modeled and loaded to a final pressure of 405300 Pa (4 bar) while subjected to leak-opening of various sizes including 2.5, 5.0, 7.5, 10.0, 12.5, 15.0, 17.5, 20.0, 22.5, 25.0, 27.5, 30.0, 32.5 and 35.0 mm hole diameter. It was assumed that the pipe undergoes a maximum temperature change (decrease and increase) of 30 °C (from 20 °C to 50 °C in a hot summer day) and of 15 °C (from 5 °C to 20 °C in a cold winter day). As stated previously, this is a typical temperature change due to maximum daily temperature change in the city of Ahvaz which is located in a hot climate zone. Based on finite element findings and using Eqs. (3.18), the percent of maximum horizontal deflection to pipe diameter for all selected circular defect sizes was less than 0.46% which is significantly below the 3 % limit. The acquired stress-responses for the aforementioned defective gas pipe along different temperature changes are illustrated on several graphs. Fig. 4.6 and Fig. 4.7 show variations in the first principal stress and maximum von Mises stress in the above ground MDPE pipe in the presence of circular defects (holes) with various sizes. The strength of the pipe for several temperatures, based on a 50 years working life is also depicted. The reduced strength is used due to the viscoelastic behavior of polyethylene that occurs over the years of service. Based on the results presented on Fig. 4.6 and 4.7, the following conclusions are reached:

1- For all investigated cases, after comparing our results with the stress values in the simple pristine (intact) pressurized pipe, it is obvious that stresses in the pipe wall are

highly affected by a complete circular leak-opening.

2- For complete circular notch shape defect, the location of peak stresses is at the inside lip of the hole at the pipe inner surface, at the edges along the length of the pipe (as estimated in the analytical solution discussed in 3.8.2). The minimum stresses occurred at the lips in 90 degrees for the edges of maximum stresses. Additionally, all pipe models display similar stress distribution patterns.

3- Maximum first principal stress and maximum von Mises stress, both increase with increasing hole diameter. This effect is more pronounced for larger holes. In other word, the curve slope increases by increasing the hole diameter. For small holes, the level of stress rise by increasing hole diameter is small. But for larger holes a small increase in the hole diameter will cause the stress to increase significantly. For example, in no temperature change case, for a small hole size of 5 mm, a 5 mm increase in hole size (increasing hole size to 10 mm) will cause only 1.9 % and 4.8 % increase in maximum first principal and maximum von Mises stresses, respectively. While, for a large hole size of 25 mm, a 5 mm increase in hole size (increasing hole size to 30 mm) will cause 12.2 % and 11.8 % increase in maximum first principal and maximum von Mises stresses, respectively, which are much higher that small holes.

4- For the case of 30 °C temperature drop, the values of both maximum first principal and von Mises stresses are high, but they are not changing by hole size significantly. Additionally, maximum stress values in the defected pipe, will decrease by 30 °C temperature drop in comparison with no temperature change case.

5- 30 °C temperature rise, 15 °C temperature drop, and no temperature change cases show approximately similar trends.

6- 30 °C temperature rise in the pipe has the most influence on both maximum first principal and maximum von Mises stresses. This temperature change imposes significant tensile stress in the defect area.

7- Comparing the values of maximum stresses and the allowable stresses for 50 years working life, it is clear that for all investigated temperature changes (and also models with no temperature change) and defect ranges, the maximum first principal stress and maximum von Mises stress are higher than their design limit, as these stresses surpass the allowable stress values, which means the stresses are in unsafe range and the pipe material can't withstand the inside pressure of 4 bar.

Based on the results, the pipe with the proposed circular hole under the application of 4 bar internal pressure and aforementioned temperature changes is not strong enough to withstand the applied loads and should be repaired properly. As the concentrated stresses exceed material's strength, material will fail quickly mostly following a crack propagation.

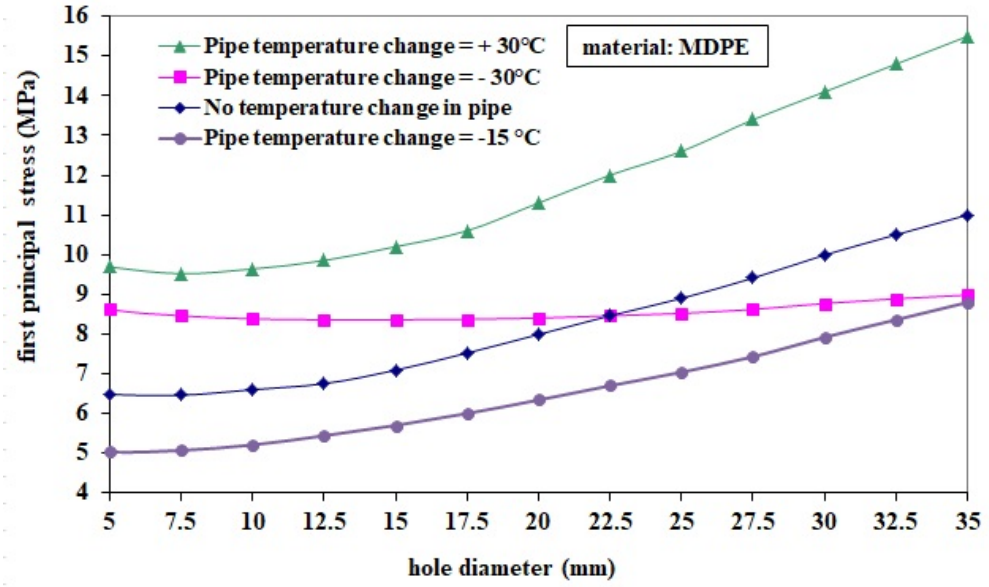

Working temperature (°C)	20	25	30	35	40	45	50
Allowable stress for PE80 (MPa)	4.00	3.75	3.50	3.20	3.00	2.80	2.60

FIGURE 4.6: Trends of maximum first principal stress in above ground pressurized pipe versus complete circular hole size (diameter) based on temperature change.

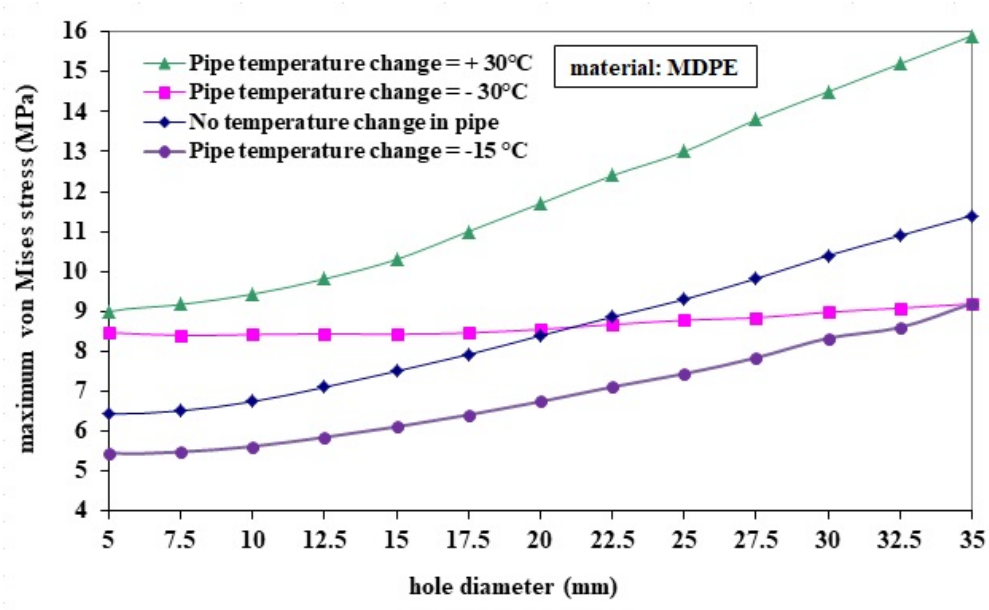

Working temperature (°C)	20	25	30	35	40	45	50
Allowable stress for PE80 (MPa)	4.00	3.75	3.50	3.20	3.00	2.80	2.60

FIGURE 4.7: Trends of maximum von Mises stress in above ground pressurized pipe versus complete circular hole size (diameter) based on temperature change.

4.3 The effect of partial through-wall round hole damage

From the previous section, where a leak opening complete hole in the above-ground gas PE pipe wall was modeled and studied, we recognize that the stress distribution in the pipe wall is highly affected by a discontinuity in the pipe wall. The maximum stress around a defect in pipe can be significantly higher than the stresses in the undisturbed region of the same pipe and also in the identical undisturbed pipe with no defect. However, in real physical problems there exist incomplete local voids (defects) which are located on the external surface of gas pipe. These volumetric defects are flaws from scratches or stones point loading on the buried polyethylene pipe or corrosion defects in steel pipes. As a volumetric defect, it is assumed that the defect geometry is a partial round hole with two main geometrical parameters as shown in Fig. 4.8. This figure shows a half section of a pipe featuring an incomplete circular hole defect where the hole size d, represents the total length of the defect in the axial and circumferential directions of the pipe, the hole depth h represents the height of the defect bottom to the original pipe external surface and which may vary from the external pipe surface toward the inside surface of the pipe, but not fully penetrate the wall thickness (the flaw is h mm deep in the radial direction). Also, a magnified view around the circular defect is depicted on this figure too, where parameter t on the figure is the pipe wall thickness. Radial partial bore diameter and depth sizes effects on the principal and von Mises stresses as well as the resulting stress concentration factors in the vicinity and along the partial holes are studied. The damage in the pipe may be a nonintensive shallow defect or ignorable threat for the pipeline which sometimes form at the pipe wall outer surface to a an extreme deep gorge forming deeply through the pipe wall, during installation procedure or along life period. While, serious defects should be repaired urgently, some nonintensive ones may not threaten the pipeline performance. Geometrical model was created by the modeling section in the preprocessing module of Ansys software. Finite element analysis was performed to investigate the hole diameter and depth size effects on the localized mechanical behavior of the above-ground defective gas PE pipe. Because of symmetry conditions half of the model described in Fig. 4.8 was simulated which means a quarter of complete pipe actual physical problem. This symmetry condition aims at decreasing computational time and costs. For all finite element simulations, 1 meter long MDPE pipe with a 4-inch nominal diameter ($k = 1.2103$) was modeled and loaded to a final pressure of 405,300 Pa (4 bar).

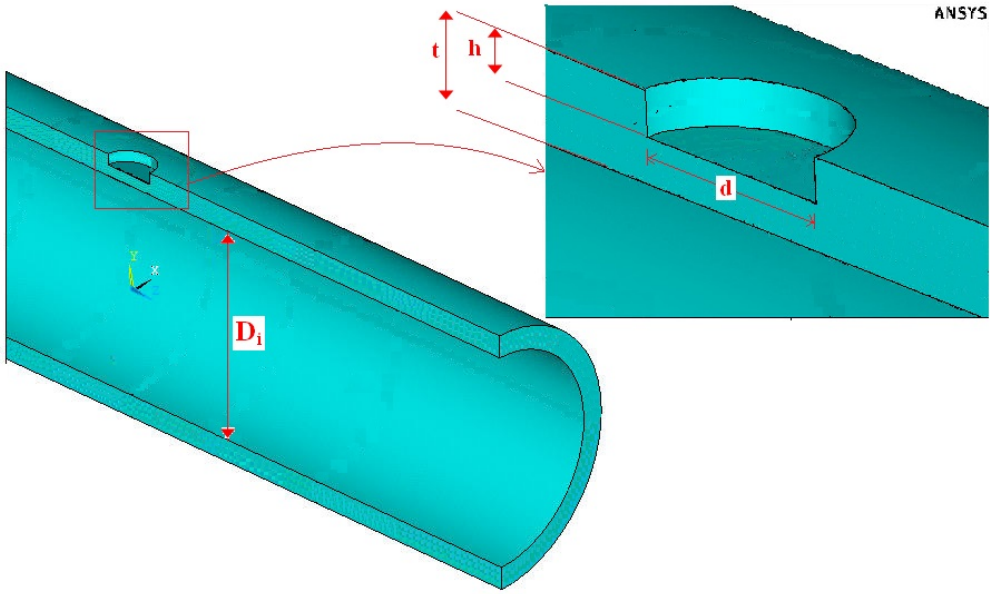

FIGURE 4.8: Incomplete circular hole defect in the pipe wall.

4.3.1 Mesh convergence study of partial through-wall round hole model

As the procedure described in Sec. 4.2.1 and before investigating several models, in order to examine the accuracy of our FEM simulations, mesh refinement was performed on two different models of PE pipes. It is always recommended to perform a mesh convergence study if one is using peak stress results. The first simulation involves the mentioned above-ground gas pipe featuring small defect of partial hole with 5 mm diameter size and depth to thickness ratio (thickness reduction) of $t/h = 1/4$ (which simulates a shallow defect of 25 % of the original thickness), while the second one includes a large defect with partial hole of 20.0 mm diameter size and depth to thickness ratio of $t/h = 3/4$ (which simulates a significant deep defect of 75 % of the original thickness). Table. 4.3 gives a summery of the finite element model and indicate the results of first principal and maximum von Mises stresses in pressurized MDPE pipe based on mesh refinement and a convergence plot of the results is depicted on Fig. 4.9 which shows how each simulation increases the stress value. As can be seen, increasing number of elements by refining mesh in the areas around the defect has a significant effect on increasing the maximum stress values in the vicinity of the hole. Additionally, as can be seen in Fig. 4.9(a), only the curve for maximum first principal stress shows a converging trend but for all other curves, the results diverge by refining mesh around the defect. Fig 4.10 shows von Mises stress distribution in pipe wall (as seen from the outside of the pipe) after the introduction of the two aforementioned partial bores of 5.0 mm and 20.0 mm diameter, for several mesh refinement around the defect region. With four different mesh sizes (2,

0.3, 0.1 and 0.1 mm) around the partial hole area, the results and default plots of the first principal and von Mises stresses look significantly different. In 5.0 mm hole size, the maximum von Mises stress is about five times as high in the model with the finest mesh that the coarsest one. For 20.0 mm hole size, the differences are more pronounced where the maximum von Mises stress is about eleven times as high in the model with the finest mesh than the coarsest one. In this case, an initial simulation reveals a maximum von Mises stress of 5.87 MPa. 1^{st} refinement of the mesh and rerunning the simulation shows a maximum von Mises stress of 8.41 MPa. A second, third, fourth and fifth refinement increase the maximum stress to 13.7, 22.4, 37.9 and 41.3 MPa, respectively. The final refinement shows yet another increase in maximum stress to 58.9 MPa.

From the model results, we imply that maximum stress values are mesh dependent. In other words, the finer mesh that are produced in the corners, the higher stress values will appear. Therefore, since the true results tend toward infinite values, the solutions will not converge. However, based on Fig. 4.10, the maximum von Mises sterss (and also principal stresses) is very localized. As can be seen in this figure, since maximum stress values are very high at singularities of the simulations with finer meshes, details of real stress fields are completely lost.

There are two different issues which can be discussed as the interpretation for this result: the first one is computational problem resulting from inappropriate finite element selection which might leads to inaccurate solutions at sharp corners, and the second is theoretical stress singularity resulting from linear elasticity equations at sharp corners. The first issue happens if one mesh the model with irregular geometry by using elements with first order displacement shape functions, and therefore in numerical solutions of physical problems, sharp corners produce a singularity in the derivatives of the dependent variables for all elliptic partial differential equations. In structural mechanics, this means that the strains can increase unlimited because displacements are the degree of freedom and therefore, stresses will become unbounded too. Meanwhile, it worth reconsidering that SOLID95 elements which are used in our damaged pipe model are quadratic (not linear) element which have their geometry fully defined by element nodes, as discussed well in Appendix A. As SOLID95 element has second order displacement shape functions, it can tolerate irregular geometries and the curvature is fully maintained around the curved edges of the defect area [141]. Second-order displacement function giving linear stress when calculating its derivative. Therefore, the interpretation for these results is that the stress is theoretically singular at the sharp corners of the models shown in Fig. 4.10. It means that if one compute the stress field analytically using the linear elasticity relations, he/she will find that the stresses approaches to infinity exactly at the location of the sharp corners. This situation is similar to the classical linear elasticity problem of a force acting on the end of a wedge. In that case, one can see that, for example the radial stress component, depending on the force direction, is

proportional to $\frac{1}{r}$ or $\frac{1}{r^2}$ where r is the distance from the vertex of the wedge. Therefore, in the next section, we investigate the same model knowing that the stress at sharp corner theoretically goes to infinity.

TABLE 4.3: Maximum stress values in above-ground MDPE transmission pipeline in the presence of partial round bore featuring sharp edge with depth to thickness ratio of $t/h = 1/4$ and 5.0 mm diameter and also with depth to thickness ratio of $t/h = 3/4$ and 20.0 mm hole diameter (for several mesh sizes).

Hole Dia. (mm)	**depth to thickness ratio (t/h)**	**No. of elements**	**No. of nodes**	**Element length (mm)**	**Max. stress (MPa) First principal**	**von Mises**
		145013	229128	2.0	4.83	4.00
5.0	1/4	150747	237238	0.3	8.63	6.10
		161074	251678	0.2	12.80	8.00
		177135	274108	0.1	30.20	19.30
		141581	224405	2.0	6.42	5.87
		146689	231950	0.3	6.44	8.41
		152660	240495	0.2	6.44	13.7
20.0	3/4	161220	252889	0.1	6.44	22.4
		210561	320808	0.07	14.70	37.90
		254890	383167	0.04	14.8	41.30
		297040	440903	0.01	14.7	58.90

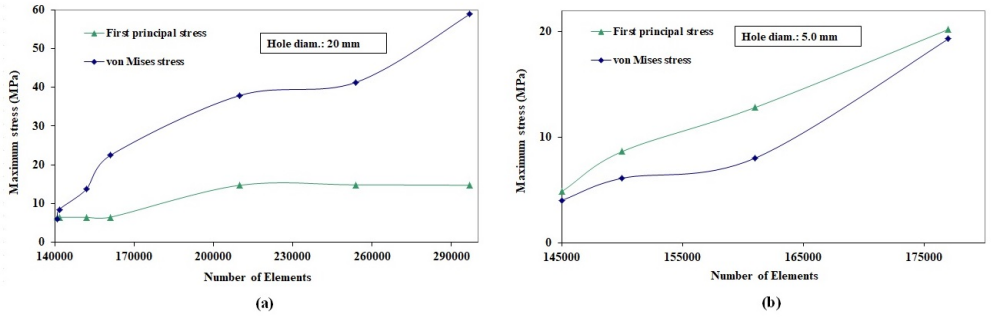

FIGURE 4.9: Trend of maximum von Mises and first principal stresses around partial round bore featuring sharp edge to study convergence problem (a) In the case of a pipe with a 20.0 mm hole diameter and depth to thickness ratio of $t/h = 3/4$, (b) In the case of a pipe with a 5.0 mm hole diameter and depth to thickness ratio of $t/h = 1/4$,.

4.3.2 Stress intensity factors at sharp corners

In the previous section, we performed a mesh refinement at the cylindrical void (damage) featuring a sharp edge in the pipe wall in order to check the results convergence and consequently we became aware of a stress singularity and the divergence in the finite element results with mesh refinement was observed. Hopefully this highlights the danger of using results without having done a mesh refinement study, even if the mesh

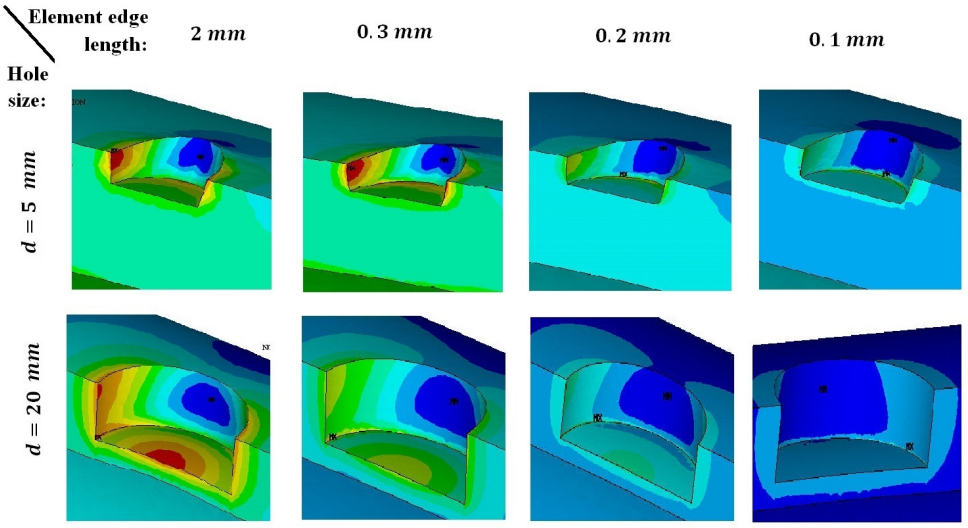

FIGURE 4.10: Mesh refinement effect in the vicinity of circular hole featuring a sharp corner in the MDPE pipe wall of above ground gas transmission line. Contour plots show the distribution of von Mises stress in the defect region, in cases of two different hole sizes.

looks good enough. The contour plots in Fig. 4.10 demonstrated singularities in the presented problem. Recognizing that we have a stress singularity requires to use fracture mechanics theory to investigate the problem from a structural collapse point of view. The objective of this section is to determine the character of the singular stress state which exists at the aforementioned sharp corners. Therefore, a standard 3D numerical simulation (FEM) model based on LEFM for the stress intensity factor characteristics in defective pipe is created to predict the stability of pipes to prevent a quasi-brittle failure to remain in good condition. This investigation will provide reasonable information that brittle failure will or will not occur in the pipe body featuring a void (damage) with sharp corners, for long life. Prior to the extensive analysis of the models featuring damages with sharp corners of different sizes, a mesh dependency study is undertaken to evaluate the influence of mesh refinement of the elements in the partial hole defect and ensure convergence of the solution. To predict the fracture parameters of damaged pipe under static loading condition, first the stress intensity factors for a defect in pressurized pipe loaded by internal pressure to $P_i = 405300$ Pa, with dimension D_o =57.22mm, SDR11.5 and with an initial defect on the outer pipe surface was modeled in ANSYS workbench platform.

Creating a finite element mesh in a region of stress singularity like crack can be a challenging and time consuming effort. ANSYS mainly offers two methods for calculating the SIFs by a postprocessing activity: Interaction integral method and displacement extrapolation method. ANSYS Mechanical APDL software does not have the ability to directly create three dimensional cracks or curved cracks through solid modeling [142].

It only provide automatic meshing capability for two-dimensional problems. Meanwhile, ANSYS workbench v19 provides pre-meshed crack option for including a crack and subsequently a sharp corner of singularity in the finite element model. In this method, first the crack model geometry is created in DesignModeler. One of the limitations of workbench is that in 3D model, the crack has to be perpendicular to the surface, so we have to create a coordinate system that $x-$axis is pointing inward in perpendicular surface as was shown previously in Fig. 3.2. For this analysis, we used "static structural" analysis capability of ANSYS workbench, which should be selected from "project schematic". There is also an engineering data source and we can select polyethylene from the library. This software uses SOLID187 elements (quadratic tetrahedral element) only, which is able to mesh any geometry. For the fracture mechanics modeling in ANSYS workbench we need to "name selection" for the crack front which for our case is the edge of interior sharp corner. Additionally, it is required to define "the top" and "the bottom" face nodes.

As a simple approximation for our static simulation, a two dimensional (2D) model of the pipe with a sharp step defect under both plane strain and axisymmetric conditions existing in ANSYS workbench were used. To check the reliability of results, three-dimensional (3D) model was also developed. The completely different results can be explained by the great difference between the 2D representation of the pressure pipe and more realistic 3D pipe geometry. Therefore, simple 2D approximation is not representative in this case and a complete 3D model with realistic shape of damage with sharp corner has to be used. Defect geometry has significant influence on the resulting stress intensity factor value. Therefore, a typical partial hole defect of 20 mm diameter size and 50 % depth to thickness ratio was selected. A typical numerical model used for calculation was symmetrical and included around 214,000 finite elements strongly non-homogenously distributed in the structure because of mesh refinement around the sharp edge of the defect, see Fig. 4.11. Owing to the advantages of symmetry, a quarter model of defective pipe is used for analyzing. The mesh in the sharp corner region is fairly refined. The tetrahedron type SOLID187, a kind of body element is used by ANSYS workbench for meshing. Material properties used for calculation correspond to Medium-Density polyethylene (MDPE). Stress intensity factor (SIF) values which are the controlling variables for predicting crack propagation, were estimated along the the curved edge of the sharp corner which represents the crack front.

In order to perform a mesh converges analysis, we vary the size of the mesh in the vicinity of the damage by defining a sphere of influence and record the fracture mechanics parameters. The effect of decreasing element lengths of 0.90 mm to 0.45 mm on the resulting maximum stress intensity factors (SIFs), (K_I, K_{II}, K_{III}) are considered. Clearly, the maximum stress is stress singularity, in each stage we reduced the mesh size, the stresses increased significantly. For different levels of mesh refinement at the sharp

edge, the deviations relative to the previous solution is calculated and the percent difference values are shown in Table. 4.4. According to Fig. 4.12, our fracture mechanics parameters didn't change significantly and therefore, the results will be mesh independent provided that a minimum refinement of 0.6 mm is used. Thus, in the following studies the element size around the damage is kept to be 0.6 mm. This conclusion gives us confidence that we can use the aforementioned fracture mechanics tool as a way to investigate the strength of the defects against fracture.

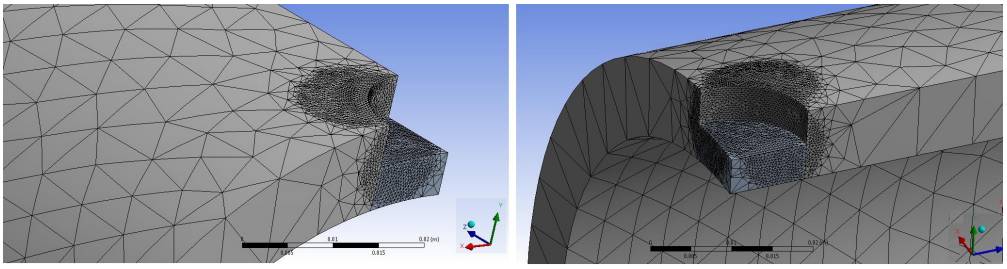

FIGURE 4.11: ANSYS workbench meshing using tetrahedron elements and mesh refinement around incomplete partial circular hole void (defect) in the pipe wall featuring sharp edge to investigate convergence problem.

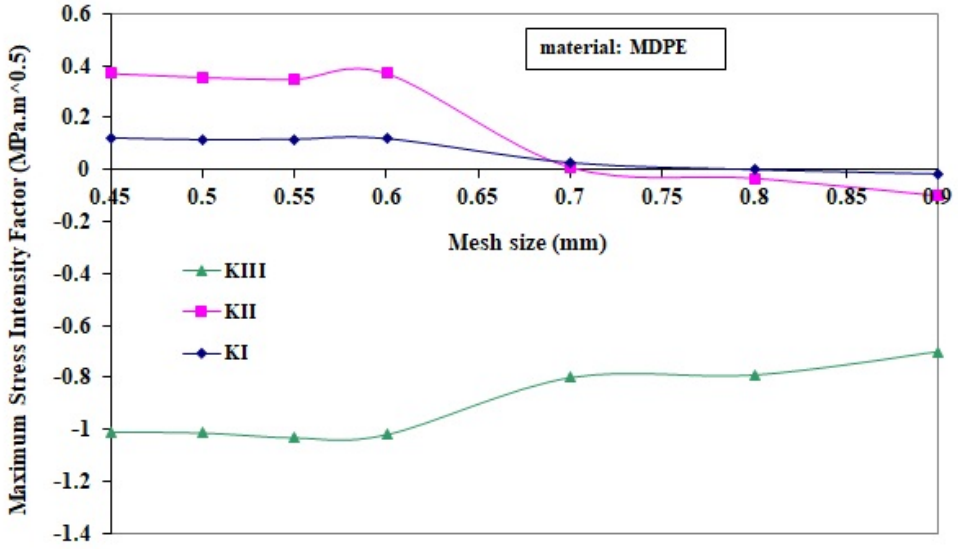

FIGURE 4.12: Trends of maximum stress intensity factors around incomplete partial circular hole void (defect) in the pipe wall featuring sharp edge to study convergence problem.

In LEFM the procedure to predict crack-growth is first to determine the stress intensity factors at sharp corners where a crack is initiated. After the crack is formed, it is then necessary to introduce an algorithm to recalculate the stress intensity factors at the crack tip. However, the present effort is concerned only with the determination of the stress intensity factors at sharp corners. The subject of crack initiation and propagation

TABLE 4.4: Mesh refinement effect for partial hole with sharp corner MDPE pipe wall.

Item	**Mesh size (mm)**	**Max. SIF change (%)**		
		KI	**KII**	**KIII**
1	0.90	–	–	–
2	0.80	106	67	10
3	0.70	97	127	1.3
4	0.60	77.5	97.6	27.5
5	0.55	1.7	2.2	1.2
6	0.50	1.7	2.0	1.8
7	0.45	5.7	4.0	0.3

TABLE 4.5: Three-dimensional FEM (ANSYS workbench) calculations of SIFs for partial hole with sharp corner in MDPE pipe wall due to internal pressure.

Hole diameter (mm)	**depth to thickness ratio (t/h)**	**Max. stress intensity factor (MPa.m$^{0.5}$)**		
		KI	**KII**	**KIII**
10.0	33 %	0.010	0.022	-0.046
15.0	33 %	0.041	0.15	-0.11
20.0	33 %	0.091	-0.06	-0.77
25.0	33 %	0.049	-0.03	-0.70
10.0	57 %	-0.001	0.27	-0.094
15.0	57 %	0.036	0.32	-0.31
20.0	57 %	0.12	0.37	-1.02
25.0	57 %	0.02	0.14	-0.76
10.0	78 %	-0.02	0.33	-0.23
15.0	78 %	0.02	1.03	-0.68
20.0	78 %	0.02	1.70	-1.18
25.0	78 %	-0.03	0.13	-0.82

are excluded in this study.

The defective pipe is more likely to fracture with a larger stress intensity factor. When the stress intensity factor is over than the critical one, the pipe is going to fracture. In other words, the stress intensity factor reaches the maximum value in a fracture initiation. Using a fracture toughness (K_{IC}) level of 5.71 MPam$^{0.5}$ for PE80 pipe material as a reference [143], we investigate if the defective pipes remain intact for the required service time.

Having determined the required element size, further analysis are performed in order to investigate the effect of the damage size and depth on stress intensity factors, and a number of finite element models are constructed. Computed values of stress intensity factors for different partial hole diameter and depth to wall thickness rations are depicted in Table. 4.5. According to this table, the current FEM (ANSYS workbench) results exhibit a high dependency of SIFs on the size of the initial defect. The comparison of the results show that for the range of the studied defect sizes, under the application of only the internal pressure, our FEM modeling yield to considerably low SIF values at the vicinity of the sharp corner which are well below the critical value. From the point

of view of brittle fracture criteria, these pipes can be expected to remain still in good order and the polyethylene material stay in use even in the presence of the defect, as the pipe ensure a sufficient stability for a continuation of the service. However, form the ductile failure mode yielding starts at sharp corners and the pipe safe operation for long life is challenging.

The proposed methodology and outcomes released from this section, act as novel design tool for the industrial engineering when is required to generate a solution for working in critical conditions. However, in real structural problems, there are rarely perfectly sharp corners. Therefore, the designer could argue that by using an accurate geometry representation all fillets, it is possible to avoid singularities [144].

4.3.3 Partial round hole damage with filleted corner

In reality, natural gas distribution lines are rarely defected by perfectly exact sharp corners and therefore, it is possible to prevent stress and strain singularities in finite element simulations by introducing fillets at the damage sharp corner edges. Furthermore, in experimental research activities which are carried out to simulate a general damage and to evaluate potential methods of pipe repair, testing companies develop and introduce a defect into pipe sections with a milling machine. Specially, they use an end mill with rounded corners to simulate short, shallow/deep damage representative of a shallow/deep isolated pipe wall defect as shown in Fig. 4.13 [145].

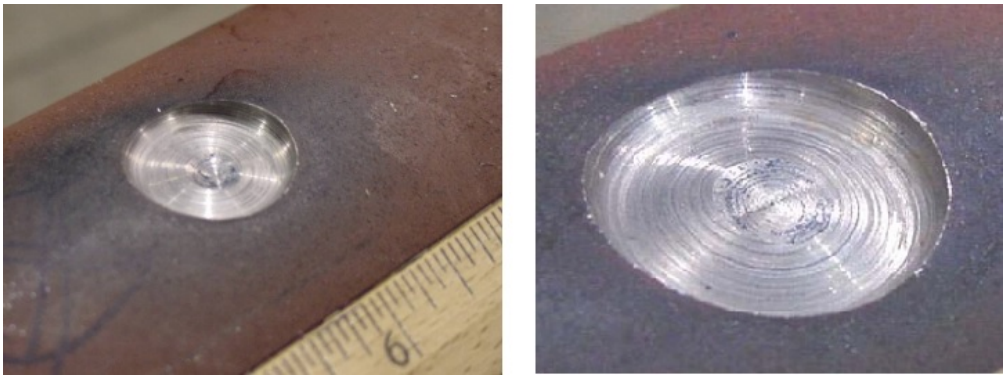

FIGURE 4.13: Pipe section with short deep simulated damage [145].

Fig. 4.14 shows the geometry of a pipe featuring a partial round hole with a small fillet at sharp corner where "r" indicates fillet radius. Additionally, a magnified view around the partial circular defect is depicted on this figure too. Geometrical model including the partial hole and related fillet was created by the modeling section in the preprocessing module of ANSYS mechanical APDL v16.2 platform. Generally, there is

no tools in modeling module of ANSYS to creat interior partial volume fillet as shown on this figure. Many attempts was performed to create this fillet volumes inside partial hole. First, appropriate volumes were created and suitable curved areas were created by extruding curved lines along other appropriate curved lines. Then these partial volume were cut and divided by the new curved areas using Boolean module in Ansys package. The excess volumes then were deleted and the remaining volumes in the form of fillets were glued to the other volumes in the hole surrounding. Fig. 4.15 shows the partial volumes which were created and glued to model a partial hole with inner fillet.

In order to investigate the effect of fillet on removing the aforementioned singularities, first, a finite element model was created for 1 meter long MDPE pipe sample with a 4-inch nominal diameter, featuring a 2.0 cm diameter hole and depth to thickness ratio of t/h= 83% and small fillet radius of 1.4 mm, using free mesh of tetrahedron SOLID95 elements, as shown in Fig. 4.16 (a). Additionally, Fig. 4.16 (b) graphically depicts von Mises stress distribution in the full model of aforementioned problem, which is obtained by full ANSYS simulation and using the post processing module of the software. For a better investigation of the high stress areas surrounding the hole, magnified view of the circular hole surrounding is also depicted on the figure, as seen from the outside of the pipe. This contour plot shows the stress concentration locations around the partial hole defect. The simulation results show that the introduction of a 20 mm diameter partial hole with depth to thickness ratio of t/h= 83%, produces a maximum first principal and von Mises stresses of 9.9 MPa and 8.6 MPa, respectively at middle of the radial bore-pipe wall intersection. This area of maximum stresses are depicted by red color and which is at the center of the thin volume which closes the circular hole at bottom and near pipe internal surface. This region can be the site of crack initiation upon the application of critical loads on the pipe wall. Increasing pressure load will cause the creation of plastic region in this area and to grow into the pipe which will reduce the pipe strength significantly.

In order to verify the accuracy of our new finite element model, and proving the mesh indedendency of the aforementioned model, the effect of mesh refinement on maximum stress values for partial hole with filleted corner is investigated and the obtained results for maximum first principal stress and maximum von Mises stress for pressurized MDPE pipe are summarized in Table. 4.6. Based on the results, for the aforementioned circular partial hole, further refinement of the generated mesh size in the region of radial partial bore, produces no significant changes in the elastic stress distribution in the region of bore. Therefore, it is implied that the model is mesh independent. For example, by refining mesh and decreasing minimum element size around the defect area from 1.2 mm to 0.01 mm (which means the new mesh is refined to a high ratio of $\frac{1}{120}$ initial mesh), the maximum first principal stress and maximum von Mises stress only change 0.9% and 1.3% respectively, which are really infinitesimal. Additionally, Fig. 4.17 shows

the contour plot of both first principal and von Mises stresses around the partial circular hole for the simulations reported in Table. 4.6. Minimum element sizes are also reported on this figure. Because of the symmetry condition, only a quarter of physical problem is simulated. According to Fig. 4.17, for all mentioned mesh sizes around the filleted partial hole, the distribution of stresses looks quite similar. Based on the results, we imply that increasing the number of elements and refining the mesh around filleted partial hole region does not significantly change the maximum stress values and stress distribution around the hole area and therefore, the new model is mesh independent.

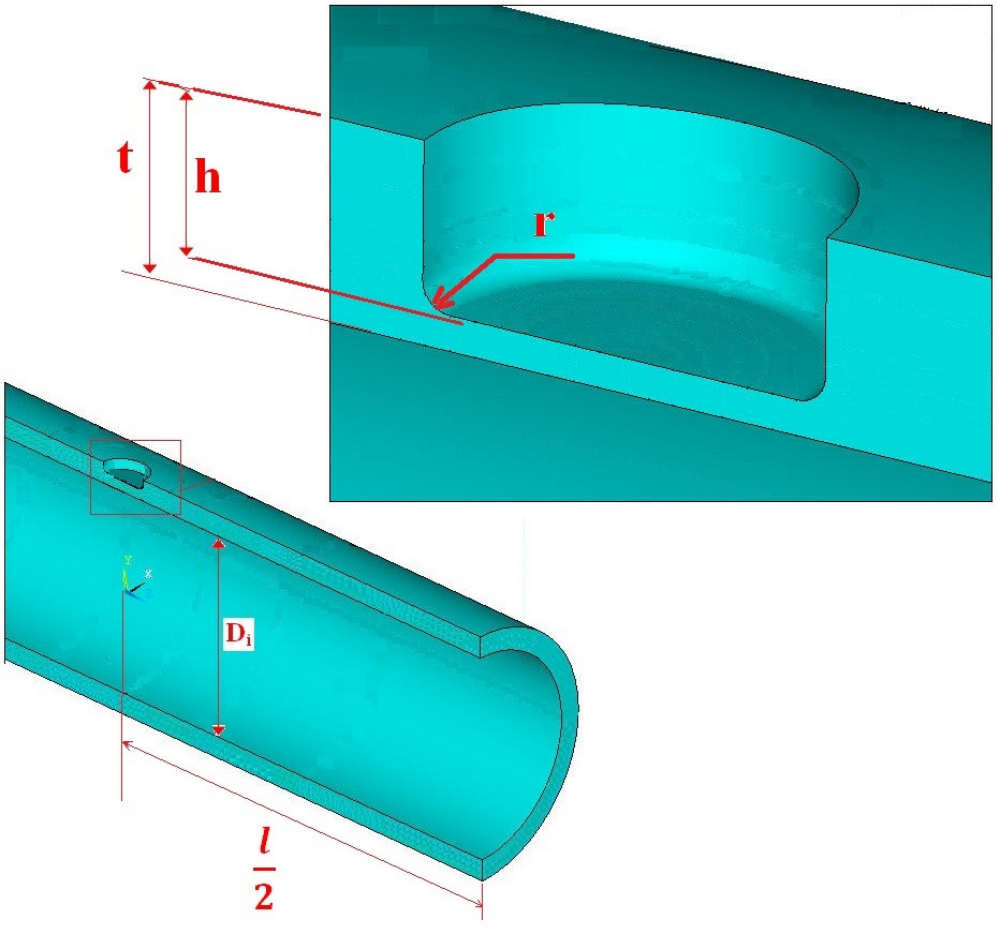

FIGURE 4.14: Geometry of the pipe featuring a partial round hole with fillet at sharp corner.

After constructing an appropriate, reliable and mesh-independent finite element model for simulating partial bores in the pipe wall, in this part of research, we study the mechanical behavior of the above ground gas pipe subjected to different sizes and depths of partial circular defect. The simulation was performed on non-intensive shallow outer surface defects to extreme deep ones. The final stress results will help us to decide if the defective pipe requires argent repair or may withstand applied loads for longer time even in the presence of defects. Also, knowledge on stress distribution in the vicinity of

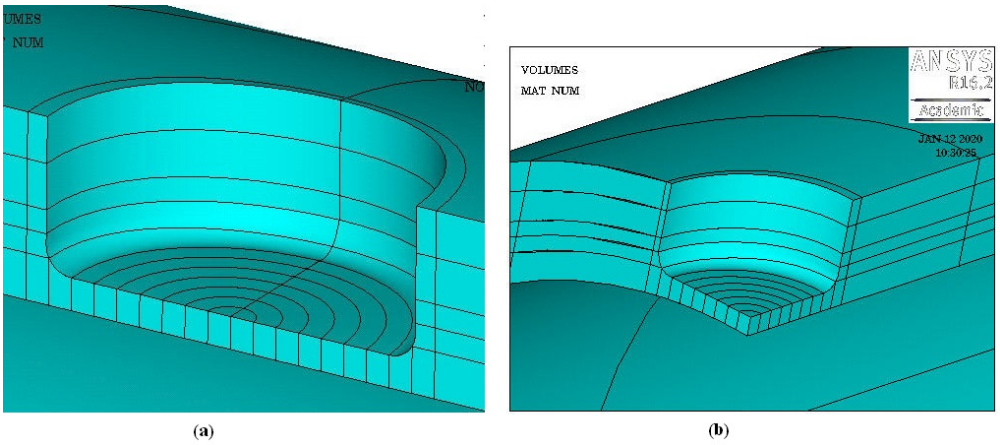

FIGURE 4.15: Partial volumes were created and glued to model a partial hole with inner fillet. (a) Half pipe model. (b) A quarter pipe model.

TABLE 4.6: Mesh refinement effect for partial hole with filleted corner MDPE pipe wall.

Hole Dia. (mm)	**Number of elements**	**Number of nodes**	**Element length (mm)**	**Maximum stress (MPa)**		
				Circum-frential	**First principal**	**von Mises**
20.0	56835	106958	1.2	9.88	9.88	8.63
	58360	109165	0.8	9.89	9.92	8.61
	78631	138149	0.4	9.89	9.89	8.61
	489836	719993	0.01	9.97	10.00	8.75

defects and the trend of maximum stresses variation with holes size and depth will help us in designing effective repair tools, i.e. patches. Additionally, in order to compare the behavior of convenient polymer pipe material, we study both MDPE (PE80) and HDPE (PE100) material properties and investigate the maximum stress values and compare the results with MDPE (PE80). The curves on Figs. 4.18 (a) and (b), depict the variation of stress concentration factor versus hole diameter for several hole radial sizes (i.e. hole depths) including a small 15 mm hole to a large 30 mm diameter in MDPE (PE80) pipe. Each curve is related to a specific hole depth to wall thickness ratios (h/t) including 8 %, 33 %, 57 %, 70 % and 83 %. Also, the same investigation was performed on HDPE (PE100) pipe material and the results are depicted on Figs. 4.18 (c) and (d). Again, both unburied MDPE and HDPE pipes were loaded to a final pressure of 405300 Pa (4 bar). For the two left side images, on Fig. 4.18 the calculations for stress concentration factor are based on maximum first principal stress. Additionally, the results according to maximum von Mises stress are depicted on the right side. To a better interpretation of the data, we draw the variation of stress concentration factor with respect to hole depth size in Fig. 4.19.

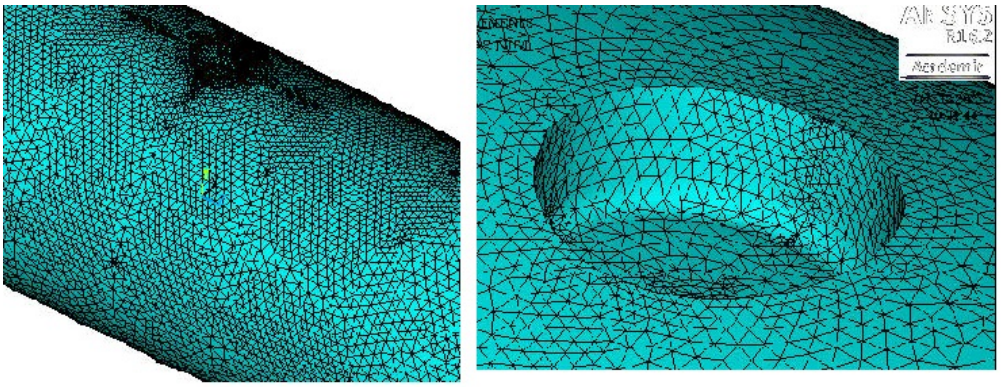

(a) Finite element model

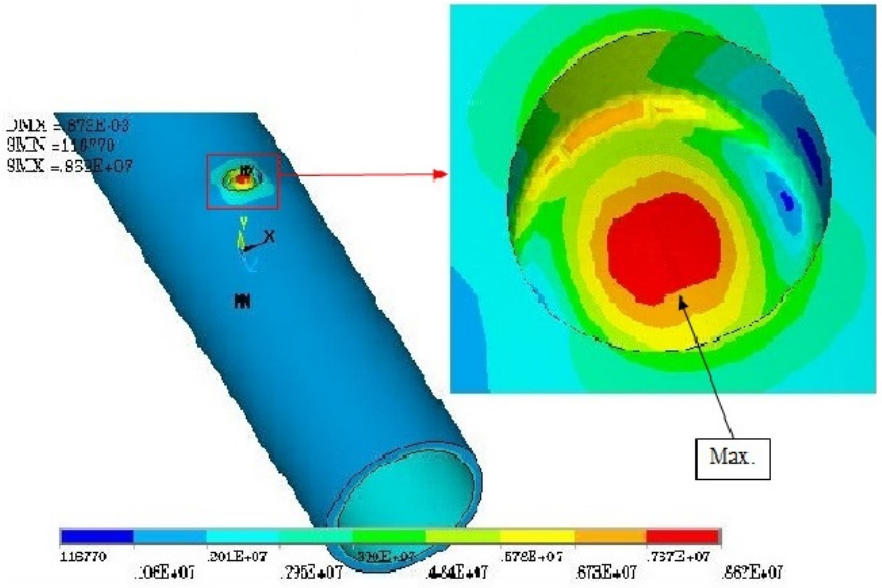

(b) Stress distribution

FIGURE 4.16: Illustration of the element plot and stress distribution (a) Full model of above ground MDPE pipe with a hole defect of 200 mm diameter size and t/h= 83% and fillet radius of 1.4 mm, created by finite element. (b) Contour plot to show von Mises stress distribution in pipe and hole surrounding. Expanded view shows stress distribution in the immediate vicinity of hole.

The curves on Fig. 4.18 show that for both MDPE and HDPE pipes, stress concentration factors (based on maximum first principal stresses and maximum von Mises stresses) generally increase with increasing hole diameter. For shallow holes and up to 57 % of hole depth ratio, the variation of stress concentration factor with respect to hole diameter increases is not significant and is approximately constant for each specific hole depth ratio. This issue is quite clear by considering the initial parts of the curves depicted on Fig. 4.19. This property is more pronounced up to about 33 % of hole depth ratio (thickness reduction) in first principal based stress concentration factors for both MDPE and HDPE pipes. For von Mises based stress concentration factors, this behavior

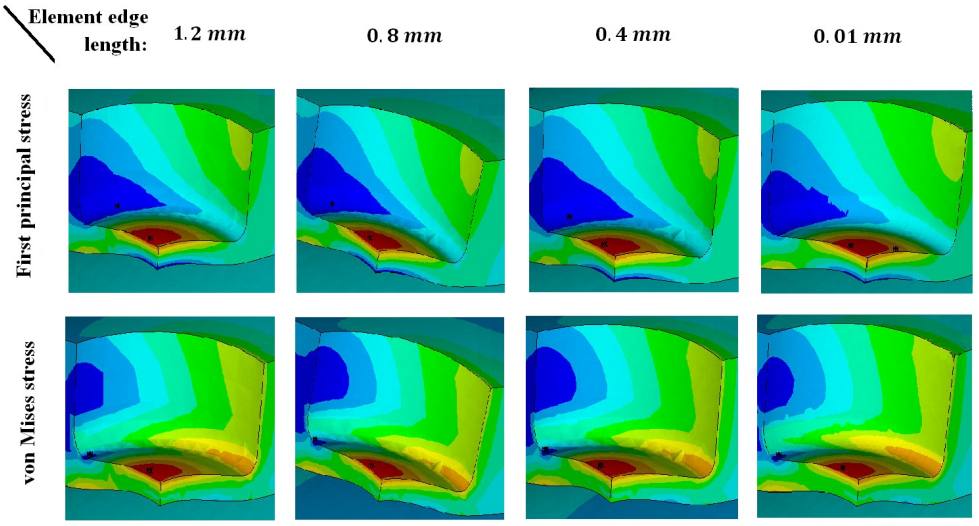

FIGURE 4.17: The effect of mesh refinement in the vicinity of circular hole featuring filleted corner in the above ground medium density polyethylene pipe wall. Contour plots show the distribution of first principal and von Mises stress in the defect region.

exists for deeper defects and is pronounced up to hole depth ratios of around 57 %. For deeper holes, the stress concentration factors increase with respect to hole diameter are notable. In other world, the curves on Fig. 4.19 display higher slopes for deeper holes. For example, for 70 % and 83 % depth ratio, the rate of stress concentration factors are very high. This issue is better understand by referring to Fig. 4.19. According to the results on this figure, for all hole diameters, stress concentrations approach to one when the hole depth ratio approaches to zero. The curves for both MDPE and HDPE pipe materials display similar trends. For shallow defects with the level of depth ratio below 8 %, for all calculations and both MDPE and HDPE pipes, the stress concentration factors are very close to unity, which means the destructive effect of these sizes of damage may not threatened the pipe life, significantly. For deeper holes up to around 33 %, all stress concentration factors remain below 2 for investigated hole diameters. For higher depths up to around 57 %, stress concentration factor do not exceed 3. However, for deeper defects, stress concentration factors, start increasing significantly so that for a 30 mm hole diameter with 83 % depth ratio, it reaches high values of around 8.

Analytical (Eq. (3.19)) and numerical solutions (FEM) show that the maximum von Mises stress and maximum first principal stress (here, maximum circumferential stress) in a similar long pristine (without defect) MDPE pipe are around 2.24 MPa and 2.15 MPa, respectively. Additionally, the estimated values for maximum von Mises stress and maximum first principal stress in the similar simple pristine (intact) HDPE pipe material are 2.22 MPa and 2.15 MPa respectively. These values are well below the allowable stress for the life expectancy of 50 years when compared to Table 3.2, even by

applying high factor of safety values of 2. However, the results of this section show that the maximum first principal and maximum von Mises stress levels are highly effected and increased by partial hole defects. Therefore, in order to investigate the load bearing capacity of the defective pipe and also to understand if the pipe subjected to defects can withstand the applied load during its lifetime, it is required to compare the stress levels in the pipe with their allowable values, under different loading conditions. Meanwhile, in order to investigate the load bearing capacity of MDPE pipe under the sole effect of internal pressure (without any temperature variation), the values of maximum von Mises stresses and maximum first principal stresses are calculated for six hole depth to pipe wall thickness ratios (h/t) including 8 %, 33 %, 57 %, 70 % and 83 % (The ratio "100 %" describes a complete hole in the pipe wall, which was disused in subsections 4.2 and 4.2.2) and the results are depicted on Figs. 4.20 and 4.21 respectively. The pipe material is yellow MDPE (PE80). Additionally, Figs. 4.22 and 4.23 show the values of maximum von Mises stress and maximum first principal stress respectively, in HDPE (PE100) pipe material with similar defects and loading condition. For all models the temperature change effect is not considered and is assumed to be zero. For the ease of evaluation, pipe allowable stresses for life expectancy of 50 years are also calculated for several working temperatures, after using the factor of safety of 2, are the values are tabulated on the bottom of each figure. Based on the finite element modeling results, following conclusions are reached:

1- In the presence of holes with the range of diameters studied here, the maximum stress values in pipes with shallow hole depth ratios (thickness reductionn) below 8 %, are very close to the values reported for simple pristine (intact) pipes of both MDPE and HDPE. The maximum first principal stress and maximum von Mises stress are below the stress limits for 50 years lifetime and reported working temperatures. That means, the pressurized pipe (only under the effect of internal pressure) has sufficient load bearing capacity to transfer natural gas even with shallow defects in pipe wall.

2- In presence of deeper defects more than 8 % up to around 33 % depth ratio and studied range of hole diameter, HDPE pipe is in safe side at working temperatures up to around 35 °C. For environments with higher working temperature, the maximum stresses imposed to the pipe are higher than the safe limit as these stresses surpass the allowable stress values. For the similar pipe of MDPE material (Figs. 4.20 and 4.21), stress levels are bellow the allowable stresses only up to around 20 °C working temperature (4 MPa) and therefore, for surroundings with working temperature higher than 20 °C, the allowable stresses are lower than the maximum stresses imposed to the defective MDPE pipe.

3- Investigating extremer defects up to around 57 % of depth ratio in the simulated range of hole diameters, shows that HDPE pipe may withstand loaded pressure at working

temperatures only around 20 °C. For higher working temperatures the pipe with simulated defects may not work safely as these stresses exceed the allowable stress values. The similar MDPE pipe shows higher levels of maximum stresses and also is not safe even in low working temperatures of around 20 °C.

4- For all other cases of both MDPE and HDPE pipe material with depth ratio higher that 57 %, maximum first principal and maximum von Mises stresses are higher than equivalent pristine (intact) pipe and particularly these stresses surpass the allowable stresses for 50 years of life expectancy. Effective repair methods including cutting off the defected pipe section and welding a new section to both ends, or other techniques such as patch repair is necessary in these situations.

5- Based on the results, increasing the hole diameter of the damaged pipe generally increase the value of maximum first principal and maximum von Mises stresses. Additionally, the hole depth effect in increasing maximum stress values is more significant. As an example, simulating a hole size of 30 mm diameter and with depth to pipe thickness ratio of 83%, will increase the maximum first principal stress to around 17 MPa. Deeper defects are more sensitive to the hole diameter size and stress increases faster than the other cases.

6- Additionally, comparing the results with a complete hole shows that, for a HDPE pipe including defects deeper than 78%, for larger hole diameters (more than 27.5 mm), the maximum stresses surpass even the identical sample with complete hole. For deeper holes (deeper than 83%), this behavior happens from smaller holes (from 17.5 mm).

Additionally, Fig. 4.24 shows the distribution of von Mises stress and also high stress areas surrounding the hole, for several hole diameters and depth to thickness ratios which were investigated in this section, as shown in Fig. 4.14. The red sites on each image show the locations of stress concentration in the neighborhood of the circular holes, which are the sites of crack initiation if the structure is subjected to critical pressure loads. These sites depends on hole depth. For slight hole depths, stress concentration sites are at the top of vertical edge of the defect around the pipe outer surface, as shown in Fig. 4.24 (a) and (b) for the ratios of 33% and 57%, respectively. For deeper defects, high stress locations appear at the middle of the thinnest section which is the close-end of the defect, as illustrated in Fig. 4.24 (c). For complete circular hole defects (Fig. 4.24 (d)), the site of probable crack initiation is at the bottom of the vertical edge of the defect, where this edge intersects the pipe internal surface.

Based on the results, 3D stress field in the neighborhood of the circular hole is a function of pipe dimension and hole shape, diameter and depth. However, stress fields in the pipeline and specially around the defect sites and the maximum stress values can be effected by pipe material.

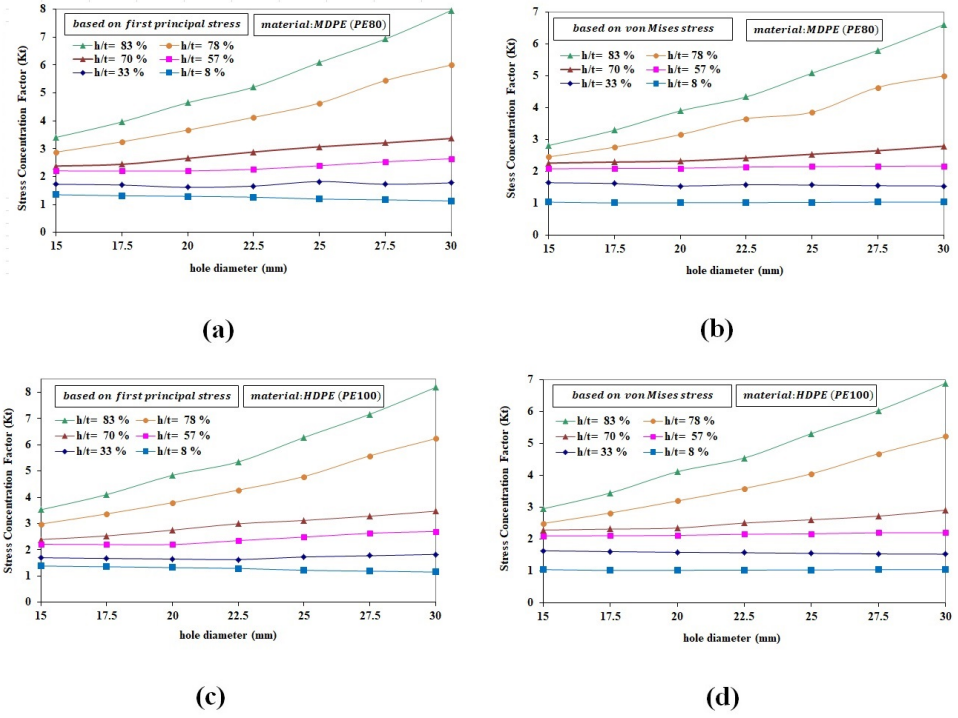

FIGURE 4.18: Trends of stress concentrations factors versus hole diameter, for above ground MDPE and HDPE pipe materials subjected to partial holes of different hole sizes and depth to thickness ratio. (a) SCF calculations based on maximum first principal stress in medium density polyethylene pipe (PE80). (b) SCF calculations based on maximum von Mises stress in medium density polyethylene pipe (PE80). (c) SCF calculations based on maximum first principal stress in high density polyethylene pipe (PE100). (d) SCF calculations based on maximum von Mises stress in high density polyethylene pipe (PE100).

4.4 Simultaneous effects of temperature variations and pressure for partial round hole in above ground PE pipe

In subsections 4.3, mechanical behavior of above ground polyethylene pipe subjected to partial holes under the sole effect of internal pressure was studied in detail. In the aforementioned section, it was assumed that the pipe is not significantly affected by environmental temperature changes and therefore, the effect of pipe temperature changes on imposed stresses was ignored. However, as mentioned previously, in some environments such as south-western Iran, daily and seasonal temperature changes are significant and therefore, thermal stresses in above ground plastic pipes are considerable and must be calculated and superimposed to the stresses resulting from pipe internal pressure. For the calculation of thermal stresses we require the information of ambient temperature of the environment where the pipeline is installed and operated. To a better evaluation, in this section we select a particular region which is city of Ahvaz located south-west

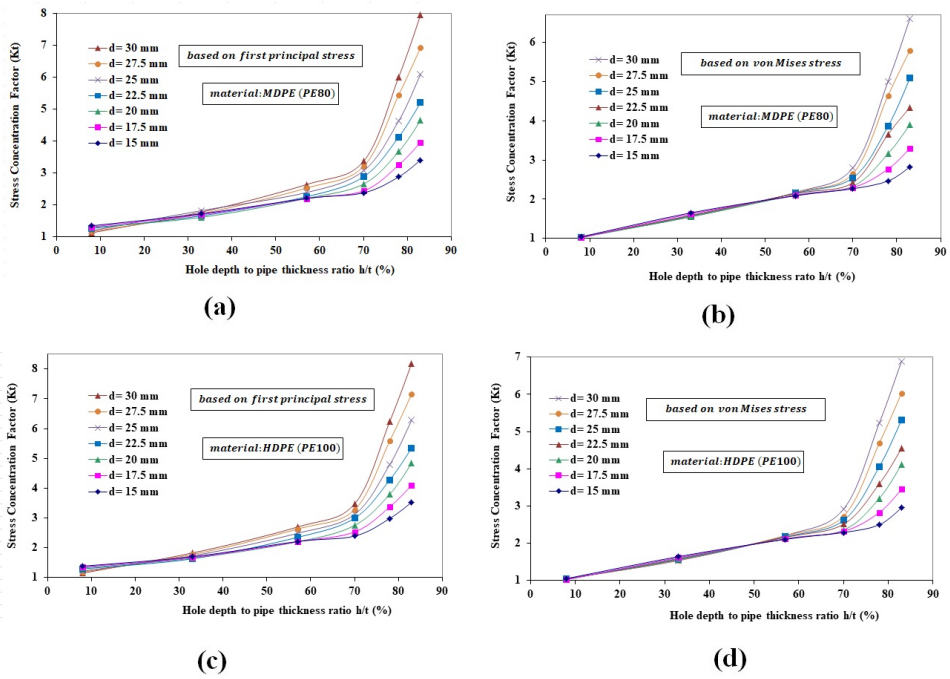

FIGURE 4.19: Trends of stress concentration factors versus depth to thickness ratio (h/t), for above ground MDPE and HDPE pipe materials subjected to partial holes of different hole sizes and depth to thickness ratio. (a) SCF calculations based on maximum first principal stress in medium density polyethylene pipe (PE80). (b) SCF calculations based on maximum von Mises stress in medium density polyethylene pipe (PE80). (c) SCF calculations based on maximum first principal stress in high density polyethylene pipe (PE100). (d) SCF calculations based on maximum von Mises stress in high density polyethylene pipe (PE100).

of Iran. Fig. 4.25 and Fig. 4.26 show the variations in the first principal stress and maximum von Mises stress in the above ground pipe for various sizes of partial circular defects (holes) subjected to a temperature drop of $-15\,^{\circ}$C. Additionally, Fig. 4.27 and Fig. 4.28 show the variations in the first principal stress and maximum von Mises stress in the above ground pipe for various sizes of partial circular defects (holes) subjected to a temperature increase of $30\,^{\circ}$C. The pipe material is medium density polyethylene (PE80), where the related strength of the pipe for several temperatures, based on a 50 years working life is also depicted on all figures. The reduced strengths are used due to the viscoelastic behavior of polyethylene material that occurs over the years of service. The model dimensions and defect sizes are similar to those reported in subsections 4.3. From the finite elemnt results it can be concluded that:

1- Temperature changes in the pipes made of polyethylene material exhibit a direct and significant effect on thermal stresses produced in the pipe.

2- For both studied temperature changes including $30\,^{\circ}$C increase and $-15\,^{\circ}$C temperature drop, maximum stresses are higher that the samples without temperature change.

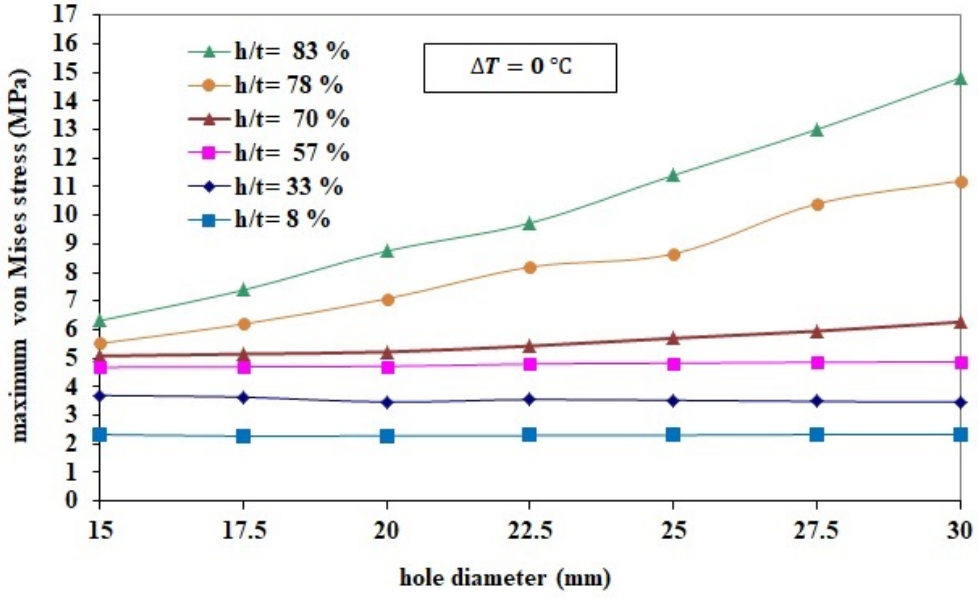

Working temperature (°C)	20	25	30	35	40	45	50
Allowable stress for PE80 (MPa)	4.00	3.75	3.50	3.20	3.00	2.80	2.60

FIGURE 4.20: Trends of maximum von Mises stress in above ground PE80 pipe material for several hole sizes and different hole depths under the sole effect of internal pressure (no temperature change).

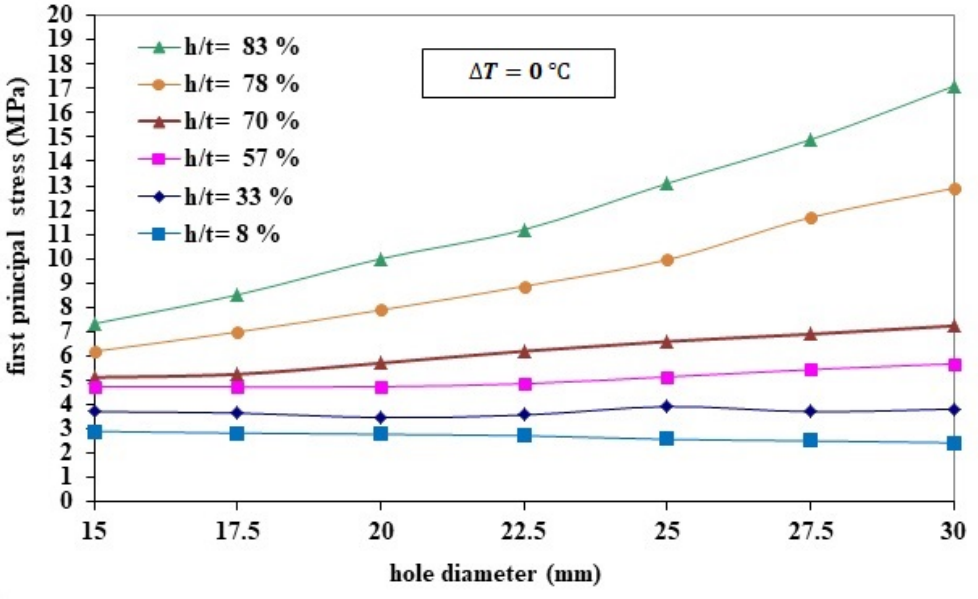

Working temperature (°C)	20	25	30	35	40	45	50
Allowable stress for PE80 (MPa)	4.00	3.75	3.50	3.20	3.00	2.80	2.60

FIGURE 4.21: Trends of maximum first principal stress in above ground PE80 pipe material for several hole sizes and different hole depths under the sole effect of internal pressure (no temperature change).

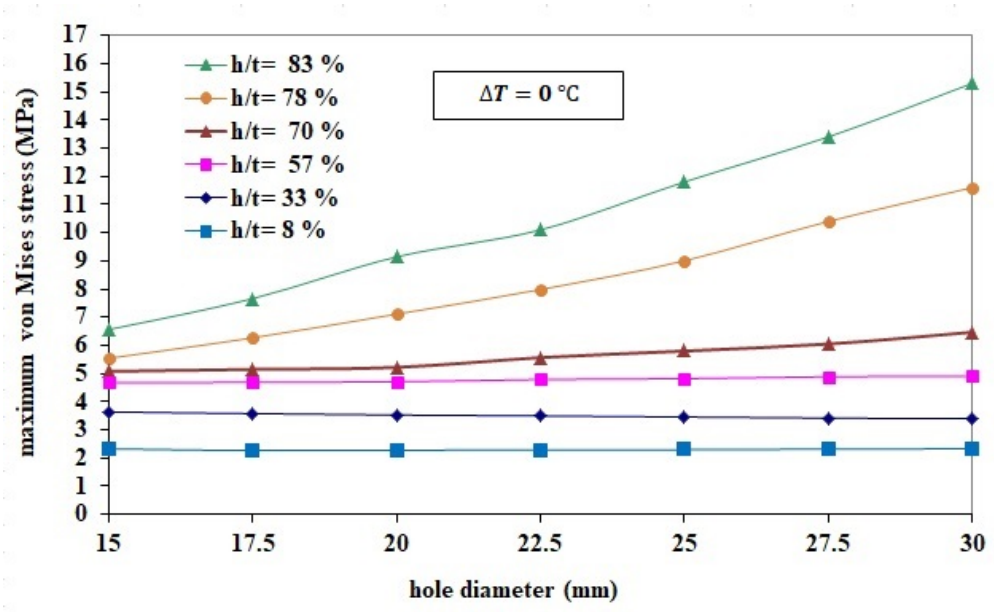

Working temperature (°C)	20	25	30	35	40	45	50
Allowable stress for PE100 (MPa)	5.00	4.70	4.35	4.00	3.65	3.30	3.00

FIGURE 4.22: Trends of maximum von Mises stress in above ground PE100 pipe material for several hole sizes and different hole depths under the sole effect of internal pressure (no temperature change).

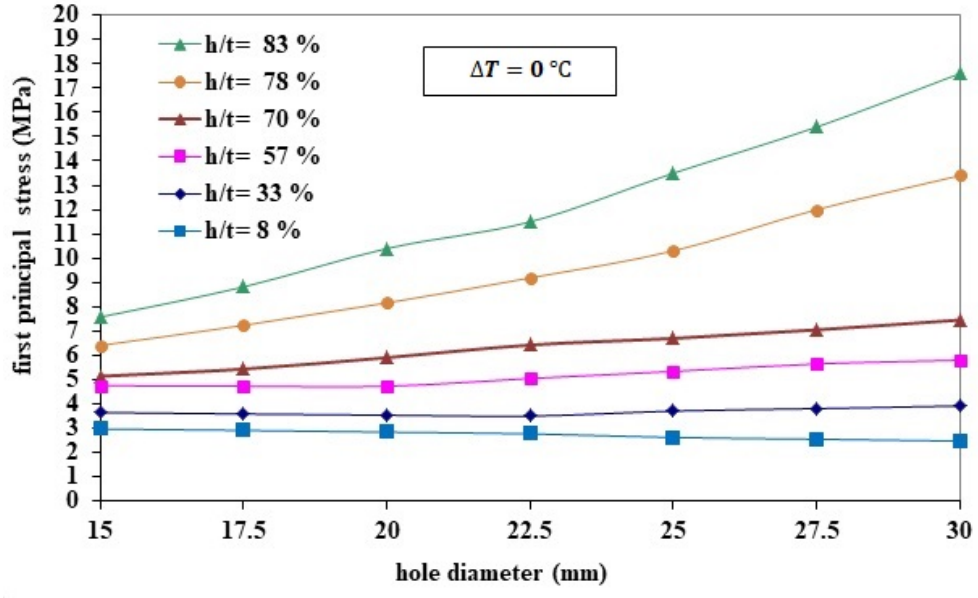

Working temperature (°C)	20	25	30	35	40	45	50
Allowable stress for PE100 (MPa)	5.00	4.70	4.35	4.00	3.65	3.30	3.00

FIGURE 4.23: Trends of maximum first principal stress in above ground PE100 pipe material for several hole sizes and different hole depths under the sole effect of internal pressure (no temperature change).

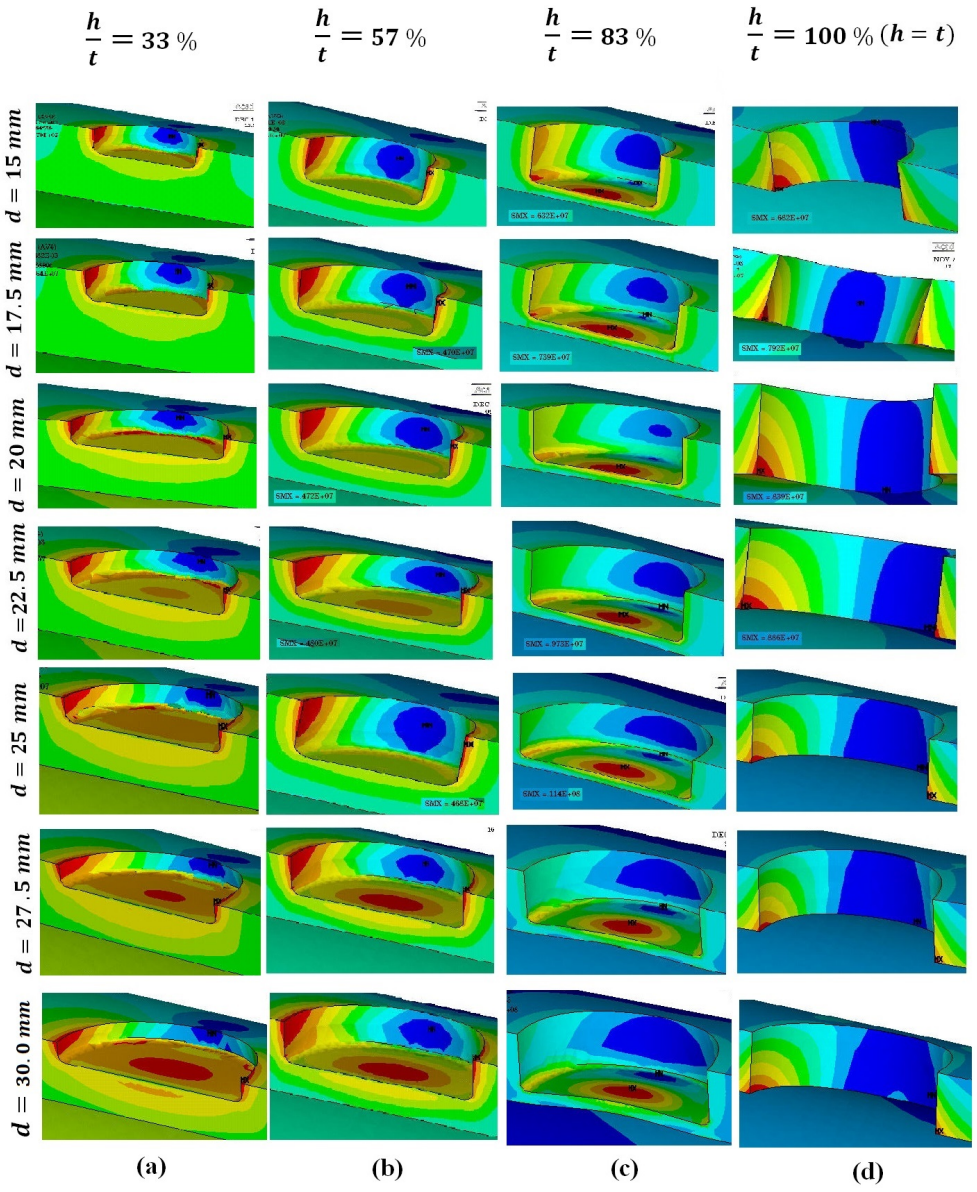

FIGURE 4.24: High stress areas of von Mises stress in the immediate vicinity of hole for several hole sizes and different hole depths of above ground medium density polyethylene (PE80) pipe.

However, the effect of 30 °C temperature increase is more pronounced than −15 °C temperature decrease.

3- A temperature increase of 30 °C, has the most effect on stress values and both maximum von Mises stress and maximum first principal stress increase by temperature rise. For example the maximum stress values are around double the values reported in the samples of 8 % depth ratio and no temperature changes. This effect is more pronounced for deeper defects in comparison to small values of depth to wall thickness rations like 8 %.

4- Considering the operating temperature of 30 °C, for above ground polyethylene pipe with defect depth less than 8 % depth to wall thickness ratio, under a temperature increase of −15 °C, both maximum von Mises stress and maximum first principal stress are well below the maximum applicable stress.

5- For deeper defects (more than than 8 %), in all cases, both maximum von Mises stress and maximum first principal stress exceed the safe limit and are above the allowable stresses, which means the pipe can't withstand the imposed temperature changes.

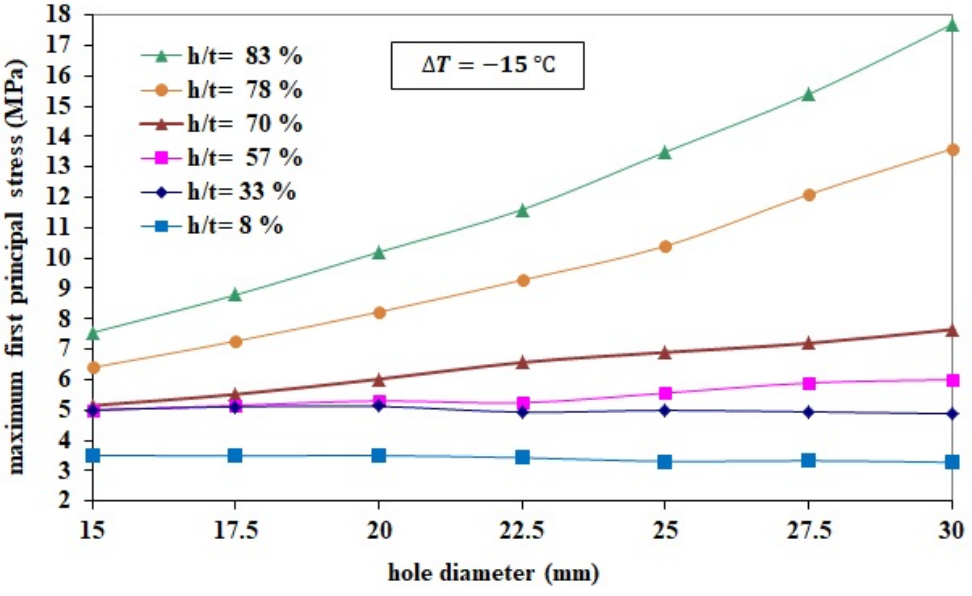

Working temperature (°C)	20	25	30	35	40	45	50
Allowable stress for PE80 (MPa)	4.00	3.75	3.50	3.20	3.00	2.80	2.60

FIGURE 4.25: Values of maximum first principal stress in above ground PE80 pipe material for several hole sizes and different hole depths subjected to a temperature drop of 15 °C.

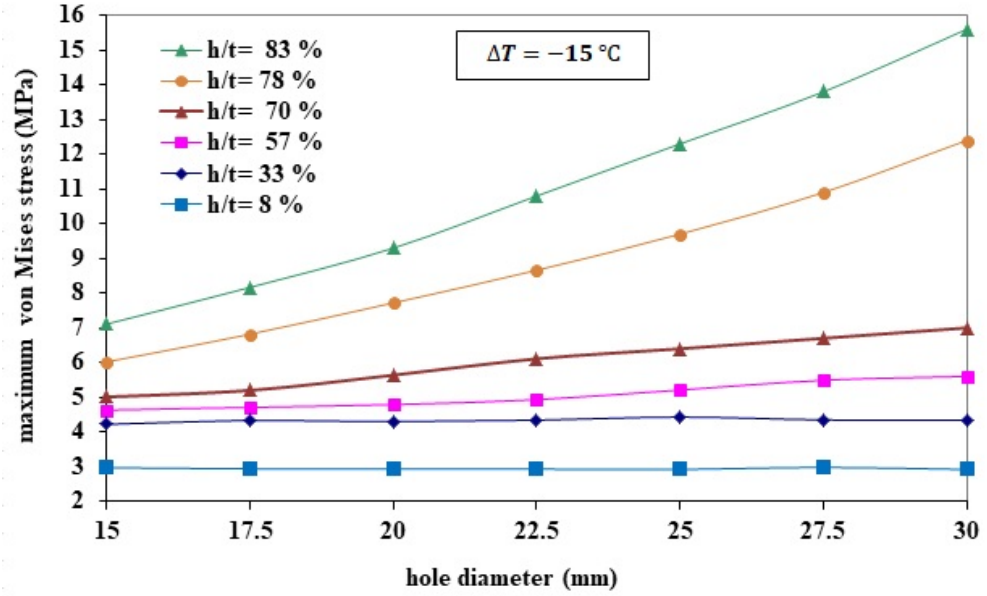

Working temperature (°C)	20	25	30	35	40	45	50
Allowable stress for PE80 (MPa)	4.00	3.75	3.50	3.20	3.00	2.80	2.60

FIGURE 4.26: Maximum von Mises stress in above ground PE80 pipe material for several hole sizes and different hole depths subjected to a temperature drop of 15 °C.

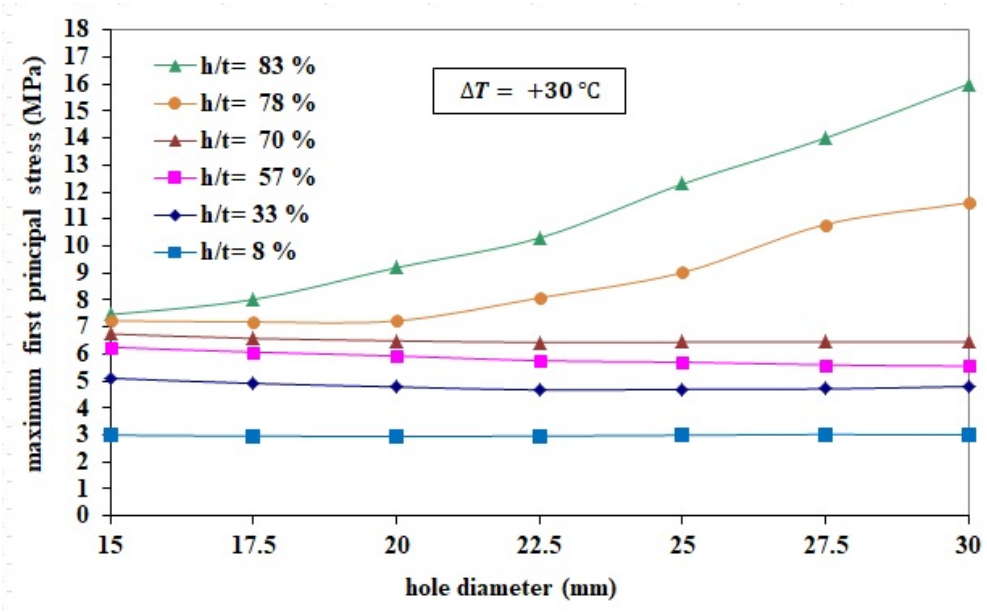

Working temperature (°C)	20	25	30	35	40	45	50
Allowable stress for PE80 (MPa)	4.00	3.75	3.50	3.20	3.00	2.80	2.60

FIGURE 4.27: Values of maximum first principal stress in above ground PE80 pipe material for several hole sizes and different hole depths subjected to a temperature increase of 30 °C.

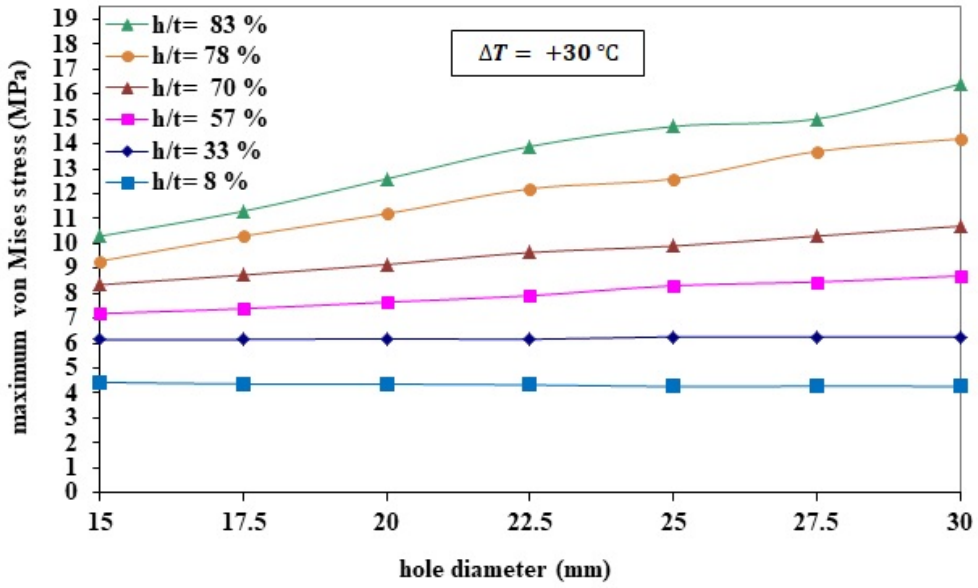

Working temperature (°C)	20	25	30	35	40	45	50
Allowable stress for PE80 (MPa)	4.00	3.75	3.50	3.20	3.00	2.80	2.60

FIGURE 4.28: Maximum von Mises stress in above ground PE80 pipe material for several hole sizes and different hole depths subjected to a temperature increase of 30 °C.

4.5 Repair patch effect and comparison between patches

Developing defective pipe strengthening techniques with the potential to manage gas blow and its ignition disasters is an important aspect of this technology. A common theme in defective pipe strengthening theories and methods is that the strengthening effect is achieved by applying repair patches, where this technique is used to efficiently plug and seal induced damages and fractures to deliberately enhance the pipe mechanical properties. The PE patches are stuck on the outer surface of the damaged PE pipe or some other structural components to cover and fix the affected area in a short time. The current understanding of defective pipe strengthening by patches and the mechanisms behind it is still under debate. The patch is an effective barrier as it seals and bridges the hole in the pipe wall and overlaps and extends on all sides of the hole and gap for strength. This technology has the potential to mitigate the ignition possibility of blowing gas and improve pipe integrity to avoid disasters. Developing defective pipe strengthening techniques with the potential to manage gas blow and its ignition disasters is an important aspect of this technology.

The repair of defects in MDPE pipe by electrofusing HDPE material patches proved its efficiency by reducing the stress intensity at the defected part. How to proceed with patch repair method depends on the shape and size of the hole in the pipe wall which

have to be fixed. Poor understanding of defective pipe strengthening physics or mechanisms and unavailability of an advanced diagnostic procedure to identify the root cause in advance are the main obstacles to develop new mitigation technologies.

TABLE 4.7: Maximum first principal and von Mises stresses in the above-ground MDPE gas pipe in the presence of circular holes defects with various sizes (hole diameter) and hole depth to pipe wall thickness ratios (h/t), repaired by a saddle fusion patch and due to an inside pressure only. These stresses are related to the pipe region around the defect which is reinforced by patch.

Hole diameter (mm)	**depth to thickness ratio (h/t)**	**Max. first principal stress (MPa)**	**percent (%) reduction**	**Max. von Mises stress (MPa)**	**percent (%) reduction**
15.0	8 %	1.66	42.8	1.78	23.6
15.0	33 %	0.92	75.2	1.44	60.4
15.0	57 %	1.61	74.7	1.2	65.5
15.0	100 %	2.68	62.2	3.09	57.5
17.5	8 %	1.66	41.3	1.78	21.6
17.5	33 %	0.90	76.8	1.48	58.7
17.5	57 %	1.14	75.9	1.62	65.5
17.5	100 %	2.69	64.2	3.09	61.0
20.0	8 %	1.66	40.0	1.78	22.0
20.0	33 %	0.84	75.8	1.46	58.6
20.0	57 %	1.08	77.2	1.65	65.0
20.0	100 %	2.68	66.5	3.09	63.2
22.5	8 %	1.66	35.0	1.78	22.6
22.5	33 %	0.85	76.2	1.59	54.5
22.5	57 %	1.00	79.4	1.58	67.0
22.5	100	2.68	64.4	3.08	61.1
25.0	8 %	1.65	35.8	1.78	22.6
25.0	33 %	0.80	79.5	1.68	51.4
25.0	57 %	1.00	80.5	1.73	64.1
25.0	100 %	2.68	69.9	3.08	66.9
27.5	8 %	1.65	34.3	1.78	23.3
27.5	33 %	0.80	78.5	1.76	48.5
27.5	57 %	0.93	82.9	1.79	63.4
27.5	100 %	2.68	71.5	3.08	68.6
30.0	8 %	1.65	32.1	1.78	23.6
30.0	33 %	0.90	76.5	1.90	44.0
30.0	57 %	0.91	84.0	1.93	60.6
30.0	100 %	2.68	73.2	3.09	70.3

In this section, numerical linear elastic modeling is employed to investigate defective pipe strengthening and therefore the three-dimensional finite element method is used to achieve a comparison between the saddle fusion and semi-cylindrical patch repairs in unburied PE pipe. These patches impart strengthening effect on the defective pipe. The comparison was done by the analysis of the mechanical stresses, in the repaired defected pipe and the distribution of the von Mises sterss for the aforementioned patch shapes. The saddle fusion patch length and thickness are assumed to be 82 mm and 4.763 mm, respectively. Fig. 4.29 illustrates three different views of a typical finite element model

of pipe featuring a partial hole defect with 20 mm diameter and depth ratio of 33 % and reinforced by a strengthening saddle fusion patch. The vectors of internal pressure are also depicted on Fig. 4.29(c).

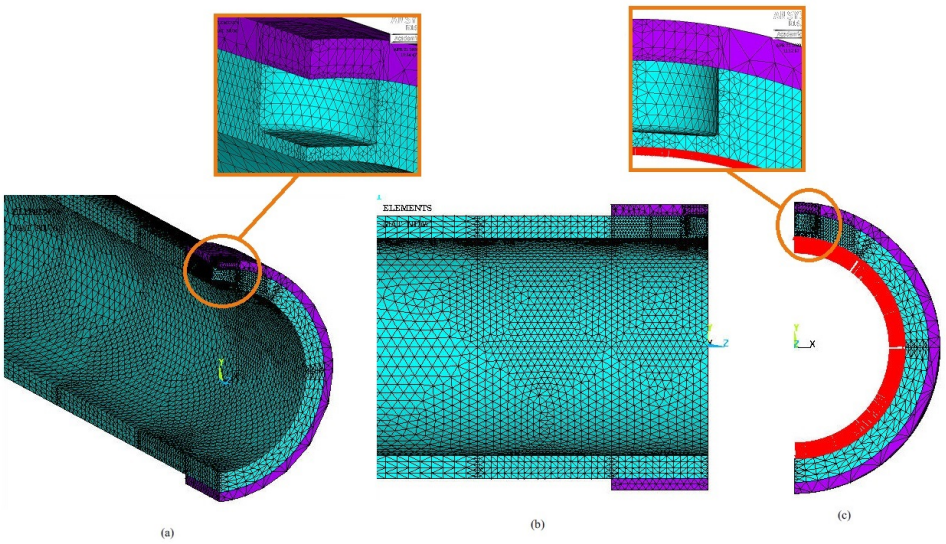

FIGURE 4.29: Illustration of finite element model of pipe featuring a partial hole defect, in the case of a 20 mm hole diameter and depth ratio of 33 %, and reinforced by a strengthening saddle fusion patch.

The effect of reinforcing patch on the strength of the stress concentration regions in the pipe is found by solving the two similar problems of the defective pipe with and without the reinforcing patch. In Sec. 4.4 mechanical behavior of defective above-ground PE gas pipe, before any treatment was well discussed. The investigated pipe featured several holes with various diameters and depth to thickness ratios (h/t) and was under the effect of an inside pressure only. As mentioned previously, Fig. 4.24 showed the distribution of von Mises stress and also high stress areas surrounding the hole, before any treatment. After applying and modeling a HDPE saddle fusion repair patch to strengthen the defect area in the pipe, we record the values of maximum first principal and von Mises stresses at similar regions in the pipe (high stress regions in unrepaired pipe) and the results are depicted in Table. 4.7. To evaluate the patch effectiveness in each stage, the reduction in stress values with respect to high stress areas in unpatched defected pipe is also calculated and is reported in %. The results indicates the significant relieving effect of the reinforcing patch on the stress concentrations at the vicinity of the borehole in PE gas pipe. Results in Table. 4.7 indicate that the application of the patch leads to a significant reduction of the von Mises stress values in the vicinity of the hole.

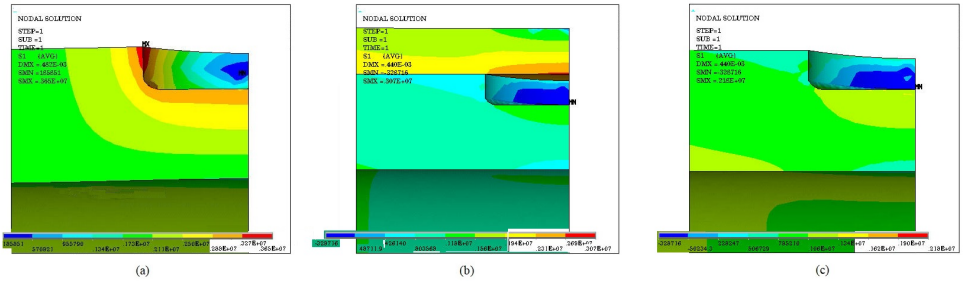

FIGURE 4.30: Distribution of first principal stress and also high stress areas surrounding the hole, before any treatment, in the presence of a hole with 17.5 mm diameter and depth ratio of 33 %. (a) Before repair (b) after repair (c) pipe only, after repair.

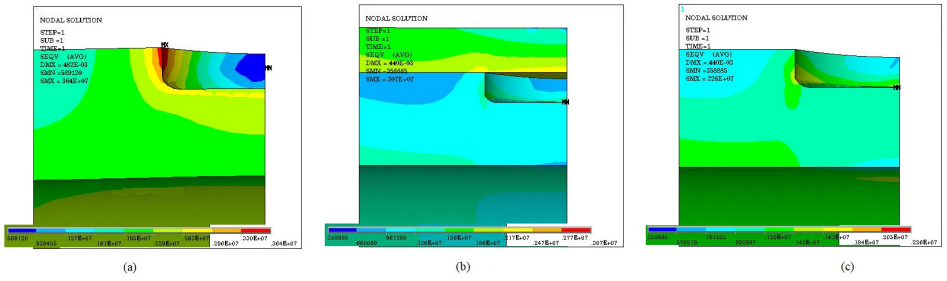

FIGURE 4.31: Distribution of von Mises stress and also high stress areas surrounding the hole, before any treatment, in the presence of a hole with 17.5 mm diameter and depth ratio of 33 %. (a) Before repair (b) after repair (c) pipe only, after repair

Fig. 4.30, and Fig. 4.31 represent the distribution of first principal and von Mises stresses and also high stress areas surrounding the hole, before any treatment, in the presence of a hole with 17.5 mm diameter and depth ratio of 33 % and also after the patch repair.

Fig. 4.32, shows a saddle fusion patch perfectly bonded on polyethylene substrate (pipe), in the presence of a partial hole with 20 mm diameter and depth ratio of 33 %. Four different views of pipe and saddle fusion patch arrangement are graphically illustrated to show von Mises stress distribution. Additionally, a magnified view in the vicinity of the hole is depicted at the top of this figure. To save computational costs, a quarter size of the pipe-patch configuration was modeled and symmetric boundary conditions were applied as shown in Fig. 4.32. On the surface $x = 0$, $x-$directional $d.o.f.s$ are fixed and on the surface $z = 0$, $z-$directional $d.o.f.s$ are fixed. Also, Figs. 4.33 (a) and (b), show results of von Mises and first principal stress distribution respectively, in only pipe of the mentioned problem, after repairing by a saddle fusion patch. Figs. 4.34(a) and (b), exhibit graphical illustration of von Mises and first principal stress distribution respectively, in only saddle fusion patch (the pipe is removed) used to repair the pipe described in Fig. 4.32. As can be seen, bonded patch is very efficient as the 3-dimensional

(3D) state of stress in the portion of the pipe which is attached to the patch (near the defect) dropped significantly and is lower that the other portion of the pipe. Figs. 4.35(a) and (b), indicate graphical illustration of first principal stress distribution in above ground PE gas pipe in the presence of a hole with 17.5 mm diameter and depth ratio of 57 %, before and after saddle fusion patch repair, respectively. According to this figure, the defect area in the pipe is well strengthened after patch repair as a significant part of the applied loads are transferred from the pipe to the patch and the maximum first principle stress is decreased around 54% which is very significant. As can be seen from Fig. 4.33 there is no red spot (maximum stress) in the vicinity of the hole and the maximum stresses region is in the unpatched pipe section, far away from the defect area and where the stress distribution is similar to the intact (not defected) pipe. By the way, for deeper defects even though the strengthening patch reduces the stresses in the vicinity of the defect significantly, there still exists red spots around the partial hole, according to Fig. 4.35 which means the defect still influence and controls high values of stress.

Figs. 4.36 and 4.37 illustrate values of maximum von Mises an first principal stresses in above-ground PE80 pipe (all over the pipe) in the presence of several hole sizes and different hole depth rations, respectively and after being repaired by strengthening saddle fusion patch. For both figures, the curves related to 8 % and 33 % cases and also the beginning part of the curve for 57 %, touch each other. Additionally, Table. 4.8 indicates the similar stresses in the reinforcing patch.

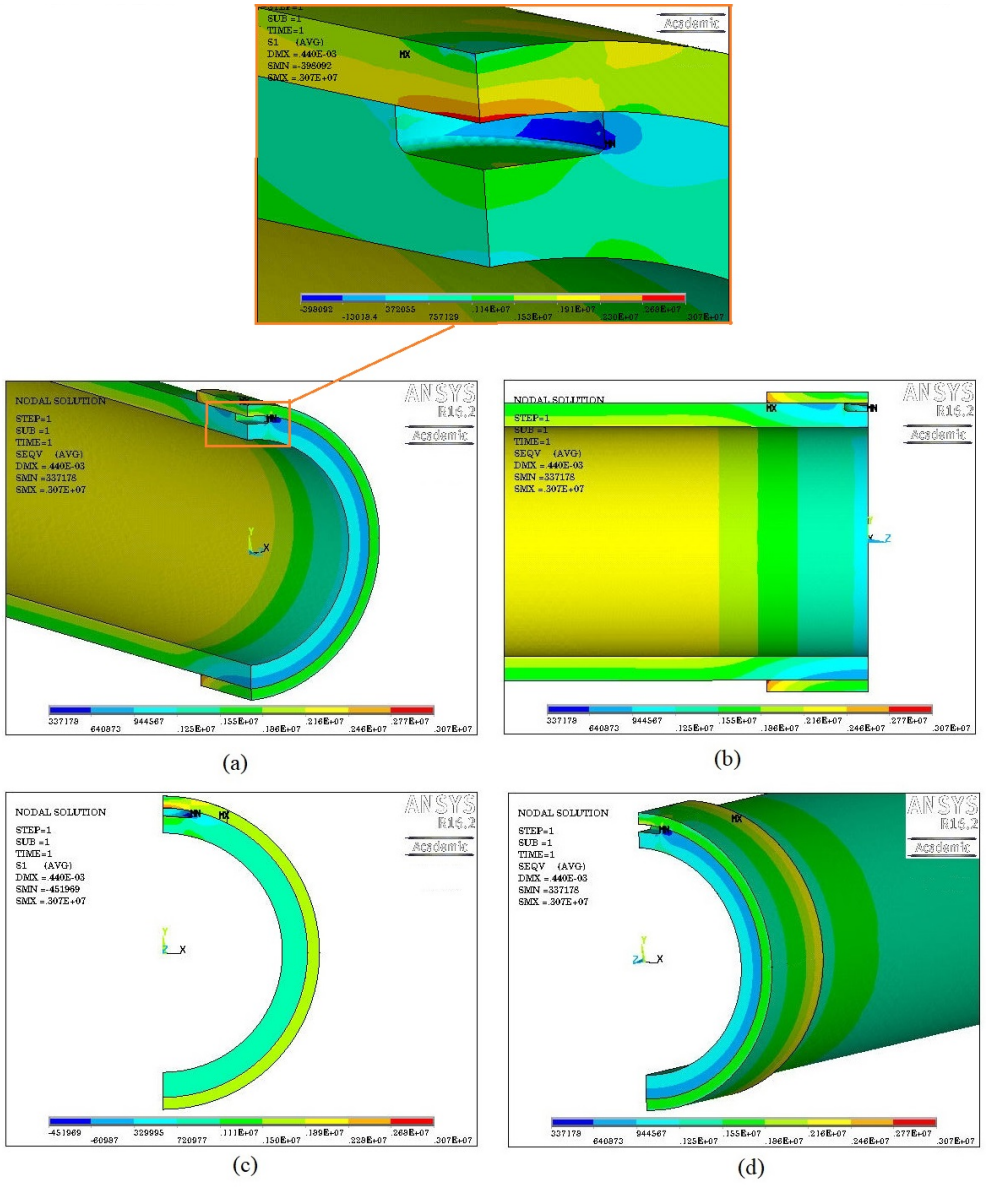

FIGURE 4.32: Four different graphical illustrations of pipe and saddle fusion patch arrangement to show von Mises stress distribution, in the presence of a hole with 20 mm diameter and depth ratio of 33 %.

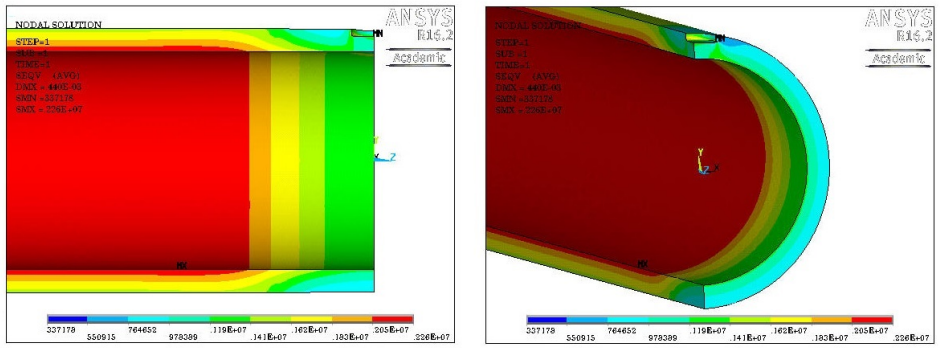

(a) Von Mises stress distribution in pipe

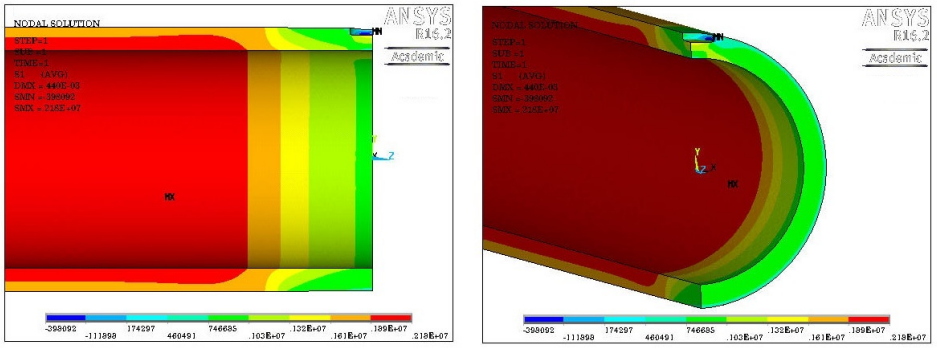

(b) First principal stress distribution in pipe

FIGURE 4.33: Graphical illustration of only pipe with a hole of 20 mm diameter and depth ratio of 33 %, after repairing by a saddle fusion patch. (a) von Mises stress distribution, (b) First principal stress distribution.

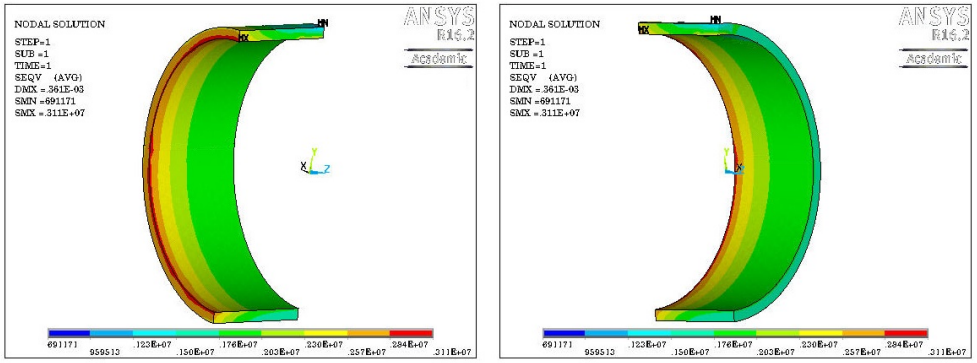

(a) Von Mises stress distribution in patch

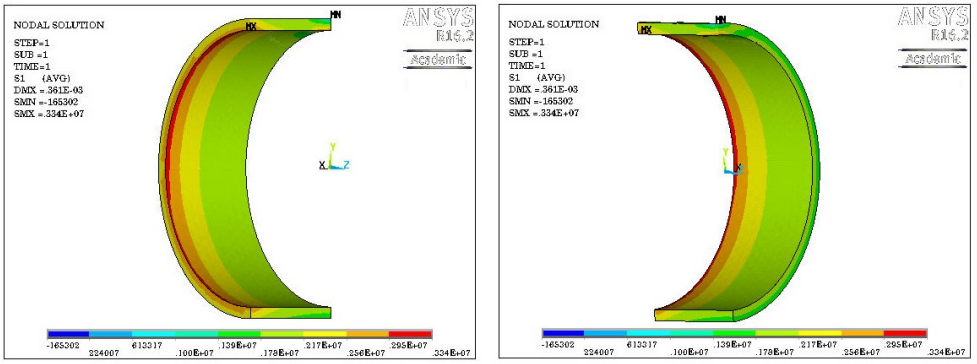

(b) First principal stress distribution in patch

FIGURE 4.34: Graphical illustration of only saddle fusion patch used to repair a hole with 20 mm diameter and depth ratio of 33 % in the pipe wall. (a) von Mises stress distribution, (b) First principal stress distribution.

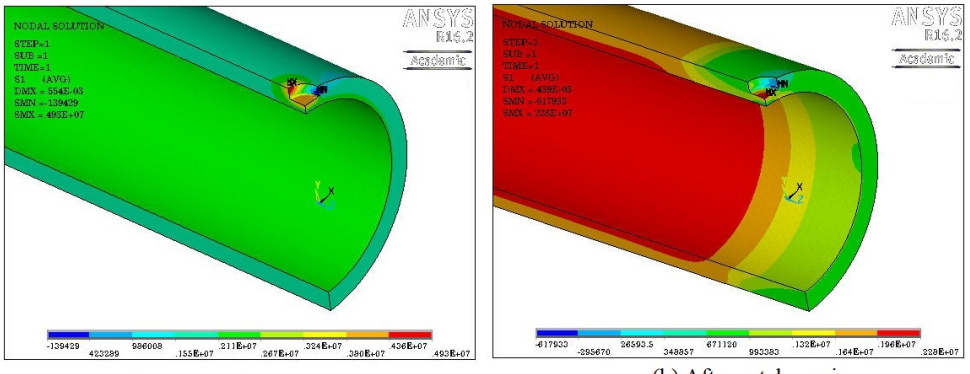

(a) Before patch repair (b) After patch repair

FIGURE 4.35: Graphical illustration of first principal stress distribution in above ground PE gas pipe in the presence of a hole with 17.5 mm diameter and depth ratio of 57 %. (a) Before saddle fusion patch repair, (b) After applying a saddle fusion patch repair.

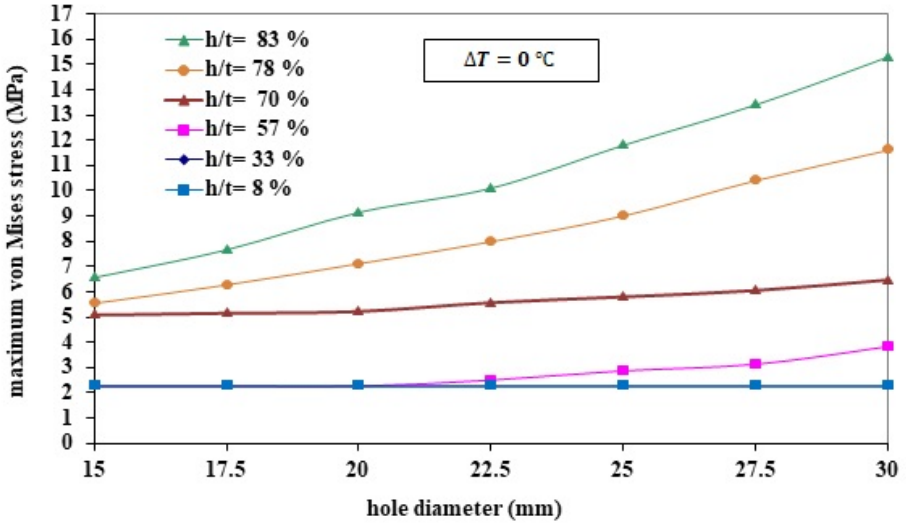

Working temperature (°C)	20	25	30	35	40	45	50
Allowable stress for PE80 (MPa)	4.00	3.75	3.50	3.20	3.00	2.80	2.60

FIGURE 4.36: values of maximum von Mises stress in patch repaired above-ground PE80 pipe in the presence of several hole sizes and different hole depths, (after repaired by saddle patch).

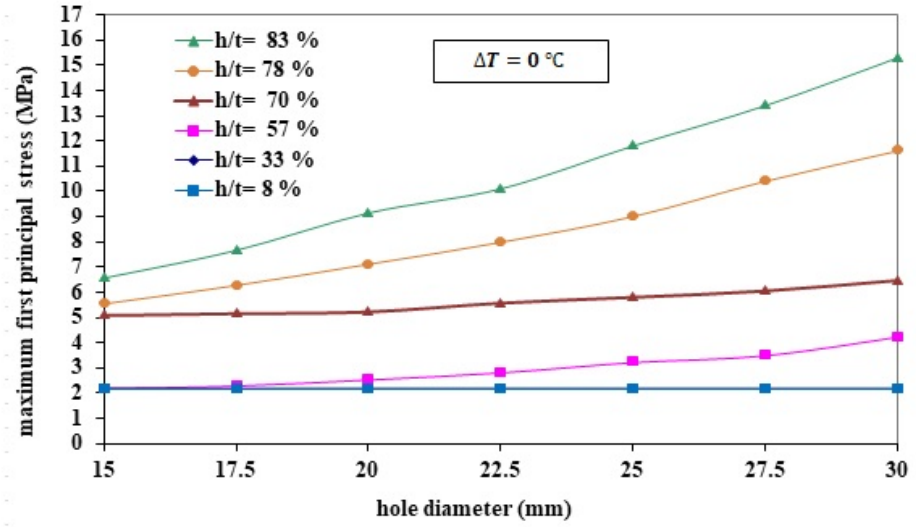

Working temperature (°C)	20	25	30	35	40	45	50
Allowable stress for PE80 (MPa)	4.00	3.75	3.50	3.20	3.00	2.80	2.60

FIGURE 4.37: values of maximum first principal stress in patch repaired above-ground PE80 pipe in the presence of several hole sizes and different hole depths, (after repaired by saddle patch).

TABLE 4.8: Maximum first principal and von Mises stresses in the saddle fusion patch used to repair above-ground MDPE gas pipe in the presence of circular holes defects with various sizes (hole diameter) and hole depth to pipe wall thickness ratios (k/h), and due to an inside pressure only.

Hole diameter (mm)	**depth to thickness ratio (t/h)**	**Max. stress (MPa) first principal**	**von-Mises**
15.0	8 %	3.34	3.11
15.0	33 %	3.34	3.11
15.0	57 %	3.34	3.10
15.0	100 %	3.43	3.19
17.5	8 %	3.34	3.11
17.5	33 %	3.34	3.11
17.5	57 %	3.33	3.10
17.5	100 %	3.43	3.11
20.0	8 %	3.34	3.11
20.0	33 %	3.34	3.11
20.0	57 %	3.33	3.10
20.0	100 %	3.36	3.13
22.5	8 %	3.34	3.11
22.5	33 %	3.34	3.11
22.5	57 %	3.33	3.11
22.5	100 %	3.37	3.14
25.0	8 %	3.34	3.11
25.0	33 %	3.34	3.11
25.0	57 %	3.33	3.11
25.0	100 %	3.39	3.16
27.5	8 %	3.34	3.11
27.5	33 %	3.34	3.11
27.5	57 %	3.42	3.11
27.5	100 %	3.45	3.37
30.0	8 %	3.34	3.11
30.0	33 %	3.34	3.11
30.0	57 %	3.50	3.11
30.0	100 %	3.65	3.55

Chapter 5

Finite Element Analysis Results of Stress Distribution in Buried Defective Polyethylene Gas Pipes

5.1 Finite element model results of buried damaged gas pipe

In this part of the study, we discuss the results of geometric and finite element simulation for buried polyethylene gas transportation pipe subjected to partial and complete holes, which were built using ANSYS 16.2 software. As mentioned previously, estimating stress distribution in buried pipe is difficult because the interaction between soil and pipe is a very complicated problem especially in the presence of geometrical singularities in the form of defects in pipe wall and also, internal pressure, traffic load and temperature variations. Trench dimension, all physical and material properties, and soil grades around the pipe's circumference were selected based on ASTM standards and specified in Sec. 3.8.4.

In order to further estimate the load bearing capacity of buried polyethylene pipeline for long life period (50 years) and include the viscoelastic behaviour of the polyethylene pipe material, peak values of the resulted first principal and von Mises stresses in the pipe are compared to their corresponding values of σ_s, which are according to their σ_{MRS} values. Based on Eq. (3.15), σ_s can be calculated by dividing σ_{MRS} values by C. In this research for safety issues, C is assumed to be equal to 2 according to reference [21]. For the ease and convenience of making decision if the pipe is able to withstand loads, allowable stresses for several working temperatures are also tabulated near the graph of

the FEM results. σ_{MRS} values of PE80 and PE100 are given on Table 3.2 for various working temperatures. The results of finite element models for buried defective PE pipes with several defects, include maximum stress values, which enables us to evaluate if the defective underground PE pipe section is unable to bear the applied loads and needs an argent repair or may withstand imposed loading, including internal pressure, soil column weight, traffic load and temperature variations at the pipe installation depth for longer time even with the presence of defects. Additionally, knowledge on stress distribution in the vicinity of defects and the trend of peak stresses variation in the pipe wall with respect to holes size and depth will be useful in choosing effective repair patches. Therefore, radial bore diameter and depth sizes effects on the principal and von Mises stresses as well as the resulting stress concentration factors in the vicinity and along the partial holes in buried PE pipes are investigated.

5.1.1 Under ground pipeline with complete and partial hole damages in pipe wall

For the buried simple pristine (intact) pipe model under the concurrent effect of aforementioned applied loads, it is observed that the compressive stresses resulting from traffic load (normal vehicles) and soil column weight are lower that the stresses imposed by pipe internal pressure, therefore, the stress distribution in the pipe wall is mainly affected by internal pressure. In this section of the research, in order to get deeper insight of internal pressure, temperature change, traffic load, and the soil weight effects on the buried pipe with respect to stress concentration stemming from the partial and complete holes, the finite element model of the repaired pipe and its surrounding area at a depth of 125 cm (from surface to pipe crown) was considered. In all finite element models, because of the symmetry conditions for both problem geometry and applied loads, only a quarter of complete actual physical problem of underground pipe and surrounding soil was modeled. This symmetry condition aims at decreasing computational time and costs. For all finite element simulations, 1 meter long MDPE and HDPE pipe with a 4-inch nominal diameter ($k = 1.2103$) was modeled and loaded to a final pressure of 405,300 Pa (4 bar). The traffic load imposed on the pavement was calculated based on Fig. 3.7.

First, finite element analysis was used to calculate maximum stresses in the buried simple pristine gas pipe with 4 inches diameter loaded to a final pressure of 405300 Pa (4 bar) and traffic load. The results for defect-free underground MDPE and HDPE pipes are shown in Table 5.1 for no temperature change case. In the following, after estimating maximum stresses in defective pipes, we compare them with the results of this table by calculating stress concentration factors.

TABLE 5.1: Maximum von Mises, circumferential and first principal stresses in buried intact (defect-free) simple PE80 and PE100 pipe under the effect of internal pressure and trafic load (no temperature change).

Pipe material	**Maximum stress (MPa)**		
	von Mises	**first principal**	**circumferential**
PE80	2.88	2.88	2.88
PE100	3.39	3.47	3.47

5.2 The effects of complete circular hole damage in buried pipe

In this section, in order to further study the concurrent effect of pipe internal pressure, daily and seasonal temperature variations, traffic load, and the soil column weight on the imposed stresses in buried defective PE pipe, finite element model is used to calculate peak stresses with respect to stress concentration stemming from the leak-openings (complete circular holes), while subjected to bore holes of various sizes including 7.5, 10.0, 12.5, 15.0, 17.5, 20.0, 22.5, 25.0, 27.5, 30.0, 32.5 and 35.0 mm hole diameter. According to FEM results, the percent of maximum horizontal deflection to pipe diameter for all pipe models with leak-opening was well bellow the limit of 3 %.

Stress concentration factors were calculated after performing finite element analysis and using maximum stresses reported in Table. 5.1. Maximum von Mises stresses and maximum first principal stresses in the vicinity of the holes were used as highest stresses (σ_{max}) and equivalent stresses in the buried simple pristine pipe (based on Table. 5.1), was used as nominal (reference) stress (σ_{nom}). The results are presented in Fig. 5.1. Stress concentrations based on maximum first principal stress and maximum von Mises stress are displayed on Figs. 5.1 (a) and (b) respectively. For example, the introduction of a 35 mm diameter bore hole is seen to produce a first principal stress concentration factor (based on first principal stress) of 3.31 and 3.20 at the radial bore-main bore intersection in buried MDPE and HDPE pipes, respectively. Clearly, when the hole diameter approaches to zero, stress concentrations approach unity. According to the graphs, rising the hole size causes increase in stress concentration factor. Comparing the curves for both MDPE and HDPE pipe materials indicates both have similar trends. In both figures, MDPE pipe material has higher stress concentration factors, compared to HDPE pipe for all hole sizes, and the related curves for HDPE pipe are below the equivalent curves for MDPE material. The values are close for both materials and the difference between stress concentrations doesn't change by increasing hole size. For example, stress concentration factor reaches around 3.5 for 35 mm hole diameter in the MDPE pipe wall, which indicates a radial hole local stress consentrator seriously increases peak stress values which threaten material elastic limit at the vicinity of the hole

and increase the danger of pipe failure especially in presence of cyclic loads. Therefore, based on the results maximum stress levels are significantly effected and increased by complete hole defects. Therefore, in the next section we analyze the stress response of underground PE pipe under considerable loading conditions.

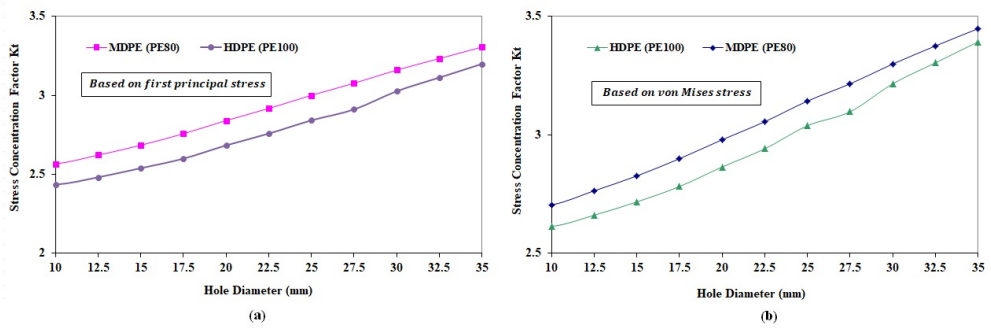

FIGURE 5.1: Stress concentrations factors for under ground MDPE and HDPE pipe materials in natural gas distribution systems. (a) Calculations performed based on first principal stresses. (b) Calculations performed based on von Mises stresses.

In Figs. 5.2 and 5.3, the results for maximum first principal and maximum von Mises stresses, respectively in buried MDPE and HDPE pipes, versus complete circular hole size (diameter) are compered with the similar stresses in above-ground pipe models (based on Sec. 4.2). No temperature change is assumed for this comparison. In both shapes the dashed lines and solid lines indicates the results for above-ground and underground pipelines, respectively. According to the curves shapes, in underground pipelines, the stresses increase rate with respect to hole diameter, is very slower than in above-ground pipelines. This behavior can be translated to the reinforcement effect of surrounding soil on strengthening the pipe. For our studied models, in MDPE pipe material, firstly, at smaller hole sizes the stresses are higher for buried pipe but the stresses increase rapidly in above ground pipeline with respect to hole size and reach the stress values of underground pipeline at 22.5 mm hole diameter and then pass them and reach higher values. in HDPE pipe material, the same behavior is observed and the maximum von Mises stress reaches the values for underground pipeline at 35.0 mm hole diameter.

The comparison of the peak stress valuse from curves of Figs. 5.2 and 5.3 with allowable stresses for several working temperatures (as tabulated at the bellow of each figure) shows that maximum first principal stress and maximum von Mises stress are significantly higher that their allowable counterpart for 50 years life expectancy, in all mentioned working temperatures. This means the stresses values are in unsafe limit and both HDPE and MDPE pipes with complete holes won't withstand the aforementioned applied loads.

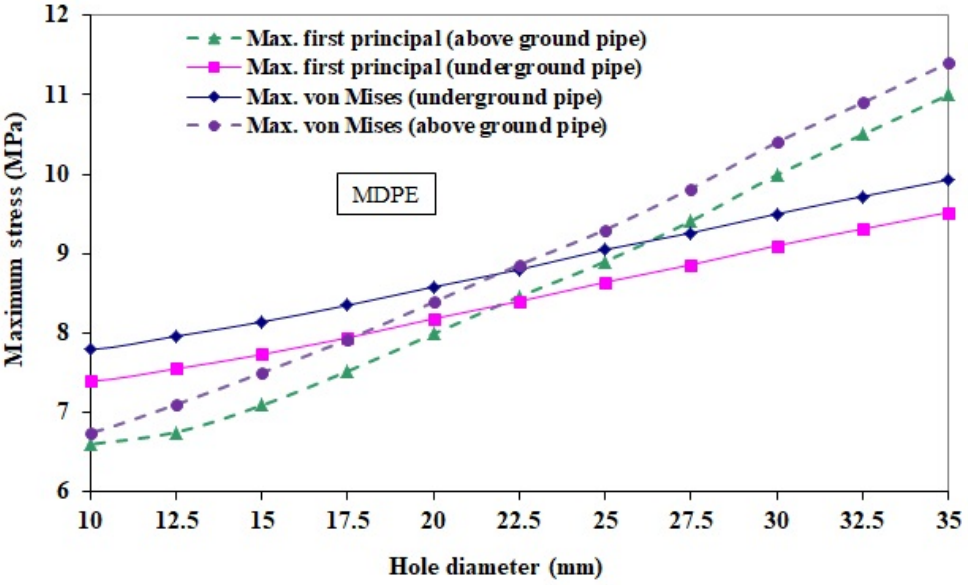

Working temperature (°C)	20	25	30	35	40	45	50
Allowable stress for PE80 (MPa)	4.00	3.75	3.50	3.20	3.00	2.80	2.60

FIGURE 5.2: Comparison of maximum first principal and von Mises stresses in buried and unburied MDPE pipe versus complete circular hole size (diameter).

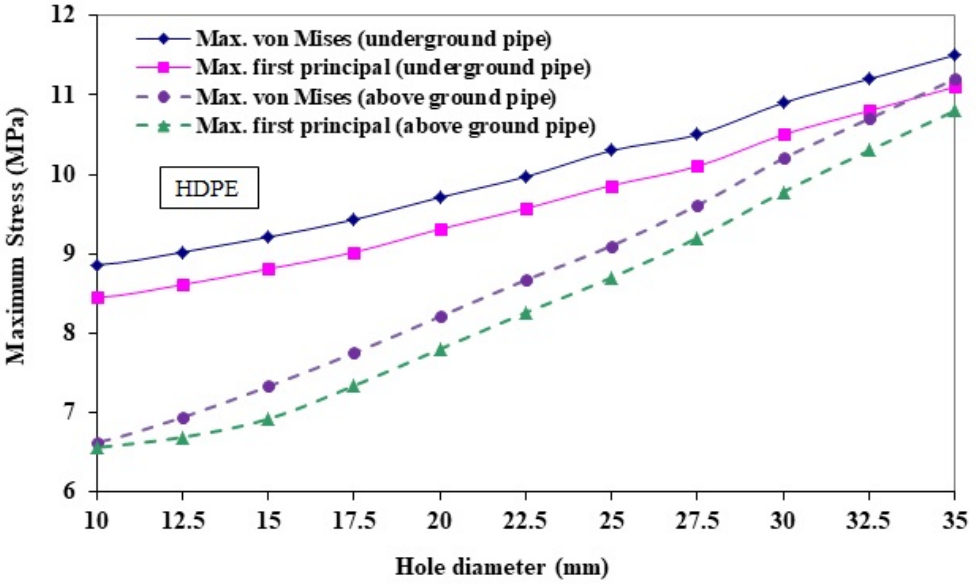

Working temperature (°C)	20	25	30	35	40	45	50
Allowable stress for PE100 (MPa)	5.00	4.70	4.35	4.00	3.65	3.30	3.00

FIGURE 5.3: Comparison of maximum first principal and von Mises stresses in buried and unburied HDPE pipe versus complete circular hole size (diameter).

Additionally, we investigate possible temperature changes effects, therefore in this section it is assumed that the underground pipeline undergoes a maximum temperature change (decrease and increase) of 22 °C (due to a seasonal change in temperature). As stated previously, this is a typical seasonal temperature change in the soil at a depth of 125 cm in the city of Ahvaz that is located in a hot climate zone. Also, as stated in Sec. 3.7.1, in the same area on a hot summer day assuming the worst case of a sudden temperature reduction in a pipe which is in direct contact with the soil, it can experience a 15 °C temperature reduction after installation.

Fig. 5.4 and Fig. 5.5 show values of first principal stress and maximum von Mises stress in buried PE80 pipe material for aforementioned complete hole sizes, respectively. At the bottom of each figure, reduced strength of MDPE pipe (according to the viscoelastic behavior of polyethylene which occurs over the long years of service) at different working temperatures, with respect to a 50 years working life is also depicted. The following conclusions are reached from the presented results:

1- Comparing finite element modeling results of defective PE pipes with the stress values in the simple defect-free pressurized buried pipe, shows that stresses in the pipe wall are highly affected by a complete circular leak-opening.

2- Similar to above-ground gas pipe, for underground pipe with complete circular notch shape defect, the location of peak stresses is at the inside lip of the hole at the pipe inner surface, at the edges along the length of the pipe (as estimated in the analytical solution discussed in 3.8.2). The minimum stresses occurred at the lips in 90 degrees for the edges of maximum stresses. Additionally, all pipe models display similar stress distribution patterns.

3- Maximum first principal stress and maximum von Mises stress, both show an increase trend with respect to increasing hole diameter of buried pipe. Although like above-ground pipeline, this effect is more pronounced for larger holes but in underground pipeline, the increase rate is slower. The reason for this behavior could be the supporting and strengthening effect of soil which encompasses the pipe. As an example, in 15 °C temperature drop case, for a small hole size of 10 mm, a 5 mm increase in hole size (increasing hole size to 15 mm) will cause 2.3 % and 2.1 % increase in maximum first principal and maximum von Mises stresses, respectively. Also, for a large hole size of 30 mm, a 5 mm increase in hole size (increasing hole size to 35 mm) will cause 4.7.2 % and 4.1 % increase in maximum first principal and maximum von Mises stresses, respectively, which are around twice the small hole case. For above-ground pipe this value was much higher (around 6 times higher).

4- All studied cases, including no temperature change, 15 °C temperature drop, 22 °C temperature rise and drop cases show approximately similar trends.

5- 30 °C temperature rise in the pipe has the most influence on both maximum first

principal and maximum von Mises stresses. This temperature change imposes significant tensile stress in the defect area.

6- Maximum stress values in the defected pipe, will decrease by 15 °C and 22 °C temperature drop in comparison with no temperature change case. The lest effect on stresses is according to 22 °C temperature drop.

7- Comparing the values of maximum stresses and the allowable stresses for 50 years working life, it is clear that for all investigated temperature changes (and also models with no temperature change) and defect ranges, the maximum first principal stress and maximum von Mises stress are higher than their design limit, which means the stresses are in unsafe range and the pipe material can't withstand the inside pressure of 4 bar.

According to the above results, the buried pipe with the proposed circular holes under the application of soil column weight, traffic load, 4 bars internal and aforementioned temperature changes is not strong enough to withstand the applied loads and should be repaired properly. As the concentrated stresses exceed material's strength, material will fail quickly mostly following a crack propagation.

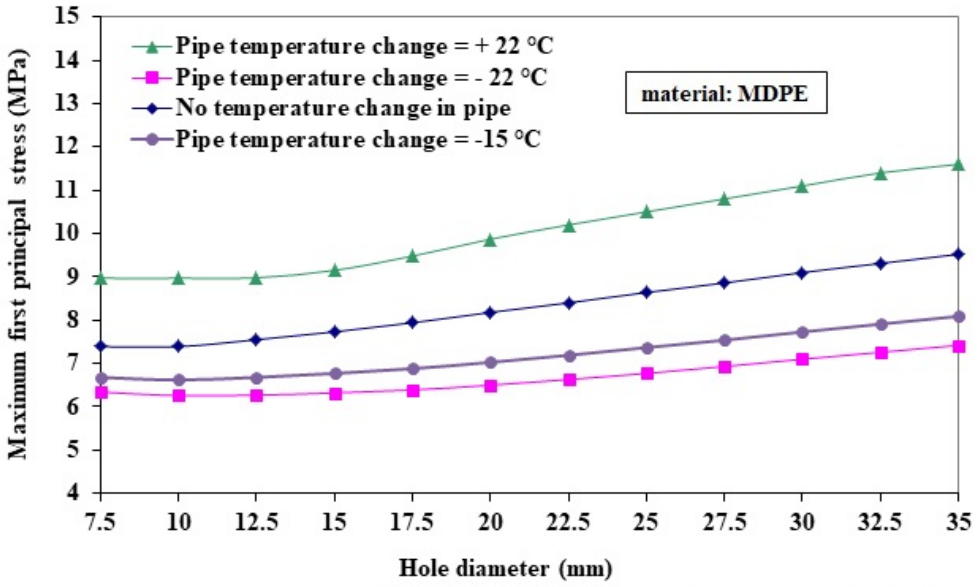

Working temperature (°C)	20	25	30	35	40	45	50
Allowable stress for PE80 (MPa)	4.00	3.75	3.50	3.20	3.00	2.80	2.60

FIGURE 5.4: First principal stress in buried pipe versus complete circular hole size (diameter) based on simultaneous effects of inside pressure, temperature changes, traffic load, and the soil weight.

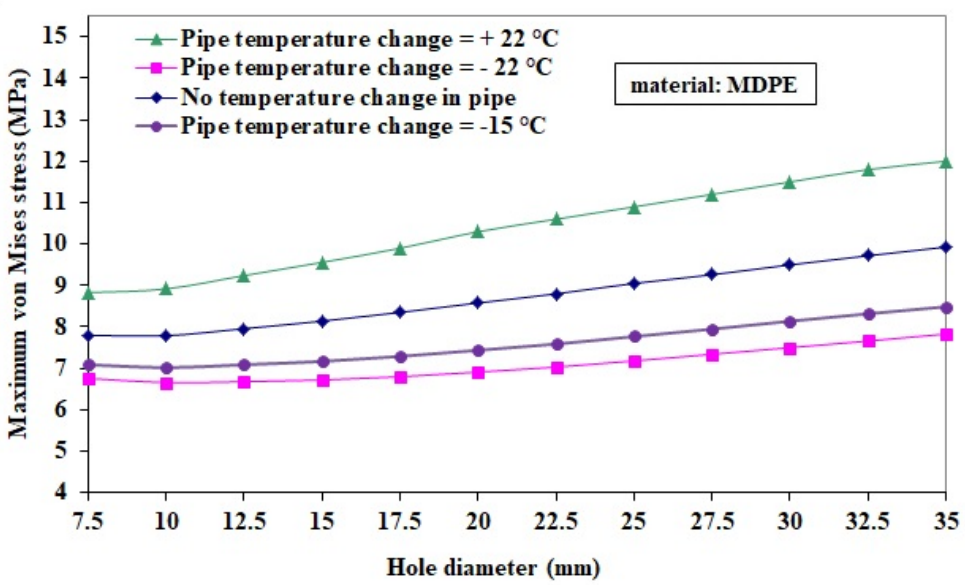

Working temperature (°C)	20	25	30	35	40	45	50
Allowable stress for PE80 (MPa)	4.00	3.75	3.50	3.20	3.00	2.80	2.60

FIGURE 5.5: Maximum von Mises stress in buried pipe versus complete circular hole size (diameter) based on simultaneous effects of inside pressure, temperature changes, traffic load, and the soil weight.

5.3 The effects of partial round hole damage in buried pipe

Based on the FE results obtained in the previous section for a buried pipe with leak opening complete hole in the pipe wall, we implied that the maximum stress values in the pipe wall is significantly higher than an undisturbed simple buried pipe with the same loading conditions. This means, the aforementioned stresses are affected by a discontinuity in the form of complete hole. However, based on gas companies reports, in real underground distribution lines, there exist incomplete defects while, defect depth may vary from the external pipe surface to inside surface of the pipe. Therefore, in this part of study, the mechanical behavior of the buried polyethylene gas pipe with respect to different diameter and depth sizes of partial circular defects is investigated. The finite element simulations were performed on a range of defects from non-intensive outer surface defects to extreme large ones extended from outer surface to inside pipe wall. Comparing the final stress results with the allowable values for 50 years working life, will help us to decide if the defective pipe may withstand applied loads in the presence of defects.

The graphs on Figs. 5.6 (a) and (b), indicates the values of stress concentration factor versus hole diameter including a small 15 mm hole to a large 30 mm diameter, for different hole radial sizes (i.e. hole depths) in MDPE (PE80) pipe material. Each curve

on the aforementioned figures belongs to a specific hole depth to wall thickness ratios (h/t) including 8 %, 33 %, 57 %, 78 % and 83 %. Buried MDPE pipes were under the concurrent effect of soil column weight, vehicle wheel load and also subjected to a final pressure of 405300 Pa (4 bar). For graphs on Fig. 5.6 (a), the calculations for stress concentration factor are according to maximum first principal stress. Additionally, the equivalent results based on maximum von Mises stress are depicted on Fig. 5.6 (b). As an example, the introduction of a 30 mm diameter partial hole with thickness ratio of 78 % is seen to produce a principal stress concentration factor of 4.34 in the vicinity of the defect in the buried MDPE pipe. These finite element results give a principal stress concentration factor of 1.58, in the presence of a 25 mm diameter partial hole with thickness ratio of 33 %. To a better interpretation of the data, we draw the variation of stress concentration factors with respect to hole depth size in Figs. 5.7 (a) and (b). Based on the results, following conclusions can be obtained:

1- The graphs on Fig. 5.7 indicate that for buried MDPE pipes, stress concentration factors (based on both maximum first principal stresses and maximum von Mises stresses) generally has increasing trend with increasing hole diameter.
2- For defect depth ratios up to 8 % stress concentration factor remains unity, which means this size of defect doesn't imposes additional stresses to the pipe in comparison to the non-defective pipe.
3- For shallow holes and up to 33 % of hole depth ratio, the variation of stress concentration factor with respect to hole diameter increase is not significant and is approximately constant for each specific hole depth ratio. This issue is quite clear by considering the initial parts of the curves depicted on Fig. 5.7 for both first principal and von Mises based stress concentration factors. For larger hole depth to thickness ratios, the increase rate of stress concentration factor with respect to hole diameter increase is more pronounced. That is why the curves on Fig. 5.6 display higher slopes for deeper holes. For example, for 78 % and 83 % depth ratios, the increase rate of stress concentration factors are very high. This issue is better understand by referring to Fig. 5.7.
4- According to the results on these figures, for all hole diameters, stress concentration factors approach to one when the hole depth ratio approaches to unity. The curves for both first principal and von Mises stresses display similar trends. For shallow defects with the level of depth ratio below 8 %, for all calculations, the stress concentration factors are very close to unity, which means the destructive effect of these sizes of damage may not threatened the pipe life, significantly. For deeper holes up to around 33 %, also all stress concentration factors remain close to unity.
5- for investigated hole diameters. For higher depths up to around 57 %, stress concentration factor are below 1.5. However, for deeper defects, stress concentration factors, start increasing significantly so that for a 30 mm hole diameter with 83 % depth ratio,

it reaches high values of around 5.5.

Additionally, finite element solutions for a similar buried long pristine (without defect) MDPE pipe show that the maximum von Mises stress and maximum first principal stress (here, maximum circumferential stress) are 2.88 MPa and 2.88 MPa, respectively. These values are well below the allowable stress for the life expectancy of 50 years when compared to Table 3.2, even by applying high factor of safety values of 2.

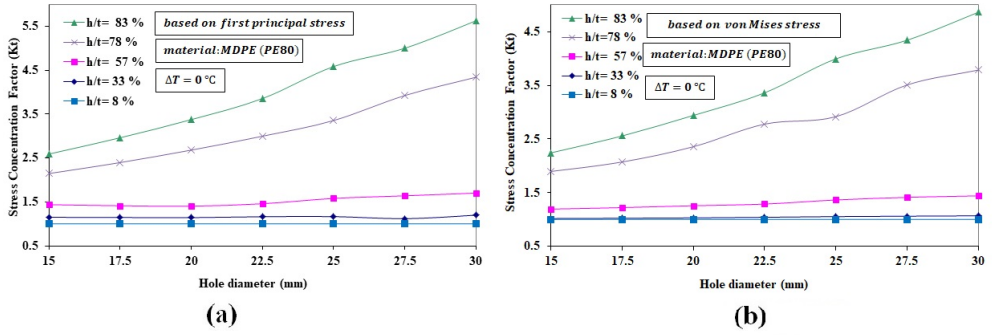

FIGURE 5.6: Stress concentrations factors versus hole diameter, for under ground MDPE pipe material subjected to partial holes of different hole sizes and depth to thickness ratio. (a) SCF calculations based on maximum first principal stress in medium density polyethylene pipe (PE80). (b) SCF calculations based on maximum von Mises stress in medium density polyethylene pipe (PE80).

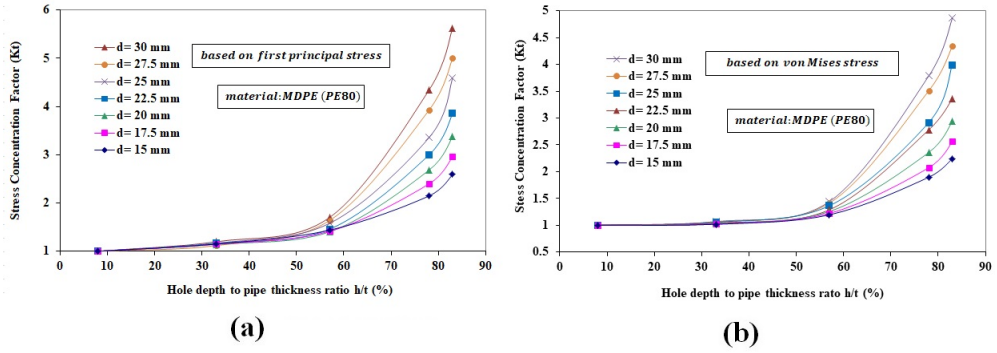

FIGURE 5.7: Stress concentration factors versus depth to thickness ratio (h/t), for under ground MDPE pipe material subjected to partial holes of different hole sizes and depth to thickness ratio. (a) SCF calculations based on maximum first principal stress in medium density polyethylene pipe (PE80). (b) SCF calculations based on maximum von Mises stress in medium density polyethylene pipe (PE80).

However, the results of this section show that the maximum first principal and maximum von Mises stress levels are highly affected and increased by partial hole defects. Therefore, in order to investigate the load bearing capacity of the buried defective PE80 pipe material and also to understand if the pipe subjected to defects can withstand the applied loads during its lifetime, it is required to compare the stress levels in the pipe with their allowable values, under different loading conditions. Meanwhile, in order to

investigate the load bearing capacity of MDPE pipe under the simultaneous effect of aforementioned loads (except temperature variation), the values of maximum von Mises stresses and maximum first principal stresses are calculated for six hole depth to pipe wall thickness ratios (h/t) including 8 %, 33 %, 57 %, 78 % and 83 % (The ratio "100 %" describes a complete hole in the pipe wall, which was disused in subsections 5.2) and the results are depicted on Figs. 5.8 and Fig. 5.9, respectively. For all models depicted on both figures, the temperature change effect is not considered and is assumed to be zero. Furthermore, as discussed before, in some regions temperature variations are significant and therefore, thermal stresses in underground polyethylene pipes are considerable and must be evaluated and added to the stresses imposed by pipe internal pressure, soil column weight and traffic loads. For the calculation of thermal stresses we select south-western Iran (city of Ahvaz). As stated previously, due to seasonal temperature changes, the ground temperature varies from 13 °C in winter to 35 °C in summer in Ahvaz region at the ground depth selected for this research (125 cm). Therefore a buried pipe experiences a 22 °C temperature change (increase and decrease) during the year. Therefore, we evaluate the effect of temperature variations as high as 22 °C at the burial depth of underground PE pipe.

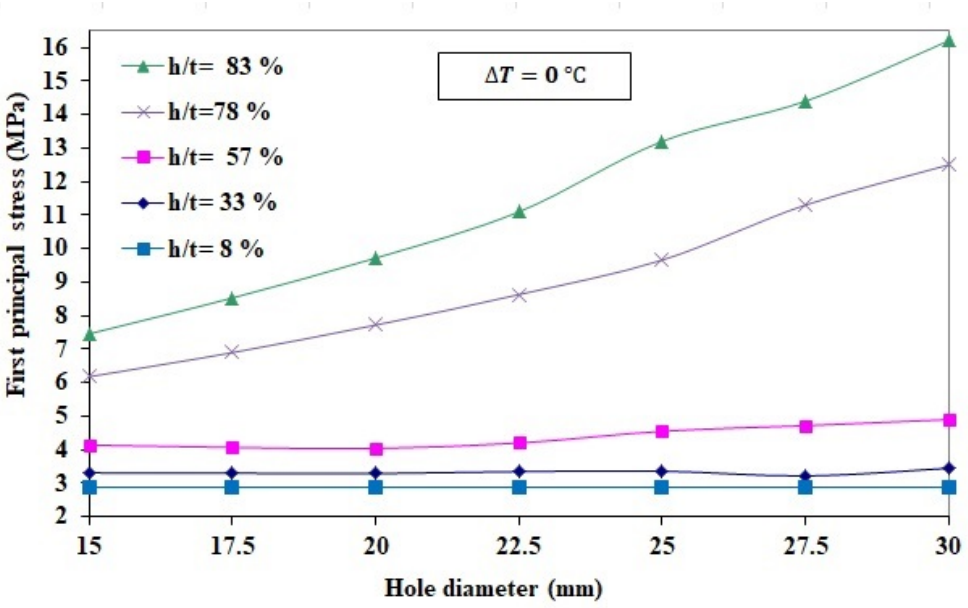

Working temperature (°C)		20	25	30	35	40	45	50
Allowable stress for PE80 (MPa)	C=2.0	4.00	3.75	3.50	3.20	3.00	2.80	2.60
	C=1.25	6.40	6.00	5.60	5.10	4.80	4.50	4.20

FIGURE 5.8: Values of first principal stress in buried PE80 pipe material for several hole sizes and different hole depths.

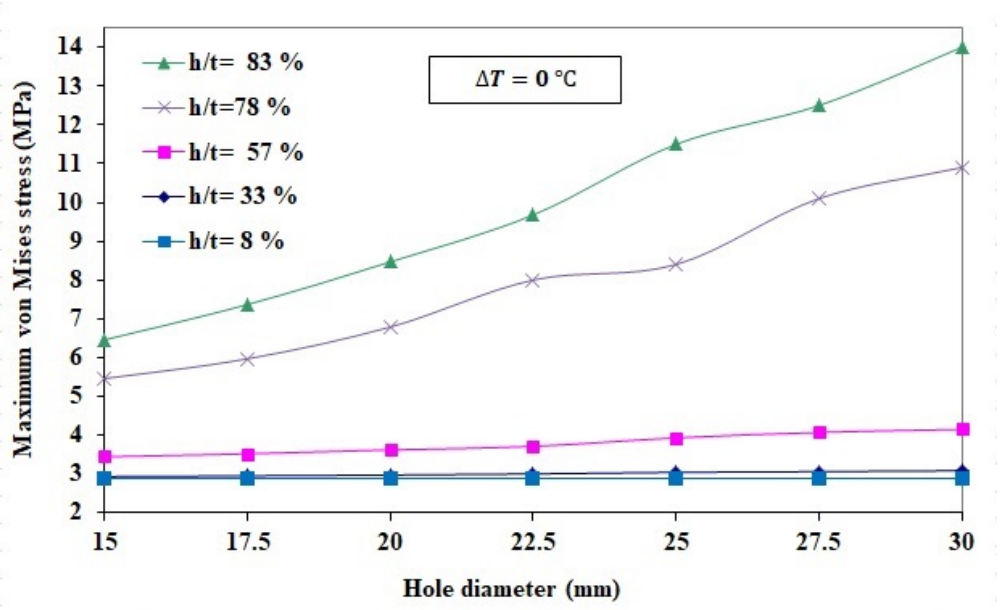

Working temperature (°C)		20	25	30	35	40	45	50
Allowable stress for PE80 (MPa)	C=2.0	4.00	3.75	3.50	3.20	3.00	2.80	2.60
	C=1.25	6.40	6.00	5.60	5.10	4.80	4.50	4.20

FIGURE 5.9: Values of maximum von Mises stress in buried PE80 pipe material for several hole sizes and different hole depths.

The results for defect-free underground MDPE pipe under the concurrent effect of internal pressure, traffic load, soil column weight and aforementioned temperature variations are shown in Table. 5.2. Based on the results, maximum von Mises stress reaches higher values in both 22 °C temperature rise and drop, with respect to no temperature change case. 22 °C temperature rise has more effects on maximum von Mises stresses. For maximum first principal stress, −22 °C temperature drop has more effect as higher stresses are imposed to the pipe wall. Comparing the results with allowable stresses show that the stresses are bellow the stress limit and the buried pipe is working safely even under aforementioned severe temperature changes.

TABLE 5.2: Maximum von Mises, circumferential and first principal stresses in buried intact (defect-free) simple PE80 pipe under the concurrent effect of internal pressure, traffic load, soil column weight and temperature variations.

Temperature change	**Maximum stress (MPa)**		
	von Mises	**first principal**	**circumferential**
0 °C	2.88	2.88	2.88
+22 °C	3.51	2.72	2.72
−22 °C	3.34	3.05	3.05

Fig. 5.10 and Fig. 5.11 show values of first principal stress and maximum von Mises stress in buried PE80 pipe material for several hole sizes and different hole depths, subjected to a temperature rise of +22 °C, respectively. Also, the variations in first principal

stress and maximum von Mises stress in the buried PE pipe for aforementioned sizes of partial circular holes subjected to a temperature drop of −22 °C are indicated in Fig. 5.12 and Fig. 5.13, respectively. For the ease of evaluation the underground PE pipe strength, pipe allowable stresses for life expectancy of 50 years are also calculated for several working temperatures, after using the factor of safeties of 1.25 and 2, and the values are tabulated on the bottom of each figure. Based on the finite element modeling results, following conclusions are reached:

1- Temperature variations in buried defective pipes made of polyethylene material exhibit a direct and significant effect on thermal stresses produced in the pipe.

2- Comparing the results of maximum first principal stress, shows that the effect of −22 °C temperature drop is more pronounced that +22 °C temperature rise and no temperature change, as maximum first principal stresses are higher that the other two cases. For temperature increase of +22 °C maximum first principal stresses are slightly lower that the equivalent samples without temperature change.

3- Comparing the results of maximum von Mises stress, shows that for both temperature changes of +22 °C increase and −22 °C temperature drop, maximum von Mises stresses are higher that the samples without temperature change. However, in most cases the effect of +22 °C temperature rise on maximum von Mises stress is more pronounced that −22 °C temperature drop.

4- Based on the results, maximum first principal and maximum von Mises stresses generally, increase with respect to increasing the hole diameter of the damaged pipe. Additionally, the hole depth effect in increasing maximum stress values is more significant. For depth ratios up to 57 %, the effect of increasing hole diameter on maximum stress values is not significant and the curves are approximately a straight line. However, for deeper defects including 78 % and 83 %, maximum stesses increase rapidly by increasing hole diameter. Deeper defects are more sensitive to the hole diameter size and stress increases faster than the other cases.

5- In buried MDPE pipes with hole depth ratios below 8 %, for the studied temperature changes of −22 °C, 0 °C and +22 °C and also range of hole diameters, maximum von Mises stress values are equal to the values reported for equivalent buried simple pristine MDPE pipe. That means maximum von Mises stress is not affected by non-intensive defect sizes which are bellow 8 % depth hole ratio. For maximum first principal stress, same behavior is observed except for −22 °C temperature drop where the stress value is around 1 MPa more than defect-free buried pipe with the same loading condition. The maximum first principal stress and maximum von Mises stress are below the stress limits for 50 years lifetime and reported working temperatures, by considering a safety factor of 1.25. That means, the buried pressurized pipe under the effect of traffic load and temperature variations, also in presence of the aforementioned defects has sufficient load bearing capacity to transfer natural gas even in presence of shallow defects in pipe

wall. Considering factor of safety 1.5, the stress values are almost below the allowable limits. The only exception is maximum first principal stress for $-22\,^{\circ}\mathrm{C}$ temperature drop which the stresses are a few higher.

6- For deeper defects more than 8 % up to around 33 % depth ratio in buried MDPE pipe, by considering factor of safety 1.5 and working temperatures up to around $35\,^{\circ}\mathrm{C}$, in the studied range of hole diameter, the results show that maximum stresses imposed to the pipe are less than the allowable limits in both cases of no temperature change and $+22\,^{\circ}\mathrm{C}$ temperature increase. However, for $-22\,^{\circ}\mathrm{C}$ temperature drop, both maximum first principal and von Mises stresses are higher than the safe values. For the same problem and loading conditions, by accepting factor of safety 1.25, all stresses will remain below allowable stresses.

7- Investigating deeper defects including 57 %, 78 % and 83 % of depth ratio in the simulated range of hole diameters, shows that buried MDPE pipe may not withstand applied loads at working temperatures of $35\,^{\circ}\mathrm{C}$ and higher working temperatures. The MDPE pipe shows higher levels of maximum stresses with respect to allowable stresses and also is not safe even in low working temperatures of around $20\,^{\circ}\mathrm{C}$. In other words, for all cases of buried MDPE pipe material with depth ratio higher that 57 %, maximum first principal and maximum von Mises stresses are higher than equivalent pristine pipe and particularly higher than allowable stresses for 50 years of life expectancy. Effective repair methods including cutting off the defected pipe section and welding a new section to both ends, or other techniques such as patch repair is necessary in these situations.

8- A temperature increase of $30\,^{\circ}\mathrm{C}$, has the most effect on stress values and both maximum von Mises stress and maximum first principal stress increase by tempreature rise. For example the maximum stress values are around double the values reported in the samples of 8 % depth ratio and no temperature changes. This effect is more pronounced for deeper defects in comparison to small values of depth to wall thickness rations like 8 %.

9- Considering the operating temperature of $30\,^{\circ}\mathrm{C}$, for above ground polyethylene pipe with defect depth less than 8 % depth to wall thickness ratio, under a temperature increase of $-15\,^{\circ}\mathrm{C}$, both maximum von Mises stress and maximum first principal stress are well below the maximum applicable stress.

10- For deeper defects (more than than 8 %), in all cases, both maximum von Mises stress and maximum first principal stress are above the allowable stress, which means the pipe can't withstand the imposed temperature changes.

11- Comparing the results with no temperature change case shows that maximum first principal stresses decrease slightly by a $+22\,^{\circ}\mathrm{C}$ increase in temperature. On the other hand, maximum von Mises stresses resulting from a $+22\,^{\circ}\mathrm{C}$ temperature increase are significantly higher than no temperature change counterparts.

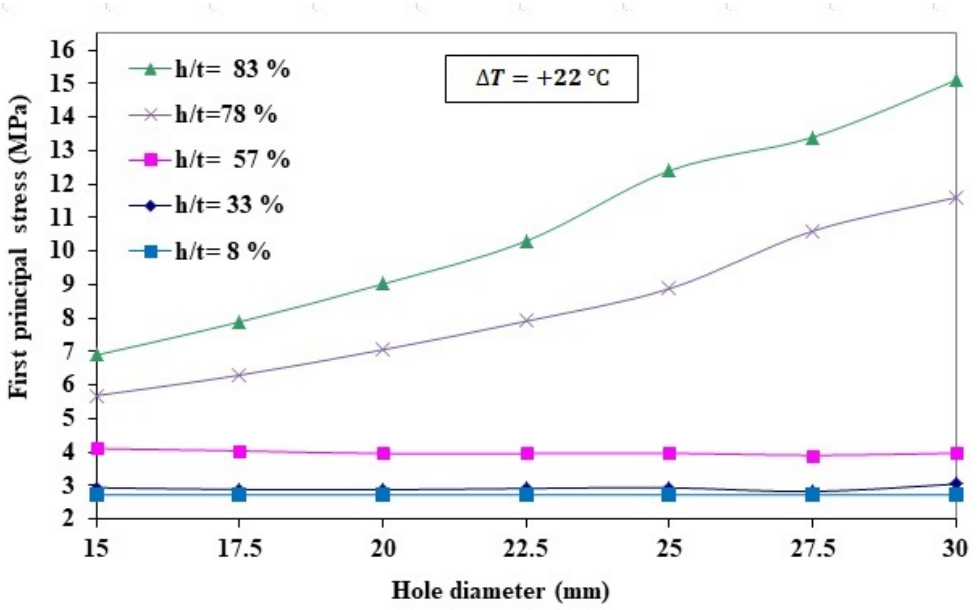

Working temperature (°C)		20	25	30	35	40	45	50
Allowable stress for PE80 (MPa)	C=2.0	4.00	3.75	3.50	3.20	3.00	2.80	2.60
	C=1.25	6.40	6.00	5.60	5.10	4.80	4.50	4.20

FIGURE 5.10: values of maximum first principal stress in buried PE80 pipe material for several hole sizes and different hole depths subjected to a temperature increase of +22 °C.

Our finite element modeling proposes the MDPE pipe material as a strong material for a service life of 50 years even with the circular hole defects as large as almost 30 mm hole diameter and upto 8 percent hole depth. Also, we found that for deep holes (from the depth of 78 percent) a further increase in hole depth causes the increase of maximum stress values significantly.

5.4 Buried Polyethylene Gas Pipes Repaired by PE Patches

In reference [57], polyethylene patch repair method to repair defective natural gas pipes was investigated, where the pipe crown was subjected to notch shape defects with specified sizes. The effect of patches on stress reduction in defective pipes was investigated by the computational modeling and analysis tools of ANSYS software. In this section which is the second fold of our buried pipes study, we continued the research in references [57] to investigate the buried PE pipe with more details and under more critical loading conditions.

The finite element code is executed for modeling and analysis of the complex problem of pipe, patch and their surrounding interactions, and since stress distribution in the

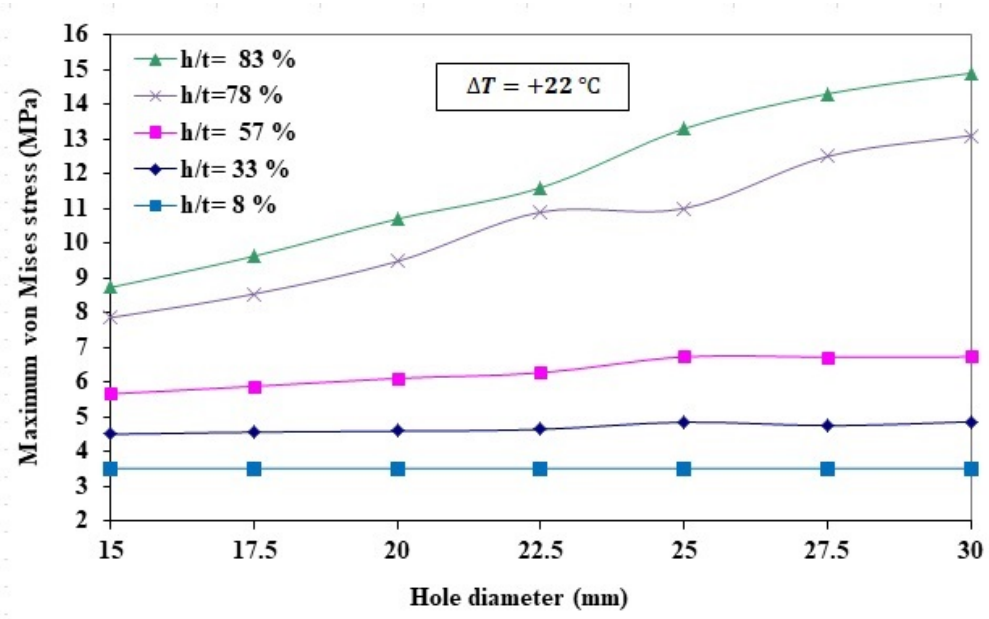

Working temperature (°C)		20	25	30	35	40	45	50
Allowable stress for PE80 (MPa)	C=2.0	4.00	3.75	3.50	3.20	3.00	2.80	2.60
	C=1.25	6.40	6.00	5.60	5.10	4.80	4.50	4.20

FIGURE 5.11: values of maximum von Mises stress in buried PE80 pipe material for several hole sizes and different hole depths subjected to a temperature increase of +22 °C.

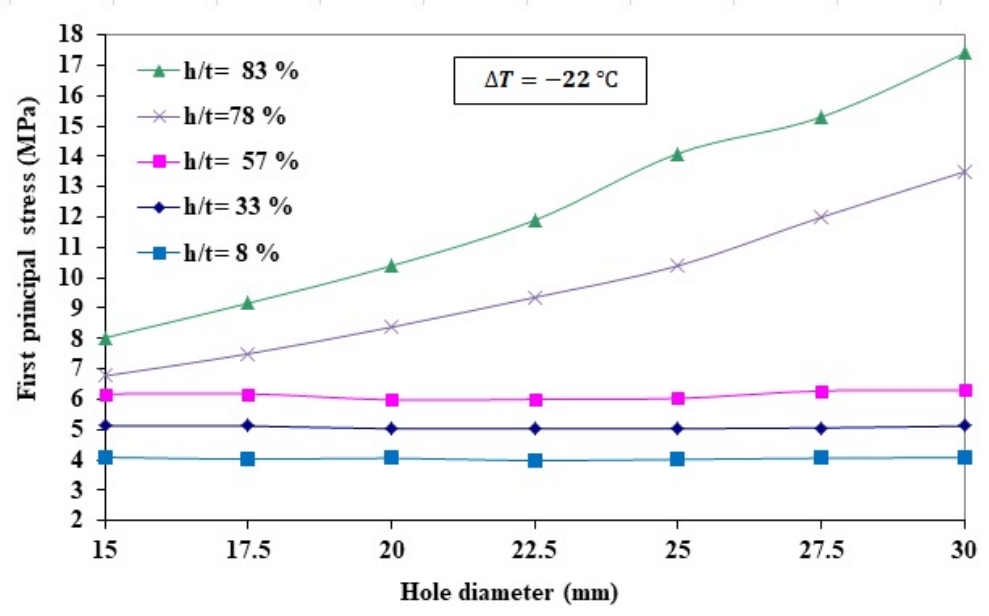

Working temperature (°C)		20	25	30	35	40	45	50
Allowable stress for PE80 (MPa)	C=2.0	4.00	3.75	3.50	3.20	3.00	2.80	2.60
	C=1.25	6.40	6.00	5.60	5.10	4.80	4.50	4.20

FIGURE 5.12: values of maximum first principal stress in buried PE80 pipe material for several hole sizes and different hole depths subjected to a temperature drop of −22 °C.

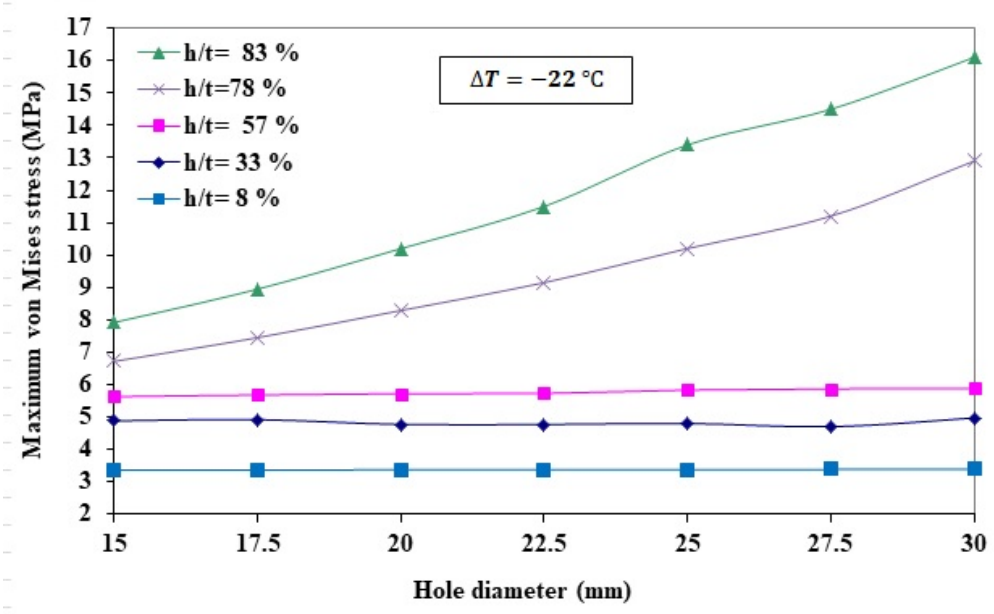

Working temperature (°C)		20	25	30	35	40	45	50
Allowable stress for PE80 (MPa)	C=2.0	4.00	3.75	3.50	3.20	3.00	2.80	2.60
	C=1.25	6.40	6.00	5.60	5.10	4.80	4.50	4.20

FIGURE 5.13: values of maximum von Mises stress in buried PE80 pipe material for several hole sizes and different hole depths subjected to a temperature drop of −22 °C.

pipe wall is very important, 3D brick-type SOLID95 elements, available in the ANSYS software package elements library, are well employed to model the physical medium. As mentioned previously, The SOLID95 element has three degrees of freedom at each node (translations in the x, y, and z coordinate directions) that makes it very suitable for solving curved boundary problems. Additionally, to have the best mesh control with a minimal number of finite elements and to reduce the computational time and costs, the hexahedral elements of the mapped (structured) finite element mesh which typically has a regular pattern, is performed to control the mesh efficiency. In this research we study the stress reduction effects on defected polyethylene gas pipes reinforced by polyethylene patches under sever thermo-mechanical loads for four various patch arrangements including semi-cylindrical, circular-partial, square-partial and saddle fusion patches to find the optimum patch shape. For the purpose of finding an appropriate patch shape and geometry, identical thickness (4.763 mm), inside diameter (114.3 mm) and material properties (PE 100) are considered for all patch types. It is assumed that the pipe and patch materials behave as linear elastic and have isotropic properties. Four typical pipe-patch arrangements including partial circular, partial square, saddle fusion and semi-cylindrical patches are illustrated in Figs. 5.14 (a), (b), (c) and (d) respectively. The length (or diameter) of patch was assumed to be identical and equal to 76 mm. The pipe cross section is illustrated in the middle of the figure which is the same for all

models. Additionally, medium density polyethylene pipe and high density polyethylene patch material mechanical properties are same as those presented in Table. 3.5.

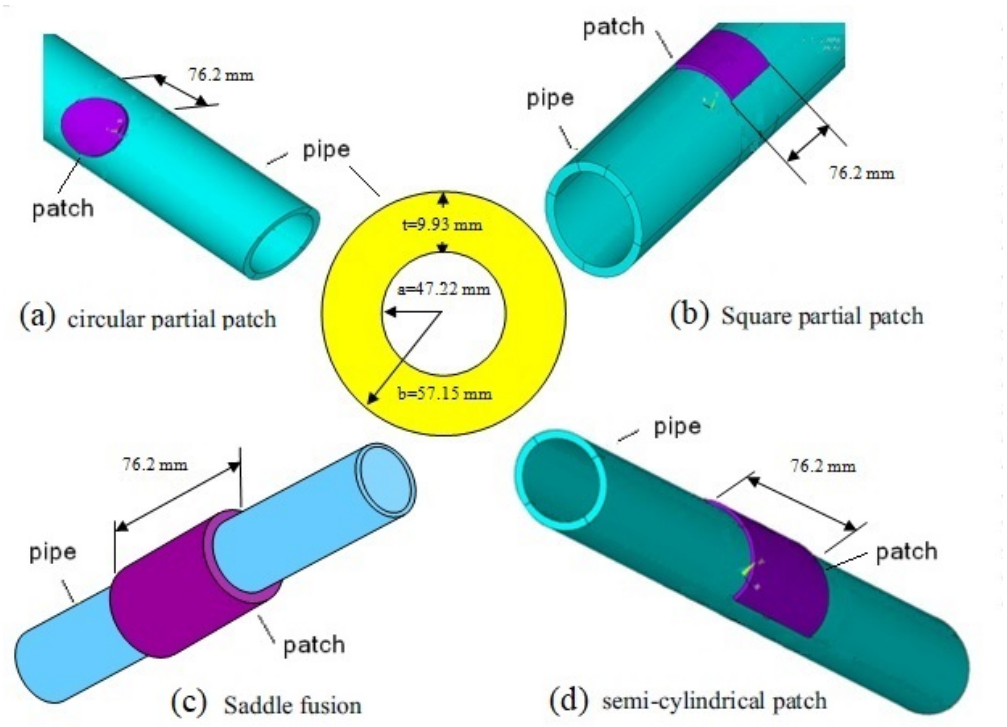

FIGURE 5.14: Three dimensional simulation of polyethylene pipe and patch arrangements, showing patch dimensions. Also, two dimensional view (dimensions in mm) of the cross section of the medium density polyethylene gas pipe is depicted [57]. (a) partial circular patch. (b) partial square patch. (c) saddle fused patch. (d) semi-cylindrical patch.

In the following section we extend and investigate the aforementioned complex models with more details by superimposing various thermal loads in the form of temperature variations to the mechanical loads including surcharge loads, soil column weight, soil-pipe interaction, and inside pressure of 4 bar imposed to the repaired defected polyethylene pipe buried under the ground and its patch. The trench dimensions and pipe surroundings are selected based on Fig. 5.15, Also, soil grades which are selected based on ASTM standards along with model dimensions are depicted on the computer simulation model in this figure. Fig. 5.15 (a), shows the expanded view of circular defect and repair patch.

5.4.1 Simultaneous Effects of Thermo-Mechanical Loads on Semi-Cylindrical Patch Arrangement

Fig. 5.16, shows the variations in the maximum values of von Mises stresses in the buried PE80 pipe that is repaired by a 76.2 mm long semi-cylindrical patch arrangement, versus defect size in the form of circular holes under simultaneous effects of mechanical loads

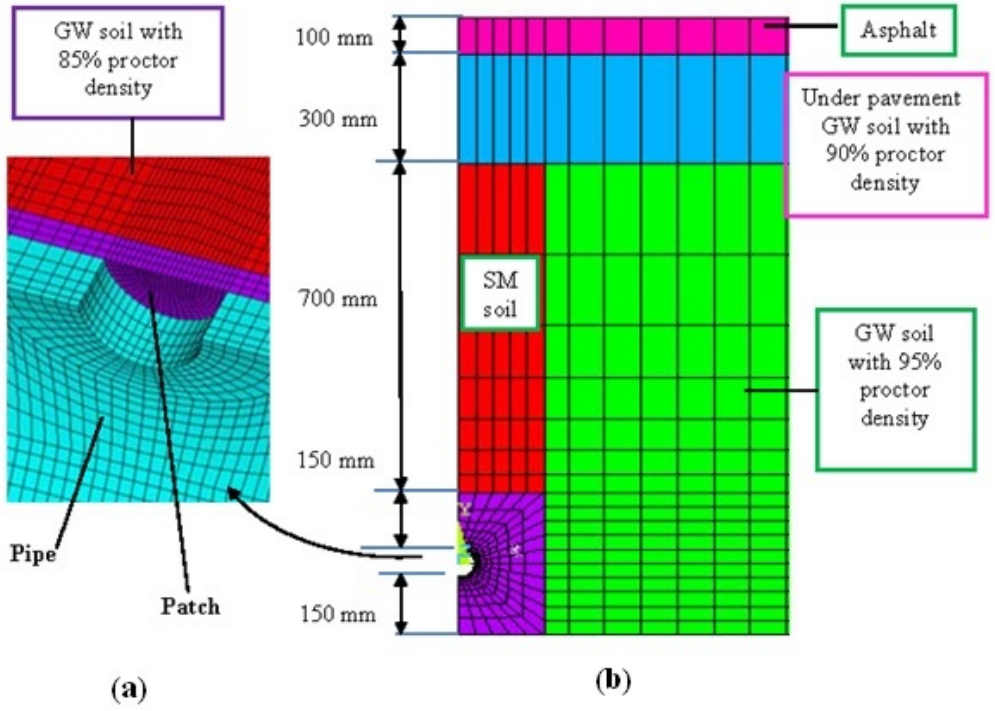

FIGURE 5.15: Three dimensional finite element model of the patched pipe with surrounding soil subjected to internal pressure. GW: Well-graded gravels; SM: Silty sand [146]. (a) Side view of full underground model. (b) expanded view to show defect and patch.

in the form of soil load, 4 bar internal pressure, vehicle wheel load and various thermal loads in the form of daily and seasonal temperature variations. The pipe material is medium density polyethylene (PE80), where the related strength of the pipe for several temperatures, based on a 50 years working life is also depicted on all figures. The reduced strengths are used due to the viscoelastic behavior of polyethylene material that occurs over the years of service. In order to show the effectiveness of proposed patch and compare the results, the values of maximum von Mises stress for the defected pipe before the application of patch repair (and with no temperature change) is also depicted which is upmost curve on this figure. The comparison of this curve with allowable stress value for a working life of 50 years shows that the imposed stresses in defected pipe are significantly higher than allowable stress values. For the other four curves which show the maximum von Mises stress values in the defected polyethylene pipe repaired by semi-cylindrical patch, the stress values are well below the results of unrepaired defected pipe. This means the aforementioned patch repair can strengthen the defected part of the pipe as well to transfer the gas fuel. Additionally, because of the reinforcement effect of patch, for the investigated defects at a constant temperature variation, the maximum von Mises stresses remain approximately constant even by increasing the hole size. The

curves for −22 °C, −15 °C, 0 °C (no temperature changes), +5 °C, and +22 °C temperature changes shows approximately similar trend with hole diameter increase where for these cases the maximum von Mises stresses are not increasing significantly for larger hole sizes. Generally stating, the maximum von Mises stress in the pipe increases for higher temperature increase. That means the patch is more effective in reinforcing defected pipe for lower temperature changes. For example, for a fixed hole diameter of 20 mm, the stress reduction percentage in the pipe wall are about 59%, 59%, 53%, 50%, and 42% for the temperature changes of−22 °C, −15 °C, 0 °C, +5 °C, and +22 °C respectively. Based on the results, among all investigated cases, maximum stress values are related to the seasonal temperature increase of +22 °C.

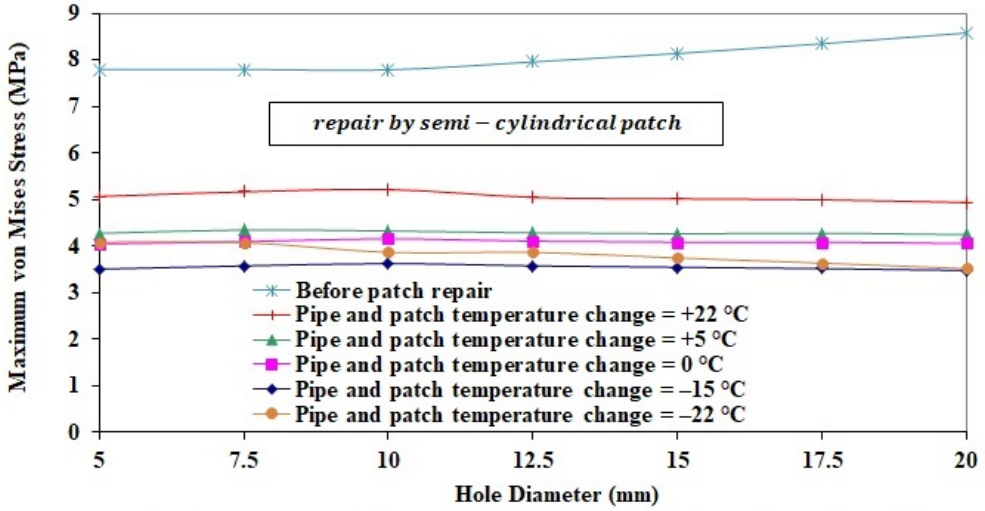

Working temperature (°C)		20	25	30	35	40	45	50
Allowable stress for PE80 (MPa)	C=2.0	4.00	3.75	3.50	3.20	3.00	2.80	2.60
	C=1.25	6.40	6.00	5.60	5.10	4.80	4.50	4.20

FIGURE 5.16: Maximum von Mises stress variations in the buried pipe for various sizes of circular hole defects repaired by semi-cylindrical patch (the simultaneous effect of soil load, internal pressure, vehicle wheel load and temperature variations).

After discussing peak stresses imposed to the pipe, we drive our attention to the patch itself. Therefore, stress distribution in the patch was visualized and the maximum stress values were recorded and plotted on some graphs. Fig. 5.17, presents maximum values of von Mises stresses in the 3" long semi-cylindrical patch arrangement versus pipe circular hole diameters under simultaneous effects of mechanical loads and various thermal loads in the form of daily and seasonal temperature variations. The patch material is high density polyethylene (PE100), where the related strength of the pipe for several temperatures, based on a 50 years working life is also depicted on all figures. Based on the obtained results, temperature variations have significant effect on the maximum von Mises stresses in the semi-cylindrical patch itself. The lowest curve on

this figure which shows the lowest values of maximum von Mises stresses belongs to the situation where no temperature change is imposed to the pipe and patch at the burial depth under the ground that means it is the case with the minimum valves of the induced maximum von Mises stresses compared to the other temperature changes. Additionally, the uppermost curve fits the data obtained for the maximum temperature change (+22 °C temperature increase, based on seasonal variations), which shows the case with highest values of induced maximum von Mises stresses among others. For the semi-cylindrical PE100 patch material it can be implied that higher temperature changes (both temperature increase and temperature decrease) impose higher maximum von Mises stresses to the patch itself. Also, for the cases of low temperature changes including 0 °C, +5 °C, the maximum von Mises stresses in the patch show an increase trend by increasing the pipe hole diameter, while for the cases of higher values of temperature changes including −15 °C, −22 °C, +22 °C, the maximum von Mises stresses will remain approximately constant even for larger hole diameters. According to the calculated results, semi-cylindrical patch can reinforce the proposed circular hole modeled defects efficiently. The only problem is that for higher temperature changes, the maximum von Mises stress values in the patch itself can be critical which requires more research and investigation on the other patch configurations.

5.4.2 Simultaneous Effects of Thermo-Mechanical Loads on Partial Circular Patch Arrangement

In this section in order to more investigate repair method and to find a proper patch, a circular partial patch arrangement is designed and its reinforcing effect on the damaged underground PE gas pipe is being studied. The results of the FE simulation in the form of variations in the maximum values of von Mises stresses in the buried PE80 pipe that is repaired by the circular partial patch arrangement, versus defect sizes in the form of circular hole under simultaneous effects of the previously mentioned mechanical loads and various thermal loads are depicted in Fig. 5.18. As mentioned previously, pipe material is medium density polyethylene (PE80), where the related strength of the pipe for several temperatures, based on a 50 years working life is also depicted on this figure.

Similar to the previous case, as expected the upmost curve is related to the values of maximum von Mises stresses for the defected pipe prior to partial-circular patch application and shows that for larger hole diameters, the maximum von Mises stress increases significantly. Based on the results of the other five presented curves which show the maximum von Mises stress in the defected polyethylene pipe repaired by circular-partial patch, the imposed stress values are significantly below the results of unrepaired defected pipe but comparing these curves with the table on the below of the figure which

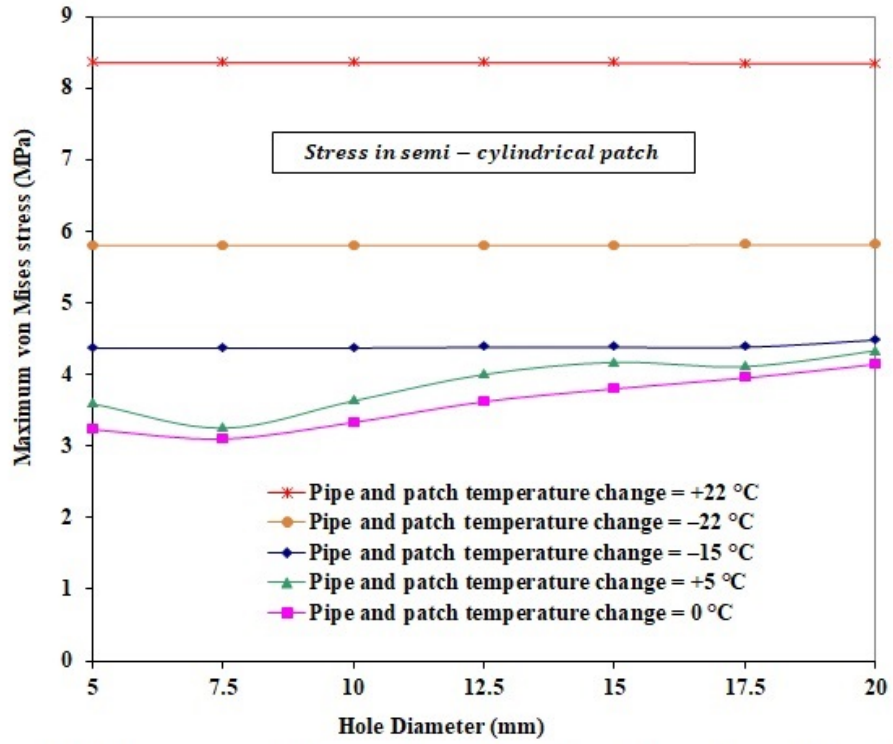

Working temperature (°C)		20	25	30	35	40	45	50
Allowable stress for PE100 (MPa)	C=2.0	5.00	4.70	4.35	4.00	3.65	3.30	3.00
	C=1.25	8.00	7.50	7.00	6.70	5.80	5.30	4.70

FIGURE 5.17: Maximum von Mises stress in the semi-cylindrical patch for various sizes of circular hole defects (the simultaneous effect of mechanical and thermal loads).

indicates allowable stress values, shows that they are slightly above the allowable stress values. Considering the case of 20 mm hole diameter, the stress reduction percentage in the pipe wall are 39%, 38%, 34%, 33%, and 31%, for the temperature changes of $-22\,^{\circ}\mathrm{C}$, $-15\,^{\circ}\mathrm{C}$, $0\,^{\circ}\mathrm{C}$, $+5\,^{\circ}\mathrm{C}$, and $+22\,^{\circ}\mathrm{C}$, respectively. The results imply that for the application of aforementioned patch repair to reinforce the damaged part of the pipe some stress relief mechanisms must be employed too. Additionally, for the investigated defects at a constant temperature variation, the maximum von Mises stresses remain approximately constant even by increasing the hole size. The curves for $-22\,^{\circ}\mathrm{C}$, $-15\,^{\circ}\mathrm{C}$, $0\,^{\circ}\mathrm{C}$, $+5\,^{\circ}\mathrm{C}$, and $+22\,^{\circ}\mathrm{C}$, temperature changes show approximately similar trend with hole diameter increase. The maximum stress values are related to the seasonal temperature increase of $+22\,^{\circ}\mathrm{C}$.

Additionally, maximum values of von Mises stresses in the circular partial patch arrangement versus pipe circular hole diameters under simultaneous effects of aforementioned mechanical loads and various thermal loads in the form of daily and seasonal temperature variations are presented in Fig. 5.19. Patch material is high density polyethylene (PE100), where the related strength of the patch for several temperatures, based on a

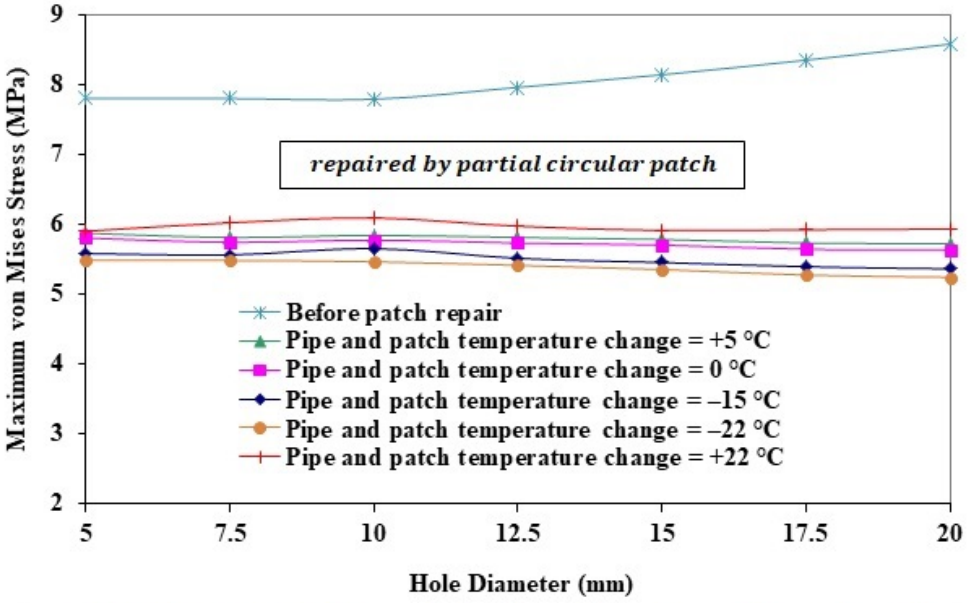

Working temperature (°C)		20	25	30	35	40	45	50
Allowable stress for PE80 (MPa)	C=2.0	4.00	3.75	3.50	3.20	3.00	2.80	2.60
	C=1.25	6.40	6.00	5.60	5.10	4.80	4.50	4.20

FIGURE 5.18: Maximum von Mises stress variations in the buried pipe for various size circular hole defects repaired by partial circular patch (the simultaneous effect of soil load, internal pressure, vehicle wheel load and temperature variations).

50 years working life is also depicted on this figure. According to the obtained results, the temperature variations have significant effect on the maximum von Mises stress variations in the circular partial patch. The lowest curve on the aforementioned figure belongs to the situation where no temperature change is imposed to the pipe and patch at the burial depth under the ground that means it is the case with the minimum valves of the induced maximum von Mises stresses. On the other hand, the uppermost curve fits the data obtained for the maximum temperature change (+22 °C, temperature decrease, based on seasonal variations), which shows the case with highest values of induced maximum von Mises stresses among others. For the partial-circular PE100 patch material it can be implied that higher temperature changes (both temperature increase and temperature decrease) impose higher maximum von Mises stresses.

For higher temperature changes, including a +22 °C, temperature increase and a −22 °C, temperature decrease, the maximum von Mises stresses are above the allowable stress which means applying circular partial patches in these areas cannot be suggested. For lower temperature changes including −15 °C, and +5 °C, the maximum von Mises stresses are well below the allowable stress limit, which means the circular partial patch is applicable in the areas with the temperature changes up to the mentioned values.

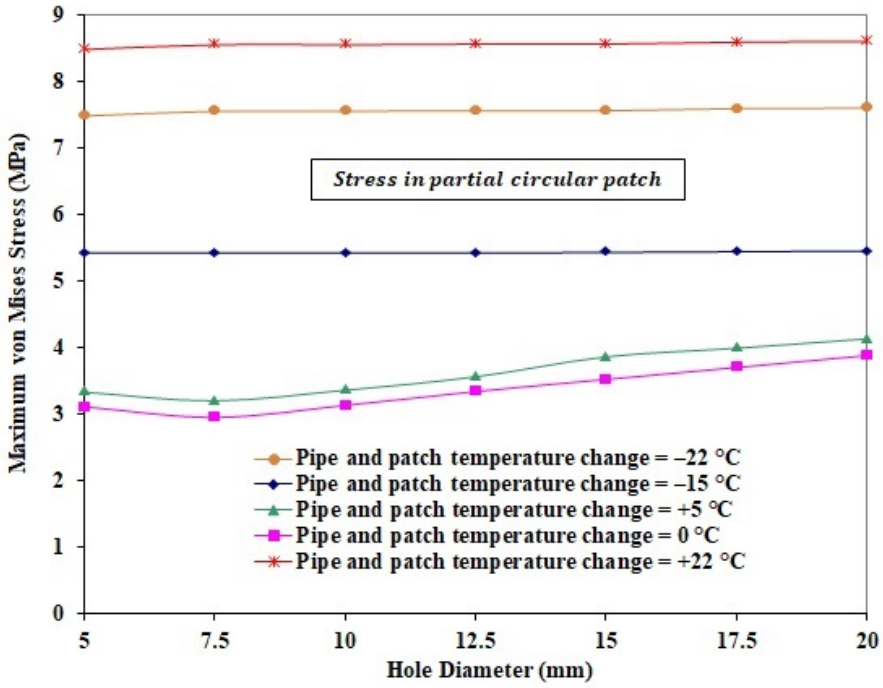

Working temperature (°C)		20	25	30	35	40	45	50
Allowable stress for PE100 (MPa)	C=2.0	5.00	4.70	4.35	4.00	3.65	3.30	3.00
	C=1.25	8.00	7.50	7.00	6.70	5.80	5.30	4.70

FIGURE 5.19: Maximum von Mises stress in the partial-circular patch for various sizes of circular hole defects (the simultaneous effect of mechanical and thermal loads).

5.4.3 Simultaneous Effects of Thermo-Mechanical Loads on Partial Square Patch Arrangement

The same procedure which was discussed for semi-cylindrical and partial circular patches in the two previous sections 5.4.1 and 5.4.2 respectively, is used to investigate partial square patch arrangement by finite element method. The results of Ansys simulation for the variations in the maximum values of von Mises stress in the buried PE80 pipe that is repaired by a partial square patch arrangement, versus defect size in the form of circular hole under simultaneous effects of mechanical loads in the form of soil load, 4 bar internal pressure, vehicle wheel load, and various thermal loads in the form of daily and seasonal temperature variations are depicted in Fig. 5.20.

Comparing the curves showing the results of maximum von Mises stress values for various temperature changes and the upmost curve which is related to the defected unrepaired pipe, shows that partial-square patch arrangement plays an important role in decreasing maximum stress values and strengthening the defected part of the pipe. For more understanding, considering the case of the 20 mm hole diameter, the results show the

stress reduction percentage in the pipe wall are 31%, 33%, 34%, 38%, 38%, for the temperature changes of −22 °C, −15 °C, 0 °C, +5 °C, and +22 °C, respectively, which shows that patch has more reinforcing effects for lower temperature changes. Even though, the partial-square patch has significant effect on reinforcing the defected pipe and decreasing the maximum von Mises stress values, but comparing the results with allowable stresses shows that the induced maximum von Mises stresses are slightly higher than allowable stress values. Therefore, if we decide to use this kind of patch, more researches should be conducted to obtain some stress relief mechanisms. Additionally, the curves show similar trends for different temperature changes. Furthermore, comparing these curves with the results obtained for partial-circular patch shows approximately similar trends between these two cases.

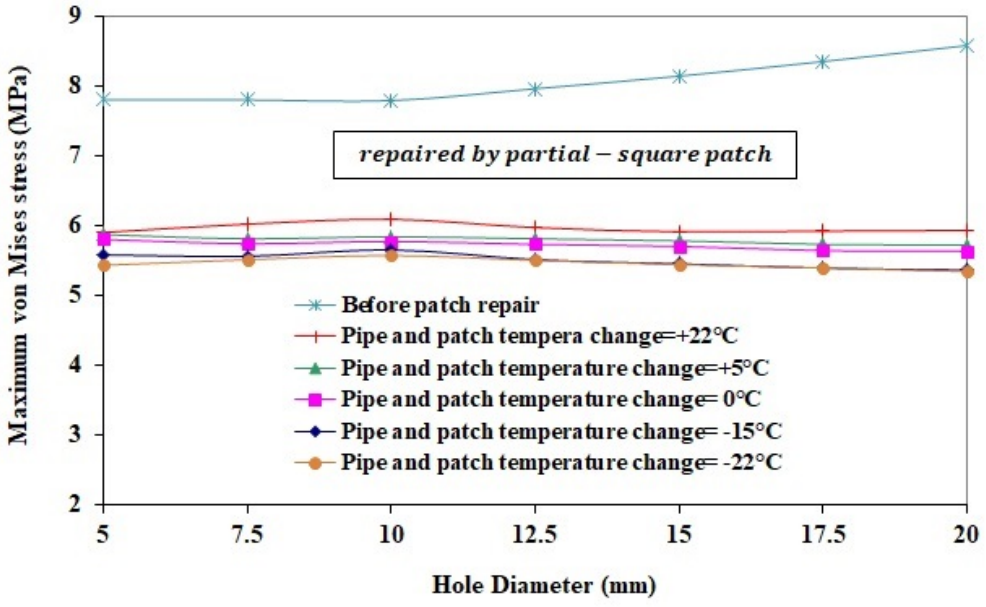

Working temperature (°C)		20	25	30	35	40	45	50
Allowable stress for PE80 (MPa)	C=2.0	4.00	3.75	3.50	3.20	3.00	2.80	2.60
	C=1.25	6.40	6.00	5.60	5.10	4.80	4.50	4.20

FIGURE 5.20: Maximum von Mises stress variations in the buried pipe for various sizes of circular hole defects repaired by partial square patch (the simultaneous effect of soil load, internal pressure, vehicle wheel load and temperature variations).

Additionally, the maximum values of von Mises stress in the square partial patch arrangement versus pipe circular hole diameter under simultaneous effects of aforementioned mechanical loads and various thermal loads in the form of daily and seasonal temperature variations are presented in Fig. 5.21. As can be implied, the temperature variations have a significant effect on the variation of the maximum von Mises stresses in the partial

square patch. The lowest curve on this figure belongs to the situation where no temperature change is imposed to the pipe and patch at the burial depth under the ground that means it is the case with the minimum valves of the induced maximum von Mises stresses. Furthermore, uppermost curve fits the data obtained for the maximum temperature change (+22 °C temperature increase, based on seasonal variations), which shows the case with highest values of induced maximum von Mises stresses among others. It is clear that for low temperature changes, including 0 °C and +5 °C, the maximum von Mises stresses in the patch increases for larger hole diameters. For higher temperature changes including −15 °C, −22 °C and +22 °C, the results will remain approximately constant even by increasing hole diameter. For the square partial PE100 patch material it can be implied that higher temperature changes (both temperature increase and temperature decrease) impose higher maximum von Mises stresses. The curves showing the data of patch stress results are below the allowable stress of the patch material except for the case of 22 °C, temperature changes (both temperature rise and drop).

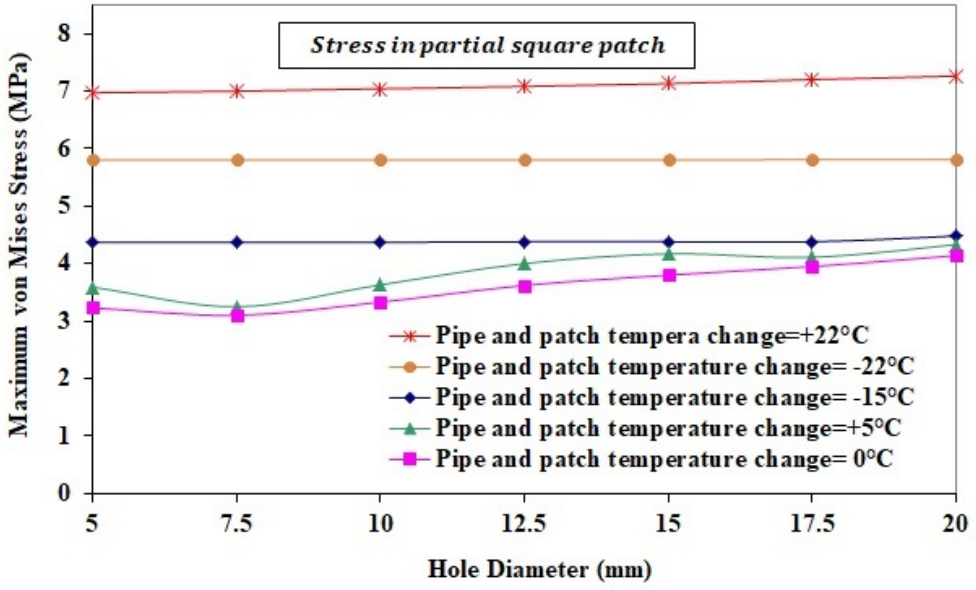

Working temperature (°C)		20	25	30	35	40	45	50
Allowable stress for PE100 (MPa)	C=2.0	5.00	4.70	4.35	4.00	3.65	3.30	3.00
	C=1.25	8.00	7.50	7.00	6.70	5.80	5.30	4.70

FIGURE 5.21: Maximum von Mises stress in the square partial patch for various sizes of circular hole defects (the simultaneous effect of mechanical and thermal loads).

5.4.4 Simultaneous Effects of Thermo-Mechanical Loads on Saddle Fusion Patch Arrangement

In the previous parts, three patch repair configurations were introduced and discussed in details. Finite element solutions for investigating the stress distribution in the aforementioned patch repairs to find the effectiveness of the proposed patch arrangements gave us the knowledge that semi-cylindrical patch configuration is more effective than partial square and circular patches in reinforcement of the defected part of the pipe. For the sake of finding a more reliable patch configuration we decide to investigate a full-cylindrical (called saddle fusion) patch repair. Fig. 5.22 shows the variations in the maximum values of von Mises stresses in the buried PE80 pipe that is repaired by a saddle fusion PE100 patch arrangement, versus defect size in the form of circular hole under simultaneous effects of mechanical loads in the form of soil load, 4 bar internal pressure, vehicle wheel load, and various thermal loads in the form of daily and seasonal temperature variations. Comparison of the curves resulted from saddle fusion patch repair for various temperature changes of $-22\,^{\circ}\mathrm{C}$, $-15\,^{\circ}\mathrm{C}$, $0\,^{\circ}\mathrm{C}$, $+5\,^{\circ}\mathrm{C}$, and $+22\,^{\circ}\mathrm{C}$, with the upmost curve which shows the maximum von Mises stress values for defected pipe before repair (under the simultaneous effect of aforementioned loads except thermal loads because temperature changes supposed to be zero in this case), shows that the saddle fusion patch repair effectively reinforces the damaged part of the pipe to reliably transfer natural gas. Additionally, comparing the mentioned five curves with the allowable stress values for PE80 pipe material shows that the maximum von Mises stress values are below the allowable stress for some cases. For more clarification considering the case of 20 mm hole diameter, the results show stress reduction percentage in the pipe wall are 60%, 57%, 52%, 50%, 43%, for the temperature changes of $-22\,^{\circ}\mathrm{C}$, $-15\,^{\circ}\mathrm{C}$, $0\,^{\circ}\mathrm{C}$, $+5\,^{\circ}\mathrm{C}$, and $+22\,^{\circ}\mathrm{C}$, respectively. All the five curves show similar trends.

Fig. 5.23, presents maximum values of von Mises stresses in the 3 inch long, saddle fusion patch arrangement versus pipe circular hole diameter under simultaneous effects of previously mentioned mechanical and various discussed thermal loads. The obtained results show that, the temperature variations have significant effect on the maximum von Mises stresses in the saddle fusion patch. Similar to the 3 previously discussed patch arrangements the lowest curve on this figure, belongs to the situation where no temperature change is imposed to the pipe and patch at the burial depth under the ground that means it is the case with the minimum valves of the induced maximum von Mises stresses. Additionally, the uppermost curve fits the data obtained for the maximum temperature change ($+22\,^{\circ}\mathrm{C}$ temperature increase, based on seasonal variations), which shows the case with highest values of induced maximum von Mises stresses among

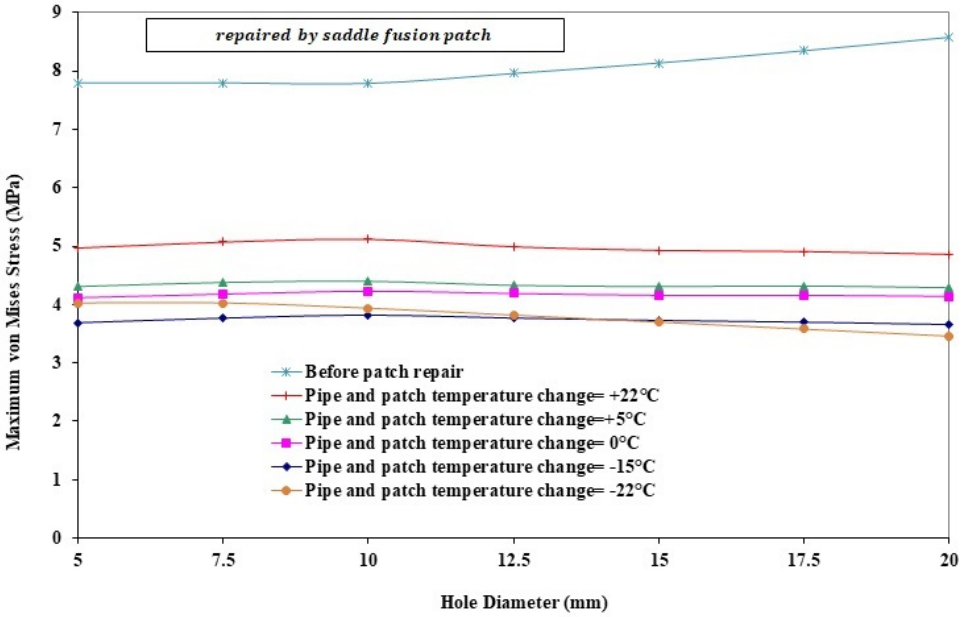

Working temperature (°C)		20	25	30	35	40	45	50
Allowable stress for PE80 (MPa)	C=2.0	4.00	3.75	3.50	3.20	3.00	2.80	2.60
	C=1.25	6.40	6.00	5.60	5.10	4.80	4.50	4.20

FIGURE 5.22: Maximum von Mises stress variations in the buried pipe for various sizes of circular hole defects repaired by saddle fusion patch (the simultaneous effect of soil load, internal pressure, vehicle wheel load and temperature variations).

others. For the saddle fusion PE100 patch material it can be implied that higher temperature changes (both temperature increase and temperature decrease) impose higher maximum von Mises stresses. For studied cases, the maximum von Mises stresses are compared to the allowable stress limit for PE100 material which can show if the saddle fusion patch is applicable to repair the proposed defects in even hot areas. Therefore, the results show the application of 3" saddle fusion patch is advisable for the proposed loading condition.

5.4.5 Conclusion of Patch Arrangements

In this research an uncomplicated and practical computational simulation is proposed to solve real industrial fully three dimensional complex problems of large bureid gas pipelines. The finite element method is employed to estimate maximum stress values in buried gas pipelines imposed to thermal and mechanical loads and stress concentrations due to variations in the geometery. The simultaneus effects of thermal and mechanical loads on maximum stress values in patch repaired undergroud pipes are well studied. For this purpose, in this reseach, 3D finite element modeling of buried gas pipe and its patch is perfomed using ANSYS software. Stress variations in the buried MDPE gas pipe and

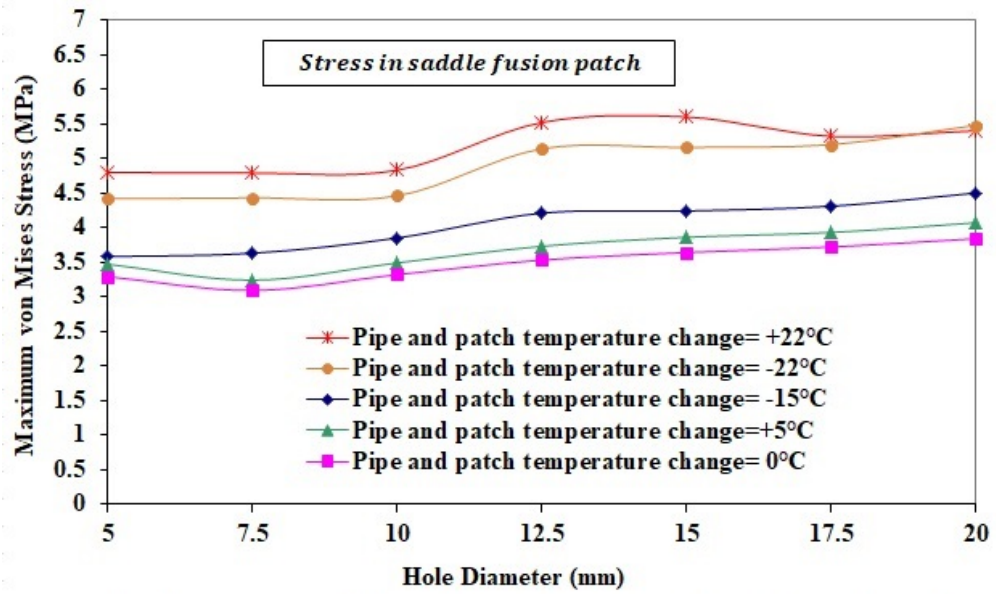

Working temperature (°C)		20	25	30	35	40	45	50
Allowable stress for PE100 (MPa)	C=2.0	5.00	4.70	4.35	4.00	3.65	3.30	3.00
	C=1.25	8.00	7.50	7.00	6.70	5.80	5.30	4.70

FIGURE 5.23: Maximum von Mises stress in the saddle fusion patch for various sizes of circular hole defects (the simultaneous effect of mechanical and thermal loads).

HDPE repair patch were fully studied in hot climate region to estimate the critical stress values caused by stress concentrations at the pipe and patch, enabling us to find the applicable method for repairing MDPE gas transportation pipeline in such areas. The optimum burial depth was found to be 1.25 m, while the maximum and minimum ground surface temperatures at this depth were calculated to be 35 °C and 13 °C, respectively. Furthermore, the soil column weight above the pipe, the surcharge loads in terms of traffic load, the gas pressure of 4 bar inside the pipe and the stress concentrations due to a local change in geometry (in the form of damage) were imposed on the pipe and its patch resulting in the following conclusions: By considering the obtained plots for stress values in buried pipe and its socket and comparing it with allowable stress values for the pipe, the correct joining method can be investigated. Based on the results for the problem of the patch repaired buried pipes, the results show that all four patch configurations have significant reinforcing effect on the defected section of the buried pipe under the aforementioned thermo-mechanical loads. Meanwhile, the maximum von Mises stresses in both pipe and saddle fusion patch are below than allowable stress limit for polyethylene material which means the saddle fusion patch is applicable to repair the proposed defects in even hot areas. Therefore, the results show the application of introduced saddle fusion patch is advisable for the proposed loading condition.

Chapter 6

Mechanical Properties of Graphene-like BC_3; A Molecular Dynamics Study

6.1 Introduction

The focus of this chapter is computational predictions of the mechanical behavior of graphene-like BC_3 films via molecular dynamics calculations, since these properties have not been totally explored yet. Defects in materials will always form due to the fact that all processes are almost always far from equilibrium. Also, engineering structures may be defected during their lifetime for several reasons. These defects can significantly decrease the ultimate tensile strength of the material. Therefore, an understanding of the fracture mechanisms and investigating the mechanical properties of materials in the presence of various defects such as cracks and notches plays an important role in materials design [147–152]. To our best knowledge, the behavior of hexagonal 2D graphene-like BC_3 material under the effect of different temperatures and in the presence of defects has not been computationally estimated yet. In the present contribution, we estimate the physical properties and thermo-mechanical responses of BC_3 monolayers, not only in pristine form but we also study models containing cracks and notch shaped defects by carrying out uniaxial tensile simulations. We predict the crack and notch propagation in two-dimensional (2D) materials for several crack lengths and notch diameters and at temperatures from 200 K to 900 K. The location of the crack and notch shaped defects which are assumed to be in the middle of nanosheet are depicted in Fig. 6.1. In this figure, L is the length of the nanosheet and N is a variable which is assumed to be 2, 3,

6 and 12 in this study.

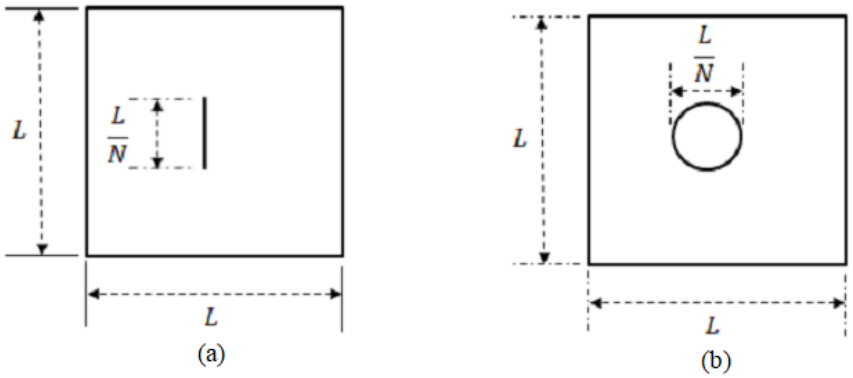

FIGURE 6.1: The defect shapes and location which is supposed to be in the middle of the square nanosheet. a) Crack shaped defect. b) Notch shaped defect.

6.2 Molecular dynamics modeling

Classical molecular dynamics simulations are employed as an alternative of experimental studies to investigate the mechanical properties of pristine graphene-like BC_3 nanosheets and also with different cracks and notches. All molecular dynamics modeling in this study were carried out using open-source software LAMMPS (Large-Scale Atomic/-Molecular Massively Parallel Simulator) [8]. It should be considered that the mechanical properties obtained by molecular dynamics simulations strongly depend on the selection of suitable loading conditions, boundary conditions and interatomic potentials. In order to determine the bonding interactions between carbon-carbon atoms, we employed the optimized Tersoff potential proposed by Lindsay [9]. Furthermore, the Tersoff potential parameters used to introduce the bonding interactions between the boron-carbon atoms were adopted from Kinaci et al. [10]. These interatomic potential files have been successfully and extensively used for modeling thermal and mechanical properties of pristine graphene [153], N and B doped graphene [74, 154], defective graphene [155, 156] and other 2D carbon based lattices like C_3N [157], C_3N_4 [158] and B/N–graphdiyne [159]. The post-processing was done with the open-source visualization software OVITO [160]. The computed stresses, strains, and the atomic locations via the uniaxial tension were recorded. Fig. 6.2, illustrates the top-view of the single layer graphene-like BC_3. Each boron atom is located between three carbon atoms in a hexagonal network via strong polar covalent bonds. This structure is similar to the graphene structure and one can assume the boron atoms are doped in the graphene structure and fill the location of

carbon atoms in defect-free graphene.

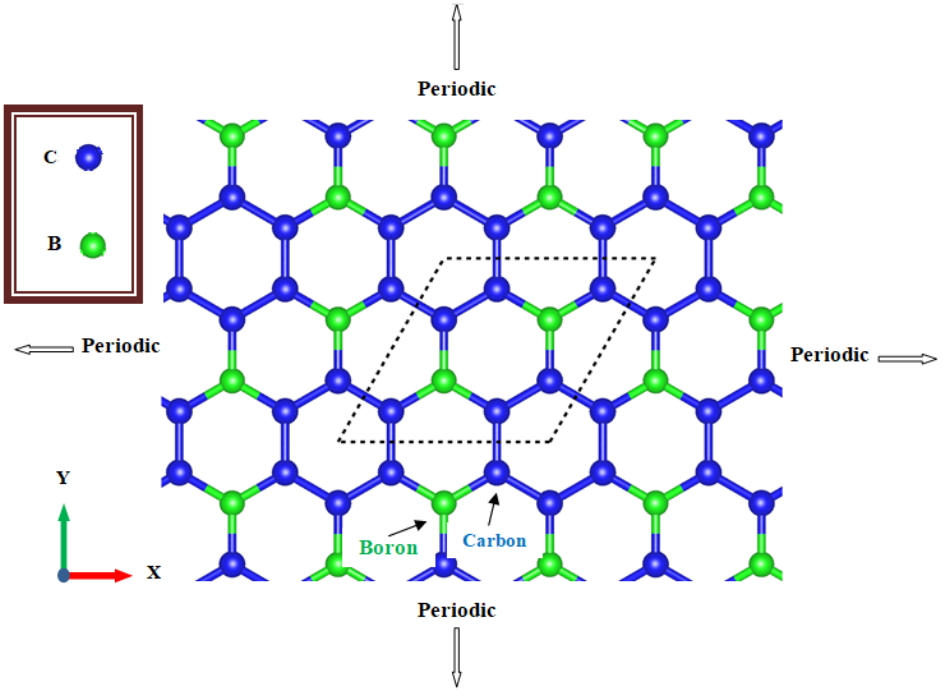

FIGURE 6.2: Top view of the BC_3 atomic configuration with a honeycomb structure comprising both carbon and boron atoms. Each boron atom is surrounded by three carbon atoms. Blue and green balls in the model represent the C and B atoms. The unit cell (dashed line) is shown in the structure of graphene-like BC_3 nanosheets that contains two boron atoms and six carbon atoms.

As graphene, monolayer BC_3 nanosheets have two principal orientations, i.e. the armchair and zigzag direction. According to Fig. 6.2, the zigzag and armchair directions are along the X and Y directions, respectively. In this research, first we explored the mechanical properties of pristine BC_3 nanosheets loaded under uniaxial tension. Then, in order to evaluate the anisotropy in the mechanical responses and to assess the effect of the loading direction, we performed uniaxial simulations along both zigzag and armchair orientations. Then the effect of cracks and notches on mechanical properties of the material was investigated. The computer models were created for a nanosheet simulation box consisting of 34,020 individual atoms. The boundary conditions are periodic along the in-plane directions. Thus, these simulations are representative of a graphene-like BC_3 nanosheet with infinite planar dimensions. Initially, the computational box was relaxed by means of the Nose-Hoover barostat and thermostat (NPT) approach to get a stress free condition. Then, an engineering strain rate of 10^8 s^{-1} was applied and a small time step size (time increment) of 0.25 fs was adopted for all calculations in the MD simulations. Also, we tested lower and higher strain rates of 10^7 and 10^9 s^{-1} and compared the results. For preventing the void formation throughout the simulation,

we rescaled the atomic positions according to the simulation box size dimensions. The stress values were determined using the Virial theorem at every time step [161]. Uniaxial loading condition were applied such that the periodic simulation box through the structure width was arranged by employing the NPT method to guarantee infinitesimal stresses in this direction [162, 163].The modified Tersoff potential used to reduce the computational complexity is given by Eq. (6.1) as follow [164]:

$$E = \frac{1}{2}\sum_{i}\sum_{i\neq j} f_C(r_{ij})[f_R(r_{ij}) + b_{ij} f_A(r_{ij})], \tag{6.1}$$

in which r_{ij} denotes the position vector between i and j atoms. The range of potential is limited by cutoff function f_C. f_A and f_R are attractive and repulsive pair potentials, respectively and b_{ij} is bound function. These functions are estimated by equations (6.2) to (6.6) as follow:

$$f_C(r_{ij}) = \begin{cases} 1, & r_{ij} < (D_i D_j)^{\frac{1}{2}}, \\ \frac{1}{2} + \frac{1}{2}cos(\pi \frac{r_{ij}-D_{ij}}{R_{ij}-D_{ij}}), & (D_i D_j)^{\frac{1}{2}} < r_{ij} < (R_i R_j)^{\frac{1}{2}}, \\ 0, & r_{ij} > (R_i R_j)^{\frac{1}{2}} \end{cases} \tag{6.2}$$

$$f_R(r_{ij}) = (A_i A_j)^{\frac{1}{2}} exp(-(\frac{\lambda_i^I + \lambda_j^I}{2})r_{ij}), \tag{6.3}$$

$$f_A(r_{ij}) = -B'_{ij} exp(-(\frac{\lambda_i^{II} + \lambda_j^{II}}{2})r_{ij}),\ B'_{ij} = (B_i B_j)^{\frac{1}{2}}\chi_{ij}, \tag{6.4}$$

$$b_{ij} = \left(1 + \beta_i^{n_i}\xi_{ij}^{n_i}\right)^{-\frac{1}{2n_i}},\ \xi_{ij} = \sum_{k\neq i,j} f_C(r_{ik}) g(\theta_{ijk}), \tag{6.5}$$

$$g(\theta_{ijk}) = \left(1 + \frac{c_i^2}{d_i^2} - \frac{c_i^2}{[d_i^2 + (cos\theta_{ijk} - h_i)^2]}\right), \tag{6.6}$$

In equations (6.5) and (6.6), the lower index k also marks an atom where i-j bond is modified by a third atom k. In Eq. (6.4), the parameter χ_{ij} was employed as a fitting parameter. The parameters of the Tersoff potential are presented in Table 6.1 as below.

TABLE 6.1: Parameters of modified Tersoff potential of BC_3 interatomic bonds.

Parameter	**B-B-B [10]**	**C-C-C [9]**	**C-B-B [10]**
A (eV)	40.0520156	1393.6	1386.78
B' (eV)	43.132016	430.00	339.068910
$\lambda^I(\mathring{A}^{-1})$	2.2372578	3.4879	3.5279
$\lambda^{II}(\mathring{A}^{-1})$	2.0774982	2.2119	2.2054
R ($\mathring{A}$)	2.0	2.05	1.95
D ($\mathring{A}$)	0.10	0.05	0.10
$\beta(10^{-7})$	16	1.572	1.5724
m	3.0	3.0	3.0
n	3.9929061	0.72751	0.72751
γ	1.0	1.0	1.0
c	0.52629	3.8049e4	3.8049e4
d	0.001587	4.3484	4.3484
cosθ	0.5	-0.93	-0.93

It is worthy to note that, in order to create a line crack in the nanosheet model, firstly two regions were created at the left and the right sides of the crack location so that the coincident edges of the regions to fall on the crack location, as depicted in Fig. 6.3. Then the interaction between atoms located at this edge was restricted by using the "neigh- modify" command which is defined in LAMMPS code. We believe that the crack created by this method, can model the real physical problem more realistic than the other crack models.

6.3 Results and discussion

In the present research, first the molecular model and the applicability of the employed tersoff potentials were verified by comparison with density functional theory (DFT) calculations of Mortazavi et al. [80]. At a temperature of 2 K, 2D graphene-like BC_3 nanosheet showed a Young's modulus (E) of 799.43 GPa in armchair direction and 815.02 GPa in zigzag orientation. These results show that our molecular dynamic simulations overestimate the modulus of elasticity around 2.96 % and 4.81 % in armchair and zigzag orientations, respectively. Then, a defect-free BC_3 nanosheet with dimensions of 300×300 $\mathring{A}$ was employed to investigate the effect of temperature (200, 300, 400, 500,

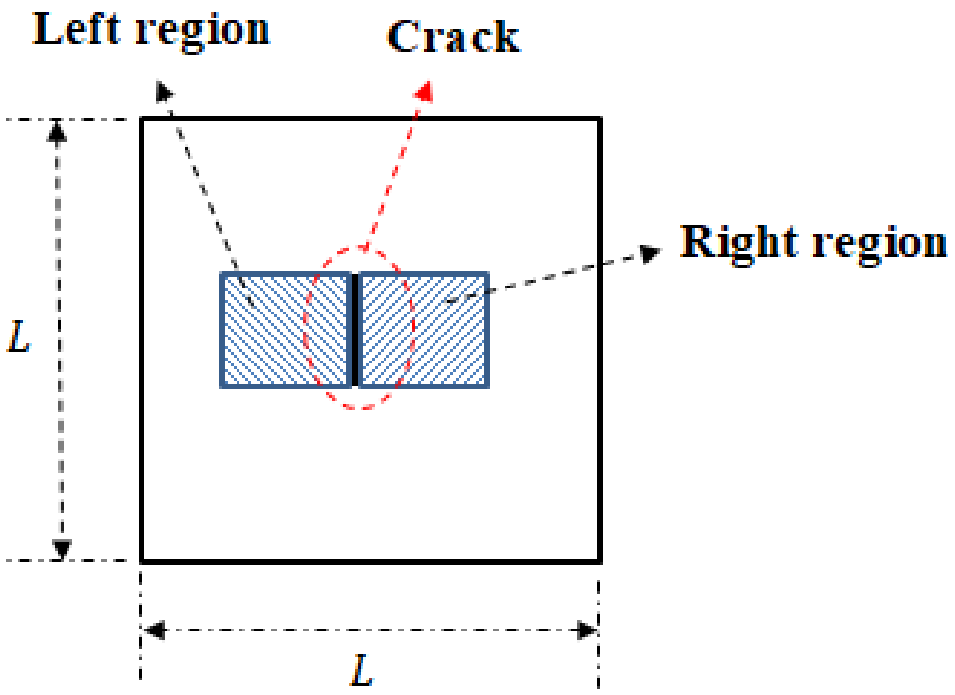

FIGURE 6.3: Defining two regions to create a line crack in the nanosheet model.

600, 700 and 900 K). Then we tested the effect of crack and notch shape defects on the aforementioned graphene-like BC_3 monolayer. To simulate the mechanical properties of large-area and single-layer BC_3, we used periodic boundary conditions in planar Cartesian directions. Otherwise, the free atoms on the edge may influence the estimated mechanical properties. Once the applied periodic boundary conditions (PBCs) in all planar directions and a large super-cell were established, the obtained results were found to be size independent. The models were loaded in tension in both armchair and zigzag orientations and the extracted uniaxial stress-strain results for pristine and defective graphene-like BC_3 nanosheets are depicted on several graphs. It worth mentioning that in the calculation of stresses, we choose the structure volume using a thickness of 3.3 $\AA$ [74, 155, 157] for the single layer BC_3 sheet.

6.3.1 Temperature effects

In this section, we investigate the influence of several temperatures on the mechanical behavior of pristine graphene-like BC_3 nanosheets. The extracted uniaxial stress-strain responses predicted by MD calculations for pristine graphene-like BC_3 nanosheets loaded in armchair orientation at 200, 300, 500, 700 and 900 K are depicted in Fig. 6.4. Further, the acquired results for aforementioned defect-free material loaded in zigzag orientation at 200, 300, 400, 500 and 600 K have plotted in Fig. 6.5. The MD results illustrated in

Figs. 6.4 and 6.5 show that increasing the temperature will decrease the ultimate tensile strength and strain-to-failure of the nanosheet. Distances between the neighbors atoms increase by raising temperature, decreasing the atoms interaction energy. Therefore, the tensile strength has a tendency to decrease as the temperature increases. A slight decrease in the elasticity modulus is observed at higher temperatures. The factors that affect the interatomic spacing and forces between atomic bands (like temperature) will also affect the modulus of elasticity of material. Because the binding energy between atoms decreases as the temperature increases, it can be seen that young's modulus of BC_3 sheets decreases with increasing temperature. Also, the kinetic energy is transferred into strain energy through the deformation during tensile loading. Therefore, increasing the temperature decreases strain energy because of the increasing kinetic energy. This results in the decrease of strain to failure for a higher temperature condition [165]. According to Fig. 6.4, for a BC_3 monolayer loaded in armchair direction, at room temperature (300 K), the ultimate stress is 116.554 GPa at a strain-to-failure of 0.21445. The tensile stress is 73.465 GPa when the temperature is increased to 900 K which is 37 % lower than the ultimate stress at 300 K. The maximum tensile stress occurs at 200 K at a strain of 0.227 which is 120.114 GPa while the strain-to-failure at highest simulated temperature is 0.121, which is about 46.7 37 % less than the maximum strain at 200 K. With respect to Fig. 6.5, for a BC_3 monolayer loaded in zigzag direction, at 300 K, the ultimate stress is 122.009 GPa at a strain-to-failure of 0.20775. When the temperature is increased to 600 K, the tensile strength is 75.592 GPa which is 45.8 % lower than the ultimate stress at 200K. The maximum tensile stress happens at 200 K which is 139.34 GPa at a strain rate of 0.23495. The elevation of temperature will cause the nanosheet to elongate less compared to sheets at room temperature, since the molecules have less molecular motion.

According to figures 6.4 and 6.5, for all studied cases, the initial portion of each stress-strain graph is theoretically a straight line, which means the relation between stress and strain is linear. The modulus of elasticity of the material can be estimated through the slope at this zone. As the values of the Young's modulus (E) reveal the particular importance in material properties and especially for micro/nano-electromechanical systems, therefore, in this section, Young's modulus (E) at aforementioned temperatures for BC_3 nanosheets in armchair and zigzag orientations are estimated and presented in tables 6.6 and 6.3 respectively. For estimating the Young's modulus we used the strain value of 0.04 to consider a specific zone and fit a curve at initial part. According to the results of tables 6.6 and 6.3, the lower modulus of elasticity (E) occurs at higher temperatures. Note that at atomic length scales, the Young's modulus is related to the chemical bonds which are weakened at elevated temperatures. Following the linear part,

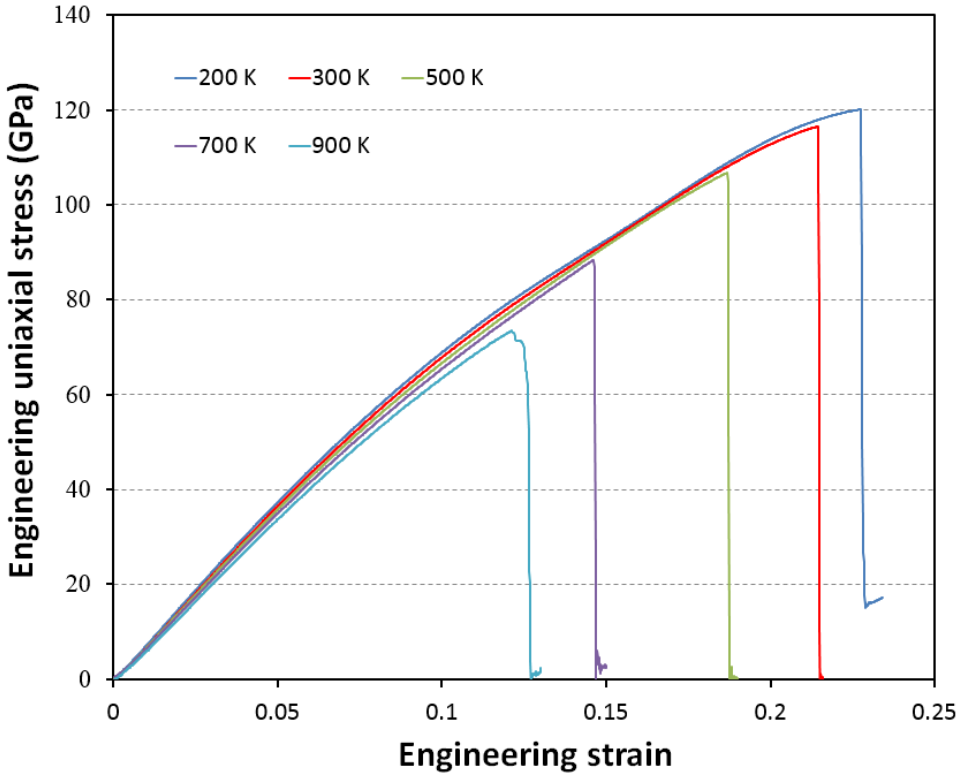

FIGURE 6.4: Calculated uniaxial tensile stress-strain response of the defect-free and single-layer graphene-like BC_3 films in armchair orientation under the effect of various temperatures including 200, 300, 500, 700 and 900 K.

there is the nonlinear region until fracture of the nanosheet.

TABLE 6.2: Young's modulus (E) of the pristine BC_3 nanosheet in armchair orientation at the 200, 300, 500, 700 and 900 K.

T (K)	200	300	500	700	900
E (GPa)	767.77	755	736.02	714.05	697.72

TABLE 6.3: Young's modulus (E) of the pristine BC_3 nanosheet in zigzag orientation at the 200, 300, 400, 500 and 600 K.

T (K)	200	300	400	500	600
E (GPa)	768.33	762.37	758.49	747.26	741.01

The uniaxial tension simulation results for defect-free nanosheets in armchair orientation at room temperature (300 K) show that the tensile strength of 2D graphene-like BC_3 film is slightly lower than the values obtained for graphene and C_3N. That means molecular dynamics models yield tensile strengths of 132 GPa for pristine graphene [157] and 128 GPa for pristine C_3N [3], which are 13.3 % and 9.8 % higher than the values we obtained for BC_3. Following the linear portion, a nonlinear trend is observed up to the ultimate tensile strength point. At this point the single-layer material indicates its maximum

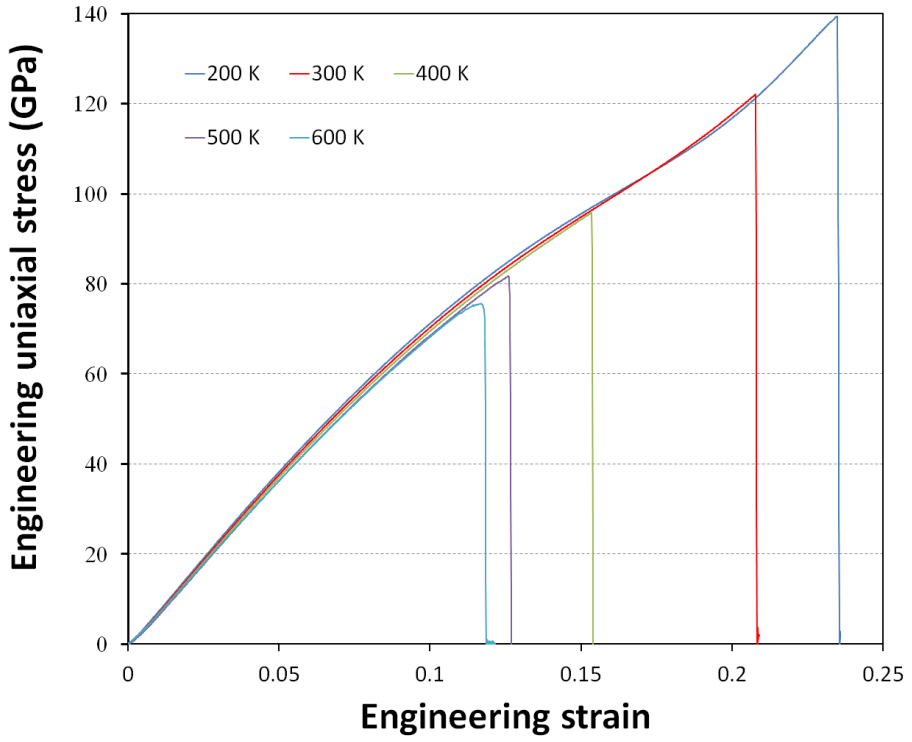

FIGURE 6.5: Calculated uniaxial tensile stress-strain response of the defect-free and single-layer graphene-like BC_3 films in zigzag orientation under the effect of various temperatures including 200, 300, 400, 500 and 600 K.

load bearing ability and then the stress reduces until the material failure. Our obtained results in Fig. 6.4 and Fig. 6.5, reveal that for studied sheets at high temperatures, the films along the zigzag direction can indicate higher strengths, while at low temperatures the sheets along armchair direction can show higher tensile strengths with respect to loading. Nonetheless, the differences between the results of armchair and zigzag directions are not very remarkable. Comparing the results presented in tables 6.6 and 6.3, shows that the elastic modulus of the considered structure stretched along the zigzag direction are generally higher than those stretched along the armchair direction. This behavior of the 2D graphene-like BC_3 structure can be translated into higher ductility in the zigzag direction.

6.3.2 Strain rate effects

In this section we study the effect of several strain rates on the mechanical properties of the graphene-like BC_3 monolayers. Figs. 6.6 (a) and (b) illustrates the ultimate tensile strength of crystalline carbon bromide sheets as a function of strain rate at different

temperatures in armchair and zigzag orientations, respectively. As the strain rate increases, the ultimate tensile strength indicates an increasing trend. However, the strain rate effect on the tensile strength of graphehe-like BC_3, nanosheet in zigzag orientation is more significant than the armchair orientation.

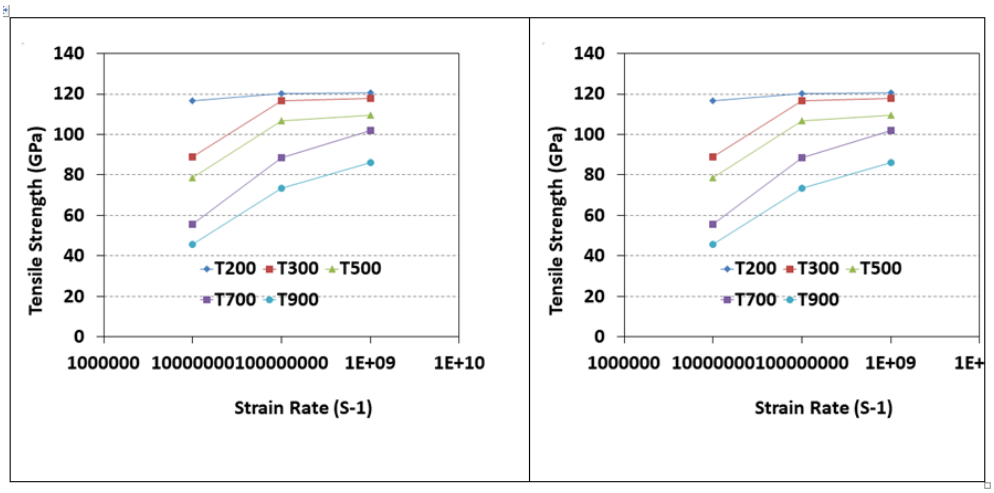

FIGURE 6.6: Ultimate tensile strength of defect-free and single-layer graphene-like BC_3 as a function of strain rate in armchair and zigzag orientations are shown in (a) and (b), respectively.

6.3.3 Crack effects

The propagation of cracks is influenced by the crack orientation [166]. Subsequently, we investigate cracks wherein the imposed loading is perpendicular to the crack orientation. As described in the introduction, to construct the models subjected to cracks, we use disconnected interatomic bonds for the atoms located at both sides of the crack. Several crack lengths including L/12, L/6, L/3 and L/2 are examined, in which L is the length of one side of the square graphene-like BC_3 monolayers. Fig. 6.7 shows maximum tensile stress values after applying tensile loads at different temperatures. The MD solutions for the cracked models are compared with the data for crack-free graphene-like BC_3 nanosheets (0L). Obviously, the cracks significantly decrease the tensile strength of two dimensional BC_3 material. As expected, tensile strength decreases with increasing crack length. Furthermore, the temperature increase has a weakening effect on the ultimate tensile strength of the two dimensional graphene-like BC_3 material.

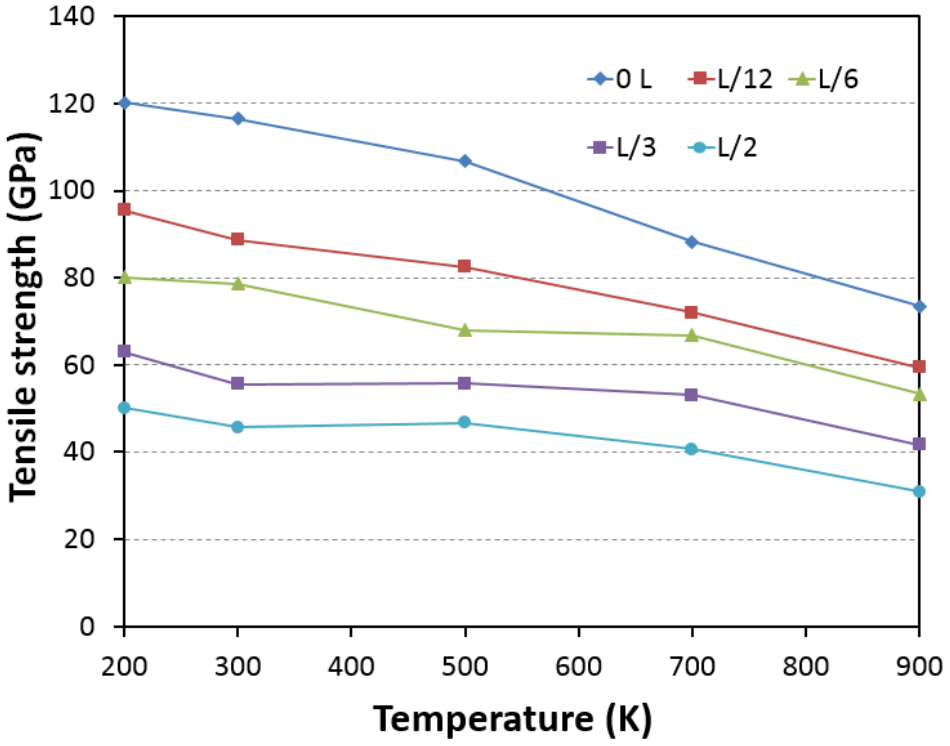

FIGURE 6.7: Ultimate tensile strength of single-layer graphene-like BC_3 sheet including several cracks with different lengths which imposed to a range of temperature from 200 K to 900 K.

Strain at ultimate tensile strength point is also a principal parameter which describes how much the nanosheet material can be stretched prior to losing its load bearing capability because of the structural changes stemming from the uniaxial deformation. Strains-at-failure are plotted in Fig. 6.8 and the values obtained for pristine sheets are significantly higher compared to their cracked counterparts. The difference is more pronounced at lower temperature.

Assuming an ideal flat and sharp crack, there are three modes of crack displacement. Based on linear elastic fracture mechanics (LEFM), in mode I or opening mode of fracture, the tip of the crack is subjected to normal stress which separates the crack faces symmetrically regarding to the crack front so that the displacements of crack surfaces are perpendicular to the crack plane ([167]). The other two modes which are mode II or in-plane shearing mode (sliding mode) and mode III or out-of-plane mode (tearing mode) are depicted in Fig. 6.9. Mode I is the most important loading case in the majority of the scientific and engineering applications. For this reason, most of the fracture mechanics work has concentrated on the Mode I stress intensity factor.

Assuming isotropic linear elastic material model, it is feasible to derive a closed-form solution for the stresses in certain cracks. The stress intensity factor or fracture toughness,

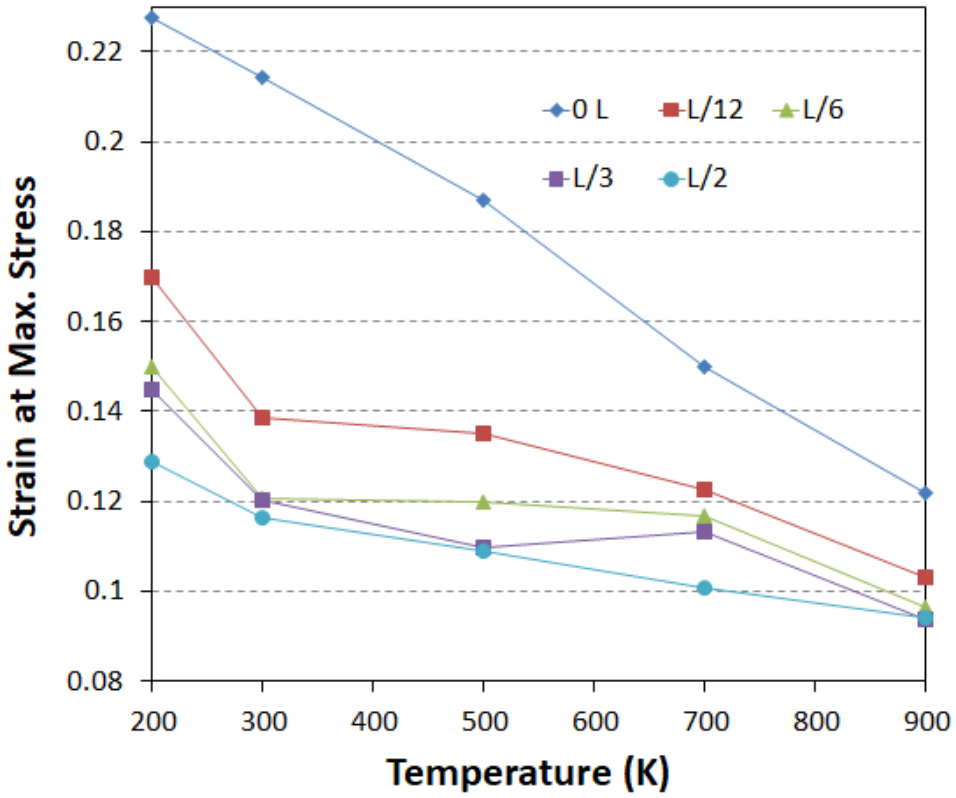

FIGURE 6.8: Engineering axial strain at ultimate tensile strength of the single-layer graphene-like BC_3 sheet in presence of several cracks with different lengths under the effect of several temperatures from 200 K to 900 K.

K_{IC}, is the magnitude of the crack tip stress field for a particular mode in a homogeneous linear elastic material. In addition, Fig. 6.10 illustrates a periodic configuration of collinear cracks having equal length. According to linear elastic fracture mechanics (LEFM), the critical stress intensity factor for a plate having periodic centered cracks under mode I fracture is calculated according to Eq. (6.7) as follow [166]:

$$K_{IC} = \sigma_f \left(2htan\frac{\pi a}{2h}\right)^{\frac{1}{2}}, \tag{6.7}$$

in which σ_f is the fracture stress, 2h is the width of the nanosheet and 2a is the crack's initial length which are expressed in the list of symbols.

We employed Eq. (6.7) for the periodic structure of graphene-like BC_3 two dimensional material. As an example to investigate crack propagation, we have estimated the critical stress intensity factor for a typical crack as large as L/12 at several temperatures. The fracture stress values used to substitute in Eq. (6.7) to calculate K_{IC} are according to

the corresponding curve in Fig. 6.7.

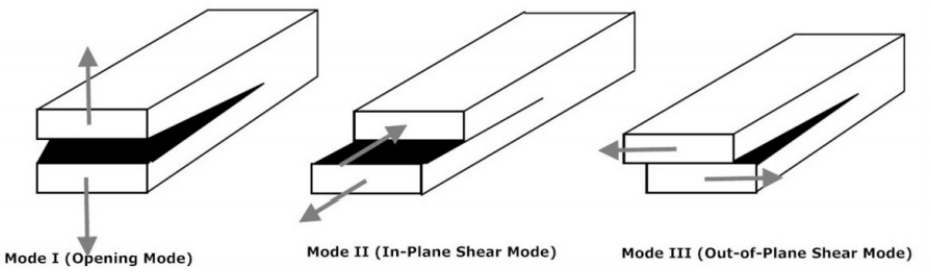

FIGURE 6.9: Three modes of crack tip displacement.

According to Fig. 6.11 stress intensity factor decreases with increasing temperature. Simulations were performed for five samples with uncorrelated initial conditions in order to determine the error-bars in acquired results. Crack propagation stages in a single-layer graphene-like BC_3 film for a crack length of L/6 at 300 K are visualized with OVITO and depicted in Fig. 6.12. Stress concentrations can be observed near the crack tip. Strains at each stage are depicted on each picture as well.

6.3.4 Notch effects

Finally, we investigate the effect of notch shaped defects on the mechanical behavior of 2D graphene-like BC_3 nanosheets. The investigated defects range from a L/12 notch size to a notch diameter of L/2. The other studied notch diameters are L/6 and L/3. These sizes are selected similar to the length of previously studied cracks, enabling a comparison between these two kinds of defects. The peak tensile stresses versus notch diametral sizes are shown in Fig. 6.13, for several temperature values. The values for pristine models are also represented. Maximum tensile stresses have a decreasing trend with respect to the increase in notch diameter and the temperature increase as well. The peak tensile stress for notch free model at 300K is 116 GPa which is significantly higher compared to a value of 46.5 GPa for a graphene-like BC_3 nanosheet containing a notch of length L/2 at 300 K. In other words, the maximum tensile stress value decreases about 60%. This consistent reducing trend in tensile strength exists for all simulations with respect to the temperature increase from 300 to 900 K. For the pristine model at 900 K, the peak tensile stress is 74 GPa which is well above this value for a notch of L/2 defect size which is about 30 GPa.

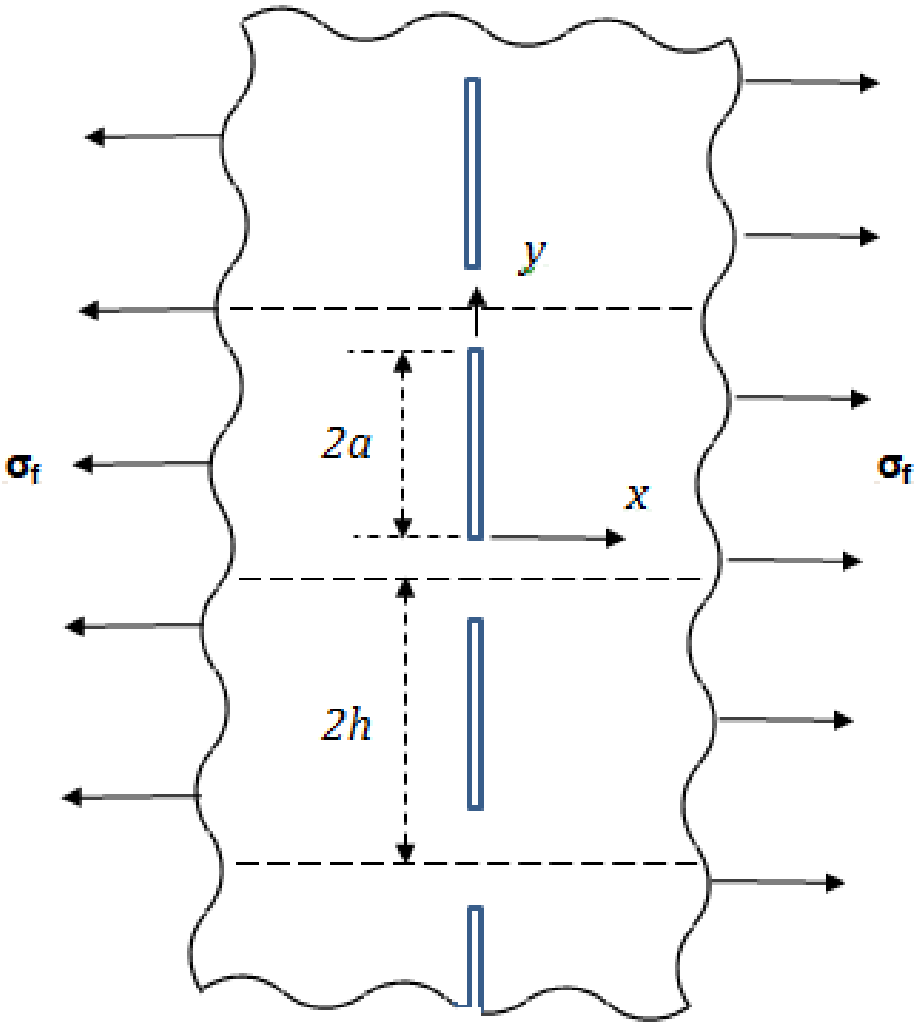

FIGURE 6.10: Periodic configuration of collinear cracks.

Furthermore, strains-at-failure values are shown in Fig. 6.14. The maximum strain decreases with increasing temperature and increasing notch diameter. The graphene-like BC_3 nanosheets experience large deformations during fracture process. Stress concentrations are observed close to the initially circular notches as expected.

Fig. 6.15 shows the failure process in a two dimensional graphene-like BC_3 nanosheet subjected to a notch shaped defect of L/6 diameter at a uniform temperature of 500 K. The orientation of defect propagation is perpendicular to the loading direction. It can be observed from step (a) of notch propagation on Fig. 6.15 that the nanosheet is in linear zone and the engineering strain is 0.02, while after defect propagation, at the step (f) material experiences a large deformation of 0.1320 engineering strain.

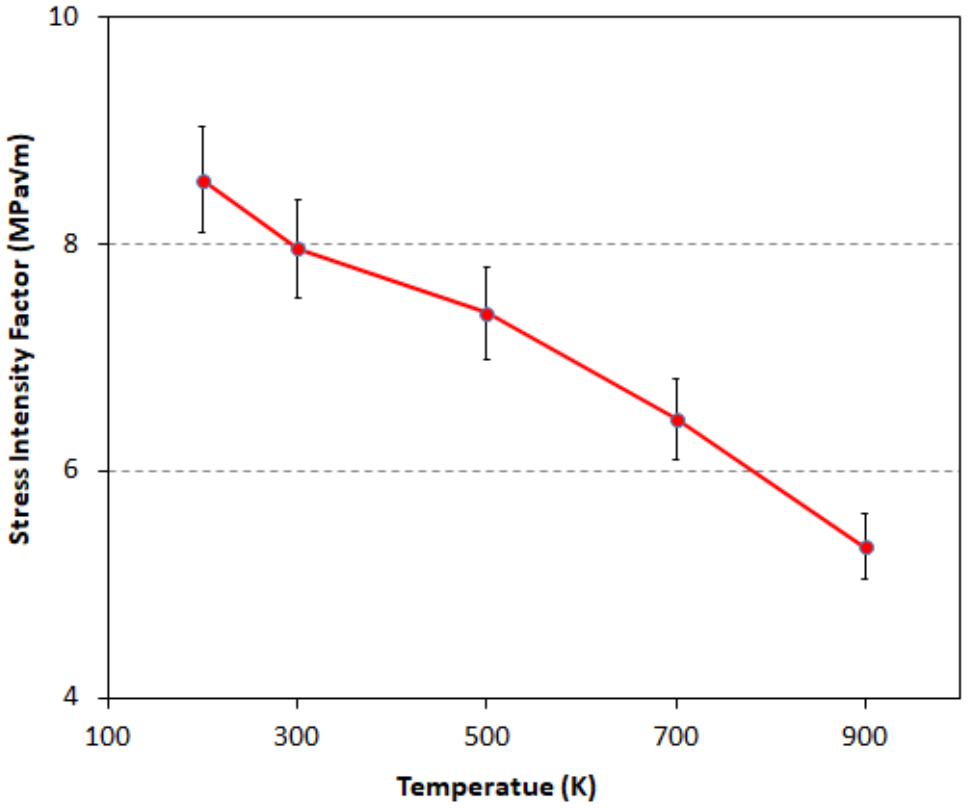

FIGURE 6.11: Stress intensity factor for graphene-like BC_3 nanosheets including the crack of length L/12 imposed to a range of temperature including 200, 300, 500, 700 and 900 K.

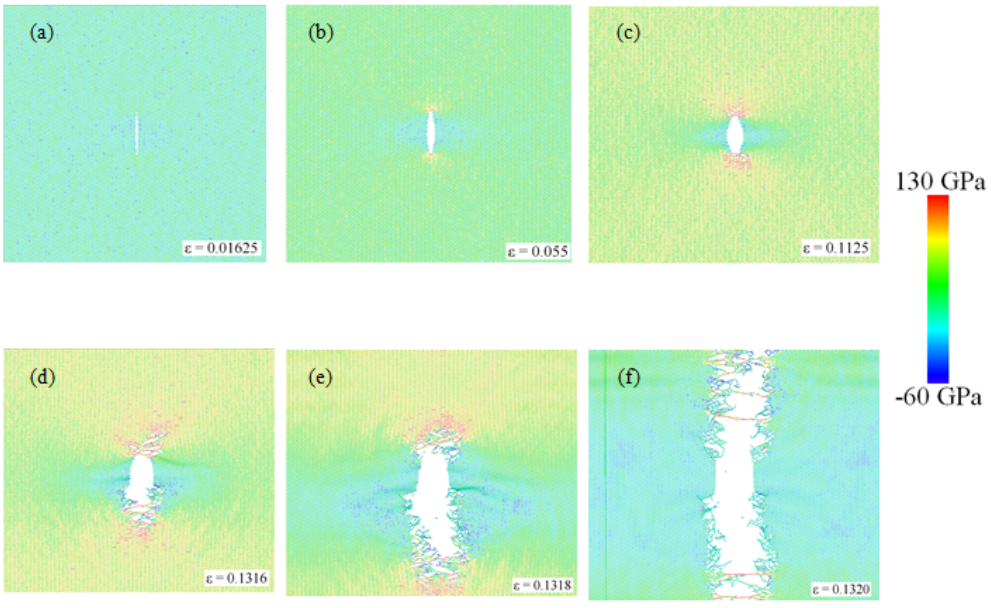

FIGURE 6.12: Crack propagation stages (a-f) in a graphene-like BC_3 nanosheet including the crack of length L/6 imposed to the room temperature (300 K).

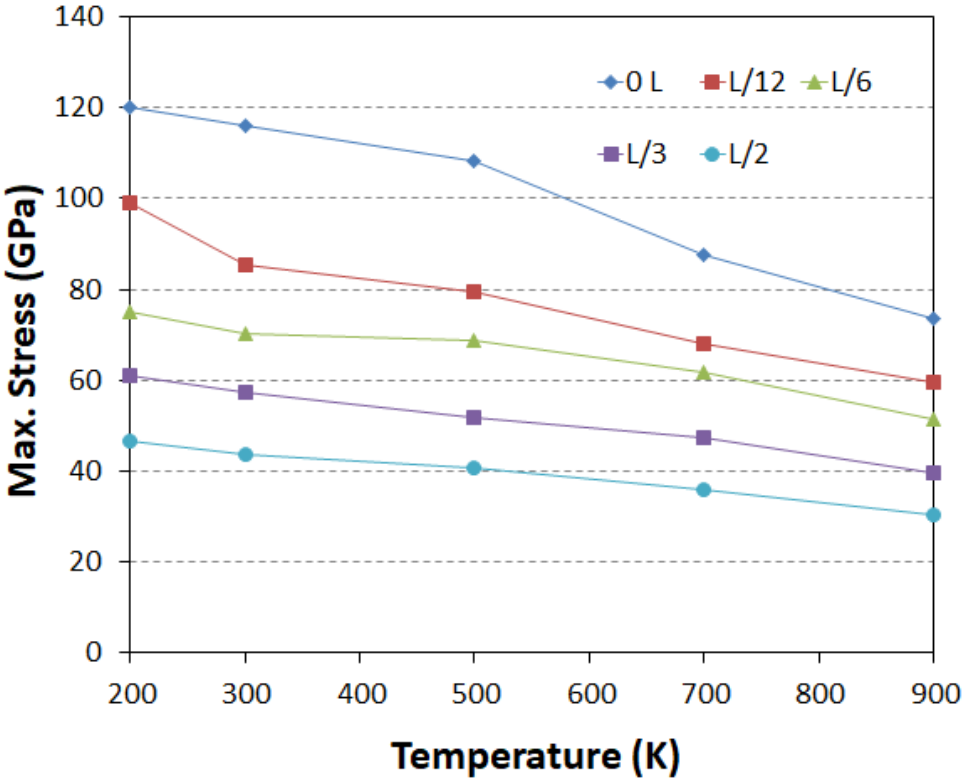

FIGURE 6.13: Ultimate tensile strength of graphene-like BC_3 nanosheet subjected to notch shape defects of different sizes imposed to the temperature variations of 200, 300, 500, 700 and 900 K.

6.3.5 Comparing the results

Fig. 6.16 shows the maximum tensile stress values versus temperature for pre-cracked and pre-notched two dimensional graphene-like BC_3 nanosheet samples. Ultimate tensile strengths are close for both cases.

TABLE 6.4: Comparing uniaxial strength of cracked nanosheets of graphene-like C_3N [63] and BC_3 materials at different temperatures of 200, 300, 500, 700 and 900 K (relative increase percentage).

Crack length	**Relative difference between uniaxial strength of cracked BC_3 and C_3N monolayers (%)**				
	200 K	300 K	500 K	700 K	900 K
L/12	26.4	24.0	30.2	13.8	39.8
L/6	16.1	19.7	14.9	22.3	17.8
L/3	5.9	5.1	26.9	50.1	19.4
L/2	22.0	14.3	48.3	44.1	9.5

To gain a deeper understanding of the effectiveness of graphene-like BC_3 nanosheets under uniaxial loading conditions, we calculated the relative difference between tensile strength of graphene-like BC_3 and C_3N from Ref. [63]. The results for nanosheets

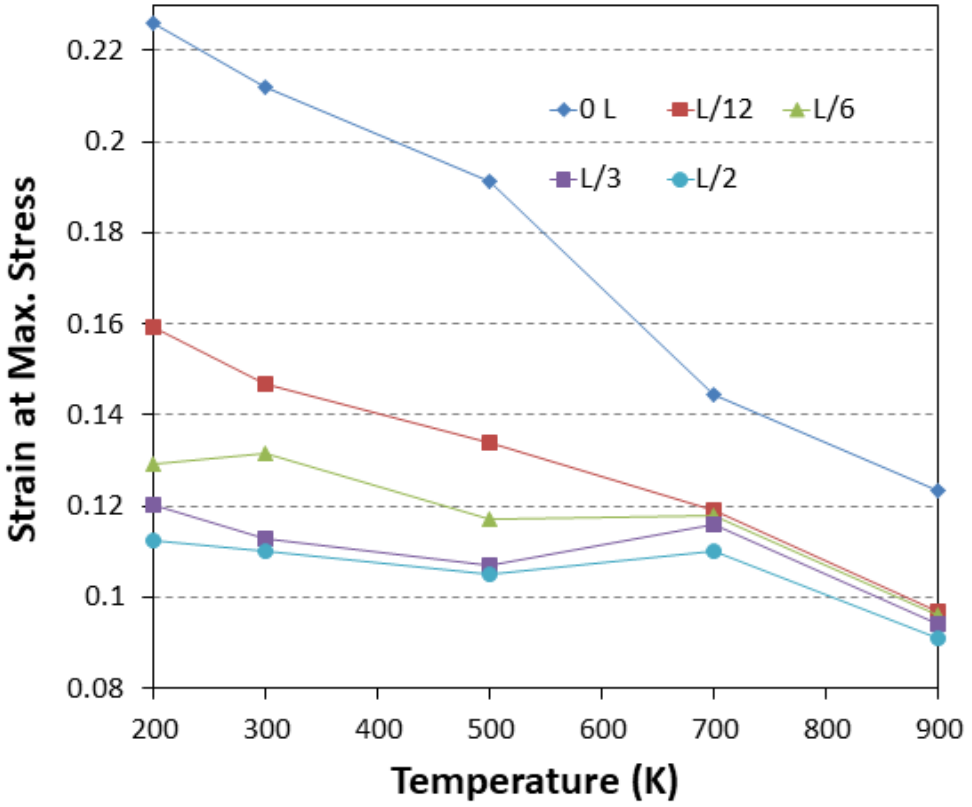

FIGURE 6.14: Engineering strain corresponding to ultimate tensile strength of graphene-like BC_3 nanosheet subjected to notch shape defects of different sizes imposed to the temperature variations of 200, 300, 500, 700 and 900 K.

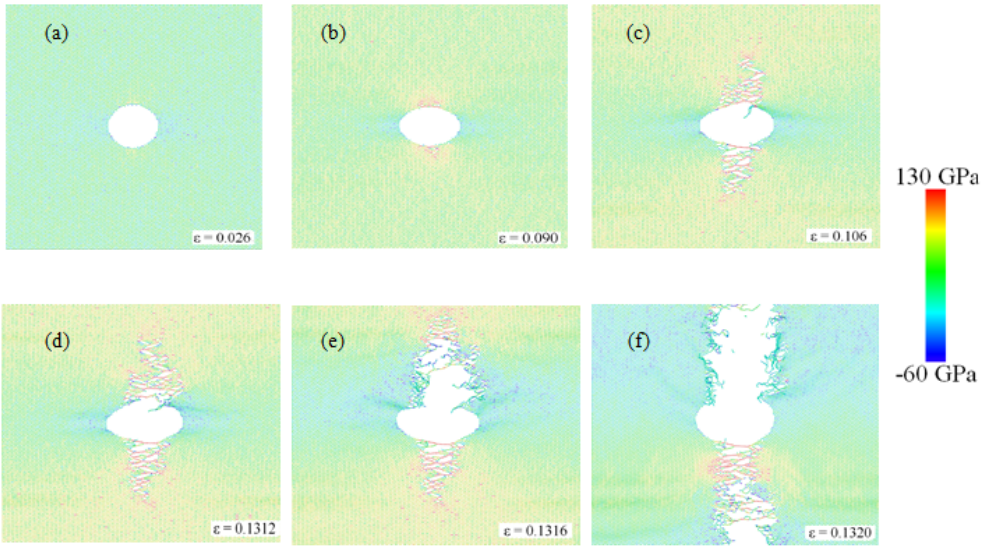

FIGURE 6.15: Failure process in a two dimensional graphene-like BC_3 nanosheet subjected to a notch shape defect of L/6 diameter at 500 K.

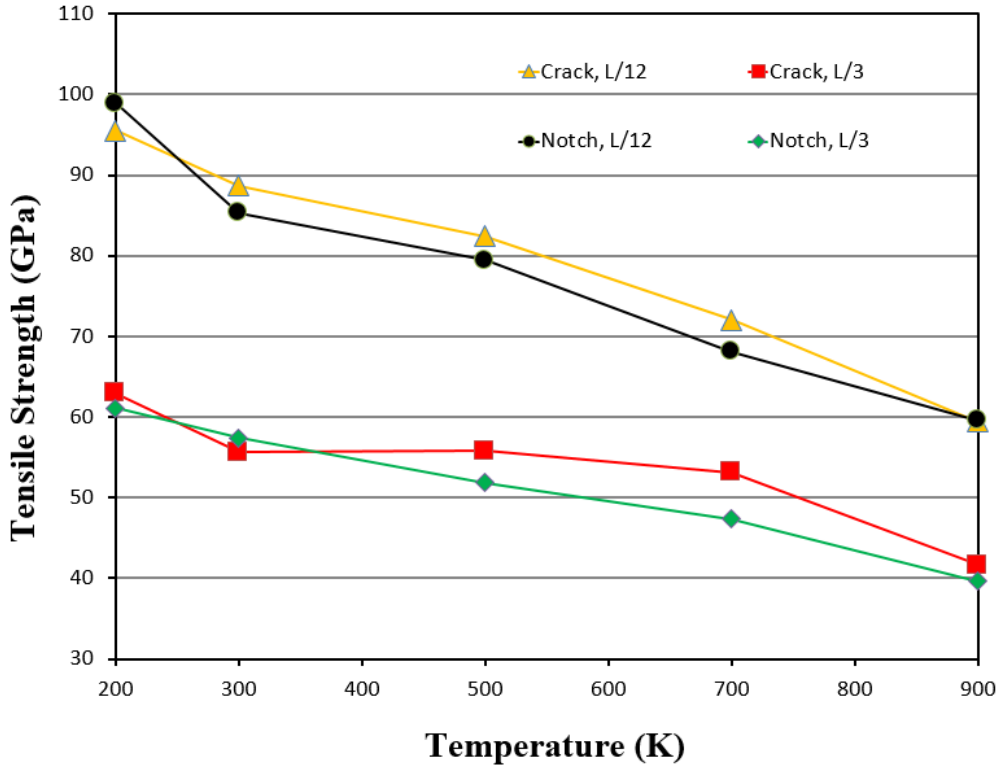

FIGURE 6.16: Comparison between two dimensional graphene-like BC_3 nanosheets contains notch shape and crack defects.

containing cracks and notch shaped defects under the same loading conditions and temperature are presented in Tables 6.4 and 6.5 respectively. For most cases, defective graphene-like BC_3 nanosheet hase a slightly large uniaxial tensile strength.

TABLE 6.5: Comparing uniaxial strength of notched nanosheets of graphene-like C_3N [63] and BC_3 materials at different temperatures of 200, 300, 500, 700 and 900 K (relative increase percentage).

Notch diameter	**Relative difference between uniaxial strength of notched BC_3 and C_3N monolayers (%)**				
	200 K	300 K	500 K	700 K	900 K
L/12	17.4	3.6	14.7	4.9	4.3
L/6	7.4	7.2	14.7	7.7	4.6
L/3	7.7	6.4	8.5	8.2	3.1
L/2	-6.3	-1.5	0.6	4.8	3.2

Additionally the obtained values for modulus of elasticity of pristine BC_3 atomic layers in armichair orientation are compared with those acquired for C_3N nanosheets from Ref. [63] at same temperatures. Table 6.4 shows relative difference between tensile elastic modulus of graphene-like BC_3 and C_3N from Ref. [63]. These results show that the elastic moduli of BC_3 nanosheets are lower than that of the monolayer C_3N counterparts. The relative differences show similar trend for different temperatures. The

higher values of tensile elastic modulus highlight the stiffening role of C-N bonds when compared with C-B ones.

TABLE 6.6: Relative difference (%) between Young's modulus (E) of the pristine BC_3 and C_3N nanosheets in armchair orientation at the 200, 300, 500, 700 and 900 K.

T (K)	200	300	500	700	900
Relative difference in E (%)	19.4	19.6	19.2	19.3	19.5

6.4 Conclusions

In the present contribution we used tensile loading simulations by classical MD calculations to predict the mechanical response of graphene-like BC_3 nanosheet and studied the response of pristine and defective graphene-like BC_3 nanosheets at different temperatures, where defects were assumed to be cracks with different lengths and notches with different diameter sizes. The results revealed that loading the defect-free BC_3 nanosheets along the zigzag direction results in higher modulus of elasticity than the armchair orientation. For both orientations, the lower modulus of elasticity (E) occurs at higher temperatures. With respect to the maximum tensile stresses, the results indicate that for studied nanosheets at high temperatures, the BC_3 films along the zigzag direction can show higher strengths than the sheets loaded in armchair orientations, even though, at low temperatures the sheets along armchair direction can indicate higher tensile strengths. Graphene-like BC_3 films subjected to cracks and notch shape defects have significantly lower ultimate tensile strength compared to their pristine material. The molecular dynamic simulations were performed for different crack lengths including, L/12, L/6, L/3 and L/2 and also for different notches with identical diameter sizes. Furthermore, graphene-like BC_3 monolayer models were tested at several temperatures including 200, 300, 400, 500, 600, 700 and 900 K. The results of pristine structures reveal a decreasing tensile strength with increasing temperature. Furthermore, an increasing crack length decreases the ultimate tensile strength of the material as well as the strains-to-failure. For crack models, the tensile strength of graphene-like BC_3 nanosheet decreases by increasing the temperature due to the weakening effect of the temperature on the atomic bonds. The estimation of the critical stress intensity factor (K_{IC}) for the typical crack of length L/12 at several temperatures indicates that the temperature increase has no considerable effect on this quantity and only slightly decrease the critical stress intensity factor. The results for notch shaped defects simulation revealed that the existence of such defects in BC_3 monolayers reduce the strength of the material significantly. A comparison between crack and notched models of identical length and notch diameter showed that the load bearing capacity of both cases are nearly identical. This research provides helpful result for employing ultra stiff and thermally stable

graphene-like BC_3 films for several industrial applications e.g. in nanodevices and as reinforcement of polymeric materials.

Chapter 7

Mechanical Properties of All MoS_2 Monolayer Heterostructures; Crack Propagation and Existing Notch Study

7.1 Introduction

A monolayer MoS_2 sheet has triple atomic planes with different atomic stacking sequences, in which a close-packed of molybdenum (Mo) is encompassed by two atomic layers of close-packed sulfur (S), as shown in Fig. 7.1. There exists three natural or synthetic polytypes of monolayer MoS_2 sheets, depending on (1) the coordination of sulphur atoms with respect to the central molybdenum atom and (2) the stacking order of each layer. The semi-conducting (2H) phase which is the original structure of this material, 2D atomic layers of MoS_2 sheets indicate a hexagonal lattice and an (S_{top}-Mo-S_{Bot}) ABA atomic stacking sequence (as depicted in Fig. 7.1(a)). Moreover, the metallic (1T) phase exhibits an atomic stacking sequence of (S_{top}-Mo-S_{Bot}) ABC, where the S atoms on the bottom are located in the hollow center of the hexagonal lattice. Both 2H and 1T structures have a 30 ° angle of symmetry. The loading angles of 0 and 30 ° are generally known as armchair and zigzag directions, respectively as illustrated in Fig. 7.1(b). In addition to the aforementioned 2H and 1T phases, there are samples of 2H/1T heterostructures. The letter T stands for trigonal, and H for hexagonal structures. Amazingly, laboratory findings validate the probability of production of MoS_2

heterostructure composed of semiconducting and metallic phases in a mono-layer configuration as shown in Fig. 7.1(c). The aforementioned experimental achievements in addition to the theoretical evaluations suggest MoS_2 nano-sheets as a material suitable for a wide range of industrial applications [86].

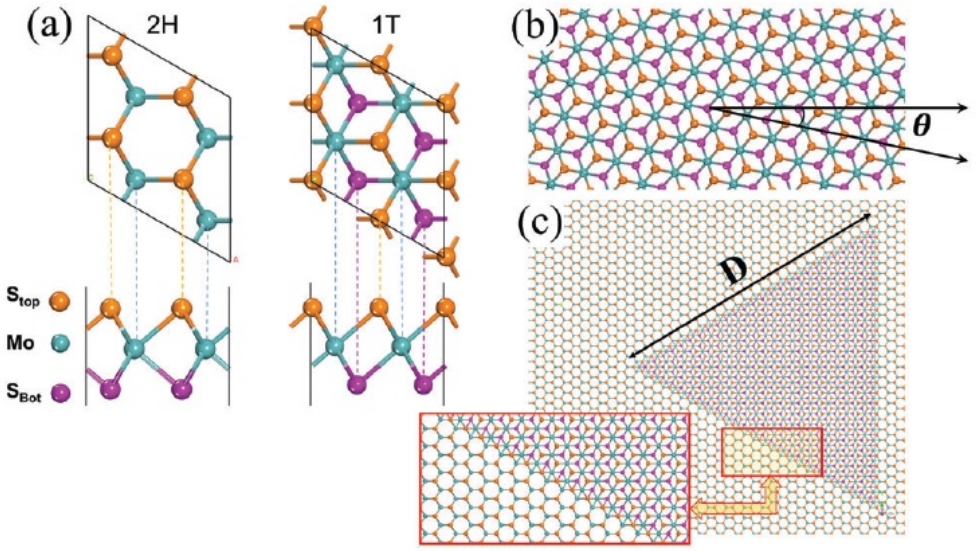

FIGURE 7.1: (a) Molecular dynamics representation of semi-conducting (2H) and metallic (1T) mono-layered MoS_2 phases on the basal plane and their related side view. The semi-conducting (2H) structure represents a hexagonal lattice with three-fold symmetry, whereas in metallic (1T) structure the underlying sulfur atom (S_{Bot}) is located in the void space at the center of the 2H hexagonal lattice. (b) Schematic illustration of 1T nonosheet where $\theta = 0$ is the armchair direction. (c) A triangular domain of 1T phase inside the 2H phase which represents the periodic atomistic model ([86]).

In order to guarantee that nanomaterials and nanodevices manufactured from monolayer MoS_2 sheets maintain their structural integrity throughout service life, it is required to obtain a basic knowledge of the mechanical behavior of monolayer MoS_2 nanosheets under different loading conditions.

As mentioned before, fracture is a key problem in many engineering applications. The existence of defects in structures can cause catastrophic failure of whole structure in the worst case. Cracks, holes and notches are among the most popular defects appearing in structures. Numerous studies on the fracture behavior of nanomaterials have been carried out in the past. Initial flaws or fractures play a prominent role in two-dimensional materials impacting their mechanical behavior. In order to evaluate the influence of defects and impurities on mechanical behavior of MoS_2 films, ReaxFF reactive molecular dynamic simulation seems to be valuable choice. It worth mentioning that, molecules

are formed through atomic static bonds that do not allow bond formations. This limitation prevents applying classical molecular dynamics (MD) methods to simulate chemical reactions. For the purpose of overcoming this limitation in MD simulation, the reactive force field (ReaxFF) is employed. ReaxFF allows continuous bond-forming/breaking by replaced explicit bonds with bond orders. This method treats each atom as a separate body, which leads to the reformation of bond structures at every time-step [168]. This concept of dynamic bonding with charge redistribution together is the major difference between classical and reactive MD methods. In order to estimate and prevent mechanical failure caused by cracks and notches, it is necessary to understand the failure properties of monolayer MoS_2. However, the failure behavior of MoS_2 nanosheet is more complicated than those of graphene and other graphene-like materials which have planar surfaces with single-layer atomic structures. It is so difficult to measure and evaluate the deformation and fracture mechanism in 2D materials by experimental methods. Bao et al. [169], conducted MD simulations to investigate the propagation of nanocracks in large sheets of semiconducting (2H) MoS_2 monolayer by using the Stillinger-Webber (SW) potential. In this work, the cracks were predefined by deleting some atoms in the nanosheet.

This phase of research focuses on fracture of all phases of single-layer MoS_2, including semiconducting (2H) MoS_2 phase, metallic (1T) phase and 2H/1T hetero-structure. We therefore extended the studies in [86] and performed molecular dynamic simulations using ReaxFF force field [170].

7.1.1 Description of the research methodology

The main objective of this part of the research is to investigate the fracture properties (tensile strength, Young's modulus and failure strain) and also crack and notch propagation of all aforementioned phases of MoS_2 single-layer structures with various pre-existing crack and notch shape defects. Therefore, we conduct ReaxFF based molecular dynamics (MD) simulations and study the effect of different nano-crack sizes (lengths) and nano-notch sizes (diameters) on the single-layer MoS_2 mechanical and failure response, predicting the macroscopic Young's modulus, tensile strength and strain at failure under uniaxial tension. We employ the approach discussed in our previous study [171] to generate initial cracks by disconnecting the interaction between atoms located at the crack edge.

7.1.2 Molybdenum Disulfide (MoS_2) nanosheet with defects

The focus of this chapter is to computationally predict the mechanical behavior of MoS_2 films containing nano-defects via molecular dynamics calculations. We therefore extract the tensile strength, Young's modulus and strain-at-failure and model the crack and notch propagation in aforementioned two dimensional (2D) materials for several crack lengths and notch diameters at room temperature. The defect location and the orientation of the crack highly influence the nanosheet strength and associated fracture pattern. To assess the effect of the crack and notch sizes on the mechanical properties of MoS_2 structure, we created center crack and notch in the MoS_2 nanosheet as depicted in Fig. 7.2, "L" denoting the side length of the nanosheet while k refers to a variable defining the initial crack length and notch diameter. Tensile loading is in the armchair direction of the nanosheet, which is perpendicular to the crack orientation. Two regions were defined at the left and the right sides of the crack location so that the coincident edges of the regions fall on the crack location, similar to what was illustrated in Fig. 6.3. Then the interactions between atoms located at this edge are restricted by employing the "neigh- modify" command in LAMMPS.

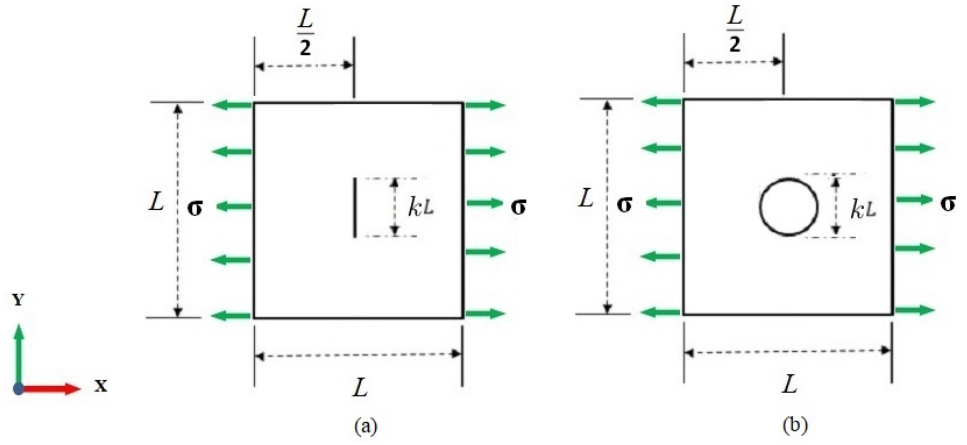

FIGURE 7.2: The nanosheet with a pre-defect which is supposed to be located at the center of the nanosheet. (a) crack-shape defect. (b) notch shape defect.

7.2 Molecular dynamics modeling

The results of molecular dynamics modeling for pristine MoS_2 nanosheets reveal that the elastic response of MoS_2 phases depends on the loading direction. Along the armchair direction MoS_2 exhibits a higher rigidity than in zigzag direction [86]. Thus, we load

both 2H and 1T phases of the pre-cracked nanosheets in armchair direction. We study samples of pre-cracked single-layer 2H/1T heterostructures where the 1T phase inside 2H phase indicates a triangular geometry with a characteristics edge length, defined by "D" [86]. We consider different composite structures with specified characteristic sizes and concentrations of 1T phase inside 2H. According to experimental observations [172], three different grain boundaries of "α", "β" and "γ" can be formed between the 2H and 1T phases. We follow the method used by Mortazavi *et al.* [86], and only consider the "β" grain boundary, which commonly exists in chemically grown polycrystalline MoS_2 films [96]. All atomistic samples are assumed to be periodic along the planar direction avoiding the influence of free atoms on the boundaries. We employed the ReaxFF bond order potential presented in [170] in all our simulations, which is a popular choice for such systems [173, 174]. Therefore, the atomic system energy (E_{system}) is additively decomposed into several parts given by:

$$E_{system} = E_{bond} + E_{val} + E_{tor} + E_{over} + E_{under} + E_{lp} + E_{vdW} + E_{Coulombic} \tag{7.1}$$

where, E_{bond}, E_{val}, E_{tor}, E_{over}, E_{under}, E_{lp}, E_{vdW} and $E_{Coulombic}$, represent the bond energy, valence-angle, torsion-angle, over-coordinate, under-coordinate, lone pair, non-bonded van der Waals and coulomb contribution, respectively. The parameters of the ReaxFF potential are obtained by a quantum mechanical (QM) dataset which introduces bond dissociation and valence angle bending in different molecules and also the energy of formation and the state of condensed-phases equations of crystalline MoS_2 nano-materials [170]. All simulations were done with the open-source software LAMMPS (Large-Scale Atomic/Molecular Massively Parallel Simulator) [8]. The post-processing was done with OVITO [160]. In order to estimate the fracture properties of all phases (semiconducting (2H) phase, metallic (1T) phase and 2H/1T hetero-structure) of MoS_2 films, we first constructed models with different nanosheet sizes and obtained similar results which showed we have a concurrent multiscale method. Therefore, we select final models consisting of around 22,000 atoms with planar dimensions of about 25 nm$\times$25 nm and apply periodic boundary conditions in both planar directions. The time increment in all simulations is fixed at 0.25 fs. First, energy minimization was performed with a 10^{-6} stopping tolerance for energy. Then, the uniaxial loading condition is applied by increasing the periodic box size along the loading direction by a constant engineering strain rate of 10^9 s^{-1}. Before subjecting the samples to uniaxial tension, the structures were relaxed and equilibrated to zero stress at room temperature taking advantage of the Nose-Hoover barostat and thermostat (NPT). This was done with damping parameters of 100 fs and 50 fs for the pressure and temperature respectively. To apply the uniaxial load, the stress on the other two directions should remain small throughout the deformation procedure. As the atoms are in contact with vacuum along the nanosheet

thickness orientation, the normal stress is insignificant. Moreover, the periodic simulation box along the width of the MoS_2 nanosheet was kept at zero stress in the mentioned direction via the NPT approach. At every time step, the applied engineering strain rate was multiplied with the step time. The extracted values of the stresses and strains were averaged during each time interval of 250 fs. Cracks are modeled through disconnected iteratomic bonds for the atoms located at both sides of the imposed nano-crack.

7.3 Results and discussion

The models were loaded in tension and the extracted uniaxial stress-strain results for defective MoS_2 nanosheets are depicted on several graphs in order to calculate mechanical properties of MoS_2 films. As mentioned, we used periodic boundary conditions (PBC) in planar directions to prevent the influence of free atoms on the edge on all mechanical properties calculations. It worth mentioning that in the calculation of stresses, we choose the structure volume using a thickness of 6.1 $\mathring{A}$ [86, 170] for the single-layer MoS_2 nanosheet.

7.3.1 Strain rate effect on pristine nanosheet

The strain rate is an effective factor influencing the strength of materials. We know that because of the enormous amount of computational costs, MD simulations can not capture strain rates as they often occur in engineering applications. However, some researches have been done to extract the mechanical behavior under quassi-static conditions [150, 175]. Commonly, the tensile strength of nanosheets increases with strain rate. Increasing strain rate decreases the relaxation time and makes it too short for atomic bonds to rotate and rearrange under stress and consequently, the tensile strength and strain-at-failure increases [176, 177].
In this section we investigate the effect of different strain rates on the mechanical responses of the pristine MoS_2 nanosheets. The tensile tests were performed for 2H phase and 1T phase of MoS_2 material and also 2H/1T composite MoS_2 structure with 5% concentration of 1T phase inside 2H phase at room temperature with strain rates ranging from 10^8 to 10^{10} s^{-1}. Let us first consider a pristine 2H MoS_2 nanosheet. The curves on Fig. 7.3 shows the stress-strain response in armchair orientation. Obviously, for low strain rates of 10^8 and 10^9 s^{-1}, the results converge against a curve. For high strain rate of 10^{10} s^{-1}, first the results approximately converge against the other two curves until the strain of around 0.23 but it shows different pattern for higher strains. Our results for 10^8 s^{-1} strain rate predict an ultimate stress of 25.8 GPa and the elastic modulus of 265.6 GPa which are in fair agreement to the results in [86].

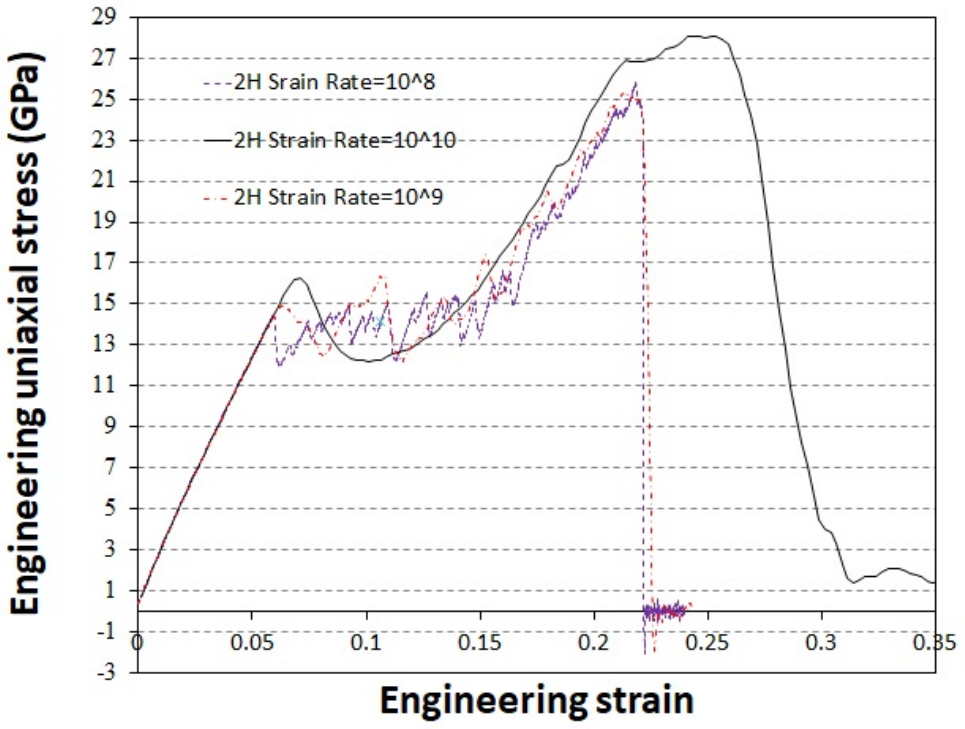

FIGURE 7.3: Uniaxial tensile stress-strain response of pristine 2H phase MoS_2 in armchair orientation.

The stress-strain curve of the phase 1T crack-free MoS_2 nanosheet can be found in Fig. 7.4. The size of the simulation box was again 25 nm×25 nm in planar dimensions. With reference to this figure, for low strain rates of 10^8 and 10^9 s^{-1}, the results approximately converge against a similar curve. This behavior is more pronounced for strains less than 0.15. The curve for high strain rate of 10^{10} s^{-1} is above the other two curves which shows higher results. The maximum tensile stress and corresponding failure strain for 10^8 s^{-1} strain rate are 9.9 GPa and 0.18 respectively, which are very close to the results reported in [86]. Finally, the stress-strain curves of the crack-free 2H/1T heterostructures of MoS_2 films in armchair loading direction are depicted in Fig. 7.5. This composite structure is made of the 1T phase with a domain size of 6 nm and with a concentration of 5%. The maximum tensile stress and corresponding failure strain in armchair direction for 10^8 s^{-1} strain rate are 19.36 GPa and 0.196, respectively which meet the results reported in [86]. Therefore, as the accuracy of the results for pristine nanosheets are verified, we conduct the same procedure to investigate the effects of pre-cracks and existing notches on the mechanical response of the equivalent MoS_2 films.

The fracture properties of the aforementioned phases of MoS_2 material which are obtained from Figs. 7.3-7.5 are summarized and compared in Fig. 7.6, which include ultimate tensile strength, Young's modulus and strain-at-failure of MoS_2 nanosheets

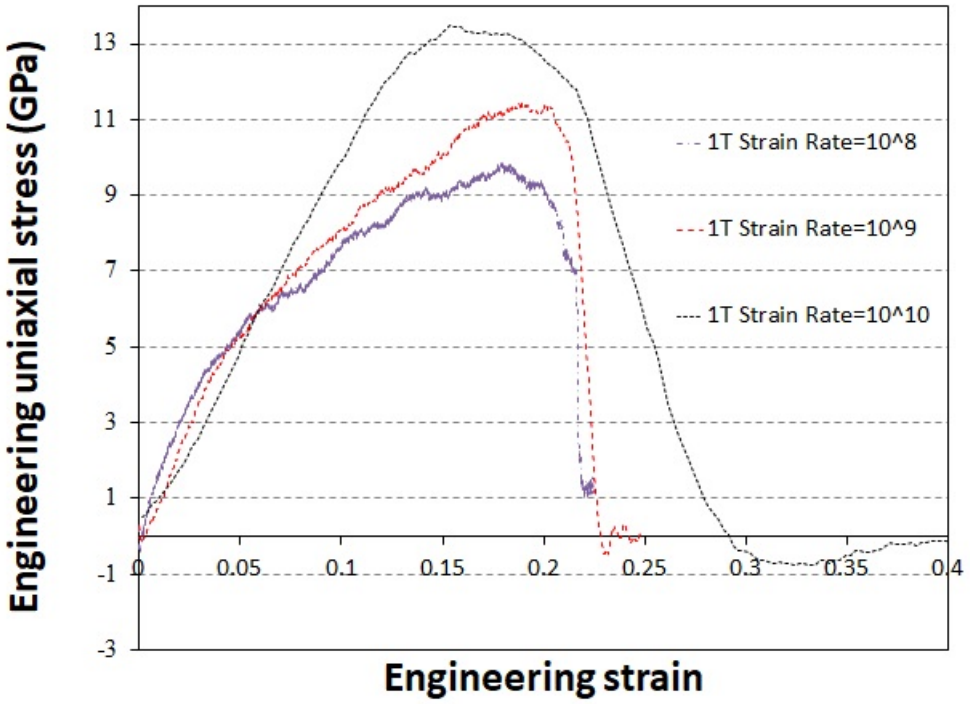

FIGURE 7.4: Uniaxial tensile stress-strain response of phase 1T pristine MoS_2 nanosheet in armchair direction.

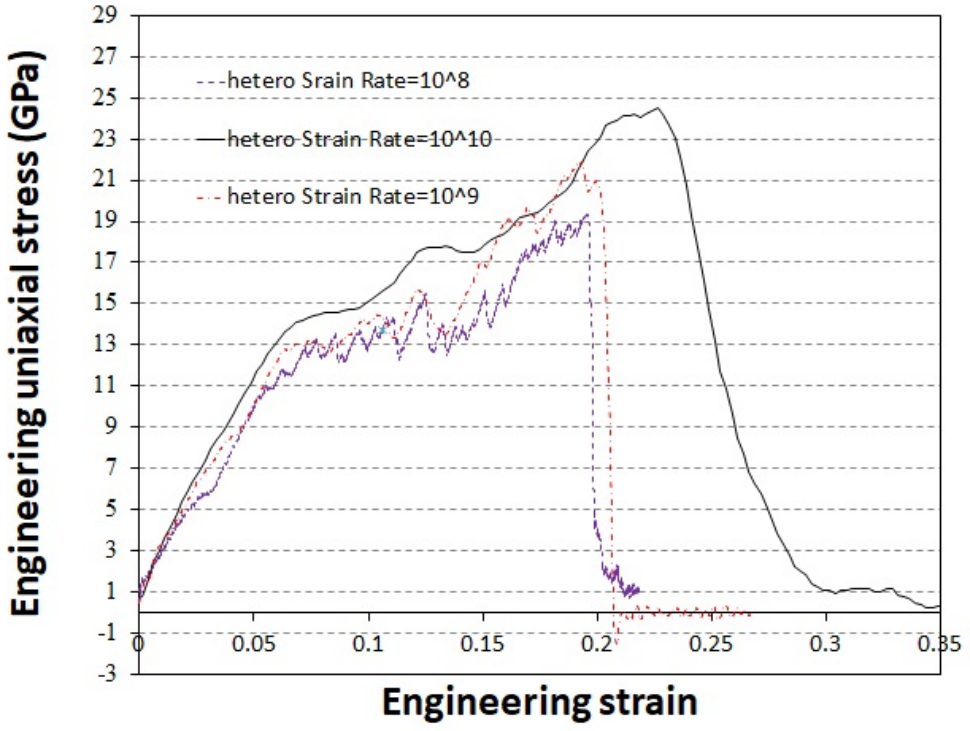

FIGURE 7.5: Uniaxial tensile stress-strain response of 2H/1T hetero-structure pristine MoS_2 nanosheet for a concentration of 5% of the 1T phase inside 2H phase.

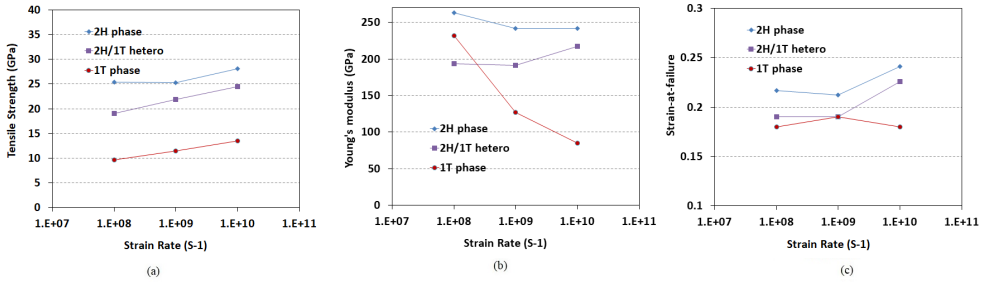

FIGURE 7.6: Fracture properties of all phases of defect-free monolayer MoS_2 heterostructures (a) Ultimate tensile strength, (b) Young's modulus as a function of strain rate (c) Engineering axial strain at ultimate tensile strength.

as a function of strain rate for different phases in armchair direction, as illustrated in Fig. 7.6 (a), (b) and (c) respectively. As the strain rate increases, the ultimate tensile strength and strain at failure indicate an increasing trend. However, the strain rate effect on the mechanical properties of 1T phase of MoS_2 nanosheet is more significant than 2H phase and hetero structure.

7.3.2 Mechanical response of the sample with initial center crack

Fracture is a phenomenon with size effects and the crack length influences the mechanical properties of the nanosheet. As mentioned before, we use ReaxFF reactive molecular dynamics modeling and estimate the fracture properties of monolayer MoS_2 nanosheets with initial center cracks under mode I loading condition in armchair direction. We created MD models with side length of 25.0 nm simulation box size consisting of around 22000 individual atoms. We consider several pre-crack lengths including L/6, L/3 and L/2 where L is the length of the square graphene-like MoS_2 monolayer.

7.3.2.1 Semiconducting (2H) MoS_2 nanosheet results

Fig. 7.7 depicts the 2H phase of single-layer MoS_2 film with a center crack size of L/3 at different time steps and associated strain values. Additionally, strains at each stage are shown on each picture which is 0.104 at the end of crack propagation process of the whole length. As can be seen, for semiconducting (2H) phase cracked MoS_2 nanosheet loaded in armchair direction, first the crack opens by increasing uniaxial tensile stains. Then by increasing crack-driving force, the crack rapidly grows perpendicular to the loading direction throughout the nanosheet. Following the nanosheet failure, the bonds between atoms are ruined and larger deformation arise. Stress concentration areas can

be distinguished near the tip of the crack. This crack patterns obtained from our MD simulation meet our common physical sense of fracture.

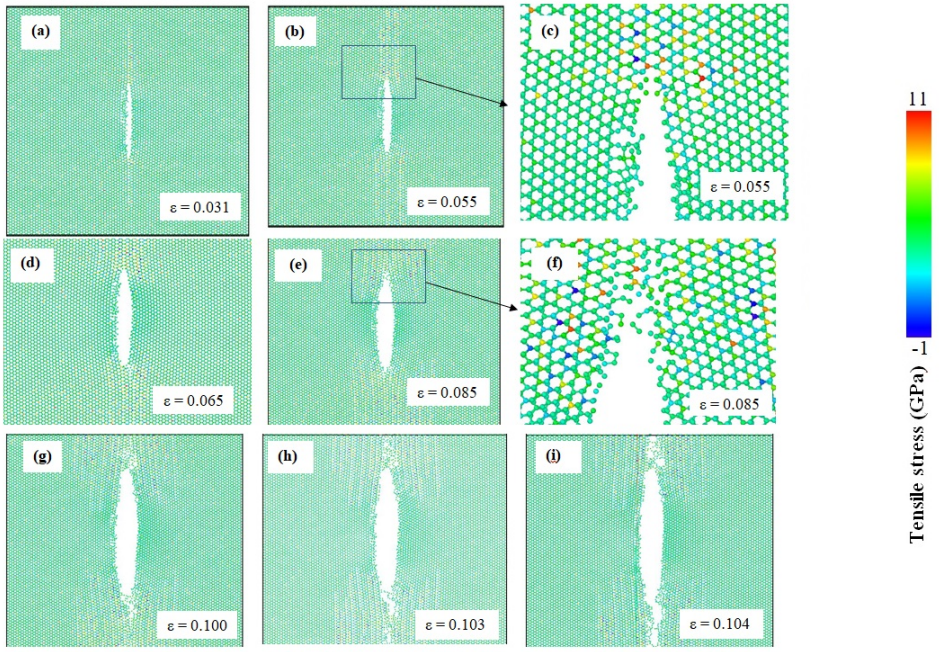

FIGURE 7.7: Crack propagation stages (a-i) in a MoS_2 nanosheet with simulation box size of 25 nm×25 nm including the crack of length L/3 imposed to the room temperature (300 K).

We compare the results of our MD modeling for the semiconducting phase (2H) MoS_2 nanosheets subjected to different crack lengths of L/6, L/3 and L/2 where L is 25 nm. The related stress-strain curves are depicted in Fig. 7.8. We also show the maximum tensile stress for crack-free MoS_2 nanosheet (0L). For L/6, L/3 and L/2 crack sizes, the ultimate stresses are 13.42 GPa, 10.11 GPa and 7.79 GPa respectively and comparing them with the crack-free MoS_2 nanosheets, which exhibits a maximum tensile stress of 25.8 GPa, shows the crack significantly decreases the tensile strength of two dimensional MoS_2 material, i.e. the reductions are around 48%, 61% and 70% for L/6, L/3 and L/2 crack sizes, respectively. Also, Fig. 7.9 (a), (b) and (c) illustrates and compares the ultimate tensile strength, strain-at-failure and Young's modulus of the 2H phase monolayer MoS_2 nanosheet for the aforementioned crack sizes. Obviously, increasing the crack length, has a weakening effect on tensile strength of 2H MoS_2 nanosheet. Additionally, strain-at-failure and Young's modulus decrease for larger crack sizes. According to Fig. 7.9 (a), a sudden reduction in the tensile strength is observed in the 2H phase of MoS_2 models with crack sizes less than L/6, while larger crack sizes showed approximately a linear trend. Also, according to Fig. 7.9 (b) a sudden decrease in strain-at-failure is distinguished in samples with crack sizes less than L/6, while for larger crack sizes the decrease was very slow. Based on Fig. 7.9 (c), for L/6, L/3 and L/2 crack sizes, the

reduction in Young's modulus of the 2H phase monolayer MoS_2 nanosheet are around 10%, 24% and 40%, respectively. It can be implied that the crack length non-linearly influences fracture properties of MoS_2 nanosheet.

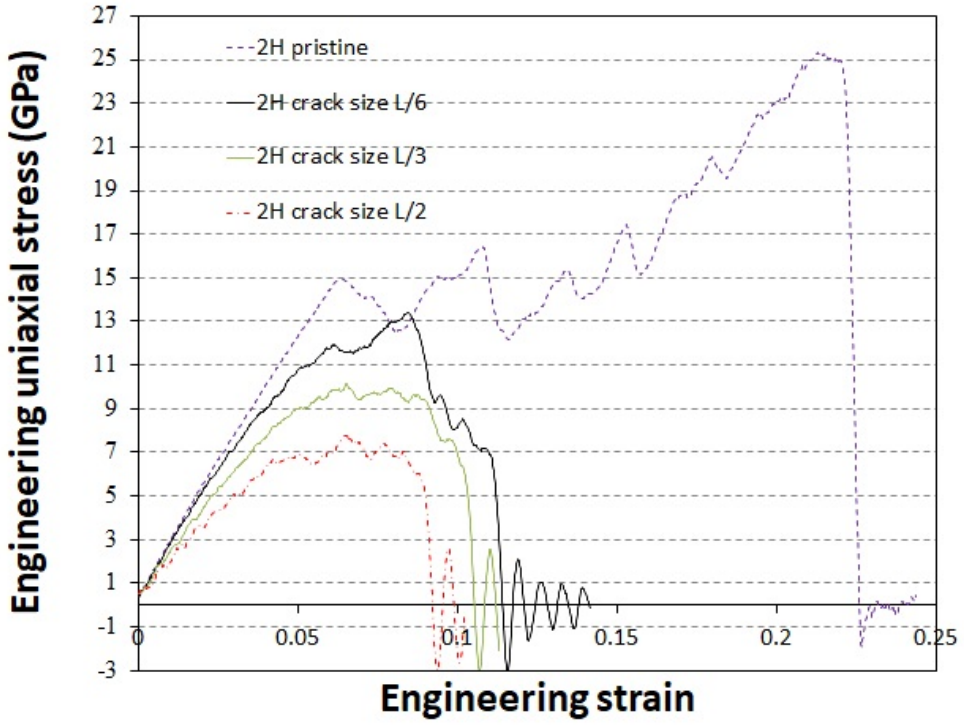

FIGURE 7.8: Plot of stress-strain diagrams to investigate crack size effect on 2H MoS_2 nanosheet models.

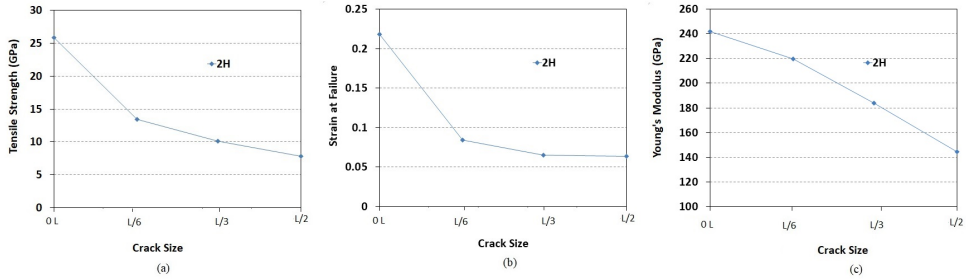

FIGURE 7.9: Fracture properties of 2H phase monolayer MoS_2 nanosheet including different crack sizes (a) Ultimate tensile strength, (b) Engineering axial strain at ultimate tensile strength (c) Young's modulus.

7.3.2.2 Metallic (1T) MoS_2 nanosheets results

In this section, we investigate the fracture properties of the metallic (1T) phase MoS_2 monolayer loaded in armchair direction. First we investigated the influence of the center

crack size on the stress-strain curves, where different crack sizes have been assumed. Fig. 7.10 shows a sample of the 1T phase single-layer MoS_2 film with a center crack size of L/6 at different time steps and associated strains. The strains at each stage are shown on each picture which is 0.362 at the end of crack propagation process of the whole length.

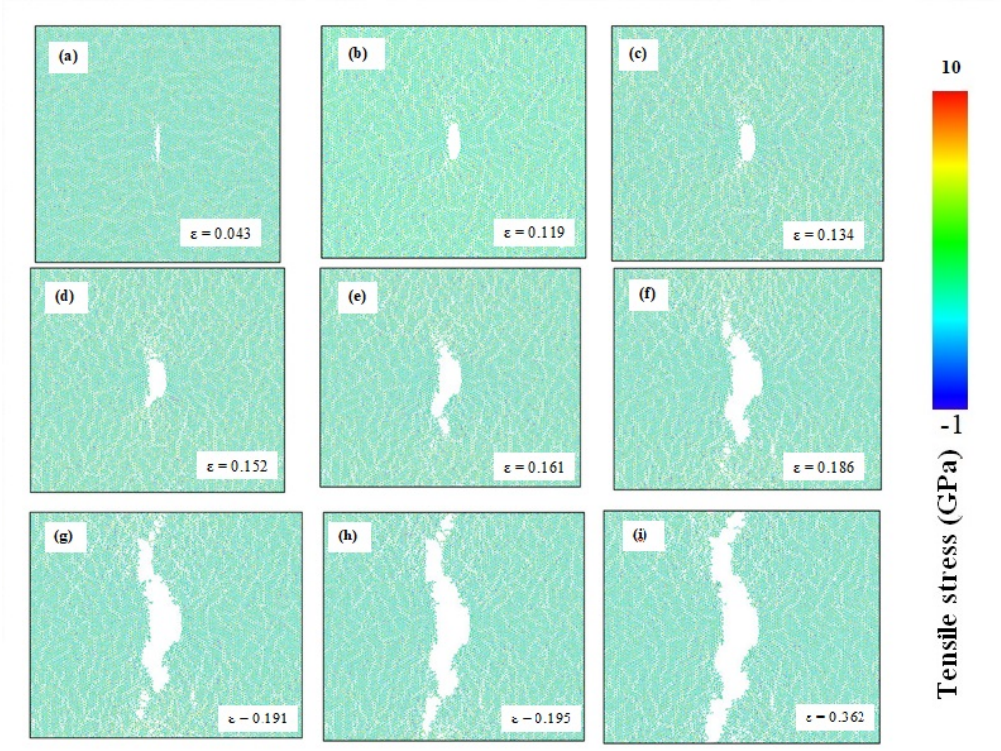

FIGURE 7.10: Loading stages (a-i) in 1T phase of MoS_2 nanosheets including the crack of length L/6 and sheet side length of 25 nm, imposed to the room temperature (300 K).

We derive our effort to compare the results of our MD modeling for metallic phase (1T) MoS_2 nanosheets subjected to different crack lengths including of L/6, L/3 and L/2 where L is 25 nm. Fig. 7.11 shows the related stress-strain curves for each crack length of 1T MoS_2 monolayer. Additionally, ultimate tensile strength, strain-at-failure and Young's modulus of 1T phase monolayer MoS_2 nanosheet for the aforementioned crack lengths are depicted on Fig. 7.12 (a), (b) and (c) respectively. In order to better evaluation of the crack effect, the maximum tensile stress for crack-free 1T phase MoS_2 nanosheet (0L) is also presented, enabling us to compare with crack results. As expected, the tensile strength of two dimensional metallic (1T) MoS_2 material decreases under the effect of crack-shape defects. Obviously, crack length increase, has a weakening effect on ultimate tensile strength of 1T MoS_2 material, as the maximum stress values decrease significantly by increasing the crack size.

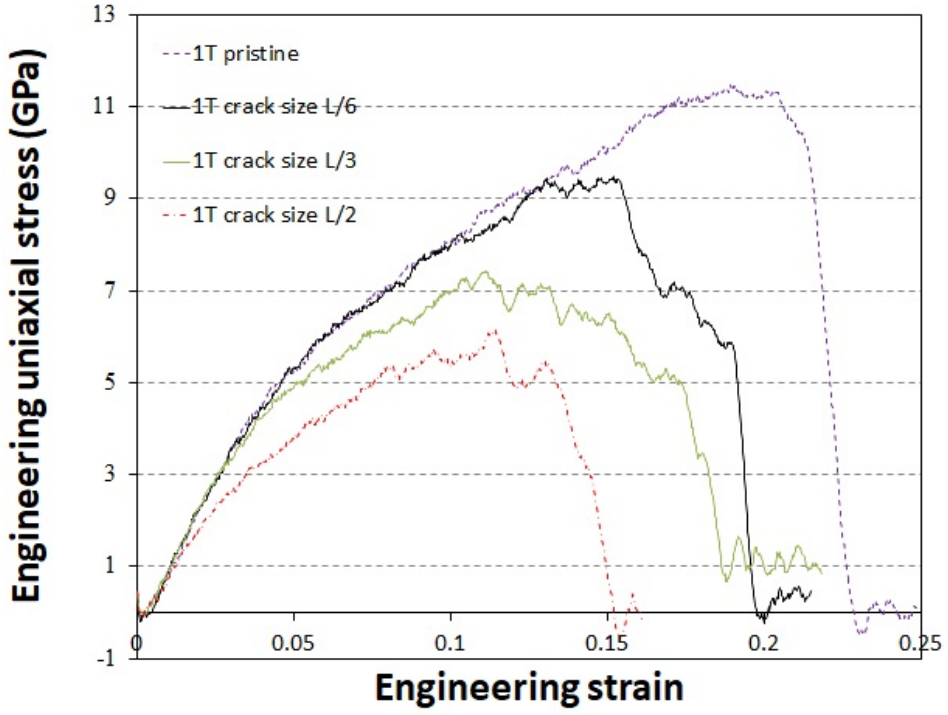

FIGURE 7.11: Plot of stress-strain diagrams to investigate crack size effect on 1T phase MoS_2 nanosheet models, under uniaxial loading at room temperature.

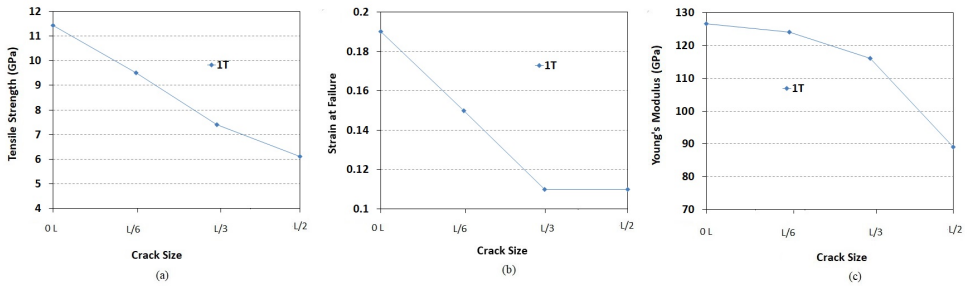

FIGURE 7.12: Fracture properties of 1T phase monolayer MoS_2 nanosheet including different crack sizes (a) Ultimate tensile strength, (b) Engineering axial strain at ultimate tensile strength (c) Young's modulus.

Maximum tensile stresses for L/6, L/3 and L/2 crack sizes are 9.49 GPa, 7.42 GPa and 6.13 GPa respectively which are around 17%, 35% and 46% below the pristine 1T phase MoS_2 sample, respectively. Obviously, strain-at-failure and Young's modulus decrease for larger crack sizes of 1T MoS_2 nanosheet. As an example, based on Fig. 7.12 (b), for a crack size as large as half of the nanosheet length (L/2), failure strain is 0.114 which is around 42% less than pristine 1T phase nanosheet. Based on Fig. 7.12 (c), for L/6, L/3 and L/2 crack sizes, the reduction in Young's modulus of the 1T phase monolayer MoS_2 nanosheet are around 2%, 8% and 29%, respectively.

7.3.2.3 2H/1T MoS_2 heterostructure results

The existence of heterogeneity which is a physical non-uniformity of the material makes the study of fracture in monolayer 2H/1T MoS_2 requiring additional terms and mechanisms to explain its failure. The heterogeneity affects fracture propagation behavior of the nanomaterial and its path and makes fracture behavior different from 2H phase and also 1T phase of MoS_2 nanomaterials. In this section, we use numerical simulations to evaluate the mechanical properties and to predict fracture geometry of 2H/1T single-layer MoS_2 heterostructures and investigate fracture initiation and crack propagation path in different samples of the nanosheet. It is likely the fracture properties (tensile strength) of 2H/1T heterostructures to be higher than that of the defective 1T phase and lower than defective 2H phase. This prediction is according to the fact that the results for the tensile strength of the defective 1T phase are almost half of that of the 2H phase. Fig. 7.13, illustrates the deformation process and crack growth of three samples of single-layer MoS_2 composite structures made of the 1T phase with a domain size of 6 nm and with 5%, 10% and 15% concentrations. All the samples are subjected to a pre-crack of length L/6, where the sheet side length is 25 nm. The various stages of the uniaxial tensile strains (ϵ) at room temperature are depicted as well. This figure indicates that the crack opening widens more over the time of load application. For all three samples, the crack rapidly grows perpendicular to the loading direction and passes through the surrounding 2H phase and then passes through 1T domains and finally leads to the sample rupture. However, we can imply that the 2H/1T composite nanosheet is remarkably stronger than the original 1T phase.

Figs. 7.14, 7.15 and 7.16 show the related stress-strain curves for each crack length of composite MoS_2 monolayer with 5%, 10% and 15% concentrations respectively. Our results for the mechanical and fracture properties of different 1T concentrations of 2H/1T MoS_2 heterostructures and three crack sizes are summarized in Fig. 7.17. Ultimate tensile strengths of 2H/1T MoS_2 heterostructure for the previously mentioned crack lengths are compared on Fig. 7.17 (a). With respect to further estimating the effect of the pre-crack in nanosheet, the maximum tensile stress for crack-free MoS_2 nanosheet (0L) is also presented, for making a comparison with cracked samples. As expected, the tensile strength of two dimensional composite 2H/1T MoS_2 heterostructure decreases under the effect of crack-shape defects. Obviously, crack length increase, has a weakening effect on ultimate tensile strength of composite 2H/1T MoS_2 heterostructure, as the maximum stress values drop significantly by increasing the crack size. With reference to

Fig. 7.17 (a), a sharp reduction in the tensile strength is observed in all composite MoS_2 structures with crack sizes less that L/6, while larger crack sizes showed approximately a linear trend. Additionally, according to Fig. 7.17 (b) an approximately sudden decrease in strain-at-failure is distinguished in samples with crack sizes less than L/6, while for larger crack sizes the decreases were very slow.

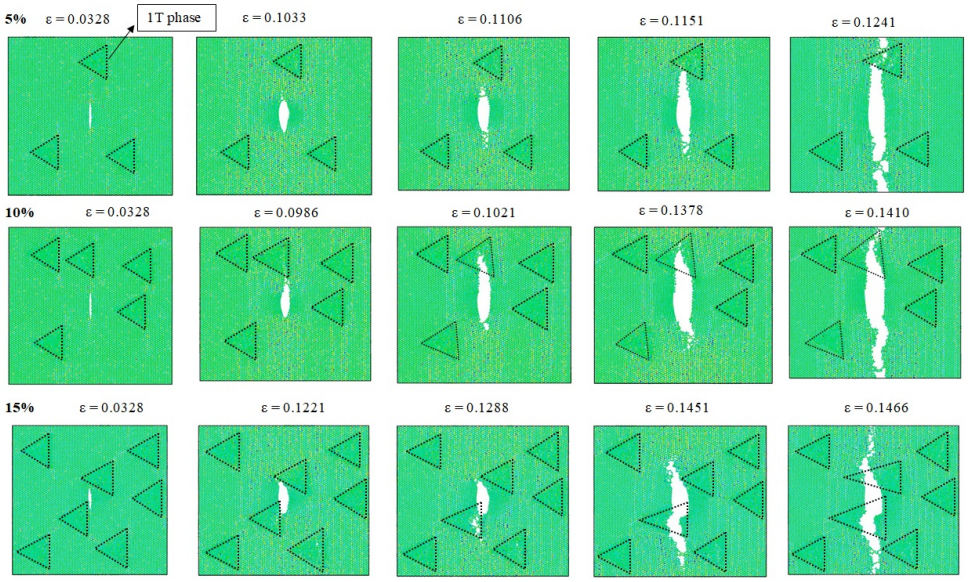

FIGURE 7.13: Deformation processes of single-layer MoS_2 heterostructures for different concentrations of 5%, 10% and 15% of the 1T phase inside the 2H phase including a crack of length L/6 and sheet side length of 25 nm at various stages of the uniaxial tensile strains (ϵ) at room temperature.

7.3.3 The effect of pre-existing notch on the mechanical response

Finally, we investigate the effect of notch shaped defects on the mechanical behavior of MoS_2 nanosheets. The impact of the notch on the mechanical properties highly depends on the location of the notch in the samples. Furthermore, fracture is a phenomenon with size effects and the notch diameter influences mechanical properties of the two-dimensional material. Therefore, we investigate notches located in the center of the nanosheet where their diameter range are L/6, L/3 and L/2. These sizes are selected similar to the length of previously studied cracks, enabling a comparison between these two kinds of defects. The existence of notch leads to a decrease in the tensile strength, Young's modulus and strain-at-failure compared to the samples without pre-existing notch.

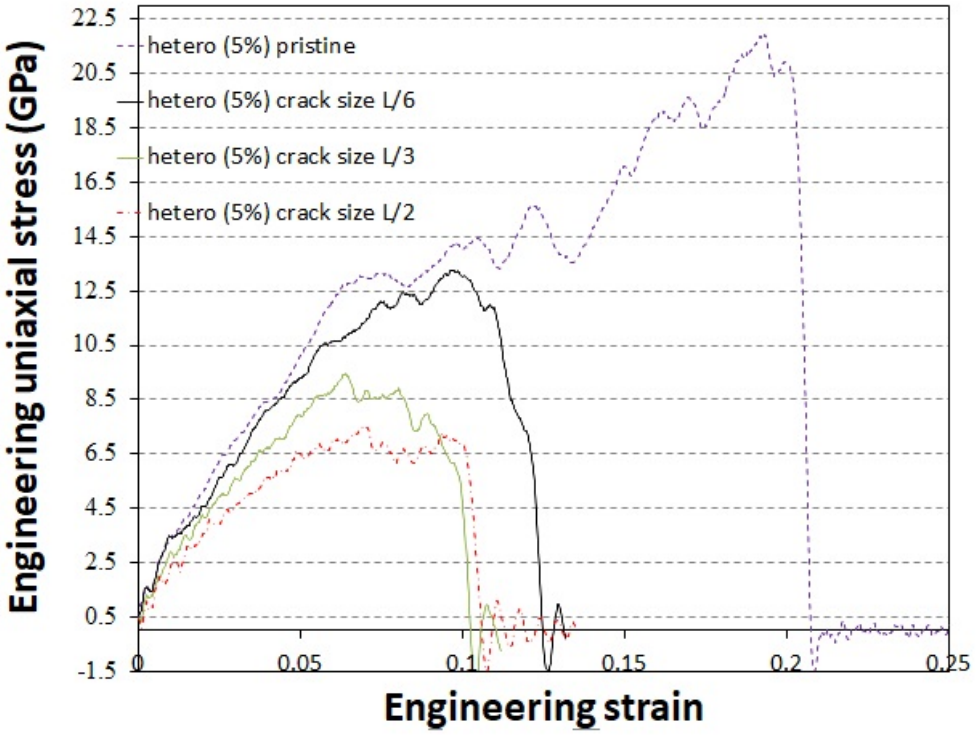

FIGURE 7.14: Plot of stress-strain diagrams to investigate crack size effect on single-layer MoS_2 heterostructures for concentrations of 5% under uniaxial loading at room temperature.

Fig. 7.18 depicts the 2H phase of single-layer MoS_2 film with a pre-existing center notch with L/6 diameter size at different time steps and associated strain values. Additionally, strains at each stage are shown on each picture which is 0.1581 at the end of notch propagation process of the whole length. The obtained stress-strain curves for the samples with pre-exiting notches in 2H phase MoS_2 nanosheet have been shown in Fig. 7.19. With reference to Fig. 7.20 (a), a sudden reduction in the tensile strength is observed in 2H phase MoS_2 models with notch sizes less that L/6, while larger notch sizes showed approximately a linear trend. As it can be seen in this figure, the tensile strength drops by 42%, 47% and 61% for samples with L/6, L/3 and L/2 of notch sizes, respectively.
Fig. 7.21 illustrates the obtained stress-strain curves for the samples with pre-exiting notches in 1T phase MoS_2 nanosheet. According to Fig. 7.22(a), the tensile strength drops by 18%, 39% and 45% for samples with L/6, L/3 and L/2 of notch sizes, respectively. Based on Fig. 7.22(c), the Young's modulus drops by 12%, 22% and 40% for samples with L/6, L/3 and L/2 of notch size, respectively.
In the next step we draw our attention to 2H/1T MoS_2 heterostructures. Figs. 7.23, 7.24 and 7.25 illustrates the obtained stress-strain curves for the samples with pre-exiting notches in composite MoS_2 nanosheets with 5%, 10% and 15% concentration of 1T phase in 2H phase, respectively.

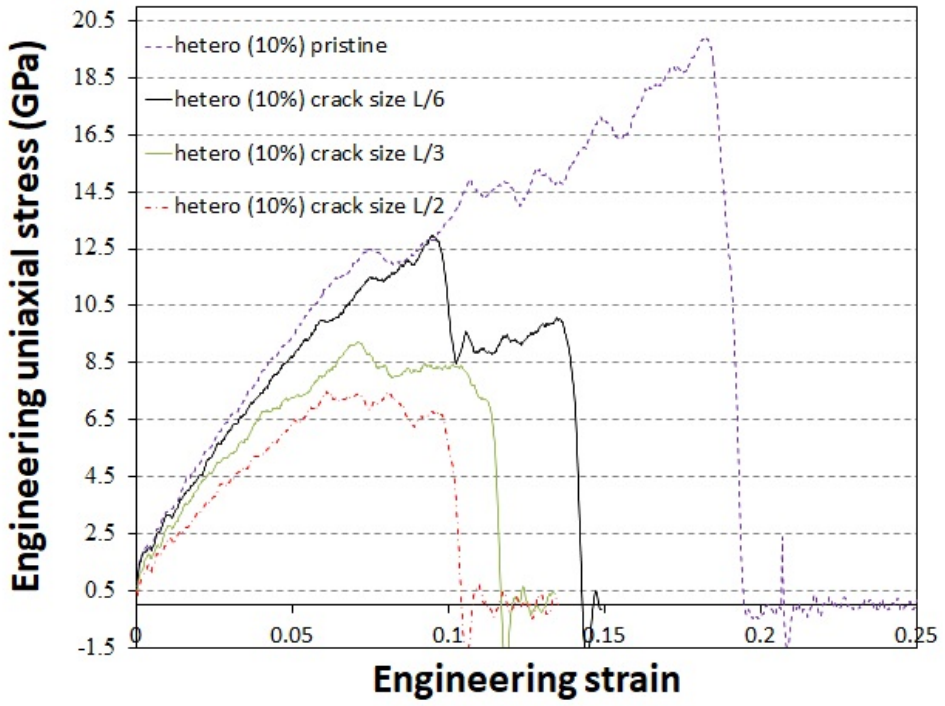

FIGURE 7.15: Plot of stress-strain diagrams to investigate crack size effect on single-layer MoS_2 heterostructures for concentrations of 10% under uniaxial loading at room temperature.

Fig. 7.26 summarizes our results for the fracture mechanics properties of the above mentioned different 1T concentrations of 2H/1T heterostructures and three notch sizes. Ultimate tensile strengths of 2H/1T MoS_2 heterostructure for the previously mentioned notch diameters are compared on Fig. 7.26 (a). With respect to further estimating the effect of the existing notches in nanosheet, the maximum tensile stress for notch-free MoS_2 nanosheet (0L) is also presented, for making a comparison with notched samples. As expected, the tensile strength of the two dimensional composite 2H/1T MoS_2 heterostructure decreases under the effect of notch-shape defects. Obviously, notch diameter increase, has a weakening effect on ultimate tensile strength of composite 2H/1T MoS_2 heterostructure, as the maximum stress values drop significantly by increasing the notch size. Additionally, among the three mentioned studied composite samples, for 10% concentration model a drop in the tensile strength and failure strain is more pronounced compared to the defect-free specimen.

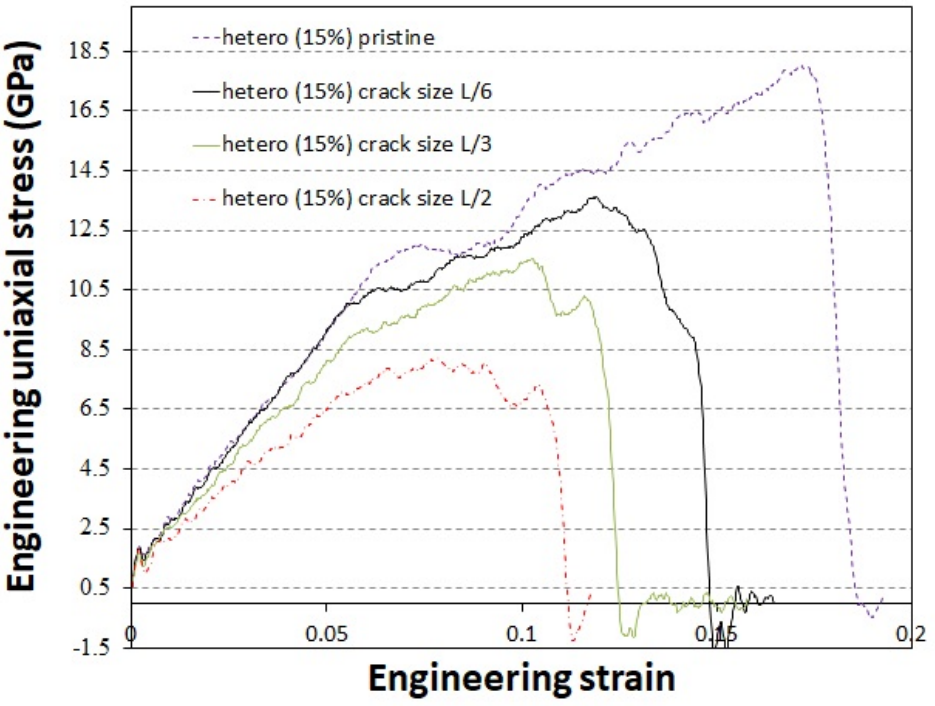

FIGURE 7.16: Plot of stress-strain diagrams to investigate crack size effect on single-layer MoS_2 heterostructures for concentrations of 15% under uniaxial loading at room temperature.

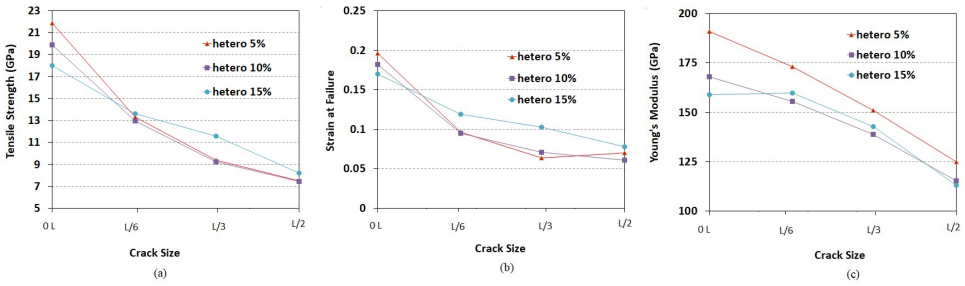

FIGURE 7.17: Fracture properties of monolayer MoS_2 nanosheet heterostructures including different crack sizes and for concentrations of 5%, 10% and 15% at room temperature (a) Ultimate tensile strength, (b) Engineering axial strain at ultimate tensile strength (c) Young's modulus of MoS_2 under uniaxial loading.

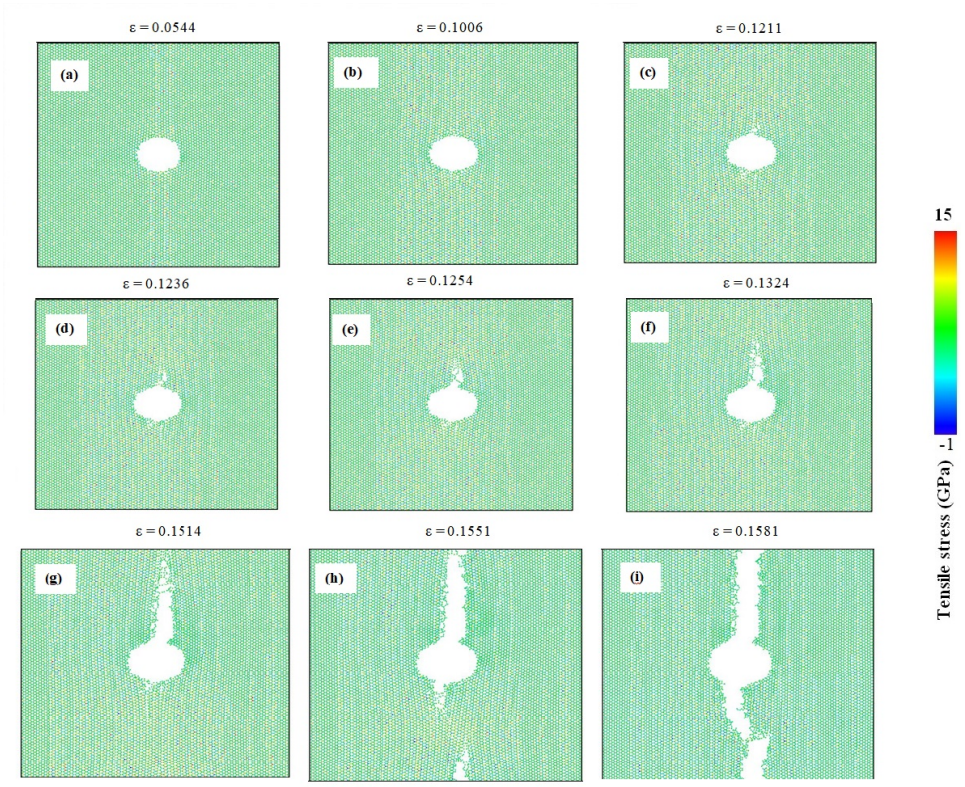

FIGURE 7.18: Deformation processes of 2H phase single-layer MoS_2 including L/6 notch diameter and sheet side length of 25 nm at various stages of the uniaxial tensile strains (ϵ) at room temperature.

7.3.4 Comparing the results of all pre-cracked and notched MoS_2 nanosheet heterostructures

In order to have further understanding of the effectiveness of all three phases of MoS_2 single-layer structures, under the effect of uniaxial loading condition at room temperature, in the presence of defects, and comparing fracture properties of all monolayer MoS_2 nanosheet heterostructures, we show all the obtained ReaxFF molecular dynamics results for pre-cracks and pre-notches in Figs. 7.27 and 7.28, respectively. With reference to these figures, for all studied crack and notch sizes, 2H phase of MoS_2 films has larger strength and Youngs modulus. Also, for this phase a drop in tensile strength and failure strain is more pronounced compared to the defect-free specimen. The lowest strength and Young's modulus belongs to 1T phase. The results for 2H/1T MoS_2 heterostructure with different concentrations are below the equivalent 2H phase but higher than 1T phase. However, tensile strength and Young's modulus of cracked and notched nanosheets of 1T phase are well below both single-layer 2H and all studied 2H/1T composite structures of MoS_2. According to the results (Table 7.1 and Fig. 7.27(a)), for the MoS_2 samples of 2H phase, hetero (5%), hetero (10%), hetero (15%) and 1T phase

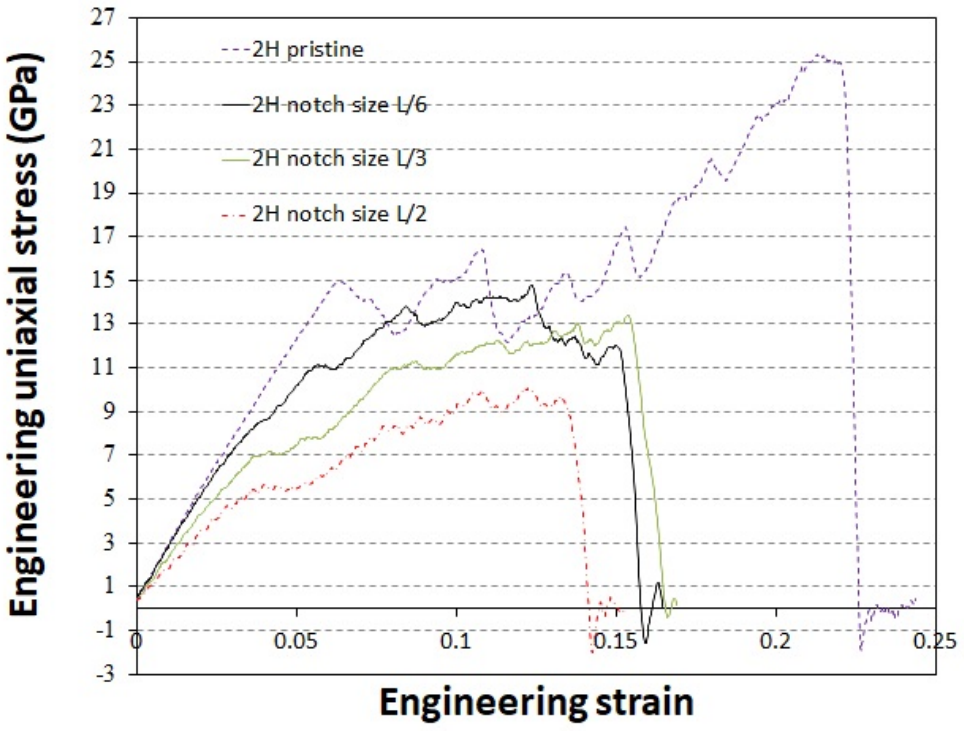

FIGURE 7.19: Plot of stress-strain diagrams to investigate notch size effect on single-layer 2H MoS_2 nanosheet models.

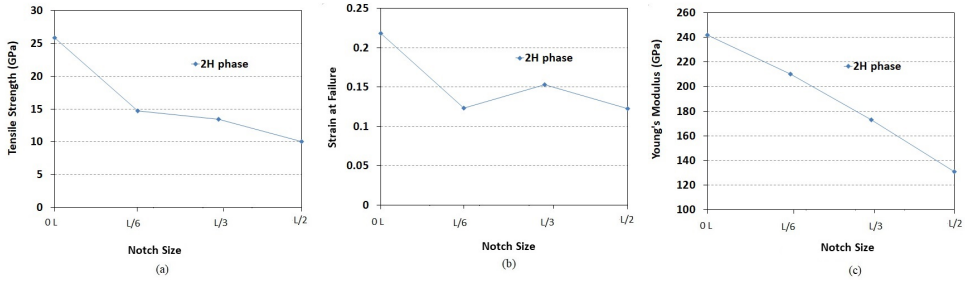

FIGURE 7.20: Fracture properties of 2H phase monolayer MoS_2 nanosheet including different notch sizes under uniaxial loading at room temperature (a) Ultimate tensile strength, (b) Engineering axial strain at ultimate tensile strength (c) Young's modulus.

at room temperature, shifting the samples from crack-free to having L/6 initial center-crack, lead to a large drop in the tensile strength by 48%, 39%, 35%, 24% and 17%, respectively. For the aforementioned phases, when the initial center-crack length increases from L/6 to L/3, a decrease in tensile strength of 25%, 29%, 29%, 15% and 22% is observed respectively. Also, according to Fig. 7.27(b) for the samples of 2H phase, hetero (5%), hetero (10%), hetero (15%) and 1T phase, a pronounced drop in failure strain is observed. The strain-at-failure is reduced by 61%, 51%, 48%, 30% and 20% compared to the defect-free samples, respectively. A drop of 23%, 34%, 25%, 16% and

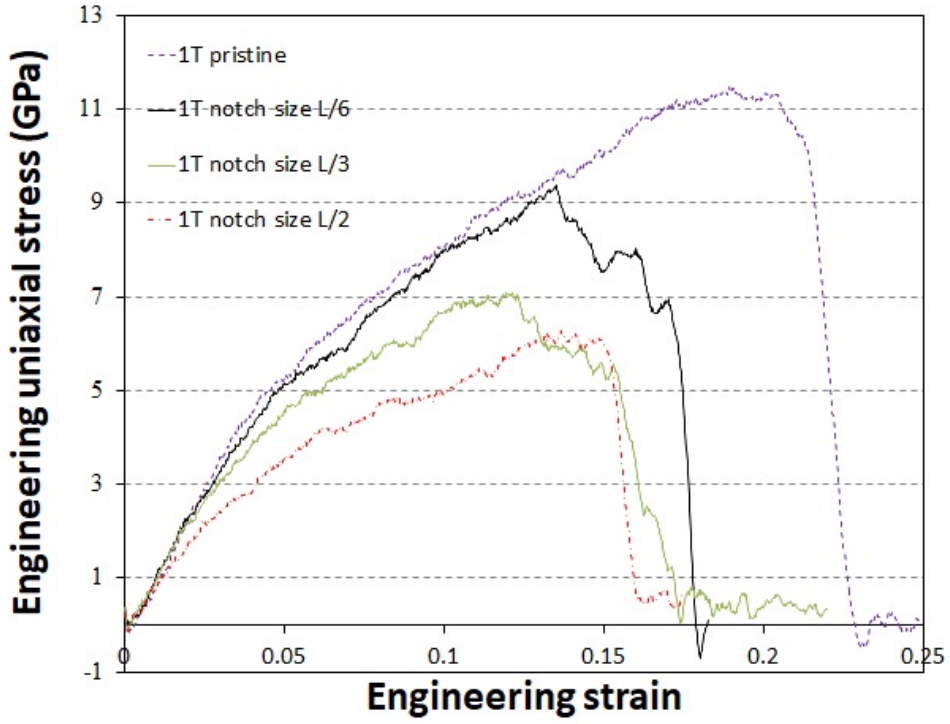

FIGURE 7.21: Plot of stress-strain diagrams to investigate notch size effect on single-layer 1T MoS_2 nanosheet models.

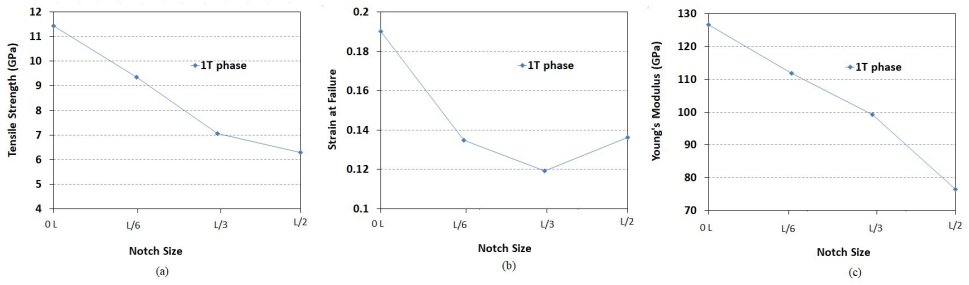

FIGURE 7.22: Fracture properties of 1T phase monolayer MoS_2 nanosheet including different notch sizes under uniaxial loading at room temperature. (a) Ultimate tensile strength, (b) Engineering axial strain at ultimate tensile strength (c) Young's modulus.

20% in strain-at-failure also occurs when initial crack length is increased from L/6 to L/3.

With respect to the results (Fig. 7.28(a)), for the MoS_2 samples of 2H phase, hetero (5%), hetero (10%), hetero (15%) and 1T phase at room temperature, shifting the samples from pristine to having L/6 pre-existing center-notch, lead to a large drop in the tensile strength by 43%, 17%, 34%, 21% and 18%, respectively. A drop in tensile strength of 9%, 40%, 24%, 8% and 24% is observed when the pre-existing center-notch diameter increases from L/6 to L/3, respectively.

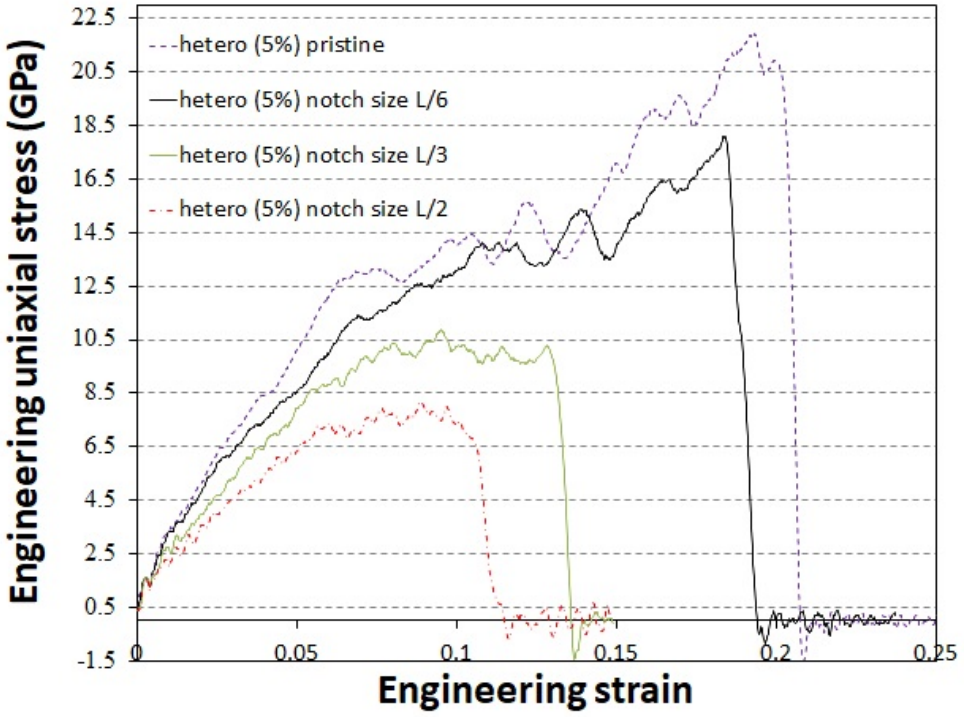

FIGURE 7.23: Plot of stress-strain diagrams to investigate notch size effect on single-layer MoS_2 nanosheet heterostructure models with 5% concentration of 1T phase.

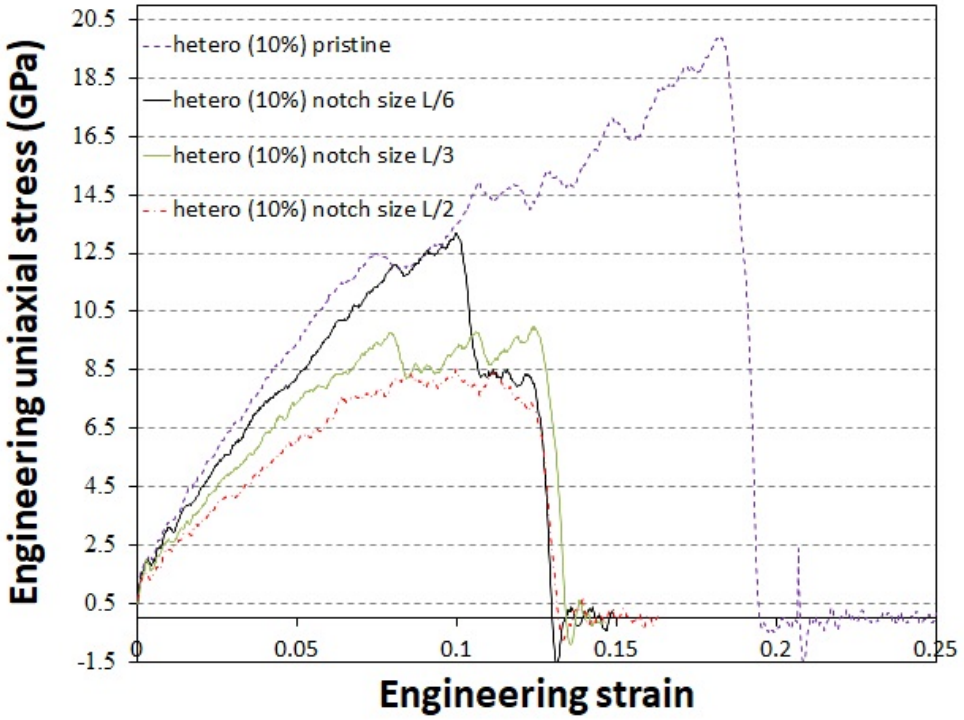

FIGURE 7.24: Plot of stress-strain diagrams to investigate notch size effect on single-layer MoS_2 nanosheet heterostructure models with 10% concentration of 1T phase.

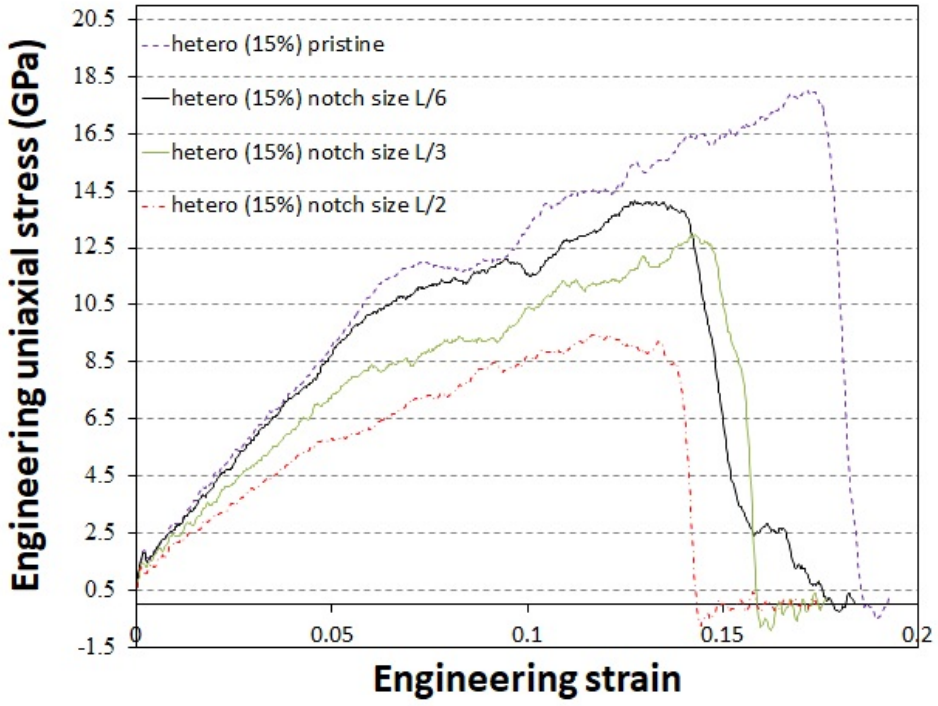

FIGURE 7.25: Plot of stress-strain diagrams to investigate notch size effect on single-layer MoS_2 nanosheet heterostructure models with 15% concentration of 1T phase.

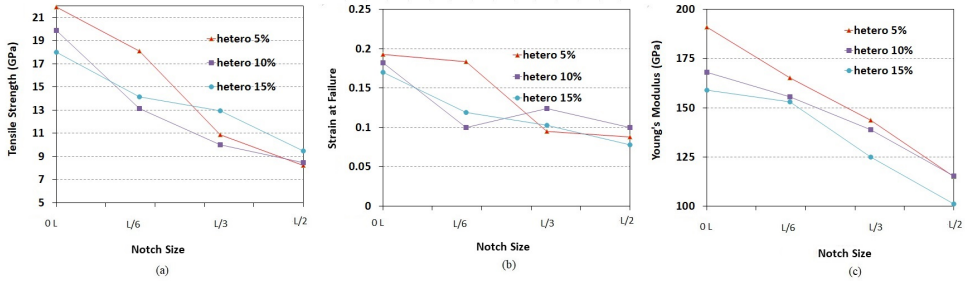

FIGURE 7.26: Fracture properties of monolayer MoS_2 nanosheet heterostructures including different notch sizes and for concentrations of 5%, 10% and 15% at room temperature (a) Ultimate tensile strength, (b) Engineering axial strain at ultimate tensile strength (c) Young's modulus of MoS_2.

Fig. 7.29 shows the plots of the fracture properties versus defect size for pre-cracked and their corresponding values for pre-notched samples of monolayer 2H MoS_2 material enabling us to make a comparison between the results. The comparison of the results for cracked and notched 2H MoS_2 nanosheet models shows that the ultimate tensile strength and strain-at-fracture of the notch samples are higher than the samples with crack, while the Young's modulus of notch samples are lower than the cracked ones with similar sizes. Therefore, the load bearing capacity of the notched samples of 2H phase MoS_2 nanosheets are higher than the cracked ones.

TABLE 7.1: Comparing uniaxial strength of cracked nanosheets of all-MoS_2 single-layer heterostructures at room temperature.

Crack length	**Uniaxial tensile strength (GPa) of all-MoS_2 monolayers**				
	2H	1T	2H/1T (5%)	2H/1T (10%)	2H/1T (15%)
L/6	13.40	9.50	13.30	12.97	13.60
L/3	10.11	7.40	9.40	9.23	11.56
L/2	7.78	6.13	7.50	7.46	8.23

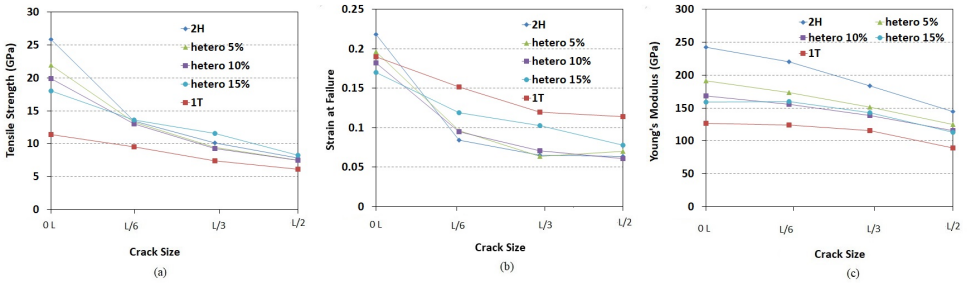

FIGURE 7.27: Fracture properties of all phases of monolayer MoS_2 nanosheet including different crack sizes (a) Ultimate tensile strength, (b) Engineering axial strain at ultimate tensile strength (c) Young's modulus.

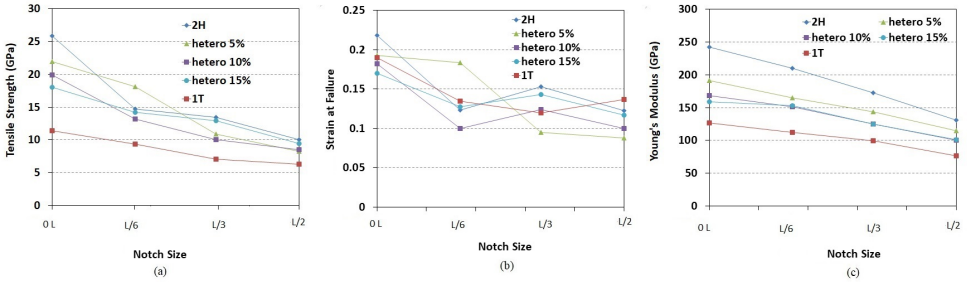

FIGURE 7.28: Fracture properties of all phases of monolayer MoS_2 nanosheet including different notch sizes (a) Ultimate tensile strength, (b) Engineering axial strain at ultimate tensile strength (c) Young's modulus.

Additionally, for monolayer 1T MoS_2 models, the comparison of results for cracked and

notched samples with identical crack length and notch diameter indicates that the ultimate tensile strength and strain-at-fracture of the notch and crack samples are close and therefore load bearing capacity of both cases are almost identical (see Figs. 7.30 (a) and (b)). However, the Young's modulus of cracked samples of 1T phase MoS_2 nanosheets are a little higher than the notched ones with similar size (see Fig. 7.30(c)). According to Fig. 7.31 for all studied composite 2H/1T heterostructures with 5%, 10% and 15% concentrations of 1T phase inside 2H phase, the ultimate tensile strength and strain-at-fracture of the notch samples are higher than the samples with crack, while the Young's modulus of the notch samples are lower than the cracked ones with similar sizes, as shown in Fig. 7.31(c), (f) and (i).

Our molecular dynamic (MD) modeling results confirm that the fracture is a phenomenon with size effect and the crack size and notch diameter non-linearly influence fracture properties of all-MoS_2 heterostructures. Also they are remarkably strong and flexible materials, even in the presence of the defects.

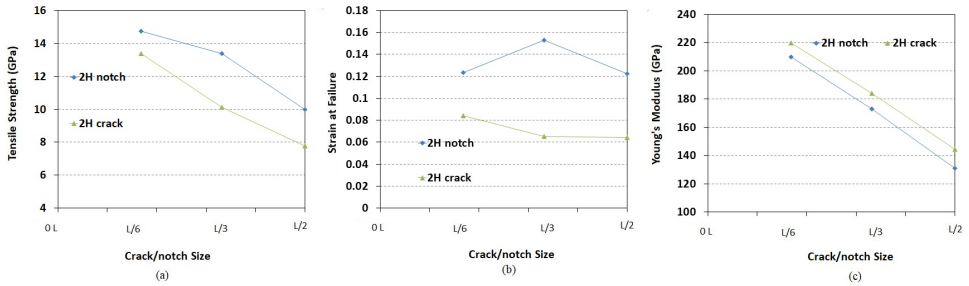

FIGURE 7.29: Comparison between 2H phase of monolayer MoS_2 nanosheets containing pre-crack and pre-notch defects (a) Ultimate tensile strength, (b) Engineering axial strain at ultimate tensile strength (c) Young's modulus.

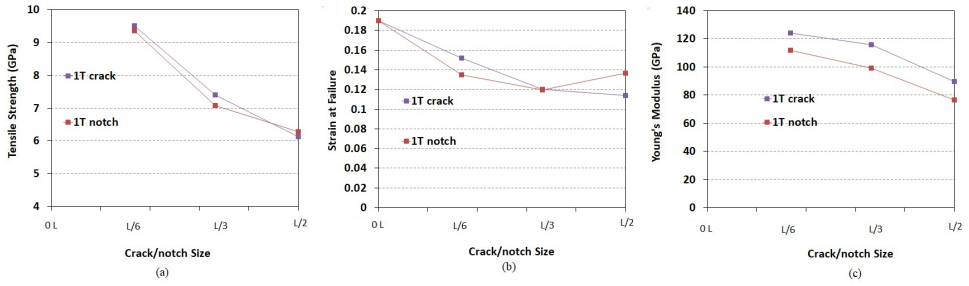

FIGURE 7.30: Comparison between 1T phase of monolayer MoS_2 nanosheets containing pre-crack and pre-notch defects (a) Ultimate tensile strength, (b) Engineering axial strain at ultimate tensile strength (c) Young's modulus.

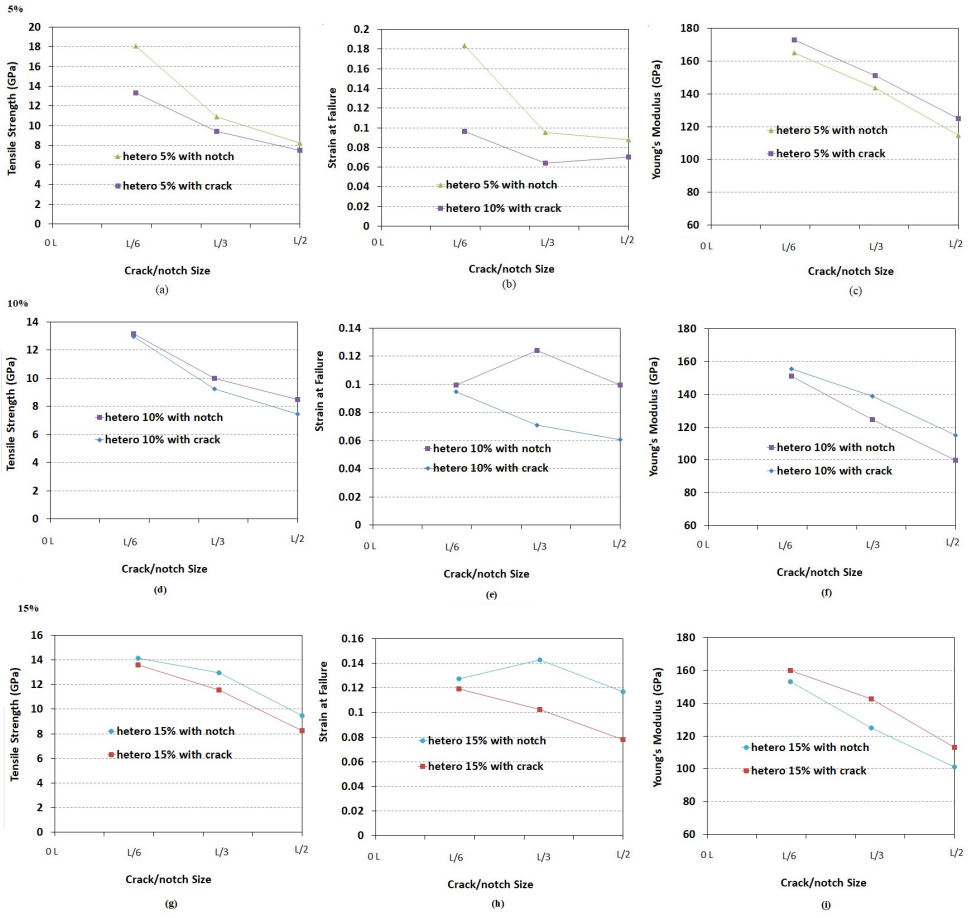

FIGURE 7.31: Comparison between composite MoS_2 nanosheets with different concentration containing pre-crack and pre-notch defects (a) Ultimate tensile strength for nanosheets with 5% concentration. (b) Engineering axial strain at ultimate tensile strength for nanosheets with 5% concentration (c) Young's modulus for nanosheets with 5% concentration. (d) Ultimate tensile strength for nanosheets with 10% concentration. (e) Engineering axial strain at ultimate tensile strength for nanosheets with 10% concentration. (f) Young's modulus for nanosheets with 10% concentration. (g) Ultimate tensile strength for nanosheets with 15% concentration. (h) Engineering axial strain at ultimate tensile strength for nanosheets with 15% concentration (i) Young's modulus for nanosheets with 15% concentration.

Chapter 8

Conclusion

8.1 Summary of Achievements

The aim of current research is two folds. The first fold is dedicated to investigate the effect of several loading conditions on three-dimensional elastic stress distribution of above-ground and underground polyethylene pipelines for gas transportation in the presence of circular hole defects with different hole depth and diameter, and also to examine the effectiveness of polyethylene (PE) repair patches which are perfectly bonded and electrofused onto the gas pipes and buried under the ground, by estimating stress distribution using finite element method (FEM). Several problems with complicated pipe soil interactions and defect sizes is reached using the finite element models, and after imposing boundary conditions and ladings proposed in this research. The results of stress calculations enables us to know if the defective pipe section needs an argent repair or may withstand imposed loading conditions for longer time even with the presence of defects. Also, understanding stress distribution in the vicinity of defects and the trend of maximum stresses variation with respect to holes size and depth will be helpful in selecting effective repair patches. The proposed approximate method can be used as a simple and efficient numerical engineering analysis and design tool to predict three-dimensional elastic stresses in patch bonded on buried PE pipes. Owing to the symmetrical nature of the problem, only a quarter of the physical problem was analysed using appropriate elements incorporated within Ansys package. The mesh generation was made finer in the highly stressed regions of major interest. Obviously, the stresses at the tip of sharp corners resulting from voids in pipe wall, is "stress singularity", which means the stress is very sensetive to the mesh and we can't get accurate results. Therefore, the defective polyethylene pipe material may show ductile or brittle manner. For all the results produced in this fold of research, and assuming ductile behavior, it

was assume that no local yielding occurred at the defect region and elsewhere in the pipe and patch. In order to capture the results at stress singularities and to investigate sharp corner defects, we used fracture mechanics methods and SIFs were calculated and compared to their critical values. From the work that has been done in the first fold, the conclusions are summarized as follow:

- The results show a tendency of the stress distributions, as well as stress concentration factors on radial bore diameter and depth sizes. The first principal and von Mises stress distributions and stress concentration factors presented in this research, show that the introduction of a radial hole into a polyethylene pipe wall significantly increases the aforementioned stresses and consequently stress concentration factors that would otherwise be present in the similar plain undisturbed PE pipe.

- In both above-ground and underground polyethylene gas pipes, for outer pipe surface defects with depth ratios higher that 8%, stress concentration factors and therefore maximum stress values around the hole region is significantly larger than the stresses in the rest region of the pipe. For defect depth ratios below 8% and hole diameters up to 30 mm, the peak stresses is close to pristine simple pipe and is not influenced significantly by the damage itself, therefore these defects can be considered as non-intensive.

- Localized pipe behavior is mostly affected by circumferential (hoop) stresses. stress concentration factors, maximum first principal stresses and maximum von Mises stresses generally show an increase trend by increasing defect size, including hole diameter and hole depth. This effect is more pronounced for larger defects. As an example, for a circular hole defect with 30 mm diameter and 83 % depth to thickness ratio, stress concentration factor reached high valuse as 5.5 and 8 for underground and above-ground pipes, respectively.

- For complete circular hole defects, the location of stress concentrations and maximum stresses are at the inside lip of the hole at the pipe inner surface, at the edges along the length of the pipe.

- Temperature changes in the defective PE pipe exhibits a direct and significant effect on thermal stresses produced in the defective pipe. The reason is that polyethylene exhibits a high value of coefficient of thermal expansion when compared to metals. This effect must be considered accurately in all stress calculations.

- FE modeling results show that patch repair can strengthen the defected pipe section and reduce the imposed first principal and von Mises stresses significantly

even under severe temperature changes of the pipe. For a defective buried pipe with 4 inches diameter and under the simulataneus effect of 4 bar internal pressure, soil column weight, trafic load and severe temperature change of 22 °C, a 3 inch long saddle fusion HDPE patch with 4.76 mm thickness, successfully repiars circular holes up to 20 mm diameter in the pipe wall.

- For above-ground PE pipe subjected to complete circular hole, comparing the values of maximum stresses and the allowable stresses for 50 years working life, it is clear that for all investigated temperature changes (and also models with no temperature change) and defect ranges, the maximum first principal stress and maximum von Mises stress are higher than their design limit, which means the stresses are in unsafe range and the pipe material can't withstand the inside pressure of 4 bar.

- Comparing the results for maximum first principal and maximum von Mises stresses versus circular hole size, in buried PE pipe with the similar stresses in above-ground pipe shows that in underground pipelines, the stresses increase rate with respect to hole diameter, is very slower than in above-ground pipelines. This behavior can be translated to the reinforcement effect of surrounding soil on strengthening the pipe.

- For underground PE gas pipe with complete holes, maximum first principal stress and maximum von Mises stress are significantly higher that their allowable counterpart for 50 years life expectancy, in all mentioned working temperatures. This means the stresses values are in unsafe limit and both HDPE and MDPE pipes won't withstand the aforementioned applied loads.

- For underground PE gas pipe with complete holes, 30 °C temperature rise in the pipe has the most influence on both maximum first principal and maximum von Mises stresses. This temperature change imposes significant tensile stress in the defect area.

- For underground PE gas pipe with complete holes, comparing the values of maximum stresses and the allowable stresses for 50 years working life, shows that for all investigated temperature changes (and also models with no temperature change) and defect ranges, the maximum first principal stress and maximum von Mises stress are higher than their design limit, which means the stresses are in unsafe range and the pipe material can't withstand the inside pressure of 4 bar.

- For defect depth ratios up to 8 % in underground PE gas pipe, stress concentration factor remains unity, which means this size of defect doesn't imposes additional

stresses to the pipe in comparison to the non-defective pipe.

The second objective is to study the defects and crack propagation in two dimensional nanosheets by performing a molecular dynamics simulation. The studied materials are Graphene-like BC_3 and different phases of MoS_2 nanosheets. Based on the MD calculations the resulted can be summarized as below:

- loading the defect-free BC_3 nanosheets along the zigzag direction results in higher modulus of elasticity than the armchair orientation. For both orientations, the lower modulus of elasticity (E) occurs at higher temperatures.
- With respect to the maximum tensile stresses, the results indicate that for studied nanosheets at high temperatures, the BC_3 films along the zigzag direction can show higher strengths than the sheets loaded in armchair orientations, even though, at low temperatures the sheets along armchair direction can indicate higher tensile strengths.
- Graphene-like BC_3 films subjected to cracks and notch shape defects have significantly lower ultimate tensile strength compared to their pristine material.
- The results of pristine structures reveal a decreasing tensile strength with increasing temperature.
- increasing crack length decreases the ultimate tensile strength of the material as well as the strains-to-failure. For crack models, the tensile strength of graphene-like BC_3 nanosheet decreases by increasing the temperature due to the weakening effect of the temperature on the atomic bonds.
- The results for notch shaped defects simulation revealed that the existence of such defects in BC_3 monolayers reduce the strength of the material significantly.
- A comparison between crack and notched models of identical length and notch diameter showed that the load bearing capacity of both cases are nearly identical.
- For all studied crack sizes, 2H phase of MoS_2 films has larger strength. Fracture properties of composite 1T/2H MoS_2 nanosheet are higher than those for the equivalent 1T phase. We can imply that the pre-cracked composite structure is remarkably stronger than equivalent 1T phase.

8.2 Scope of Future Work

In the work presented at the first part of the research, different defect models are introduced and studied in 3D and used to study above ground and under ground pipelines and also in the presence of the repair patches. Some suggested extensions in order to further widening the scope of the first fold of research to the current work could be:

- An important trenchless method of installing underground utilities such as pipes is horizontal directional drilling (HDD). This technique offers significant environmental advantages over traditional cut and cover pipeline installations. Once drilling occurs, a cylindrical volume of the formation will be removed and this will change the stress regime near borehole. The investigation of mechanical behavior of gas pipelines installed underground by HDD is highly recommended.
- Investigating other shapes of defect in buried pipelines including crack defects and the crack propagation path. Additionally, the effect of defects at polyethylene fittings and joints on stress distribution should be studied.
- In this research, PE was treated as a linear elastic material and the resulting stresses were compared with the minimum required strength (MRS). Therefore, it is recommanded to include viscoelastic behavior of polyethylene in any modeling process to stress calculation, as polyethylene pipes are viscoelastic in nature.
- There are differences between the real and finite element models due to uncertain parameters such as geometrical and physical properties, which can be reduced by updating the model. To determine the uncertain parameters, local and global sensitivity analyses should be performed. Therefore, it is suggested to Perform sensitivity analysis of different effective parameters in the underground structures operation in order to investigate the most effective parameters in the buried defective and patch repaired pipe behavior under several loadings.
- Under the cyclic stress conditions, the fatigure life of the pressure vessel or piping system is severely reduced. Investigating dynamic loads including dynamic gas pressure in the pipe and the seismic effects and loads which may be imposed to defective buried pipe is suggested.
- If the bore axis is offset from the radial center-line of the cylinder, the stress distribution and therefore the life of this pipe will be substantially different from that of a similar pipe containing a radial hole. Therefore, we recommand to investigate defects with offset configuration.

- Estimated lifetime of underground oil and gas pipelines under severe oscillating mechanical and thermal stresses.
- Available in several sizes, the patches can be used separately or side by side to repair large areas. It is recommended to investigate the effect of applying separate patches on several nearby defects in a pipe.
- Investigating other patch configuration and also the variation of patch thickness and size. Also, the effect of other patch materials like composite patches need to be investigated.
- In this research it was amused that the patches are bonded to defective pipes by using fusion technique. However, an important technique, besides the use of fusion that is used to bond materials is to bond materials together by adhesives or resins. It is recommended to conduct similar investigation with adhesive bonds between pipe and patch.
- In order to validate and evaluate the results, it is recommended to investigate the current problem with other methods such as Isogeometric Analysis (IGA), Differential Quadrature method (DQM) and comparing the results obtained from new method with the present method (FEM) and also compare the computation costs.

In the work presented at the second part of the research, different pristine and defective models are introduced and studied in 2D and used to study nanosheets. Some suggested extensions in order to further widening the scope of the second fold of research to the current work could be:

- The development of the models of Graphene-like BC_3 and MoS_2 for the new synthesized, high energy, high performance, and long-life two-dimensional materials.
- Investigating the effects of 1T phase concentration and domain size on the fracture properties of the composite 2H/1T MoS_2 structure and also temperature effect on pre-cracked all-MoS_2 single-layer heterostructures.
- Investigating the effect of other modes of fracture on fracture properties of both Graphene-like BC_3 nanosheets and 2H phase, 1T phase and composite 2H/1T MoS_2 structures.

Appendix A

Finite Element Method (FEM) and ANSYS

In numerical procedures, the first step is discretization. This process divides the medium of interest into a number of small sub regions and nodes. The common classes of numerical methods which are used to find approximate solutions for a wide range of engineering applications are: finite element methods (FEM), finite difference methods, boundary element, finite volumes and meshless methods. Each method has its own benefits and drawbacks. For example, with finite difference methods, the differential equation is written for each node, and the derivatives are replaced by difference equations. This approach results in a set of simultaneous linear equations. Although finite difference methods are easy to understand and employ in simple problems: they become difficult to apply for problems with complex geometries or complex boundary conditions.
The finite element method has become a powerful tool for the numerical technique which gives approximate solutions to differential equations that model a wide range of problems arising in physics and engineering. The advantage of the FE method is that in principle any problem can be solved, irrespective of the geometry and even considering complex constitutive relations. While FEM was introduced by Clough [178], in a paper on vibration in plates but this idea returns back to many years before this publication. With the advances in computer technology, nowadays finite element method becomes one of the most well known and strong tools between other strong numerical methods for modeling and simulation of various problems in science and industry. The method however, can be used in other disciplinary such as agriculture, medical, physics and many other areas. One application of FEM is solid mechanics where a group of physical laws, mathematical equations and numerical and computational algorithms should be solved in order to understand structural behavior of different materials under the effect of

several initial, boundary and loading conditions. This technique which is a superior discretization method can be described from both mathematical and physical standpoint. In physical FEM the concept is to subdivide the mathematical model into separated segments of simple geometry which are called elements. Every element is presented by a finite number of degrees of freedom which are defined as an unspecified function value, as a group of nodal points. The result of the mathematical model is finally estimated via the discrete model achieved by assembling the collection of all elements [179–181]. The finite element method was first applied to structural related problems such as stress analysis; and has since, due to its versatility, been applied to other problems of continua. In all applications, the analyst seeks to evaluate a field quantity. In stress analysis, it is the displacement field or stress field. In problems involing thermal analysis it is the temperature field or the heat flux. In fluid flow problems, it is the stream function or the velocity potential function. FE analysis does not produce a formula as a solution, nor does it solve a class of problems. Additionally, the solution is approximate unless the problem is so easy that the stiffness matrix can be solved explicitly. A simple description of the FE method is that it involves cutting a structure into several elements (piece of structure), describing the behavior of each element in a simple procedure, and then reconnecting elements at "nodes".

This approach results in a set of simultaneous algebraic equations. In stress analysis these equations are equilibrium equations of the nodes. In a finite element model, equilibrium is approximated by a finite set of equations by introducing interpolation functions. The interpolation is assumed to be based on material coordinates in the material skeleton [182]. In order to accomplish the FE analysis, these set of equations need to be solved by computer. Generally, a FE method solves a problem through piecewise polynomial interpolation. In other words, over an element, a field quantity such as displacement is interpolated from the values of the field quantity at nodes. By connecting elements together, the field quantity becomes interpolated over the entire structure in piecewise fashion. The minimization process generates a set of simultaneous algebraic equations for values of the field quantity at nodes. Matrix symbolism for this set of equations is:

$$[K]\{U\} = \{F\} \tag{A.1}$$

Where U is the vector of unknowns (values of the field quantity at the nodes), F is a vector of unknown loads, and K is a matrix of unknown constants. In stress analysis, K is known as a "stiffness matrix". In order to formulate a finite-element model, it is required to follow several steps before model can be run. These steps can be summarized as: could be:

- Collecting governing equations.
- Physical process identification and description.
- Input data collection.
- Mesh generation, discretization and verification.
- Material model assignment.
- Initial loads and boundary conditions.
- Simulations run.
- Results extraction, analysis and verification.

Following the governing equations are initialized then it is necessary to have a conceptual perspective of the problem. This provides an initial estimate of the expected behavior under imposed conditions. Predicting the physical process, stress and displacement fields play a pivotal role in finite-element analysis. Some questions and/or concerns should be asked when identifying physical processes. For instance: Is the process linear or nonlinear or combination of both? Following identifying the behavior type in the model, the upcoming question will be what kind of material model to be used? Typical material models can include elastic-plastic, poro-elastic, thermo-elastic, thermo-poro-elastic, visco-elastic, and viscoelasto-plastic [182]. Another concern can be existence of discontinuities in the model. Typical discontinuities can be joints, fissures, fractures and faults. Special features are required to have discontinuities in the numerical model. Having discontinuity in the model often leads in more complexity, numerical errors and convergence problems. Initial and boundary conditions of a numerical model are very critical. Numerical simulation's results can vary significantly if correct conditions are not assigned in the model. Another challenge in assigning these conditions is selecting the best method to apply them in the model. Having symmetry in the model also helps to reduce computation time and complexity of the model. The last, but not the least, step in identifying a physical process is numerical results verification. Analytical equations, lab experiments, field observations and the analysis of natural analogues are often used to verify numerical results. Analytical solutions are often not available when modeling complex physical problems. Conducting laboratory experiments can also be time-consuming and costly.

Proper meshing guidelines are required in order to obtain accurate results from finite-element models. These guidelines can be summarized as [183]:

- Using quadratic elements in model to increase results accuracy and prevent artificial stress effects.
- Selecting sufficiently small element size in order to minimize the error of approximation within acceptable bounds.
- Assigning element's aspect ratios less than five in order to prevent degradation of numerical performance.

ANSYS softwae: Finite element analysis solvers are available in several widely used commercial softwares like Ansys, Nastran, Abaqus, Ls-Dyna and Sap. Among a variety of soft wares, ANSYS can be considered as the global leader in engineering simulation. Since its foundation in 1970, Analysis Systems Inc. (ANSYS) develops, markets and supports engineering simulation software used to predict how product designs will behave in real-world environments. Ansys develops and markets finite element analysis software used to simulate engineering problems. Its graphical user interface ability makes it easier to use [184]. Ansys is a huge program with integrated capabilities which made numerous acquisitions of other engineering design companies, acquiring additional technology for fluid dynamics, electromagnetics, electronics design, acoustics and other physics analysis through the related elements which exist in its element library. Ansys regularly advance simulation solutions by developing very advanced technologies, integrating them into a unified simulation platform capable of complex, multiphysics solutions and providing system services, including high-performance computing (HPC) and cloud solutions, to manage simulation processes and data. Ansys multiphysics simulation allows users explore real-world physical interactions which a complex product may encounter during use. These interactions can impact product performance, safety and longevity to help users examine these effects in any combination, achieving the highest fidelity solution to eliminate reliability problems and design safe and effective products [185]. Most Ansys simulations are performed using the Ansys Workbench and Ansys mechanical APDL softwares, which are among the company's main products. Picking appropriate element type from the large library of elements in ANSYS code (more than 200 types of elements are available) for the required analysis is of special importance. Elements are organized into groups of similar characteristics, for example LINK, BEAM, PLANE, SHELL and SOLID elements for structural analysis. An important reason for such a large number of elements in ANSYS code is computational efficiency.

Element order: Element order refers to the interpolation of an element's nodal results to the interior of the element. This determines how results can vary across an element, and is important if there is high gradients of strain in the model. As an example for this phenomena, consider a beam or plate in bending, where the strain is changing sign over

a potentially very small distance. Element order can be **linear** or **quadratic**. Linear elements do not have midside nodes. Generally, the strain can only vary linearly from one node to another and therefore, a linear element is computationally faster than a quadratic element. Quadratic elements have midside nodes. The shape function for strains varies in some nonlinear fashion between the corner nodes. Whereas linear elements ae flat on both the sides and in-plane, a quadratic element can follow a curvature in both directions and is more accurate for a given number of nodes in the model [186].
SOLID95 3-D 20-Node Structural Solid: There are several volumetric (3D) element types available in Ansys element library. First the volumes could be created in the ANSYS preprocessor or imported from a CAD system and the meshed in model analysis with proper mesh type. Hexahedral elements (brick) can be used to mesh regularly shaped rectangular type volumes, while tetrahedral elements (tets) can be used to mesh any volume. Fig. A.1 illustrates a SOLID45 element which is a 3-D basic linear solid element which is used to mesh volumes in ANSYS and has 8 unique nodes and shape functions of 1^{st} order. Another important element is SOLID95 which is a higher version of the SOLID45 and has a 2^{nd} order shape function [187]. It can tolerate irregular shapes without as much loss of accuracy. These elements can also be tetrahedral and can automatically transition between hexahedral and tetrahedral using pyramids. A model meshed and made of SOLID45 elements takes less computer resources and runs faster than a model of SOLID95 elements because the number of nodes are less than the model meshed with SOLID95. However, the advantage of SOLID95 elements is that, they have compatible displacement shapes and are "parabolic" elements, which their edge-functions are 2-order polynomials, so they can approximate curved edges and therefore are well studied to model curved boundaries. The element is defined by 20 nodes having three degrees of freedom per node: translations in the nodal x, y, and z directions. The element may have any spatial orientation. The element has plasticity, creep, stress stiffening, large deflection, and large strain capabilities. The geometry, node locations, and the coordinate system for this element are shown in Fig. A.2. A Tetrahedral-shaped element may be formed by defining the same node numbers for nodes K, L, and S; nodes M, N, O, P, U, V, W and X. Pressures may be input as surface loads on the element faces as shown by the circled numbers on Fig. A.2. Positive pressures act into the element. Temperatures may be input as element body loads at the nodes. The node I temperature T(I) defaults to TUNIF. If all other temperatures are unspecified, they default to T(I). If all corner node temperatures are specified, each midside node temperature defaults to the average temperature of its adjacent corner nodes. For any other input temperature pattern, unspecified temperatures default to TUNIF. The element must not have a zero volume. Also, the element may not be twisted such that the element has two separate volumes. This occurs most frequently when the element is

not numbered properly [188]. In this research, The elements used for discretization in ANSYS APDL 16.2 are SOLID95.

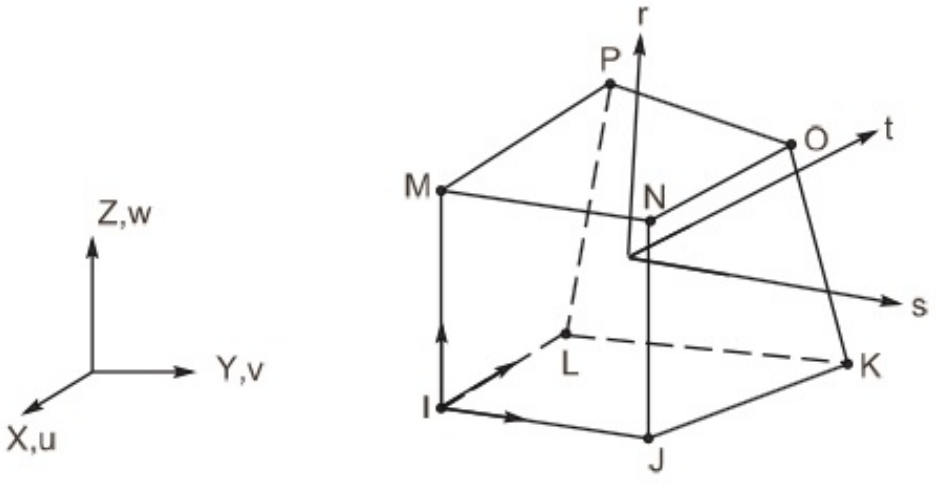

FIGURE A.1: A schematic illustration of SOLID45 3-D 8-Node Structural Solid.

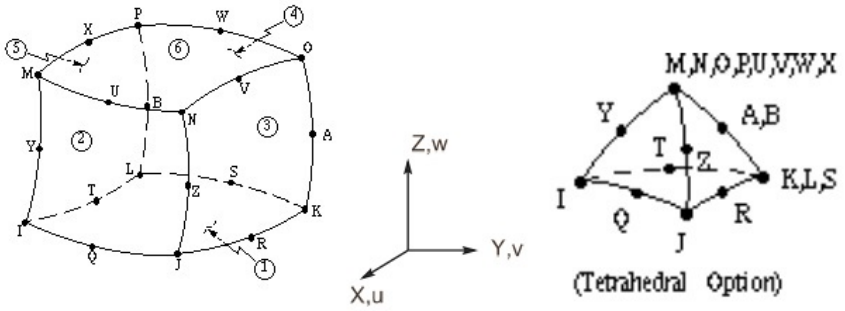

FIGURE A.2: SOLID95 3-D 20-Node Structural Solid.

Simulation run: After all aforementioned steps were accomplished, it would be more effective to run simple test model samples first, prior to running detailed models. This procedure will provide further insight for realizing model limitations. It is always tempting to increase complexities of the models, because it makes it more realistic. Nevertheless, in some cases, adding complexities will have little effect on the model response, so they should be eliminated. Simple runs can also give shortcomings than can be fixed before any significant effort can be invested in the analysis. For example, starting with linear-elastic models always assists to observe and judge model response, and they are very simple to be implemented. Advanced material models can be added to simulations when other issues like proper boundary conditions, element type and time increment

were finalized. It worth mentioning that structural problems are generally more computationally costly compared to other problems such as heat flow. Solid elements for structural models have 3 degrees of freedom on each node (x,y,z displacement). Also, Small features in the geometry create stress concentrations that must be resolved with many small elements because we are interested in the maximum stress.

Appendix B

Molecular Dynamics (MD) Simulation

Computer simulation gives molecular insight that is experimentally unavailable. Molecular dynamics (MD) is a computational method for investigating material behavior by considering the material as a set of discrete atoms. In this method, atoms and molecules are allowed to interact for a fixed period of time and the properties of material which is under several boundary, initial and loading conditions is characterized by this interaction between atoms. By applying initial velocities to a configuration of atoms, molecular dynamics simulates motion and velocity of atoms under applied forces within sometime frames. It uses classical mechanics of Newton's equation of motion to model molecular systems and interaction between atoms. Because, in this kind of problems a very great number of particles are involved, it is impracticable to estimate the behavior of such complicated system by analytical solutions. Therefore, molecular dynamics simulation circumvents this problem by employing algorithmic numerical methods to solve newton's equations for a system of interacting particles and to trace the path of atoms. The interatomic connections and potential energy of all systems are calculated via force fields which is a function of atom positions. In this technique thermal energy is included using a thermostat, which allows potential energy barriers to be overcome, in a realistic manner. The main advantage of the method is that the dynamical evolution of a system, with time, may be followed, which allows comparison with additional experimental techniques such as NMR and quasi-elastic neutron scattering. The data from these simulations provides precise information regarding the coordinates of all atoms within the model at any point in time during the simulation period. This allows the interlayer arrangement and dynamics of for example, organic and water molecules to be evaluated with equal precision [189].

The last step in every molecular dynamics modeling is to display the simulation results. The atomic motions can be formulated as the following equation:

$$m_j \ddot{r}_j = F_j \tag{B.1}$$

$$F_j = -\frac{\partial U}{\partial r_j} \tag{B.2}$$

where, $j = 1, 2, ..., N$, denotes the number of atoms used in simulation. F_j is the atomic interaction and can be evaluated by the potential field (U), which is a function of the atomic position. Several numerical methods can be employed to find atomic trajectories [190]. Numerical solutions were applied over a discretized time where equally distributed time steps (Δt) are considered. The aim of molecular dynamics simulation is to estimate the atomic location (r) after a time step, with respect to its former position at previous time step. After obtaining the trajectory of all atoms, it will be possible to estimate important parameters which are required to characterize material properties.

LAMMPS software: A widely used classical molecular dynamics open source code with a focus on materials modeling is LAMMPS. It's an abbreviation for Large-scale Atomic/Molecular Massively Parallel Simulator. LAMMPS has potentials simulation of solid-state materials and soft matters and also mesoscopic systems. In other words, LAMMPS is a parallel particle simulator at the atomic, meso, or continuum length scales. LAMMPS uses algorithms and techniques that allow the code to exhibit a near linear relationship (scaling) between the number of processors used, or the size of the model system of interest, and time taken for the simulation to be performed [191]. In a molecular dynamics simulation, the style of units should be set by units command, typically at the beginning of an input script, to determine the units of all quantities specified in the input script and data file, as well as quantities output to the screen, log file, and dump files.

Bibliography

[1] Hull JB and John VB. *Non destructive testing*. McMillan Education Ltd, 1972.

[2] Young-Shin Lee and Myung-Jee Chung. A study on crack detection using eigen-frequency test data. *Computers and structures*, 77(3):327–342, 2000.

[3] R Khademi Zahedi, P Alimouri, Hung Nguyen-Xuan, and Timon Rabczuk. Crack detection in a beam on elastic foundation using differential quadrature method and the bees algorithm optimization. In *International Conference on Advances in Computational Mechanics*, pages 439–460. Springer, 2017.

[4] R Khademi-Zahedi. Application of the finite element method for evaluating the stress distribution in buried damaged polyethylene gas pipes. *Underground Space*, 4(1):59–71, 2019.

[5] R Khademi-Zahedi and M Shishesaz. Application of a finite element method to stress distribution in burried patch repaired polyethylene gas pipe. *Underground Space*, 4(1):48–58, 2019.

[6] Reza Khademi-Zahedi and Pouyan Alimouri. Finite element analysis to the effect of thermo-mechanical loads on stress distribution in buried polyethylene gas pipes jointed by electrofusion sockets, repaired by pe patches. *Energies*, 11(10):2818, 2018.

[7] Heung Soo Kim, Maenghyo Cho, Jaehun Lee, Antoine Deheeger, Michel Grediac, and Jean-Denis Mathias. Three dimensional stress analysis of a composite patch using stress functions. *International journal of mechanical sciences*, 52(12):1646–1659, 2010.

[8] Steve Plimpton. Fast parallel algorithms for short-range molecular dynamics. *Journal of computational physics*, 117(1):1–19, 1995.

[9] L Lindsay and DA Broido. Optimized tersoff and brenner empirical potential parameters for lattice dynamics and phonon thermal transport in carbon nanotubes and graphene. *Physical Review B*, 81(20):205441, 2010.

[10] Alper Kinaci, Justin B Haskins, Cem Sevik, and Tahir Cagin. Thermal conductivity of bn-c nanostructures. *Physical Review B*, 86(11):115410, 2012.

[11] R Khademi-Zahedi, M Makvandi, and M Shishesaz. Technical analysis of the failures in a typical drilling mud pump during field operation. In *Proceedings of the 22nd Annual International Conference on Mechanical Engineering—ISME2014, Ahvaz, Iran*, pages 22–24, 2014.

[12] R Khademi-Zahedi, M Makvandi, and M Shishesaz. The applicability of casings and liners composite patch repair in iranian gas and oil wells. In *Proceedings of the 22nd Annual International Conference on Mechanical Engineering—ISME2014, Ahvaz, Iran*, pages 22–24, 2014.

[13] Mehran Makvandi, Heidar Bahmani, and Reza Khademi-Zahedi. Technical analysis of the causes of blowout in bibihakimeh well no. 76. In *Proceedings of the National Conference in New Research of Industry and Mechanical Engineering, Tehran, Iran*, pages 17–18, 2015.

[14] Alireza Bahadori. *Natural gas processing: technology and engineering design*. Gulf Professional Publishing, 2014.

[15] Andrew J. Peacock. Handbook of polyethylene: Structures, properties, and applications. *New York: Marcel Dekker.*, 2000.

[16] Popelar C. F. Characterization of mechanical properties for polyethylene gas pipe materials. *M.S. Thesis*, 1986.

[17] Hirschler M. Cullis C.F. The combustion of organic polymers. *Clarendos press, Oxford*, 1981.

[18] Kenneth H Green, Willie E Rochefort, Nick Wannenmacher, John A Clark, and Kevin Harris. Development of a remote external repair tool for damaged or defective polyethylene pipe. Technical report, Timberwolf Corp, 2006.

[19] American Association of State Highway and USA Transportation Officials: Washington, DC. Aashto standard specifications for transportation materials and methods of sampling and testing. *Washington DC, USA*, 15th ed., 1990.

[20] L. R. Watkins R. K., Anderson. Structural mechanics of buried pipes. *CRC press*, pages 22–57, 2000.

[21] Mohammad Shishesaz and Mohammad Reza Shishesaz. Applicability of medium density polyethylene gas pipes in hot climate areas of south-west iran. *Iranian Polymer Journal*, 17(7):503–517, 2008.

[22] Mohamad Reza Shishesaz. Determination of design parameters in large size reinforced polyethylene pipes. *Iranian Polymer Journal*, 12(2):109–114, 2003.

[23] Wen-mo Chen. *Investigation of the stress intensity factors at sharp corners of arbitrary cutouts in finite plates.* PhD thesis, Georgia Institute of Technology, 1977.

[24] Joseph Edward Shigley. *Shigley's mechanical engineering design.* Tata McGraw-Hill Education, 2011.

[25] BN Cole. Strategy for cross-bores in high pressure containers. *Journal of Mechanical Engineering Science*, 11(2):151–161, 1969.

[26] M. Timoshenko and J.N. Goodler. Theory of elasticity, 2nd edition. *New York: McGraw-Hill*, 1951.

[27] Mohamed Salama and Norio Hasebe. Stress concentration factors at an elliptical hole on the interface between bonded dissimilar half-planes under bending moment. 1996.

[28] KN Shivakumar and JC Newman Jr. Stress concentration equations for straight-shank and countersunk holes in plates. 1995.

[29] BN Cole, G Craggs, and I Ficenec. Strength of cylinders containing radial or offset cross-bores. *Journal of Mechanical Engineering Science*, 18(6):279–286, 1976.

[30] LM Masu. Plastic analysis and cross bore size effects on the fatigue strength of thick walled cylinders. *East African Journal of Engineering*, 1(2):22, 1994.

[31] LM Masu and G Craggs. Fatigue strength of thick-walled cylinders containing cross bores with blending features. *Proceedings of the Institution of Mechanical Engineers, Part C: Journal of Mechanical Engineering Science*, 206(5):299–309, 1992.

[32] JH Faupel and DB Harris. Stress concentration in heavy-walled cylindrical pressure vessels-effect of elliptic and circular side holes. *Industrial and Engineering Chemistry*, 49(12):1979–1986, 1957.

[33] JC Gerdeen and RE Smith. Experimental determination of stress-concentration factors in thick-walled cylinders with crossholes and sideholes. *Experimental Mechanics*, 12(11):530–536, 1972.

[34] LM Masu. Stress and fatigue behavior model for a pressure vessel containing a cross bore. *East African Journal of Engineering*, 1(2):7–21, 1994.

[35] T Iwadate, K Chiba, J Watanabe, S Mima, K Tokai, and H Takedo. Safety analysis at a cross bore corner of high pressure polyethylene reactors. In *International Conference of Pressure Vessels and Piping: Materials, Nuclear Engineering and Solar Energy. Trans. ASME*, volume 103, pages 117–125, 1981.

[36] CL Tan. Stress redistributions in thick-walled cylinders due to the introduction of a cross-bore after autofrettage. *The Journal of Strain Analysis for Engineering Design*, 21(3):177–183, 1986.

[37] LM Masu. Numerical analysis of cylinders containing circular offset cross-bores. *International journal of pressure vessels and piping*, 75(3):191–196, 1998.

[38] The Plastic Pipe Institute. Handbook of polyethylene pipe. *Washington DC*, 7: 261–303, 2006.

[39] Folkman S. Moser A. P. Buried pipe design. *Mc-Graw Hill book company*, third edition(Chapter 7):387, 2008.

[40] Andrzej Kolonko and Cezary Madryas. Modernization of underground pipes in towns in poland. *Tunnelling and Underground Space Technology*, 11(2):215–220, 1996.

[41] Goddard J.B. Plastic pipe design. *Columbus, Ohio, ADS*, Technical note 4.103: 1–30, 1994.

[42] HA Alawaji. Temperature effects on polyethylene (hdpe) and fiberglass (grp) pipes, 2008.

[43] SH Teoh and EH Ong. Tensile and pressure rupture behaviour of flow-formed high density polyethylene pipes. *polymer*, 36(1):101–107, 1995.

[44] Hossein Talebi, Mohammad Silani, and Timon Rabczuk. Concurrent multiscale modeling of three dimensional crack and dislocation propagation. *Advances in Engineering Software*, 80:82–92, 2015.

[45] Hossein Talebi, Mohammad Silani, Stephane PA Bordas, Pierre Kerfriden, and Timon Rabczuk. A computational library for multiscale modeling of material failure. *Computational Mechanics*, 53(5):1047–1071, 2014.

[46] T Rabczuk and J Eibl. Modelling dynamic failure of concrete with meshfree methods. *International Journal of Impact Engineering*, 32(11):1878–1897, 2006.

[47] Timon Rabczuk and Ted Belytschko. Application of particle methods to static fracture of reinforced concrete structures. *International Journal of Fracture*, 137 (1-4):19–49, 2006.

[48] PR Budarapu and T Rabczuk. Multiscale methods for fracture: A review. *Journal of the Indian Institute of Science*, 97(3):339–376, 2017.

[49] Timon Rabczuk. Computational methods for fracture in brittle and quasi-brittle solids: state-of-the-art review and future perspectives. *ISRN Applied Mathematics*, 2013, 2013.

[50] Hamid Ahmad Mehrabi and Jeremy Bowman. Electrofusion welding of cross-linked polyethylene pipes. *Iranian Polymer Journal*, 6:195–204, 1997.

[51] Kevin E Harris. Squeeze-off and gel patch repair methods for polyethylene pipe in natural gas distribution lines. 2007.

[52] Rochefort W. E Willie E. and Green H. Polyethylene pipe patching systems and methods. *U.S. patent application 186256*, 2006.

[53] JD Mathias, Mf Grediac, and X Balandraud. On the bidirectional stress distribution in rectangular bonded composite patches. *International Journal of Solids and Structures*, 43(22-23):6921–6947, 2006.

[54] K.M Chua. Time dependence interaction of soil and flexible pipe, ph.d. thesis. *Texas ATM university, college station*, 1986.

[55] CF Popelar, CH Popelar, and VH Kenner. Viscoelastic material characterization and modeling for polyethylene. *Polymer Engineering and Science*, 30(10):577–586, 1990.

[56] A. Nasirian. Investigating the application of polyethylene gas pipes for gas trasportation, master's thesis. *Shahid Chamran University, Ahvaz, Iran*, 2007.

[57] R. Khademi Zahedi. Stress distribution in patch repaired polyethylene gas pipes., master's thesis. *Shahid Chamran University, Ahvaz, Iran*, 2011.

[58] Nam Vu-Bac, Tom Lahmer, Xiaoying Zhuang, Trung Nguyen-Thoi, and Timon Rabczuk. A software framework for probabilistic sensitivity analysis for computationally expensive models. *Advances in Engineering Software*, 100:19–31, 2016.

[59] Khader M Hamdia, Mohammad Silani, Xiaoying Zhuang, Pengfei He, and Timon Rabczuk. Stochastic analysis of the fracture toughness of polymeric nanoparticle composites using polynomial chaos expansions. *International Journal of Fracture*, 206(2):215–227, 2017.

[60] Timon Rabczuk, Robert Gracie, Jeong-Hoon Song, and Ted Belytschko. Immersed particle method for fluid–structure interaction. *International Journal for Numerical Methods in Engineering*, 81(1):48–71, 2010.

[61] Andre K Geim and Konstantin S Novoselov. The rise of graphene. In *Nanoscience and Technology: A Collection of Reviews from Nature Journals*, pages 11–19. World Scientific, 2010.

[62] Marcelo ZS Flores, Pedro AS Autreto, Sergio B Legoas, and Douglas S Galvao. Graphene to graphane: a theoretical study. *Nanotechnology*, 20(46):465704, 2009.

[63] AHN Shirazi, R Abadi, M Izadifar, N Alajlan, and T Rabczuk. Mechanical responses of pristine and defective c3n nanosheets studied by molecular dynamics simulations. *Computational Materials Science*, 147:316–321, 2018.

[64] Xiaozhi Xu, Zhihong Zhang, Jichen Dong, Ding Yi, Jingjing Niu, Muhong Wu, Li Lin, Rongkang Yin, Mingqiang Li, Jingyuan Zhou, et al. Ultrafast epitaxial growth of metre-sized single-crystal graphene on industrial cu foil. *Science bulletin*, 62(15):1074–1080, 2017.

[65] Xuan Wang, Linjie Zhi, and Klaus Mullen. Transparent, conductive graphene electrodes for dye-sensitized solar cells. *Nano letters*, 8(1):323–327, 2008.

[66] dS Ghosh, I Calizo, D Teweldebrhan, Evghenii P Pokatilov, Denis L Nika, Alexander A Balandin, Wenzhong Bao, Feng Miao, and C Ning Lau. Extremely high thermal conductivity of graphene: Prospects for thermal management applications in nanoelectronic circuits. *Applied Physics Letters*, 92(15):151911, 2008.

[67] Toby Sainsbury, Sam Gnaniah, Steve J Spencer, Sandro Mignuzzi, Natalie A Belsey, Keith R Paton, and Amro Satti. Extreme mechanical reinforcement in graphene oxide based thin-film nanocomposites via covalently tailored nanofiller matrix compatibilization. *Carbon*, 114:367–376, 2017.

[68] Ali Rajabpour, Saeed Bazrafshan, and Sebastian Volz. Carbon-nitride 2d nanostructures: thermal conductivity and interfacial thermal conductance with the silica substrate. *Physical Chemistry Chemical Physics*, 21(5):2507–2512, 2019.

[69] Mohammed A Msekh, NH Cuong, Goangseup Zi, P Areias, X Zhuang, and Timon Rabczuk. Fracture properties prediction of clay/epoxy nanocomposites with interphase zones using a phase field model. *Engineering Fracture Mechanics*, 188: 287–299, 2018.

[70] Khader M Hamdia, Mohammad Silani, Xiaoying Zhuang, Pengfei He, and Timon Rabczuk. Stochastic analysis of the fracture toughness of polymeric nanoparticle composites using polynomial chaos expansions. *International Journal of Fracture*, 206(2):215–227, 2017.

[71] Atiyeh Alsadat Mousavi, Behrouz Arash, Xiaoying Zhuang, and Timon Rabczuk. A coarse-grained model for the elastic properties of cross linked short carbon nanotube/polymer composites. *Composites Part B: Engineering*, 95:404–411, 2016.

[72] Behrouz Arash, Harold S Park, and Timon Rabczuk. Coarse-grained model of the j-integral of carbon nanotube reinforced polymer composites. *Carbon*, 96: 1084–1092, 2016.

[73] Kateryna Shavanova, Yulia Bakakina, Inna Burkova, Ivan Shtepliuk, Roman Viter, Arnolds Ubelis, Valerio Beni, Nickolaj Starodub, Rositsa Yakimova, and Volodymyr Khranovskyy. Application of 2d non-graphene materials and 2d oxide nanostructures for biosensing technology. *Sensors*, 16(2):223, 2016.

[74] Bohayra Mortazavi and Said Ahzi. Molecular dynamics study on the thermal conductivity and mechanical properties of boron doped graphene. *Solid State Communications*, 152(15):1503–1507, 2012.

[75] H Tanaka, Y Kawamata, H Simizu, T Fujita, H Yanagisawa, S Otani, and C Oshima. Novel macroscopic bc3 honeycomb sheet. *Solid state communications*, 136 (1):22–25, 2005.

[76] Yu Qie, Junyi Liu, Shuo Wang, Sheng Gong, and Qiang Sun. C3b monolayer as an anchoring material for lithium-sulfur batteries. *Carbon*, 129:38–44, 2018.

[77] Yanan Tang, Xiao Cui, Weiguang Chen, Dalei Zhu, Huaduo Chai, and Xianqi Dai. A theoretical study on metal atom-modified bc3 sheets for effects of gas molecule adsorptions. *Applied Physics A*, 124(6):434, 2018.

[78] Sadegh Mehdi Aghaei, MM Monshi, I Torres, SMJ Zeidi, and I Calizo. Dft study of adsorption behavior of no, co, no2, and nh3 molecules on graphene-like bc3: A search for highly sensitive molecular sensor. *Applied Surface Science*, 427:326–333, 2018.

[79] Yanan Tang, Minghui Zhang, Zigang Shen, Jincheng Zhou, Huadou Chai, and Xianqi Dai. Non-metal atom anchored bc 3 sheet: a promising low-cost and high-activity catalyst for co oxidation. *New Journal of Chemistry*, 42(5):3770–3780, 2018.

[80] Bohayra Mortazavi, Masoud Shahrokhi, Mostafa Raeisi, Xiaoying Zhuang, Luiz Felipe C. Periera, and Timon Rabczuk. Outstanding strength, optical characteristics and thermal conductivity of graphene-like bc3 and bc6n semiconductors. *Carbon*, Manuscript Number: CARBON-D-19-00480:Under review, 2019.

[81] Nurul Haque Bhuiyan. Synthesis of molybdenum (iv) sulphide: I. reaction of hydrogen sulphide with molybdenum (vi) oxide in the presence of ammonium chloride. *Journal of Chemical Technology and Biotechnology*, 28(11):745–750, 1978.

[82] Intek Song, Chibeom Park, and Hee Cheul Choi. Synthesis and properties of molybdenum disulphide: from bulk to atomic layers. *RSC Advances*, 5(10):7495–7514, 2015.

[83] Intek Song, Chibeom Park, Misun Hong, Jaeyoon Baik, Hyun-Joon Shin, and Hee Cheul Choi. Patternable large-scale molybdenium disulfide atomic layers grown by gold-assisted chemical vapor deposition. *Angewandte Chemie International Edition*, 53(5):1266–1269, 2014.

[84] V Giacometti, B Radisavljevic, A Radenovic, J Brivio, and A Kis. Single-layer mos2 transistors. *Nat. Nanotechnol*, 6:147–150, 2011.

[85] Qing Hua Wang, Kourosh Kalantar-Zadeh, Andras Kis, Jonathan N Coleman, and Michael S Strano. Electronics and optoelectronics of two-dimensional transition metal dichalcogenides. *Nature nanotechnology*, 7(11):699, 2012.

[86] Bohayra Mortazavi, Alireza Ostadhossein, Timon Rabczuk, and Adri CT Van Duin. Mechanical response of all-mos2 single-layer heterostructures: a reaxff investigation. *Physical Chemistry Chemical Physics*, 18(34):23695–23701, 2016.

[87] Simone Bertolazzi, Jacopo Brivio, and Andras Kis. Stretching and breaking of ultrathin mos2. *ACS nano*, 5(12):9703–9709, 2011.

[88] Andres Castellanos-Gomez, Menno Poot, Gary A Steele, Herre SJ Van der Zant, Nicolás Agraït, and Gabino Rubio-Bollinger. Mechanical properties of freely suspended semiconducting graphene-like layers based on mos 2. *Nanoscale research letters*, 7(1):1–4, 2012.

[89] Junwen Li, Nikhil V Medhekar, and Vivek B Shenoy. Bonding charge density and ultimate strength of monolayer transition metal dichalcogenides. *The Journal of Physical Chemistry C*, 117(30):15842–15848, 2013.

[90] Junhua Zhao, Jin-Wu Jiang, and Timon Rabczuk. Temperature-dependent mechanical properties of single-layer molybdenum disulphide: Molecular dynamics nanoindentation simulations. *Applied Physics Letters*, 103(23):231913, 2013.

[91] Jan-Ole Joswig, Tommy Lorenz, Tsegabirhan Berhane Wendumu, Sibylle Gemming, and Gotthard Seifert. Optics, mechanics, and energetics of two-dimensional mos2 nanostructures from a theoretical perspective. *Accounts of chemical research*, 48(1):48–55, 2015.

[92] C Ataca, Mehmet Topsakal, E Akturk, and SJTJ Ciraci. A comparative study of lattice dynamics of three-and two-dimensional mos2. *The Journal of Physical Chemistry C*, 115(33):16354–16361, 2011.

[93] Khanh Q Dang and Douglas E Spearot. Effect of point and grain boundary defects on the mechanical behavior of monolayer mos2 under tension via atomistic simulations. *Journal of Applied Physics*, 116(1):013508, 2014.

[94] JL Feldman. Elastic constants of 2h-mos2 and 2h-nbse2 extracted from measured dispersion curves and linear compressibilities. *Journal of Physics and Chemistry of Solids*, 37(12):1141–1144, 1976.

[95] Tommy Lorenz, Jan-Ole Joswig, and Gotthard Seifert. Stretching and breaking of monolayer mos2—an atomistic simulation. *2D Materials*, 1(1):011007, 2014.

[96] Wu Zhou, Xiaolong Zou, Sina Najmaei, Zheng Liu, Yumeng Shi, Jing Kong, Jun Lou, Pulickel M Ajayan, Boris I Yakobson, and Juan-Carlos Idrobo. Intrinsic structural defects in monolayer molybdenum disulfide. *Nano letters*, 13(6):2615–2622, 2013.

[97] Sina Najmaei, Zheng Liu, Wu Zhou, Xiaolong Zou, Gang Shi, Sidong Lei, Boris I Yakobson, Juan-Carlos Idrobo, Pulickel M Ajayan, and Jun Lou. Vapour phase growth and grain boundary structure of molybdenum disulphide atomic layers. *Nature materials*, 12(8):754–759, 2013.

[98] Sydney Ross and Alan Sussman. Surface oxidation of molybdenum disulfide. *The Journal of Physical Chemistry*, 59(9):889–892, 1955.

[99] Santosh KC, Roberto C Longo, Robert M Wallace, and Kyeongjae Cho. Surface oxidation energetics and kinetics on mos2 monolayer. *Journal of Applied Physics*, 117(13):135301, 2015.

[100] A Baker et al. *Bonded repair of aircraft structures*, volume 7. Springer Science and Business Media, 2012.

[101] Det Norske Veritas. Dnv-os-f101 2013: Submarine pipeline systems. *Oslo, Norway*, 2013.

[102] AA Barbosa, AP Teixeira, and C Guedes Soares. Strength analysis of corroded pipelines subjected to internal pressure and bending moment. In *Progress in the Analysis and Design of Marine Structures*, pages 803–812. CRC Press, 2017.

[103] FA Simonen. Pressure vessels and piping systems: Reliability, risk and safety assessment. *Encyclopedia of Desalination and Water Resources (DESWARE), UK*, 2010.

[104] Xiaoben Liu, Mengying Xia, Dinaer Bolati, Jianping Liu, Qian Zheng, and Hong Zhang. An ann-based failure pressure prediction method for buried high-strength pipes with stray current corrosion defect. *Energy Science and Engineering*, 8(1): 248–259, 2020.

[105] Chio Lam and Wenxing Zhou. Statistical analyses of incidents on onshore gas transmission pipelines based on phmsa database. *International Journal of Pressure Vessels and Piping*, 145:29–40, 2016.

[106] Abolfazl Zolfaghari and Moein Izadi. Burst pressure prediction of cylindrical vessels using artificial neural network. *Journal of Pressure Vessel Technology*, 142(3), 2020.

[107] Costel Plescan, Mariana D Stanciu, and Matyas Szasz. The effect of internal pressure on radial strain of steel pipe subjected to monotonic and cyclic loading. *Materials*, 12(18):2849, 2019.

[108] Xiangpeng Luo, Jianfeng Shi, and Jinyang Zheng. Mechanism of slow crack growth in polyethylene: a finite element approach. In *Pressure Vessels and Piping Conference*, volume 57007, page V06BT06A047. American Society of Mechanical Engineers, 2015.

[109] Jingyu Zhang. *Experimental study of stress cracking in high density polyethylene pipes*. Drexel University, 2005.

[110] S Laczek, J Rys, and AP Zielinski. Load capacity of a thick-walled cylinder with a radial hole. *International Journal of Pressure Vessels and Piping*, 87(8):433–439, 2010.

[111] GB Sinclair and M Kondo. On the stress concentration at sharp re-entrant corners in plates. *International journal of mechanical sciences*, 26(9-10):477–487, 1984.

[112] C Inglis. Stress in a plate due to the presence of sharp corners and cracks. *Trans. Roy. Inst. Naval Architects*, 60:219–241, 1913.

[113] Andreas Frank. *Fracture mechanics based lifetime assessment and long-term failure behavior of polyethylene pressure pipes*. na, 2010.

[114] LM Masu. Cross bore configuration and size effects on the stress distribution in thick-walled cylinders. *International journal of pressure vessels and piping*, 72(2): 171–176, 1997.

[115] R. O. Ritchie. Mechanisms of fatigue-crack propagation in ductile and brittle solids. *International Journal of Fracture*, 100:55–83, 1999.

[116] S. Maiti and P. H. Geubelle. Cohesive modeling of fatigue crack retardation in polymers: Crack closure effect. *Engineering Fracture Mechanics*, 7(3):22–41, 2006.

[117] C. S. Shin and C. Q. Cai. A model for evaluating the effect of fatigue crack repair by the infiltration method. *Fatigue Fracture Engineering Materials Structure*, 23: 835–845, 2000.

[118] *https://www.dictionary.com/browse/patch.* .

[119] Ian D Moore. Buried pipes and culverts. In *Geotechnical and geoenvironmental engineering handbook*, pages 541–567. Springer, 2001.

[120] W Michael Lai, David H Rubin, Erhard Krempl, and David Rubin. *Introduction to continuum mechanics*. Butterworth-Heinemann, 2009.

[121] Ameri M. Tabatabaii A. and Behbahani H. Prediction of asphalt cover temperature in city of ahvaz (iran). *Journal of Engineering, Tabriz University, College of Engineering*, 22, 1999, (in persian).

[122] The Plastic Pipe Institute. Thermal expansion and contraction in plastics piping systems. TR-21, 2001.

[123] Chevron Philips Chemical Company LP. Buried pipe design. *Bull, PP900*, Book 2(Ch. 7):81–115, 2003.

[124] I.; Miska S.Z.; Mitchell R.D. Aadnoy, B. S.; Cooper and M. L. Payne. *Advanced Drilling and Well Technology*. SPE publications, 2009.

[125] Chris O'Connor. The nature of polyethylene pipe failure. *Modern Plastics Worldwide*, 88(2):20–22, 2011.

[126] International Organization For Standardization (ISO) 12162. Thermoplastics materials for pipes and fittings for pressure applications – classification and designation – overall service (design) coefficient. 2004.

[127] DIN EN ISO 9080. Plastics piping and ducting systems - determination of the long-term hydrostatic strength of thermoplastics materials in pipe form by extrapolation. 2003.

[128] Andreas Frank, G Pinter, and RW Lang. Prediction of the remaining lifetime of polyethylene pipes after up to 30 years in use. *Polymer Testing*, 28(7):737–745, 2009.

[129] European Committee for Standardization. Plastic piping systems for the supply of gaseous fuels – polyethylene (pe) – part 1: General. EN 1555 – 1, 1996.

[130] T Christopher, BSV Rama Sarma, PK Govindan Potti, B Nageswara Rao, and K Sankarnarayanasamy. A comparative study on failure pressure estimations of unflawed cylindrical vessels. *International Journal of Pressure Vessels and Piping*, 79(1):53–66, 2002.

[131] Aseer Brabin, T Christopher, and Nageswara Rao. Investigation on failure behavior of unflawed steel cylindrical pressure vessels using fea. *Multidiscipline Modeling in Materials and Structures*, 2009.

[132] Zbigniew Brzoska. *Strength of structural elements*, volume 26. Elsevier, 2013.

[133] American Society for Testing and Material. Plastic pipe and building products. in astm annual book of astm standards. *American Society for Testing and Material: Philadelphia, PA, USA.*, 1991.

[134] Uponor Aldyl Company. Polyethylene gas pipe systems, uponor aldyl company installation guide. *Uponor Aldyl Company*, 2004.

[135] Kenneth H Huebner, Donald L Dewhirst, Douglas E Smith, and Ted G Byrom. *The finite element method for engineers*. John Wiley and Sons, 2001.

[136] Symons I. F. International mdpe yellow gas pipe. *J-M Manufacturing Company Inc. catalogue.*, 1997.

[137] European Committee for Standardization. En 1555 – 1, plastic piping systems for the supply of gaseous fuels – polyethylene (pe). *Part 1: General*, 1996.

[138] Lori Freitag, P Plassmann, and M Jones. An efficient parallel algorithm for mesh smoothing. Technical report, Argonne National Lab., IL (United States), 1995.

[139] Anand Pardhanani and Graham F Carey. Optimization of computational grids. *Numerical Methods for Partial Differential Equations*, 4(2):95–117, 1988.

[140] Pablo D Zavattieri, Enzo A Dari, and GUSTAVO C BUSCAGLIA. Optimization strategies in unstructured mesh generation. *International Journal for Numerical Methods in Engineering*, 39(12):2055–2071, 1996.

[141] Release Ansys. 11.0 documentation for ansys. *Theory reference*, 2007.

[142] Tina Louise Panontin and Sheri Sheppard. Fatigue and fracture mechanics: Twenty-ninth volume. ASTM, 1999.

[143] Zhi Bin Zhu, Xiao Xiang Yang, Li Jing Chen, Nai Chang Lin, Zhi Tuo Wang, and Zhe Fang Wang. Finite element analysis of polyethylene pipe butt fusion joints with circumferential surface cracks. In *Advanced Materials Research*, volume 785, pages 1151–1158. Trans Tech Publ, 2013.

[144] *https://www.comsol.com/blogs/singularities-in-finite-element-models-dealing-with-red-spots/*. .

[145] Bill Bruce, Nancy Porter, George Ritter, Matt Boring, Mark Lozev, Ian Harris, Bill Mohr, Dennis Harwig, Robin Gordon, Chris Neary, et al. Internal repair of pipelines. Technical report, Edison Welding Institute, 2005.

[146] Reza Khademi Zahedi, Pouyan Alimouri, Hooman Khademi Zahedi, and Mohammad Shishesaz. Investigating peak stresses in fitting and repair patches of buried polyethylene gas pipes. *Frontiers of Structural and Civil Engineering*, pages 1–22.

[147] Mohammadreza Izadifar, Rouzbeh Abadi, Ali Hossein Nezhad Shirazi, Naif Alajlan, and Timon Rabczuk. Nanopores creation in boron and nitrogen doped polycrystalline graphene: A molecular dynamics study. *Physica E: Low-dimensional Systems and Nanostructures*, 99:24–36, 2018.

[148] Timon Rabczuk, Mohammad Azadi Kakavand, Raahul Palanivel Uma, Ali Hossein Nezhad Shirazi, and Meysam Makaremi. Thermal conductance along hexagonal boron nitride and graphene grain boundaries. *Energies*, 11(6):1553, 2018.

[149] Ali Hossein Nezhad Shirazi. Molecular dynamics investigation of mechanical properties of single-layer phagraphene. *Frontiers of Structural and Civil Engineering*, pages 1–9, 2018.

[150] Rouzbeh Abadi, Raahul Palanivel Uma, Mohammadreza Izadifar, and Timon Rabczuk. The effect of temperature and topological defects on fracture strength of grain boundaries in single-layer polycrystalline boron-nitride nanosheet. *Computational Materials Science*, 123:277–286, 2016.

[151] Rouzbeh Abadi, Raahul Palanivel Uma, Mohammadreza Izadifar, and Timon Rabczuk. Investigation of crack propagation and existing notch on the mechanical response of polycrystalline hexagonal boron-nitride nanosheets. *Computational Materials Science*, 131:86–99, 2017.

[152] Rouzbeh Abadi, Ali Hossein Nezhad Shirazi, Mohammadreza Izadifar, Mohammad Sepahi, and Timon Rabczuk. Fabrication of nanopores in polycrystalline boron-nitride nanosheet by using si, sic and diamond clusters bombardment. *Computational Materials Science*, 145:280–290, 2018.

[153] Bohayra Mortazavi and Timon Rabczuk. Multiscale modeling of heat conduction in graphene laminates. *Carbon*, 85:1–7, 2015.

[154] Bohayra Mortazavi, Said Ahzi, Valerie Toniazzo, and Yves Remond. Nitrogen doping and vacancy effects on the mechanical properties of graphene: A molecular dynamics study. *Physics Letters A*, 376(12-13):1146–1153, 2012.

[155] Bohayra Mortazavi and Said Ahzi. Thermal conductivity and tensile response of defective graphene: A molecular dynamics study. *Carbon*, 63:460–470, 2013.

[156] Bohayra Mortazavi and Gianaurelio Cuniberti. Atomistic modeling of mechanical properties of polycrystalline graphene. *Nanotechnology*, 25(21):215704, 2014.

[157] Bohayra Mortazavi. Ultra high stiffness and thermal conductivity of graphene like c3n. *Carbon*, 118:25–34, 2017.

[158] Bohayra Mortazavi, Gianaurelio Cuniberti, and Timon Rabczuk. Mechanical properties and thermal conductivity of graphitic carbon nitride: A molecular dynamics study. *Computational Materials Science*, 99:285–289, 2015.

[159] Bohayra Mortazavi, Masoud Shahrokhi, Xiaoying Zhuang, and Timon Rabczuk. Boron–graphdiyne: a superstretchable semiconductor with low thermal conductivity and ultrahigh capacity for li, na and ca ion storage. *Journal of Materials Chemistry A*, 6(23):11022–11036, 2018.

[160] Alexander Stukowski. Visualization and analysis of atomistic simulation data with ovito–the open visualization tool. *Modelling and Simulation in Materials Science and Engineering*, 18(1):015012, 2009.

[161] DH Tsai. The virial theorem and stress calculation in molecular dynamics. *The Journal of Chemical Physics*, 70(3):1375–1382, 1979.

[162] Bohayra Mortazavi, Yves Remond, Said Ahzi, and Valerie Toniazzo. Thickness and chirality effects on tensile behavior of few-layer graphene by molecular dynamics simulations. *Computational Materials Science*, 53(1):298–302, 2012.

[163] Bohayra Mortazavi, Obaidur Rahaman, Timon Rabczuk, and Luiz Felipe C Pereira. Thermal conductivity and mechanical properties of nitrogenated holey graphene. *Carbon*, 106:1–8, 2016.

[164] Katsuyuki Matsunaga, Craig Fisher, and Hideaki Matsubara. Tersoff potential parameters for simulating cubic boron carbonitrides. *Japanese Journal of Applied Physics*, 39(1A):L48, 2000.

[165] T FANG, W CHANG, and Jhih-Chin Yang. Temperature effect on mechanical properties of graphene sheets under tensile loading. *Dig. J. Nanomater. Biostruct*, 7:1811–1816, 2012.

[166] Dietmar Gross and Thomas Seelig. *Fracture mechanics: with an introduction to micromechanics*. Springer, 2017.

[167] Barry N Whittaker, Raghu N Singh, and Gexin Sun. *Rock fracture mechanics: principles, design, and applications*, volume 570. Elsevier Amsterdam, 1992.

[168] Hasan Metin Aktulga, Sagar A Pandit, Adri CT van Duin, and Ananth Y Grama. Reactive molecular dynamics: Numerical methods and algorithmic techniques. *SIAM Journal on Scientific Computing*, 34(1):C1–C23, 2012.

[169] Hongwei Bao, Yuhong Huang, Zhi Yang, Yunjin Sun, Yu Bai, Yaping Miao, Paul K Chu, Kewei Xu, and Fei Ma. Molecular dynamics simulation of nanocrack propagation in single-layer mos2 nanosheets. *The Journal of Physical Chemistry C*, 122 (2):1351–1360, 2018.

[170] Alireza Ostadhossein, Ali Rahnamoun, Yuanxi Wang, Peng Zhao, Sulin Zhang, Vincent H Crespi, and Adri CT van Duin. Reaxff reactive force-field study of molybdenum disulfide (mos2). *The journal of physical chemistry letters*, 8(3): 631–640, 2017.

[171] Reza Khademi Zahedi, AHN Shirazi, Pouyan Alimouri, Naif Alajlan, and Timon Rabczuk. Mechanical properties of graphene-like bc3; a molecular dynamics study. *Computational Materials Science*, 168:1–10, 2019.

[172] Yung-Chang Lin, Dumitru O Dumcenco, Ying-Sheng Huang, and Kazu Suenaga. Atomic mechanism of the semiconducting-to-metallic phase transition in single-layered mos 2. *Nature nanotechnology*, 9(5):391, 2014.

[173] Md Mahbubul Islam, Alireza Ostadhossein, Oleg Borodin, A Todd Yeates, William W Tipton, Richard G Hennig, Nitin Kumar, and Adri CT van Duin. Reaxff molecular dynamics simulations on lithiated sulfur cathode materials. *Physical Chemistry Chemical Physics*, 17(5):3383–3393, 2015.

[174] Kichul Yoon, Alireza Ostadhossein, and Adri CT van Duin. Atomistic-scale simulations of the chemomechanical behavior of graphene under nanoprojectile impact. *Carbon*, 99:58–64, 2016.

[175] N Vu-Bac, MA Bessa, Timon Rabczuk, and Wing Kam Liu. A multiscale model for the quasi-static thermo-plastic behavior of highly cross-linked glassy polymers. *Macromolecules*, 48(18):6713–6723, 2015.

[176] Tongwei Han, Ying Luo, and Chengyuan Wang. Effects of temperature and strain rate on the mechanical properties of hexagonal boron nitride nanosheets. *Journal of Physics D: Applied Physics*, 47(2):025303, 2013.

[177] Zhi Yang, Yuhong Huang, Fei Ma, Yunjin Sun, Kewei Xu, and Paul K Chu. Temperature and strain-rate effects on the deformation behaviors of nano-crystalline graphene sheets. *The European Physical Journal B*, 88(5):135, 2015.

[178] R.W. Cloughi. The finite element method in plane stress analysis. *Proceeding of 2nd ASCE Conference on Electronic Computation, Pittsburgh PA, September 8-9*, 1960.

[179] Alan Arnold Griffith. Vi. the phenomena of rupture and flow in solids. *Philosophical transactions of the royal society of london. Series A, containing papers of a mathematical or physical character*, 221(582-593):163–198, 1921.

[180] MA. Msekh. Phase field modeling for fracture with application to homogeneous and heterogeneous materials, phd's thesis. *Bauhaus University Weimar, Germany*, 2017.

[181] Reza Khademi-Zahedi and Pouyan Alimouri. Finite element model updating of a large structure using multi-setup stochastic subspace identification method and bees optimization algorithm. *Frontiers of Structural and Civil Engineering*, 13(4): 965–980, 2019.

[182] Olek C Zienkiewicz and Robert L Taylor. *The finite element method for solid and structural mechanics*. Elsevier, 2005.

[183] Bryan J Mac Donald. *Practical stress analysis with finite elements*. Glasnevin publishing, 2007.

[184] Ansys. Pennsylvania technology directory. p. 25. 1999.

[185] ANSYS. Inc. Ansys academic research mechanical, release 16.2, help system. https://www.ansys.com/. 2015.

[186] Paul Dufour. Picking an element type for structural analysis. *Belcan Engineering Group*, page 5, 2003.

[187] R Mahdavinejad. Finite element dimensional design and modeling of an ultrasonic transducer. 2005.

[188] ANSYS INC. *Theory Reference for the Mechanical APDL and Mechanical Applications. https://www.ansys.com/*. ANSYS, INC, 2009.

[189] Richard L Anderson, H Christopher Greenwel, James L Suter, Rebecca M Jarvis, and Peter V Coveney. Towards the design of new and improved drilling fluid additives using molecular dynamics simulations. *Anais da Academia Brasileira de Ciências*, 82(1):43–60, 2010.

[190] Adam Hospital, Josep Ramon Goñi, Modesto Orozco, and Josep L Gelpí. Molecular dynamics simulations: advances and applications. *Advances and applications in bioinformatics and chemistry: AABC*, 8:37, 2015.

[191] Joachim Hein, Fiona Reid, Lorna Smith, Ian Bush, Martyn Guest, and Paul Sherwood. On the performance of molecular dynamics applications on current high-end systems. *Philosophical Transactions of the Royal Society A: Mathematical, Physical and Engineering Sciences*, 363(1833):1987–1998, 2005.

Academic Curriculum Vitae

Reza Khademi Zahedi

Institute of Structural Mechanics
Bauhaus-University Weimar
Marienstrasse 15
99423 Weimar
Germany
Email: reza.khademi.zahedi@uni-weimar.de
reza.khademi.zahedi@gmail.com

Educations

- Ph.D Candidate in Chair of Computational Mechanics: Institute of Structural Mechanics, Faculty of Civil Engineering, Bauhaus-University Weimar, Germany, 2015- 2020.
- Master of Mechanical Engineering: Applied Design (Solid Mechanics), Shahid Chamran University, Ahvaz, Iran, 2008-2011. .
- Bachelor of Mechanical Engineering: Thermo Fluid, Shiraz University, Shiraz, Iran, 1999-2003.

Publications

1. **R. Khademi Zahedi**, P. Alimouri, H. Khademi Zahedi and M. Shishesaz. *Investigating peak stresses in fitting and repair patches of buried polyethylene gas pipes.*

Frontiers of Structural and Civil Engineering, 14(1):147-168, 2020. https://doi.org/10.1007/s11709-019-0587-6.

2. **R. Khademi Zahedi**, AHN. Shirazi, P. Alimouri, N. Alajlan, and T. Rabczuk. *Mechanical properties of graphene-like BC3; a molecular dynamics study.* Computational Materials Science, 168:1-10, 2019.

3. **R. Khademi Zahedi**, and P. Alimouri. *Finite element model updating of a large structure using multi-setup stochastic subspace identification method and bees optimization algorithm.* Frontiers of Structural and Civil Engineering, 13(4):965-980, 2019.

4. **R. Khademi Zahedi**. *Application of the finite element method for evaluating the stress distribution in buried damaged polyethylene gas pipes.* Underground Space, 4(1):59-71, 2019.

5. **R. Khademi Zahedi**, and M. Shishesaz. *Application of a finite element method to stress distribution in buried patch repaired polyethylene gas pipe.* Underground Space, 4(1):48-58, 2019.

6. **R. Khademi Zahedi**, and P. Alimouri. *Finite element analysis to the effect of thermo-mechanical loads on stress distribution in buried polyethylene gas pipes jointed by electrofusion sockets, repaired by PE patches.* Energies, 11(10):2818, 2018.

7. **R. Khademi Zahedi**, P. Alimouri, H. Nguyen-Xuan and T. Rabczuk. *Crack detection in a beam on elastic foundation using differential quadrature method and the Bees algorithm optimization.* International Conference on Advances in Computational Mechanics, pages:439-460. Springer, 2017.